Centre Énergie, Matériaux Télécommunications

OXYGEN REDUCTION REACTION ON ORIENTED THIN FILMS: AN ALTERNATIVE APPROACH TO ELECTROCATALYTIC STUDIES ON MODEL SURFACES

Par

Cybelle Palma de Oliveira Soares

Thèse présentée pour l'obtention du grade de Philosophiae Doctor (Ph.D.)
en sciences de Énergie et Matériaux

Jury d'évaluation

Président du jury et examinateur interne:	Andreas Peter Ruediger Institut national de la recherche scientifique
Examinateur externe:	Aaron Marshall College of Engineering University of Canterbury
Examinateur externe:	Steen Brian Schougaard Université du Québec à Montréal
Directeur de recherche:	Ana Tavares Institut national de la recherche scientifique
Codirecteur de recherche:	Daniel Guay Institut national de la recherche scientifique
Codirecteur de recherche externe:	Guy Denuault University of Southampton

ACKNOWLEDGEMENTS

I would like to acknowledge all the amazing people who have given me their time, experience, and support along this journey. When I started this project, I had a romanticized view of what a Ph.D. was. I know that without appropriate guidance, I would easily get lost. Fortunately, I had Ana and Daniel to supervise and guide me in everything I needed to learn. Thank you, Ana, and Daniel, for accepting me into your groups and for leading me on this project. I am so thankful for your support, supervision, and advice. Thanks for teaching me how to be better and how to work with clear objectives in mind. Working with you made me better in most aspects of my life, it went beyond research. You are the best supervisors I could have, Ana and Daniel, thank you for everything.

I would also like to thank Professor Guy Denuault for his kind help, patience, and willingness to teach me during this project and especially during my internship in his group. I feel honored for the opportunity of working with you, thanks for accepting to be my external co-supervisor. During my academic pathway, many times I studied the electrochemistry books written by professors from the University of Southampton. Since then, I have dreamed of visiting the University. The whole experience of the internship was unique, and a dream come true. Thank also to Denuault's research group and professor Denuault's wife, Selina Denuault, who welcomed us generously and kindly, making me quickly feel part of the group. I would also like to express my gratitude to Dr. Oliver Rodríguez and Dr. Tammy Nimmo for all the help, guidance in the University subjects, the assistance in their labs, and the scientific discussions.

Similarly, I would like to thank the postdocs and the research associate who helped me in this project for their patience and support, their help was precious. Thank you very much, Dr. Matteo Duca, Dr. Gaëtan Buvat, and Dr. Sebastien Garbarino. You played a vital role in developing my project, helping me to make decisions in the laboratory, and forming my character as a researcher. Without you, everything would be much more difficult, time-consuming, and tedious. I am a better experimentalist because you were there with me, thank you very much!!! I would be unable to enumerate all the fundamental and experimental tricks that you showed me. Thank you for spending your time listening and helping me to think about my results and improving my experiments! I will always remember these moments with great affection. Thank you so much for being there when I needed to, for being patient, and for explaining the same things hundreds of times! Thank you very, very much! Dr. Matteo Duca, working with you was a great honor and very inspiring, it showed me I could go further and be better. Seeing how diligently and passionately you worked had me willing to be a researcher like you. Dr. Gaëtan Buvat, I am also so happy for having you as my colleague and you are also a fundamental person in my pathway, thanks for everything you taught me so patiently and kindly. Dr. Sebastien, thank you for being so kind, friendly, and always ready to help. If you got a penny for each time I went to your office for help, you would be a millionaire! Thanks for keeping us motivated, cheering us up, and making the conference trips a great time!

I also thank Julie Gaudet, Madam Swagelok, always kind and ready to help. I cannot say how many times she helped me in the laboratory. Thanks, Julie, for being accessible and for all the guidance provided. I could not have managed many things without your help. I am also grateful for having Dr. Nicolas Sacré and Dr. Erwan Bertin to guide me and help start my research at INRS. You both made my beginning at INRS smoother and friendly. Thanks a bunch!

Thanks to the entire INRS staff, who attentively helped in the most different subjects. Thank you to the technicians who train us and keep the instruments ready for us, especially Christophe Chabanier, who kindly helped me with the diffractometer and issues associated with the XRD. I also thank my colleagues from both Ana and Daniel’s research groups: Hela, Yuting, Jiyun, José, Benjamim, Fabiola, Uriel Bruno, José, and Mengyang.

I also want to thank my great professors at the University of Lisbon. They provided a solid ground for my academic foundations and supported me through my days as a student. A special thank you goes to Professor Isabel Pereira. She is responsible for guiding me in the electrochemistry laboratory's first steps and fired up my passion for electrochemistry. I will never forget her lessons. Thank you, Professor Isabel. I am incredibly grateful to have met and worked with you, thanks for your patience, your faith in me, and for teaching me so much.

I wish I could thank my father for his teachings, support, and instructions. I grew up listening to him telling me that I would not have money as an inheritance, but he would provide me the best education he could afford because education was the pathway to success. One of the reasons I made it through here is due to him, and for that, thanks, daddy. Of course, my mother has her share on my journey as well. She is the most resilient and strong person I have ever met. If I manage to stay strong and finish what I have started, it was because I replicated her behavior towards life. Thank you, mom. My husband, Thiago, deserves so much credit. He supported me since the first moment by saying that he was following me everywhere I wanted to go. Thanks, Thiago, for your patience, love, and support. My family is the solid foundation in my life. Each of them has their role in my life, Marcelo, my brother, and one of my closest friends, my sister Camila, and my precious daughter Allana. Thanks, Bee, for being so supportive and understanding. It means the world to me. My achievements are their achievements as well. Thanks for being around and keep loving and supporting me.

I also want to thank my friends because they provided a supportive, pleasant, and encouraging environment. Their presence in my life was fundamental to my progress. The experience of being a student at INRS is something really special and unforgettable. Such a multicultural environment is a great place to learn. I have met great students from different countries and learned many things from their culture and for that, I am very grateful. Thus, many thanks to my INRS friends: Esen, Samira, Maria João, Bruno Guerreiro, Ahlem Z., Ahlem M. I am sorry if I forgot someone. Thanks for supporting me, listening to me, for sharing part of your lives with me, and for bringing me to reality. Thank you so much for making me see things differently and for our coffee breaks filled with science, politics, and amenities. I could not have written this thesis during the pandemic without you. Thanks, Ahlem Meziadi, for your help with this thesis synopsis. You saved me!

Last but not least, I would like to thank the jury members who kindly agreed to evaluate this thesis and take part in the realization of one of my biggest dreams, the doctorate project. Finally, I am also grateful to the FRQNT for the funding by awarding me a PBEEE scholarship to carry out my research project.

RÉSUMÉ

Les piles à combustible (PC) peuvent aider à atténuer les effets délétères de l'utilisation de combustibles fossiles sur l'environnement, mais leur coût élevé et leur fonctionnement limité à long terme entravent leur commercialisation. Pour résoudre ces problèmes, de nouveaux matériaux d'électrode sont nécessaires pour remplacer le platine (Pt) dans les PC, en particulier à la cathode. Des charges élevées de Pt sont utilisées comme électrocatalyseur de réaction de réduction d'oxygène (RRO) dans cette électrode. L'RRO est une réaction lente et complexe, et même sur les surfaces Pt, elle se déroule loin de son potentiel thermodynamique, provoquant des pertes d'énergie. Les voies pour résoudre ces problèmes sont soit d'améliorer les performances du Pt, soit de développer de nouveaux matériaux pour le remplacer.

Pour concevoir de nouveaux matériaux pour l'RRO, les descripteurs d'activité doivent être bien compris. Dans cette perspective, les études de réactions électrochimiques sur des surfaces ayant une structure bien définie - c'est-à-dire les études modèles - représentent un outil important dans l'élucidation des mécanismes de réaction, pour l'identification des sites actifs et pour permettre la déconvolution de la réponse électrochimique des surfaces. Ainsi, les études sur des surfaces modèles ouvrent la voie au progrès d'électrocatalyse. Concernant l'RRO, traditionnellement, ces études sont menées à l'aide de monocristaux et de méthodes hydrodynamiques. Cependant, certains matériaux ne peuvent pas être évalués en utilisant les voies conventionnelles, et pour ces cas, nous avons besoin de voies alternatives pour étudier l'ORR.

Dans ce contexte, l'objectif principal de cette thèse est de proposer une voie alternative pour réaliser des études électrocatalytiques de l’RRO sur des surfaces modèles. A cet effet, des films minces à orientation épitaxiale déposés par dépôt laser pulsé (DLP) sont présentés comme des surfaces modèles appropriées. Des films minces de Pt et Au ont été déposés sur des substrats de MgO(hkl) et caractérisés structurellement par diffraction des rayons-X et électrochimiquement par voltammétrie cyclique. Pour évaluer l'activité électrocatalytique de l’RRO de ces films, la voltampérométrie du courant échantillonné (VCE) est présentée et validée comme alternative à l'utilisation des assemblages électrode à disque rotatif (EDR).

Les résultats présentés dans cette thèse démontrent que le DLP fournit des films minces épitaxiés qui se comportent comme des électrodes monocristallines. De plus, grâce aux coefficients de transfert de masse, il est possible d'obtenir des courbes de polarisation avec VCE semblables à celles enregistrées avec une configuration EDR. Par conséquent, une méthodologie complète pour étudier l'RRO sur les surfaces du modèle est fournie. Avec cette méthodologie, nous pouvons poursuivre la conception, la préparation et la caractérisation de matériaux avancés pour cette réaction, ce qui peut conduire à un progrès dans le domaine de la conversion énergétique en fournissant une meilleure compréhension des descripteurs d'activité pour l'RRO et en dévoilant de nouveaux matériaux.

Mots-clés: dépôt laser pulsé; films minces épitaxiaux; surfaces modèle; réaction de réduction de l'oxygène; voltammétrie de courant échantillonné; structure-réactivité; électrocatalyse;

ABSTRACT

Fuel cells (FCs) may alleviate the deleterious effects of the use of fossil fuels on the environment, but their high cost and limited long-term operation hinder their commercialization. To address these issues, new electrode materials are necessary to replace platinum in the FCs, especially in the cathode. High loadings of Pt are used as the oxygen reduction reaction (ORR) electrocatalyst in this electrode. The ORR is a sluggish and complex reaction, and even on Pt surfaces, it takes place far from its thermodynamic potential, causing energy losses. The pathways to solve these concerns are either to improve the performance of Pt or develop new materials to replace it.

To design new materials for the ORR, activity descriptors need to be well understood and used to devise better electrocatalysts. From this perspective, studies of electrochemical reactions on surfaces with well-defined structures – i.e., model studies – represent a fundamental tool in the elucidation of reaction mechanisms, on the identification of active sites, and the deconvolution of the electrochemical response of the surfaces. Thus, model studies pave the way for the progress of electrocatalysis. Concerning the ORR, traditionally, these studies are pursued using single crystals and hydrodynamic methods, as the rotating disk electrodes (RDE). However, some materials cannot be assessed using the conventional routes, and for those cases, we need alternative routes to study the ORR.

In this context, this thesis main objective is to provide an alternative route to perform ORR electrocatalytic studies on model surfaces. For this purpose, thin films with epitaxial orientation deposited by pulsed laser deposition (PLD) are presented as suitable model surfaces. Pt and Au thin films were deposited on MgO substrates and characterized structurally by X-ray diffraction and electrochemically by cyclic voltammetry. To assess the ORR electrocatalytic activity of these films, sampled current voltammetry (SCV) is presented and validated as an alternative to the RDE assemblies' use.

The results presented in this thesis demonstrate that PLD provides thin films with epitaxial orientation that behave similarly to single crystal electrodes. It was demonstrated how to obtain polarization curves with SCV akin to those recorded with an RDE setup by adjusting the mass transfer coefficients. Hence, a full methodology to study the ORR on model surfaces is provided. With this methodology, we can pursue the design, preparation, and characterization of advanced materials for this reaction, leading to progress in the energy conversion field by contributing to a better comprehension of the activity descriptors for the ORR and unveiling new materials.

Keywords: pulsed laser deposition; epitaxial thin films; model surfaces; oxygen reduction reaction; sampled current voltammetry; structure-reactivity; electrocatalysis

SOMMAIRE RÉCAPITULATIF

Réaction de réduction d’oxygène sur films minces orientés: une approche alternative aux études électrocatalytiques sur les surfaces modèles

1. Introduction

Les piles à combustible (PC) sont des dispositifs électrochimiques qui convertissent l’énergie chimique d’un combustible fourni par l’extérieur en énergie électrique[1]. Elles apparaissent comme une technologie prometteuse pour atténuer les effets délétères des émissions de combustibles fossiles et comme une alternative à cette dépendance vis-à-vis des combustibles à base de carbone. En raison de leur polyvalence, les piles à combustible s’adaptent à toute une série d’applications, comprenant des applications fixes, la propulsion de véhicules et des applications mobiles[2]. Le fonctionnement des piles à combustible fait référence aux principes des cellules électrochimiques galvaniques, où des réactions chimiques redox spontanées ont lieu au niveau des électrodes produisant l’électricité[3]. Ainsi, l’oxydation du combustible a lieu à l’anode de la cellule, et l’oxydant est réduit à la cathode. La figure 1-1 (page 4) montre un schéma général d’une pile à combustible à membrane échangeuse de protons (PEMFC) fonctionnant avec H_2 et O_2.

Pour obtenir le meilleur rendement possible, les FC doivent être conçus pour fonctionner en délivrant des différences de potentiel aussi proches que possible de celles prévues par la thermodynamique. La figure 1-2 (page 6) illustre les pertes d’énergie dans un PEMFC. À cet égard, l’oxydation de l’H_2 à l’anode se produit à des potentiels proches du potentiel d’équilibre, et par conséquent, les pertes de potentiel sont faibles. Inversement, la réaction de réduction cathodique de l’O_2 (RRO) se produit loin du potentiel thermodynamique et nécessite plus d’énergie pour être entraînée, ce qui exerce une chute de potentiel remarquable dans la cellule. Malgré les pertes d’énergie, les PC bien conçues peuvent atteindre un rendement de conversion énergétique de 60 %, alors que le rendement obtenu dans la plupart des moteurs à combustion interne atteint 34 %. En outre, comme certains PC produisent également de la chaleur, en utilisant la cogénération, les rendements peuvent atteindre 80%[1].

Les principaux obstacles à la généralisation des PC sont le coût élevé et la stabilité à long terme des électrocatalyseurs en platine, combinés avec les exigences de qualité, de stockage et de transport du combustible H_2. En outre, les conditions de fonctionnement oxydatives et corrosives que connaît la cathode réduisent la surface active du Pt par la dissolution du métal et la corrosion du support à base de carbone du catalyseur[4-7], ce qui affecte directement l'efficacité de la conversion énergétique. Malheureusement, ce problème touche plusieurs types de PC[8].

Ainsi, les chercheurs recherchent continuellement des matériaux pouvant remplacer le platine, coûteux et rare, comme électrocatalyseur. Trouver le meilleur électrocatalyseur pour une application spécifique nécessite des efforts continus pour comprendre les limites et le mécanisme cinétique de la réaction, y compris l'impact de la connaissance approfondie des espèces adsorbées sur la vitesse et la sélectivité de la réaction. Dans ce contexte, l'approche de la surface modèle a été adoptée avec succès pour résoudre les différentes contributions catalytiques provenant des différents sites actifs à l'activité globale des électrocatalyseurs[9-17].

Un électrocatalyseur modèle est un matériau ayant une structure et une composition bien définies avec un degré d'homogénéité élevé dans l'ordre atomique à la surface du matériau[10-11, 18-20], et des surfaces des monocristaux idéalement adaptés pour répondre à ces besoins. L'utilisation de ces monocristaux comme surfaces modèles en électrochimie est un outil fondamental pour élucider la nature des sites actifs et la manière dont ils affectent la vitesse et la sélectivité des réactions électrocatalytiques. De ce fait, ces études sont fondamentales pour le développement des piles à combustible[6, 9, 21]. La capacité à produire des surfaces modèles présentant une large gamme d'agencements structurels et de compositions chimiques en utilisant une méthode simple et directe représente une voie très prometteuse pour étendre les connaissances en matière d'électrocatalyse et promouvoir des progrès significatifs dans l'efficacité de la conversion énergétique. Les expériences utilisant des monocristaux ont apporté une contribution notable à l'électrocatalyse de la RRO en démontrant que la cinétique de la RRO présente une dépendance des orientations cristallographiques de la surface dans les milieux acides[22-24] et alcalins[25-26].

Cependant, travailler avec des monocristaux pose certains défis, puisque les normes concernant le degré d'organisation et la propreté de la surface sont élevées pour obtenir des résultats fiables. En absence d'installations appropriées, où l'on dispose des appareils nécessaires à la préparation des monocristaux, l'expérimentateur doit chercher des alternatives pour produire des surfaces modèles. Ainsi, la production de couches minces bien définies structurellement au point de se comporter comme des surfaces monocristallines représente un instrument polyvalent pour interpréter l'activité des surfaces. Les propriétés des films peuvent souvent être contrôlées pour obtenir des couches lisses et minces des matériaux actifs. Le fait que les couches soient minces implique une faible quantité de matériau nécessaire pour couvrir le substrat, ce qui affecte directement le coût et l'application des films. En particulier, le fait de travailler avec des films offre des avantages en modifiant la couche active à déposer, ce qui confère une grande polyvalence aux applications. En outre, la modification des paramètres de dépôt modifie souvent la structure, l'orientation cristallographique, la composition chimique et les propriétés de surface des films. En conséquence, le dépôt par laser pulsé (DLP) en tant que technique de production de surfaces modèles, a un grand potentiel pour mener le progrès dans l'électrocatalyse en élargissant la gamme de matériaux disponibles pour les études.

1.1 Objectifs de la recherche

La motivation de ce projet de recherche est d'apporter de nouveaux outils aux études électrocatalytiques des matériaux pour les applications de conversion d'énergie. Ainsi, ce projet vise à présenter des couches minces à orientation épitaxiale déposées par DLP comme une voie alternative simple pour produire des surfaces modèles pour les études électrocatalytiques de la RRO. Les couches minces de Pt et d'Au à orientation épitaxiale seront utilisées comme systèmes modèles dans lesquels l'orientation cristallographique et les propriétés structurelles de la surface peuvent être corrélées avec l'activité électrocatalytique de la RRO mesurée. Cependant, comme ces films ne peuvent pas être insérés dans un ensemble d'électrodes à disque rotatif, la RRO ne peut pas être étudiée avec précision, et c'est pourquoi la Voltamétrie de courant échantillonné (VCE) est présentée comme une méthode alternative pour étudier la RRO sur ces films.

Ce projet présente une méthodologie complète pour modéliser les études en électrocatalyse : il démontre comment des films minces à orientation épitaxiale déposés par DLP peuvent être utilisés comme électrocatalyseurs de surface modèles pour le RRO. Il introduit également une méthode expérimentale alternative pour étudier la RRO sur de telles surfaces, qui peut être étendue ultérieurement à d'autres réactions électrochimiques contrôlées par diffusion.

2. Réaction de réduction de l'oxygène

La RRO représente une importance primordiale pour différents types de piles à combustible et de batteries métal-air et dans la technologie de production d'H_2O_2[27]. Néanmoins, même après plusieurs années de recherche intensive, la cinétique lente de la RRO reste un problème[28-29], et persiste comme l'un des plus grands défis de l'électrocatalyse. Comme la molécule d'O_2 est très stable, l'adsorption de l'O_2 à la surface de l'électrocatalyseur est une étape essentielle pour lancer la RRO et faciliter le transfert d'électrons. Cette exigence spécifique de la réaction impose une limitation concernant les électrocatalyseurs: un électrocatalyseur prometteur pour la RRO doit être capable d'adsorber l'O_2 et les intermédiaires de la réaction, en particulier l'OH, avec une énergie de liaison optimale[29-30]. Même si les surfaces de Pt adsorbent l'espèce OH un peu trop fortement[8], elles sont proches d'atteindre l'énergie d'adsorption optimale, ce qui contribue à expliquer pourquoi le platine est l'électrocatalyseur de pointe pour la RRO, bien qu'il soit encore loin d'être idéal.

La RRO complète se présente comme une séquence d'étapes impliquant l'adsorption de l'O_2 à la surface de l'électrocatalyseur, le transfert de multiples électrons et protons, et l'adsorption et la désorption des intermédiaires de la réaction. Pour ces raisons, cette réaction nécessite des surpotentiels élevés pour se produire à des taux appréciables. Même après des décennies de recherche intensive, le mécanisme de la RRO n'est pas bien résolu[31-36], et les scientifiques s'intéressent aux voies de réaction plutôt qu'au mécanisme[37-39] comme les voies de réaction peuvent être déduites des données expérimentales.

Dans les électrolytes aqueux, au moins deux voies sont possibles pour la réduction complète de l'oxygène[3, 40-41]. La première est la voie directe (voie à quatre électrons), dans laquelle l'oxygène est directement réduit en H_2O (en milieu acide) ou en OH^- (en milieu alcalin) par l'échange de quatre électrons. Cette réaction est représentée par les équations (10) et (11) (page xliii). La seconde est la voie du peroxyde (ou voie parallèle à quatre électrons), où l'oxygène est réduit soit en H_2O (en milieu acide) soit en OH^- (en milieu alcalin) par l'échange de deux plus deux électrons, formant un peroxyde comme intermédiaire, représenté dans les équations (12) à (17) (page xliii).

Traditionnellement, la distinction entre ces voies est effectuée à l'aide d'un ensemble d'électrodes à disque à anneau rotatif (EDAR)[39, 42-45]. Les méthodes hydrodynamiques en régime permanent assurent des taux de transfert massique élevés et contrôlés d'O_2 du sein de la solution à la surface de l'électrode et permettent une analyse simple des données. Ainsi, les EDR et EDAR sont les techniques les plus utilisées pour étudier la RRO[3, 46-47]. En outre, les données cinétiques peuvent être facilement extraites des diagrammes de Koutechy-Levich et de Tafel[3, 37, 43, 46]. Lorsque l'on utilise l'EDR ou l'EDAR pour extraire des informations cinétiques, l'avantage le plus significatif est la possibilité de séparer la composante de courant de transfert de masse de la cinétique, ce qui permet d'analyser l'une ou l'autre composante pour extraire les informations souhaitées.

Les électrocatalyseurs à base de platine jouent un rôle fondamental dans les principaux processus de conversion et de stockage de l'énergie, à savoir les piles à combustible[48] et les électrolyseurs[49]. Le platine (Pt) possède des propriétés chimiques et physiques uniques, et il est stable et résistant aux attaques chimiques. Ce qui le rend l'électrocatalyseur de pointe pour un certain nombre de réactions d'électrodes, y compris la RRO. En milieu alcalin, l'Au(100) est l'électrocatalyseur le plus actif connu et des recherches supplémentaires sont nécessaires pour comprendre l'activité électrocatalytique de cette surface vers la RRO. Pour ces raisons, ces matériaux ont été choisis comme matériaux standards pour valider la méthodologie présentée dans cette thèse.

3. Méthodologie

Les recherches présentées dans cette thèse ont deux objectifs principaux. Le premier consiste en la validation de la VCE comme méthode d'étude de la ORR et le second implique le dépôt de films de Pt et Au orientés par épitaxie, suivie de leur caractérisation structurale et électrochimique. Ensuite, les caractéristiques des films sont comparées à celles des monocristaux correspondants pour garantir un comportement homologue.

La validation de la VCE a été effectuée à l'aide de deux réactions électrochimiques différentes, la réduction du ferricyanure et la RRO. Ces expériences ont été réalisées en utilisant un Pt EDR polycristallin qui a été tourné à des taux fixes pour enregistrer les voltammogrammes hydrodynamiques, et il a été maintenu au repos pour enregistrer les transitions de courant utilisé pour reconstruire les voltammogrammes de courant échantillonnés. Dans les deux cas, le critère utilisé pour la validation était la similitude entre les voltammogrammes de courant échantillonnés et les EDR. Une série supplémentaire d'expériences visant à trouver les meilleures conditions expérimentales pour l'étude de la RRO par VCE et à comprendre comment les conditions expérimentales affectent les SCV reconstruites pour la RRO a été également réalisée.

Le dépôt par laser pulsé a été utilisé pour déposer des couches minces de Pt et d'Au orientées par épitaxie pour les études sur les modèles. Des films minces de Pt ont été déposés sur des substrats de MgO(hkl), avec (hkl) = (001), (110) et (111), pour produire des films orientés dans les plans de base du *fcc*. La caractérisation structurelle de ces films a été réalisée par diffraction des rayons X (DRX). Une fois qu'il a été confirmé que les films se développaient de manière épitaxiale dans la direction (hkl) souhaitée, ils ont été caractérisés électrochimiquement. La voltampérométrie cyclique a été utilisée pour évaluer le comportement électrochimique de la surface des films. Pour le film mince en Pt/MgO(110), la voltampérométrie en présence de CO a été utilisée pour caractériser davantage la surface du film et la VCE a été utilisé pour accéder à la RRO en milieu acide. D'autres expériences utilisant des films minces en Pt/MgO(hkl) ont été réalisées, où la VCE a été utilisé pour étudier la désorption des espèces d'oxygène de la surface afin de relier ces résultats à l'activité de la RRO.

Des couches minces d'Au/MgO(001) ont également été déposées par DLP. Dans le but d'obtenir des couches minces qui se comportent aussi bien que possible comme le monocristal, les paramètres de dépôt ont été modifiés et l'effet résultant sur les propriétés structurelles et électrochimiques des couches a été évalué. Les variables testées ont été deux couches tampons métalliques et la température du substrat pendant le dépôt. Une fois que les conditions optimales pour la croissance des films Au/MgO(001) ont été déterminées, l'épaisseur des films a été modifiée de ≈ 25 nm à 82 nm dans le but d'introduire délibérément une contrainte dans le réseau des films et d'observer l'effet sur l'activité de la RRO.

4. Résultats

4.1. Validation de la voltampérométrie du courant échantillonné

La VCE est une technique voltampérométrique qui applique des échelons de potentiel à l'électrode de travail et enregistre la variation du courant en fonction du temps pour générer un ensemble de courants transitoires, figure 3-1 (page 38). Le potentiel de l'électrode passe d'un potentiel neutre où un courant négligeable circule dans la cellule — appelé potentiel de repos — à un potentiel où la réaction se produit, et le transfert d'électrons génère un courant faradique à l'interface[3, 46, 50]. L'échantillonnage du courant mesuré à un moment fixe dans chaque transition et le tracé en fonction du potentiel d'étape produit un voltampérogramme, le voltampérogramme de courant échantillonné reconstruit. En échantillonnant à un moment fixe, la dépendance temporelle de l'intensité du courant est supprimée, et pour un réactif soluble subissant un transfert d'électrons affecté par le transport de masse, les VCE ont une forme sigmoïdale indépendamment du moment d'échantillonnage choisi[50].

L'analyse des voltammogrammes VCE est plus simple et plus polyvalente que l'analyse des voltammogrammes classiques, et selon le temps d'échantillonnage, des processus avec des constantes de temps différentes peuvent être mis en évidence. En outre, les voltammogrammes de courant échantillonnés reconstruits en utilisant différents temps d'échantillonnage peuvent révéler des informations cinétiques et de diffusion, et des conditions de transfert de masse élevées, impossibles à obtenir avec des configurations EDR, peuvent être obtenues en modulant le temps d'échantillonnage et les conditions expérimentales.

Le coefficient de transfert de masse, k_m, est suffisant pour établir la correspondance entre les voltammogrammes VCE et les voltammogrammes à balayage linéaire EDR. La vitesse de rotation de l'électrode détermine le coefficient de transfert de masse en régime permanent, tandis qu'à la VCE, l'échantillonnage détermine le coefficient de transfert de masse. Ainsi, en estimant le coefficient de transfert de masse délivré par une vitesse de rotation spécifique dans l'EDR, il est possible de trouver le temps d'échantillonnage qui fournit des conditions équivalentes. Les tableaux 1 et 2 (pages 41 et 42) illustrent comment le taux de rotation de l'EDR et les temps d'échantillonnage correspondants varient en fonction de la réaction pour la réduction du ferricyanure.

Les courbes de polarisation EDR enregistrées pour les processus redox des ferri-ferrocianyde (figure 3-4a), page 47) et les voltampérogrammes de courant échantillonnés obtenus dans des conditions de repos, reconstruits à l'aide des temps d'échantillonnage indiqués dans le tableau 1 (figure 3-4b)) présentent une forme sigmoïdal et semblent identiques. La superposition des courbes de polarisation obtenues avec les deux méthodes, figure 3-4c) et d), montre que les courbes se chevauchent sur toute la fenêtre de potentiel. Ces résultats démontrent que pour un système d'oxydoréduction modèle, sans limitation cinétique ni adsorbats impliqués dans les processus d'oxydoréduction, la VCE à une électrode stationnaire produit des voltampérogrammes similaires à ceux de l'EDR lorsque les temps d'échantillonnage et les taux de rotation sont sélectionnés pour donner le même coefficient de transfert de masse.

Les courbes de polarisation de la RRO et l'EDR (figure 3-5a), page 49) présentent les caractéristiques de la ORR contrôlée par diffusion sur le Pt polycristallin dans des solutions d'acide sulfurique[51-53], y compris une hystérésis due à l'adsorption d'espèces d'oxygène sur le Pt au début du balayage cathodique[9, 53-55]. Après soustraction des courants de fond, figure 3-5c), les courants limites de la VCE sont proches de ceux obtenus avec l'EDR. De plus, les courants au pied de l'onde RRO se chevauchent, comme on l'observe dans les voltampérogrammes de l'EDR. Cela suggère que le courant supplémentaire observé à des temps d'échantillonnage courts au pied de l'onde de la VCE provient de la réduction des espèces adsorbées à l'oxygène au Pt qui s'est produite pendant la période de repos. Si l'on compare directement, figure 3-5d), la VCE soustraite du bruit de fond se superpose presque entièrement au balayage cathodique du voltampérogramme EDR. La correspondance entre la branche cathodique du voltampérogramme EDR et la VCE est due au fait que dans les deux cas, les espèces d'oxygène adsorbées entravent le RRO et déplacent le début de la réaction vers des potentiels plus négatifs.

En raison de l'adsorption d'oxygène à la surface du Pt pendant le potentiel de repos dans les expériences VCE, la surface du Pt partage l'état oxydé induit par le potentiel de repos pour toute la fenêtre de potentiel de la RRO. Cela contraste avec la voltampérométrie classique, où l'état de la surface change pendant le cycle de potentiel, et où le potentiel d'électrode précédent appliqué à la surface affecte chaque point du voltampérogramme.

En milieu acide, il est impossible de trouver un potentiel de repos approprié lorsque la surface du Pt est exempte d'espèces d'oxygène, car le début de la réduction de l'oxygène chevauche le début de la formation d'oxyde. Ceci est intrinsèque à la surface du platine en milieu acide[54-56].

Il a été démontré que la VCE est capable de produire des courbes de polarisation équivalentes à celles obtenues avec une installation EDR. Cependant, les conditions expérimentales doivent être soigneusement prises en compte lors de la conception des expériences. La constante de temps de la cellule doit être estimée et l'utilisateur doit s'assurer que le temps d'échantillonnage le plus court est au moins cinq fois supérieur à la constante pour éviter la contribution de la double couche de charge. En outre, si des processus d'adsorption interviennent dans la réponse globale au courant, il est nécessaire d'estimer cette contribution pour éviter que cela n'affecte les courants faradiques.

4.2. Étude de l'adsorption d'oxygène sur la surface du platine pendant le potentiel de repos

Dans la fenêtre potentielle où la RRO a lieu, les surfaces de Pt peuvent être couvertes par des espèces oxygénées, et l'extension de cette couverture est potentiellement dépendante. Il est donc important d'apprendre comment la couverture d'oxygène adsorbé est liée au potentiel de repos et le comportement électrocatalytique de la surface est fondamental pour comprendre l'applicabilité et les limites de la VCE. Par conséquent, une série supplémentaire d'expériences de la RRO sur une EDR Pt où la valeur et la durée du potentiel de repos varient a été réalisée dans du H_2SO_4 0,5 M saturé en N_2 et O_2. L'objectif était de minimiser la couverture de l'oxygène adsorbé sur la surface de l'électrode et de clarifier comment cette couverture affecte les voltampérogrammes reconstruits. La compréhension de ces processus est essentielle pour établir des conditions expérimentales appropriées pour enregistrer les transitoires afin d'éviter toute perturbation dans les courbes de polarisation reconstruites.

Bien qu'ils aient été enregistrés en l'absence d'O_2, les voltampérogrammes reconstruits enregistrés en N_2 ont montré des courants cathodiques qui variaient en fonction du potentiel de repos et du temps d'échantillonnage. L'apparition de tels courants est liée à l'arrachement d'une couche d'oxygène adsorbée à la surface du platine pendant le potentiel de repos, et l'extension dans laquelle l'oxygène s'adsorbe à la surface dépend du potentiel fixé comme potentiel de repos. La couverture d'oxygène la plus élevée a été trouvée pour le 1.002 V, et elle a diminué de façon linéaire avec l'application du potentiel de repos. En considérant les potentiels de repos testés, la fraction de la surface couverte d'oxygène variait de 0.1 à 0.4. Les études réalisées dans un électrolyte saturé en N_2 ont également indiqué que la durée du potentiel de repos n'affecte pas la couverture en oxygène à la surface.

Les tracés reconstruits de la VCE résultant des transitoires enregistrés dans l'électrolyte saturé en O_2 ont montré que l'activité de la RRO — reflétée dans les courbes de polarisation — change avec l'établissement et la durée du potentiel de repos. La raison principale est le changement de la concentration d’O_2 en surface observé dans les cas où le potentiel de repos était suffisamment négatif pour réduire l’O_2, ou le potentiel de repos était trop court pour permettre le réapprovisionnement en O_2 à la surface de l’électrode.

Par conséquent, le choix du potentiel de repos et de sa durée est de la plus haute importance pour la fiabilité et la qualité des données enregistrées. Le potentiel de repos ne doit pas consommer l’espèce active et doit être suffisamment long pour permettre à la concentration d’O_2 à la surface de se rétablir avant l’application de l’étape du potentiel. La durée idéale peut être ajustée en définissant l’étape du potentiel comme un potentiel à diffusion contrôlée et en faisant varier la durée du potentiel de repos.

Malgré la gamme des potentiels de repos testés, on n’a pas trouvé de potentiel où la surface du Pt était exempte d’oxygène adsorbé et ne consommait pas d’oxygène. Cela est dû aux caractéristiques électrochimiques intrinsèques du Pt dans l’acide sulfurique (qui est également étendu aux conditions alcalines[57]). Ainsi, le potentiel du circuit ouvert (1.002 V) est le plus approprié, mais dans de telles conditions, l’activité RRO observée dans la VCE correspond à la surface oxydée du Pt.

Si l’adsorption des espèces dans la même fenêtre de potentiel de la RRO ne pose pas de problème, il est plus facile de fixer le potentiel de repos. Ceci est montré plus loin dans l’étude de la RRO sur des électrodes d’Au(100).

4.3. Application de la VCE à la RRO sur film Pt/MgO(110)

Le Pt(110) est la facette la plus active du Pt pour la RRO[22, 24], et pour ces raisons, il a été choisi comme modèle pour démontrer la qualité de l’épitaxie des films et la sensibilité du VCE à refléter une variation même discrète de l’activité.

Le diffractogramme du Pt/MgO(110), montre que concernant la phase cristalline du Pt, le seul pic de diffraction (220) apparaît dans le diffractogramme Figure 6-1 (page 87) . Cela signifie que le film s’est développé uniquement dans la direction [110] reproduisant l’orientation cristallographique du substrat de MgO(110), et que la croissance épitaxiale a été réalisée avec succès. Le voltampérogramme cyclique enregistré pour l’électrode Pt/MgO(110) après son activation est illustré à la figure 6-2 (page 89). Le profil voltampérométrique du film de Pt/MgO(110) montre une paire de pics nets et réversibles à environ 0.140 V correspondant à la réaction d’adsorption et de désorption d’hydrogène aux sites de symétrie (110)[58-60]. Par conséquent, la réponse voltampérométrique du film de Pt/MgO(110) est similaire à celle décrite dans la littérature pour les électrodes monocristallines de Pt(110), à savoir que seules les facettes du Pt(110) sont exposées à la surface des films. Une caractérisation électrochimique supplémentaire par l'analyse du profil d'oxydation du CO obtenu pour le film fournit davantage de preuves que le comportement électrochimique du film est similaire à celui signalé précédemment pour les électrodes monocristallines en Pt(110)[61-62], figure 6-3 (page 90).

L'activité de la RRO a été évaluée sur Pt/MgO(110) en examinant la réponse du film à la VCE, figure 6-7a) (page 94). L'électrolyte de travail utilisé dans ces expériences était du H_2SO_4 saturé en O_2 à 0.05 M + $KClO_4$ à 0.1 M. Quel que soit le temps d'échantillonnage, les voltammogrammes reconstruits montrent des courbes qui se chevauchent à la fenêtre de potentiel cinétique et à une partie de la fenêtre de potentiel mixte contrôlé. Cependant, les courbes présentent des formes distinctes à mesure que le temps d'échantillonnage augmente, et à des temps d'échantillonnage plus courts, un pic large émerge plutôt que le plateau de courant limite prévu. La figure 6-7b) (page 94), montre un tracé des courants limites en fonction de la racine carrée du temps d'échantillonnage et la relation linéaire obtenue confirme que la RRO sur le film est contrôlée par diffusion. Enfin, l'activité de la RRO du film mince de Pt/MgO(110) est comparée à celle du Pt polycristallin, figure 6-8a) et b) (page 95). La VCE reconstruite du film est déplacée vers un potentiel plus positif par rapport à l'électrode en Pt polycristallin, et le déplacement du potentiel demi-vague du film est d'environ 42 mV. Par conséquent, le film est plus actif pour la RRO que le Pt polycristallin, ce qui est encore remarqué par les tracés de Tafel.

Les techniques de caractérisation ont fourni des résultats qui confirment la qualité de l'épitaxie du film mince déposé par DLP. La caractérisation structurelle par DRX a démontré que le film déposé a exclusivement grandi dans la direction [110]. La voltampérométrie cyclique et le stripping au CO corroborent les résultats de la DRX, renforçant l'épitaxie du film mince de Pt sur le substrat de MgO(110). Il est important de noter que les techniques de voltampérométrie sondent le comportement de la surface des électrodes, et que cet accord entre l'analyse de rayons X et la voltampérométrie démontre que la surface ne se réarrange pas et ne reflète pas l'orientation cristallographique globale.

Par conséquent, l'étude a démontré que la DLP produit des films de Pt bien orientés qui se développent sur les substrats de MgO(110) et la caractérisation électrochimique a prouvé que ces films servent de surfaces modèles pour l'étude de la RRO. En outre, l'ensemble des expériences a permis de s'assurer que la voltampérométrie du courant échantillonné est suffisamment sensible pour montrer de petits changements dans l'activité catalytique résultant de différentes concentrations d'électrolytes de support, de l'adsorption spécifique des ions et de l'orientation cristallographique du substrat.

4.4. Dépôt de couches minces d’Au/MgO(100)

Dans le but d’obtenir des films minces orientés préférentiellement vers l’Au(100) avec une épitaxie de haute qualité, l’effet de certaines variables sur la structure des films a été étudié, à savoir le dépôt d’une couche tampon entre le substrat et le film et la température du substrat pendant le dépôt. Des monocristaux de MgO(100) ont été utilisés comme substrats, et ils ont été nettoyés avant le dépôt, comme indiqué dans la section expérimentale. Le nickel (Ni) et l’argent (Ag) ont été utilisés comme couches tampons pour comprendre leurs effets sur la structure et les caractéristiques des films. Des dépôts supplémentaires visant à optimiser la température du substrat ont été effectués. Le Ni a été utilisé comme couche tampon dans ces dépôts, et la température du substrat a varié de la température ambiante à 600 °C.

L’épaisseur des films était d’environ 35 nm pour les deux couches tampons Ag et Ni, et la couche tampon n’a pas entraîné de changements significatifs dans l’épaisseur des films, tableau 7. Les balayages θ-2θ obtenus pour les films déposés sur les deux couches tampon ont confirmé que la phase Au n’a augmenté que dans la direction [100], figure 7-2 (page 100). La principale différence entre les diffractogrammes des deux films est que le film déposé sur le dessus de la couche tampon en Ni présente un pic de diffraction intense et net à $2\theta = 44{,}25°$ qui provient de la phase Au, alors que pour le film déposé sur la couche tampon en Ag, seul un large épaulement s’estompe à une position similaire. Les diffractogrammes suggèrent que le film déposé sur la couche tampon de Ni favorise une meilleure croissance épitaxiale de la couche d’Au sur le substrat de MgO(100).

Les résultats des figures de pôle ont montré que le film déposé sur la couche tampon de Ni présente un ordre d’organisation plus élevé des cristallites, alors que le film déposé sur la couche tampon d’Ag fournit un cristal avec un degré de mosaïcité plus élevé concernant les cristallites qui construisent le film, figure 7-4 (page 103). Malgré les différences signalées, l’intensité mesurée pour les quatre pics est proche de celle attendue pour une structure cubique et indique que dans les deux cas, les films se sont développés avec une relation épitaxiale cube-sur-cube Au(100)[010]//[010](100)MgO, comme observé précédemment pour les films métalliques *fcc* sur des substrats céramiques[63].

Les voltammogrammes cycliques obtenus en milieu acide et alcalin pour les films suggèrent un comportement électrochimique similaire, car ils se sont avérés similaires, figure 7-5 (page 104) et 7-7 (page 107). Ensuite, la comparaison avec les voltammogrammes disponibles dans la littérature a révélé que les caractéristiques voltampérométriques observées dans les deux films étaient similaires à celles des monocristaux d’Au(100) dans des conditions similaires. Cependant, les voltamogrammes actuels reconstitués ont montré que seul le film déposé sur la couche tampon de Ni présentait une activité ORR comparable à celle d'une surface de monocristal d'Au(100).

La température du substrat pendant le dépôt joue un rôle fondamental dans la structure et la morphologie des films déposés. Les résultats de la radiographie ont montré que la température de dépôt optimale pour obtenir des films épitaxiaux de Au/MgO(001) est de 100 à 200 °C, figure 7-11 (page 112). Des températures plus basses ou plus élevées entraînent une réorganisation de la structure en facette (111), qui est la plus stable sur le plan thermodynamique, tableau 9 (page 113).

Les voltampérogrammes cycliques enregistrés en milieux acide et alcalin pour les échantillons déposés à 100, 200 et 400 °C présentaient des caractéristiques similaires, figure 7-13 (page 115). Quelle que soit la température de dépôt, ces échantillons présentent des voltammogrammes dont les profils ressemblent à ceux obtenus pour le monocristal d'Au (100) dans des électrolytes analogues[26, 64]. Les VCE reconstruits fournissent des informations concernant l'activité de la RRO des films, figure 7-14 (page 116). Pour les échantillons déposés à 100 et 200 °C, les VCE présentent une activité de RRO similaire, et leur comportement correspond à la RRO catalysée par une surface d'Au(100) dans un électrolyte alcalin[26]. Cependant, l'activité obtenue pour le film déposé à 400 °C montre une activité plus faible pour la RRO, et son potentiel demi-vague est d'environ 50 mV plus négatif que celui mesuré pour les échantillons déposés à 100 °C et 200 °C. L'échantillon à 400 °C présente également une sélectivité plus faible, et la RRO se produit principalement par l'échange de 2 électrons seulement pour produire du peroxyde comme produit final. Malgré la croissance préférentielle dans la direction [100] à 400 °C, le diagramme DRX de l'échantillon montre également des caractéristiques de diffraction provenant de sites avec un arrangement (111). Le nombre de sites présentant cette symétrie à la surface est si faible qu'ils n'apparaissent pas sur les voltammogrammes ; il semble toutefois qu'ils soient suffisants pour entraver la RRO.

Il a été démontré que la couche tampon de Ni favorise la croissance de films orientés Au(001) sur des substrats de MgO(100) composés de cristallites ayant un degré d'ordre et de symétrie supérieur dans le cristal. Les voltammogrammes Au/Ni/MgO(100) et Au/Ag/MgO(100) ont montré des caractéristiques qui correspondent à celles observées sur les monocristaux d'Au(100) dans des électrolytes acides et alcalins. Cependant, le film tamponné au Ni présentait une activité RRO plus élevée, similaire à celle du monocristal d'Au(100).

La température du substrat affecte les propriétés structurelles et électrochimiques des films Au/Ni/MgO(100). La température de dépôt optimale pour réaliser l'épitaxie dans la direction [100] sur les substrats de MgO(100) est comprise entre 100 et 200 °C. La température ambiante et les températures supérieures à 200 °C favorisent la croissance du film dans la direction [111] et nuisent à l'activité RRO.

4.5. RRO sur des films Au/MgO(100) d'épaisseurs différentes

L'objectif principal de la variation de l'épaisseur des films est de produire des films déformés et d'observer comment cette déformation influence leur activité RRO. Ainsi, pour produire des films d'épaisseurs différentes, le nombre d'impulsions frappant la cible Au a varié de 15 000 à 100 000. L'analyse des courbes de réflectivité des rayons X a montré que l'épaisseur des films augmente avec le nombre d'impulsions appliquées, et l'épaisseur estimée des films varie de ≈ 25 nm (15 000 impulsions) à ≈ 71,7 nm (70 000 impulsions). Pour le film de 100 000 impulsions, les données de réflectivité n'ont pas permis de distinguer des franges, et son épaisseur a été estimée par extrapolation des données expérimentales de ≈ 81,7 nm, figure 8-2a) et b) (page 122).

Quelle que soit l'épaisseur du film, l'épitaxie dans la direction [100] a été obtenue, comme le montrent les balayages θ-2θ, figure 8-3a) (page 123) et les figures polaires, figure 8-4 (page 124). Les données cartographie de l'espace réciproque par diffraction de rayons X (CER) ont révélé que dans la direction du plan, la valeur maximale de la déformation dans le réseau des films est d'environ 0,25 %. Les valeurs de la longueur cohérente latérale, L, et de l'angle d'inclinaison, T, entre les domaines des films et le substrat sous-jacent, ont également été calculés, et leur variation avec l'épaisseur du film est représentée sur la figure 8-7 (page 127). Les graphiques montrent que la longueur cohérente latérale augmente et que l'inclinaison diminue avec l'épaisseur des films. Ces résultats signifient qu'à mesure que les films deviennent plus épais puis plus continus, les domaines des cristaux augmentent de manière plus cohérente, c'est-à-dire mieux alignée les uns par rapport aux autres.

La voltampérométrie cyclique a montré des caractéristiques similaires pour tous les films, quelle que soit leur épaisseur, figure 8-8 a) à d) (page 128). La principale différence entre eux réside dans les densités de courant, causées par des différences dans leur surface électrochimiquement active. Les voltammogrammes ont montré que, quelle que soit l'épaisseur des films, ils présentent un comportement électrochimique similaire à celui du monocristal analogue. De plus, la caractérisation du plomb sous-potentiel dépôt corrobore les données structurelles et voltampérométriques montrant un comportement électrochimique caractéristique d'une surface cristallographique de Au(100).

La VCE a été utilisé pour évaluer l'activité électrocatalytique RRO des couches minces en fonction de leur épaisseur, figure 8-12a) et b) (page 133). Les SCV reconstruites ont montré que l'activité RRO augmente avec l'épaisseur des films, figure 8-12b) (page 133). La corrélation entre l'activité des films et leur épaisseur est probablement liée aux changements structurels induits par la variation de leur épaisseur. Un graphique des paramètres cinétiques de la RRO en fonction de la longueur de cohérence latérale montre que l'activité des films augmente avec la longueur de cohérence latérale (figure 8-15, page 137). Un comportement similaire a été trouvé pour la RRO sur des monocristaux vicinaux d'Au(100), où l'activité augmente avec la largeur des (100) terrasses. Ainsi, plus les films sont épais, plus ils sont actifs, comme dans le cas des surfaces en gradins, plus les terrasses d'Au(100) sont longues en surface, meilleure est l'activité.

L'ampleur de la contrainte introduite dans le réseau Au/MgO(001) était insuffisante pour provoquer des changements significatifs dans les propriétés de surface des films. La contrainte la plus élevée trouvée dans le réseau des films était de 0.25%. Dans les films de Pt, l'amélioration de l'activité de la RRO a été obtenue pour une déformation allant de 0.30[65] à 1.47%[66], ce qui suggère que pour observer un tel effet sur les surfaces d'Au, il faudrait introduire davantage de déformation dans le réseau des films.

La conclusion la plus importante est que l'activité électrocatalytique des domaines de Au(100) dépend de leur taille et de leur ordre de grandeur. Cette observation pourrait mettre en lumière les effets de taille des nanoparticules d'Au pour la RRO[67]. Ces résultats indiquent que non seulement la présence des sites de symétrie (100) mais aussi les dimensions de ces sites actifs jouent un rôle fondamental dans l'activité des surfaces d'Au.

4.6. Le VCE appliqué à l'étude des espèces adsorbées

L'adsorption des espèces oxygénées dans la fenêtre de potentiel de la ORR affecte les réactions sur les électrodes en Pt. Ici, nous explorons l'utilisation de la VCE pour étudier l'adsorption des espèces sur des électrodes à film mince orientées Pt dans des conditions acides. À cette fin, des films minces de Pt/MgO(hkl), hkl = (100), (110) et (111) seront utilisés comme surfaces modèles.

L'orientation cristallographique des films a été évaluée par DRX et pour tous les échantillons, la phase Pt s'est développé le long de l'axe [hkl] souhaité. Les diffractogrammes sont représentés sur la figure 9-1 (page 143). La caractérisation électrochimique de la surface des films a été réalisée par voltampérométrie cyclique, figure 9-2a) à c) (page 145). Les voltampérogrammes montrent différentes caractéristiques à la fenêtre de potentiel H_{UPD} pour chaque film, en accord avec les empreintes digitales de chaque orientation cristallographique du Pt[58, 68-74]. Pour le film mince de Pt/MgO(100) et le Pt/MgO(110), les informations voltampérométriques obtenues indiquent que les caractéristiques observées à la surface des électrodes correspondent aux monocristaux analogues, ce qui concorde avec les informations structurelles extraites par radiographie. Pour l'échantillon de Pt/MgO(111), les sites de symétrie (111) sont dominants à la surface, mais l'ordre de surface à longue distance du film est insuffisant pour montrer exactement le même profil voltampérométrique que celui rapporté pour un monocristal de Pt(111) dans un électrolyte d'acide sulfurique.

Après la caractérisation du CV, les expériences VCE ont été réalisées dans un électrolyte H_2SO_4 saturé en N_2 0.5 M en utilisant la forme d'onde représentée sur la figure 3-3 (page 46). Les voltammogrammes de courant échantillonnés pour les films ont été reconstruits pour différents temps d'échantillonnage, figure 9-3a) à c) (page 148). Dans tous les cas, les densités de courant mesurées sont plus élevées pour des temps d'échantillonnage plus courts, et elles diminuent à mesure que le temps d'échantillonnage augmente, ce qui est caractéristique du transfert rapide d'électrons. Dans la fenêtre de potentiel étudiée, trois processus principaux sont observés dans tous les VCE reconstruits, la désorption d'hydrogène (H_{UPD}), la désorption d'oxygène (O_{des}) et l'adsorption d'oxygène (O_{ads}). Pour chacun de ces processus, les potentiels où ils apparaissent et les densités de courant qui leur sont associées dépendent de l'orientation cristallographique des films, figure 9-3d).

La discussion des caractéristiques s'est concentrée sur la désorption de l'oxygène des surfaces de Pt, car c'est le processus le plus important pour la ORR. La désorption de l'oxygène apparaît dans le même potentiel où la RRO a lieu, et les potentiels de pointe, les densités de courant (et les charges échangées) se sont avérés dépendre de la structure des films. Un tracé des pics de courant en fonction de l'inverse du temps donne une relation linéaire, ce qui suggère que les pics proviennent d'un processus réel d'adsorption en surface, figure 9-4a) (page 149).

L'analyse des charges obtenues expérimentalement pour la désorption de l'oxygène à la surface des films Pt/MgO(hkl) révèle une augmentation de la charge de désorption de l'oxygène de l'ordre (111) > (001) > (110), ce qui correspond à la tendance de l'activité ORR rapportée dans la littérature. L'activité ORR sur les monocristaux de Pt dans les solutions d'acide sulfurique suit la séquence (110) > (100) > (111), et l'adsorption spécifique des espèces sur les surfaces de Pt dans la fenêtre de potentiel ORR joue un rôle essentiel dans la sensibilité de cette structure[22, 75]. À cet égard, l'énergie d'adsorption des espèces oxygénées sur les surfaces de Pt est élevée[27], et le taux d'élimination de ces espèces en surface affecte le taux RRO[25].

Les résultats présentés montrent que la VCE représente une technique puissante et polyvalente dans la caractérisation électrochimique des surfaces, et qu'elle fournit un riche ensemble d'informations non seulement sur les réactions contrôlées par diffusion, mais aussi sur les processus d'adsorption de surface. La sensibilité de la technique est démontrée par les résultats distincts obtenus pour chaque surface, et la VCE est suffisamment sensible pour montrer l'adsorption d'espèces à la surface même pour des processus rapides comme le H_{UPD}.

Ces résultats préliminaires ont montré que même en l'absence d'O_2, si l'électrode est maintenue à des potentiels proches du potentiel de circuit ouvert, l'adsorption d'espèces oxygénées se produit, et la réduction de ces espèces est observée dans les VCE. Ces espèces oxygénées proviennent probablement de la décharge d'eau à la surface de l'électrode. Il est important de noter que les résultats expérimentaux indiquent que ce processus est également sensible à la structure des films de Pt/MgO(hkl), et l'analyse qualitative de la charge associée à la désorption de l'oxygène a montré qu'elle augmente dans l'ordre inverse de l'activité de la RRO sur les monocristaux de Pt(hkl). Cette corrélation suggère un effet d'empoisonnement de ces espèces adsorbées, entraînant la diminution du taux de la RRO. Pour obtenir des informations plus concluantes concernant les implications de ces espèces adsorbées sur la voie RRO sur les surfaces à faible indice de Pt, d'autres expériences sont nécessaires.

5. Conclusions et perspectives

Le premier objectif de cette thèse est de proposer des films minces à orientation épitaxiale déposés par DLP comme voie alternative pour produire des surfaces modèles pour l'investigation de la RRO. L'orientation épitaxiale du film déposé par DLP permet d'obtenir des matériaux présentant un degré élevé d'organisation structurelle et dont les caractéristiques sont remarquablement similaires à celles des monocristaux analogues. Le second objectif de cette thèse est de mettre en œuvre la méthode VCE pour étudier la RRO sur ces films minces. La VCE est apparue comme une méthode alternative pour étudier la RRO, car les substrats de MgO sont isolants, ce qui rend impossible l'utilisation des méthodes hydrodynamiques (EDR et EDAR).

Les résultats expérimentaux rapportés dans cette thèse fournissent des preuves en faveur de l'adéquation des couches minces à orientation épitaxiale comme surfaces modèles pour les études électrocatalytiques de la RRO. Des couches minces de Pt orientées selon les directions cristallographiques [100], [110] et [111] ont été déposées avec succès sur des substrats de MgO(hkl). La caractérisation électrochimique en milieu acide a montré que dans les cas du Pt/MgO(100) et du Pt/MgO(110), les surfaces des films reflètent leur orientation cristallographique globale et fournissent une réponse électrochimique très similaire à celle du monocristal respectif.

De plus, des films d’Au développés dans la direction [100] ont été déposés avec succès sur des substrats de MgO(100). La caractérisation structurelle a montré que les films d’Au déposés ont une structure bien définie dans la direction [100], et que leur comportement électrochimique est remarquablement similaire à celui du monocristal d’Au(100).

L’épaisseur des films d’Au a été variée, dans le but d’introduire intentionnellement une contrainte dans le réseau des films d’Au et d’explorer l’effet de la contrainte sur l’activité électrocatalytique de la RRO. Ainsi, les films ont été entièrement caractérisés, et l’épitaxie dans la direction [100] a été réalisée à travers toute la gamme des épaisseurs étudiées. Leur comportement électrochimique a révélé que, quelle que soit leur épaisseur, ils présentaient des caractéristiques voltampérométriques correspondant à un monocristal d’Au(100). Par la suite, l’activité de la RRO de ces films a été étudiée par voltampérométrie de courant échantillonné, et leur activité de RRO a augmenté avec l’épaisseur des films. La caractérisation structurelle a montré que les films ont une certaine contrainte dans leurs réseaux, mais l’ampleur de la contrainte générée semble être trop faible pour affecter l’activité RRO. Ainsi, la variation de l’activité observée n’était pas un effet de déformation.

La dépendance de l’activité de la RRO observée dans les films est associée à la taille du domaine (100) trouvée dans les cristallites qui construisent les films au moyen de la taille de cohérence latérale mesurée par RSM. Ainsi, il a été observé que plus la taille du domaine est grande, plus l’activité de la RRO est élevée. Si on considère la taille du domaine égale à la largeur des (100) terrasses à la surface des films, une tendance similaire a été signalée dans la littérature pour les monocristaux d’Au à gradins. Cela suggère qu’en ce qui concerne la RRO sur les matériaux en Au, non seulement la symétrie locale des sites disponibles sur la surface est importante, mais aussi leur extension. La conséquence de ces découvertes pour la conception d’électrocatalyseurs destinés à des applications pratiques est que des activités RRO aussi élevées que celles observées pour les monocristaux peuvent être réalisées dans les cas où les domaines actifs adéquats sont suffisamment larges.

La validation du courant échantillonné comme méthode alternative pour étudier la RRO est une contribution parallèle importante de ce travail dans le domaine de l’électrocatalyse. Les conditions dans lesquelles les résultats de la VCE peuvent être comparables aux résultats de l’EDR ont été dérivées et validées avec succès. Tout d’abord, la VCE reconstruite pour le couple redox ferry-ferro à l’aide d’un disque en poly-Pt a fourni des résultats qui s’adaptent très bien aux résultats EDR, validant avec succès le coefficient de transfert de masse comme paramètre clé pour faire correspondre les résultats obtenus par les deux méthodes. Par la suite, la VCE a été utilisé pour étudier le EDR sur un disque en poly-Pt, ce qui a révélé un système difficile en raison de la réactivité intrinsèque de la surface du Pt dans les solutions acides aqueuses et des limites de la VCE.

La VCE reconstruite pour la RRO sur le disque en poly-Pt correspondait au balayage cathodique dans la voltampérométrie EDR, qui fait référence à une surface de Pt légèrement oxydée. Malgré ces difficultés, une réponse satisfaisante à l'application de la VCE sur des électrodes en Pt pour étudier la RRO a été obtenue pour le disque en poly-Pt et le film en Pt/MgO(110), dont les résultats méritaient un article de recherche.

Comme la nature de l'Au diffère de celle du Pt, l'application de la VCE pour étudier la RRO a été plus facile dans le sens où il n'y a pas de problèmes avec le potentiel de repos, et la réponse attendue des films d'Au pour la RRO a été obtenue. La VCE était suffisamment sensible pour fournir des courbes de polarisation qui répondaient très bien non seulement à l'orientation cristallographique des films, mais aussi à la taille (001) des domaines de surface. Les paramètres cinétiques obtenus avec les diagrammes de Koutecký-Levich et de Tafel pour les films d'Au ont également révélé les différences d'activité et ont permis d'évaluer comment la cinétique de la RRO sur les films a répondu aux changements structurels observés.

Les résultats de la VCE démontrent la polyvalence de la technique et soulignent le potentiel de son application sur des systèmes qui ne peuvent pas être étudiés dans une installation d'EDR. Ils constituent également une réalisation importante pour l'étude de la RRO, car elle apporte une solution aux situations dans lesquelles les installations EDR/EDAR ne sont pas disponibles ou adaptées.

Ainsi, la VCE est une technique qui peut être adaptée pour étudier différentes réactions, si nécessaire, et la seule instrumentation nécessaire est un potentiostat. L'utilisation de cette technique nécessite un ensemble d'expériences pour optimiser les meilleures conditions expérimentales. Le potentiel de repos doit être considéré avec soin, car il contrôle l'état de la surface avant que la réaction n'ait lieu, et il peut être ajusté par des études de voltampérométrie cyclique dans la fenêtre de potentiel où la réaction a lieu.

Les travaux de recherche décrits dans cette thèse présentent et valident une méthodologie complète pour réaliser des études modèles en électrocatalyse de la RRO. Par conséquent, de nouveaux outils pour les études électrocatalytiques de matériaux pour des applications de conversion d'énergie sont maintenant disponibles pour les expérimentateurs dans la poursuite des nouveaux matériaux d'électrode pour les piles à combustible.

Suite aux résultats rapportés dans cette thèse, une stratégie prometteuse dans la recherche de nouveaux électrocatalyseurs consiste à profiter de la polyvalence du DLP pour préparer une large gamme de films de composition et de structure variées et les tester pour la RRO en utilisant le VCE. La préparation de films alliés à orientation épitaxiale fournit une excellente plate-forme modèle pour établir une relation structure-réactivité pour la RRO qui ne serait pas possible ou difficile, et qui prendrait du temps par d’autres moyens.

TABLE OF CONTENTS

LIST OF FIGURES

LIST OF TABLES

LIST OF EQUATIONS

(1) $\Delta G = -nF\Delta E$

(2) $\Delta \mathrm{E}_{ideal} = E^0_{cathode} - E^0_{anode}$

(3) $\eta = E^0 - E$

(4) $\Delta \mathrm{E}_{actual} = E_{cathode} - E_{anode}$

(5) $\varepsilon = \frac{\Delta G}{\Delta H} = \frac{237.1}{285.8} = 0.83 \approx 83\%$

(6) $\varepsilon_{actual} = \frac{0.83 \times E_{actual}}{\mathrm{E}_{ideal}}$

(7) $H_2 \rightarrow 2\,H^+ + 2\,e^- \quad E^0 = 0\,V$

(8) $\frac{1}{2}O_2 + 2\,H^+ + 2\,e^- \rightarrow H_2O \quad E^0 = 1.229\,V$

(9) $H_2 + \frac{1}{2}O_2 \rightarrow H_2O \quad E^0 = 1.229\,V$

(10) $O_2 + 4\,H^+ + 4\,e^- \rightarrow 2\,H_2O \quad E^0 = 1.229\,V$

(11) $O_2 + H_2O + 4e^- \rightarrow 4\,OH^- \quad E^0 = 0.401\,V$

(12) $O_2 + 2H^+ + 2e^- \rightarrow H_2O_2 \;\; E^0 = 0.670\,V$

(13) $H_2O_2 + 2H^+ + 2e^- \rightarrow 2\,H_2O \;\; E^0 = 1.77\,V$

(14) $2\,H_2O_2 \rightarrow 2\,H_2O + O_2$

(15) $O_2 + H_2O + 2e^- \rightarrow HO_2^- + OH^- \;\; E^0 = -0.065\,V$

(16) $HO_2^- + H_2O + 2e^- \rightarrow 3\,OH^- \; E^0 = 0.867\,V$

(17) $2HO_2^- \rightarrow OH^- + O_2$

(18) $i_{lim} = 0.201\,nFAD^{2/3}v^{-1/6}C_{Ox}\omega^{1/2}$

$$i = i_0 \left[exp\left(\frac{\alpha nF}{RT}\eta\right) - exp\left(\frac{(1-\alpha)nF}{RT}\eta\right)\right] \tag{19}$$

$$\eta = \frac{2.303RT}{\alpha nF}\log i_0 - \frac{2.303RT}{\alpha nF}\log i \tag{20}$$

$$\frac{1}{i_{disk}} = \frac{1}{i_k} + \frac{1}{i_{lim}} \tag{21}$$

$$i = \frac{nFAD^{1/2}C^B}{\sqrt{\pi t}} \tag{22}$$

$$i_{lim} = nFAk_m C^B \tag{23}$$

$$k_m = 0.201\, D^{2/3}\nu^{-1/6}\omega^{1/2} \tag{24}$$

$$k_m = \sqrt{\frac{D}{\pi\tau}} \tag{25}$$

$$t_{dl} = R_s C_{dl} \tag{26}$$

$$i^{-1} = \frac{\sqrt{\pi}\,\sqrt{t}}{nFAD^{1/2}C^B} \tag{27}$$

$$m = \frac{\sqrt{\pi}}{nFAD^{1/2}C^B} \tag{28}$$

$$i_{dl} = \frac{E}{R_S}e^{-t/R_S C_d} \tag{29}$$

$$C_{dl} = \frac{(Q_0 \times R_S)^{(1-n)}}{R_S} \tag{30}$$

$$\varepsilon = \frac{(a_{substrate} - a_{metal})}{a_{substrate}} \times 100\% \tag{31}$$

$$d = \frac{\lambda}{2\sin \Delta\theta} \tag{32}$$

$$\frac{L_2}{L_1} = -\frac{\cos(\epsilon)}{\cos(\varepsilon+\phi)} \text{ and } \frac{L_3}{L_2} = -\frac{\sin(\phi)}{\cos(\varepsilon)} \tag{33}$$

$$\phi = tan^{-1}\left(\frac{Q_{//}}{Q_{\perp}}\right), \varepsilon = tan^{-1}\left(\frac{\Delta Q_{//}}{\Delta Q_{\perp}}\right) \text{ and } L_3 = \sqrt{\left(\Delta Q_{//}\right)^2 + (\Delta Q_{\perp})^2} \tag{34}$$

(35) $$|L| = \frac{1}{L_1} = -\frac{\sin(\phi)}{L_3 \times \cos(\phi+\varepsilon)}, \text{ and } T = \frac{L_2}{\sqrt{Q_\perp^2 + Q_{//}^2}}$$

(36) $$H_2O \rightleftarrows O_{ads} + 2H^+ + 2e^-$$

(37) $$\text{Elastic strain (\%)} = \left(\frac{a_{exp} - a_{Au}}{a_{Au}}\right) \times 100\%$$

LIST OF ABBREVIATIONS

AES	Auger spectroscopy
AFM	atomic force microscopy
Au	gold
CV	cyclic voltammetry
DFT	density functional theory
EASA	electrochemically active surface area
fcc	face-centered cubic structure
FCs	fuel cells
HOR	hydrogen oxidation reaction
ICEs	internal combustion engines
K-L plots	Koutechý-Levich plots
LEED	low-energy electron diffraction
MMSE	mercury mercurous sulfate electrode
MMO	mercury mercurous oxide electrode
NHE	normal hydrogen electrode
ORR	oxygen reduction reaction
OCP	open circuit potential
PEMFCs	polymer electrolyte fuel cells
PLD	pulsed laser deposition

Pt	platinum
PVD	physical vapor deposition
RDE	rotating disk electrode
rds	rate-determining step
RHE	reversible hydrogen electrode
R_f	roughness factor
RRDE	rotating ring-disk electrode
RSM	reciprocal space mapping
SCV	sampled current voltammetry
STM	scanning tunneling microscopy
UHV	ultrahigh vacuum
XPS	X-ray photoelectron spectroscopy
XRD	X-ray diffraction
XRR	X-ray reflectivity

1 INTRODUCTION

1.1 The role of energy in society

The modern world is driven by energy in all aspects. Thus, the accessibility, cost, and reliability of the energy sources have dictated society's structure and development. Since the industrial revolution, the industry, transportation, and power plants have been fed by fossil fuels (oil, coal, and natural gas[76]), and their availability, implementation, and usage have propelled much of the economic and technological progress achieved since then. However, the massive use of fossil fuels has a toll on the environment and may threaten future generations' lives.

There are several issues associated with the intensive use of fossil fuels, but at the core of the problems are oils spills, pollution (smog, acid rain, and NOx formation in the atmosphere), the high greenhouse gases emissions (CO_2, CH_4) produced as a waste of the fuel's combustion, and the finitude of the fossil fuel sources. As people became aware of these deleterious effects on the environment, the remediation of these damages became a major concern. In this sense, the management and reduction of the emissions, the increase in energy efficiency, and the gradual implementation of renewable energy sources can provide significant benefits[77].

The awareness of the necessity of changes in the energy sources has shifted how people choose the energy source to a determined application. Thus, the cleanliness of energy and how it impacts the environment is becoming equally important as the cost, availability, and reliability of the energy source[78]. However, providing energy from a source that is clean, harmless to the environment but also affordable and reliable is not easy because all energies have environmental impacts and limitations to be considered and managed.

The increasing demand for energy results in another significant challenge, the scale, because of the colossal amounts of energy demanded[79]. The increase in the efficiency of the energy conversion processes is a critical approach to address the scale issue. Finding energy sources that meet all these attributes is crucial but not easy, and we can expect a slow and expensive transition from fossil fuels to any other energy source.

Even if it is slow and costly, this is a necessary transition to reduce pollutant emissions and the dependence on fossil fuels. From this perspective, the introduction of alternative energy sources may lead to the gradual replacement of fossil fuels or at least minimize the dependence on such fuels[77]. Renewable energy sources appear as a viable alternative to mitigate the main issues brought by fossil fuels because they can be replenished by themselves with time and are environment-friendly[76-77]. The energy coming from wind and water motion, sunlight and heat, and geothermal energy are a few of the available renewable sources. The most significant advantage is that renewable energy is available in abundance, unlimited, and cleaner than fossil fuels[76-77].

Nonetheless, there are challenges associated with renewable energy implementation and application on larger scales. The energy availability may be seasonal and varies with geographic location. Additionally, a high initial investment is necessary to start the operation. One of the main constraints is that these energy sources' intermittent character is a challenging feature because it affects power consistency and reliability.

Hence, highly innovative solutions are required to address the efficiency, cost, and reliability degrees necessary to replace at least partially the fossil fuels. For instance, a combination of hydrogen, biofuels, and renewable energy sources seems a promising approach.

1.2 Fuel Cells

The fuel cells (FCs) are electrochemical devices that convert the chemical energy of a fuel externally supplied into electric energy[1]. Sir William Grove conceptualized the FCs, back in 1839, but the FCs remained forgotten for a while, and they did not experience any considerable progress until a century later. In the 1960s NASA's Apollo space program performed the first practical application of the FCs in space applications using an alkaline fuel cell that conveniently provided electricity, heat, and potable water for the crew[1-2].

Generally, the FCs are classified according to the electrolyte used to build the device, and the main types are polymer electrolyte fuel cells (PEMFCs), alkaline fuel cells (AFCs), phosphoric acid fuel cells (PAFCs), molten carbonate fuel cells (MCFCs) and the solid oxide fuel cells (SOFCs)[1-2]. According to the electrolyte, the operative characteristics of the fuel cells, the operation temperature, the fuels, and the catalysts vary. Therefore, each type of FC has its challenges, advantages, and disadvantages. Due to their versatility, the fuel cells fit a range of applications, comprising stationary, vehicle propulsion, and mobile applications[2, 80].

Therefore, there are environmental and social factors supporting the development of the FCs, and for this reason, they emerge as a promising technology to mitigate the deleterious effects caused by fossil fuel emissions and as an alternative for the dependence on carbon-based fuels. The replacement of the internal combustion engines (ICEs) used in transportation by hydrogen-fueled fuel cells is an attractive route for decreasing carbon emissions. Although some engineering challenges are associated with the system's dimension and transport of the fuel, the PEMFCs are up-and-coming candidates for vehicle propulsion applications. Buses propelled by PEMFCs stacks operating with H_2 as fuel was successfully achieved in 1998 in Chicago[81], and there are companies such as Toyota, Hyundai, and Honda[82-83] producing cars powered by H_2 fuel cells.

1.2.1 Operation of the fuel cells

The operation of the fuel cells refers to the principles of the galvanic electrochemical cells. In these electrochemical cells, spontaneous chemical redox reactions take place at the electrodes generating electricity[3]. Hence, the oxidation of the fuel takes place at the anode of the cell, and the oxidizer is reduced at the cathode.

To illustrate a FC operation, Figure 1-1 shows a general scheme of a PEMFC operating with H_2 and O_2. The scheme shows that the FC setup comprises the anode and the cathode, where gas diffusion electrodes prepared with platinum nanoparticles dispersed in carbon as the catalysts are separated by the polymer electrolyte membrane (PEM) and connected by an external circuit. At the anode, the H_2 oxidation takes place, generating an electron flux that moves along the circuit to reach the cathode where O_2 is reduced to H_2O. Then, the H^+ formed as a product of the H_2 oxidation migrate through the electrolyte to combine with the OO^- produced on the cathode to form water[80].

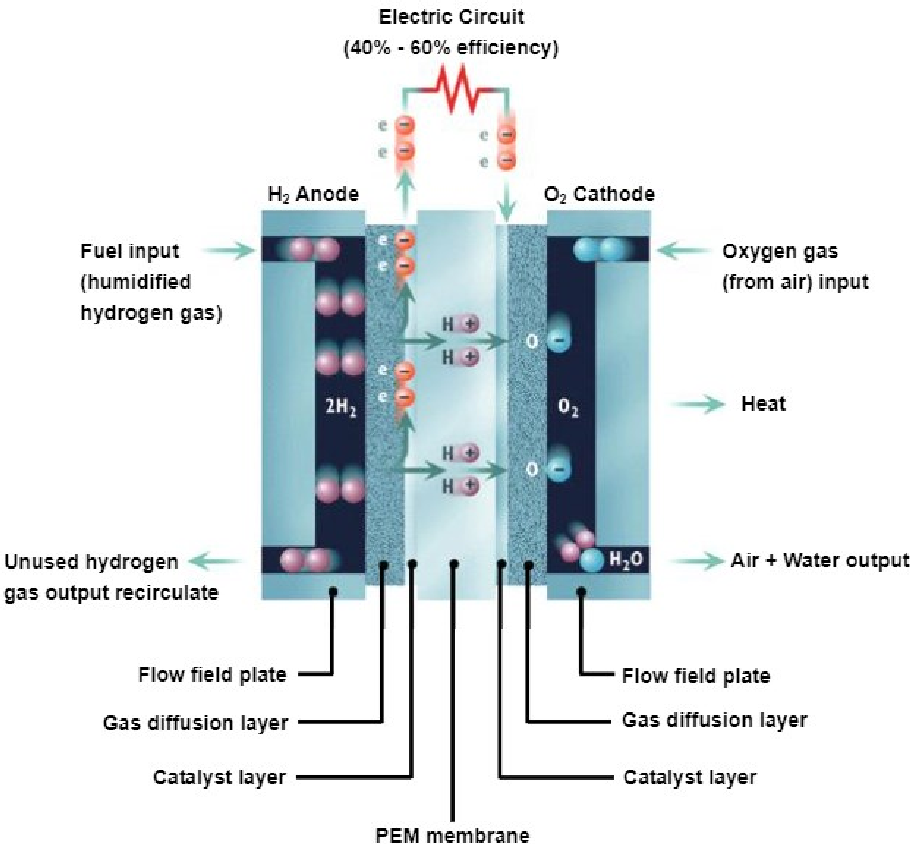

Figure 1-1: Scheme illustrating the operation of an H_2/O_2 PEMFC, taken from reference[84].

A general overview of fundamental thermodynamics on the FCs operation is a good starting point for predicting the maximum potential delivered by a fuel cell and understand their performance. Therefore, to achieve the maximum efficiency possible, the FCs must be designed to operate by delivering potential differences as close as possible to those predicted by the thermodynamics.

In this sense, the Gibbs free energy allows estimating the maximum amount of work delivered by the energy conversion performed by the FC system. The free energy change associated with the chemical reactions taking place at the cathode and the anode relates to cell potential according to:

$$\Delta G = -nF\Delta E \qquad (1)$$

Where ΔG is the Gibbs free energy, n is the number of electrons exchanged in the reaction, F is the Faraday constant, and ΔE is the cell voltage. Equation (1) shows that the energy generation scales with the number of electrons exchanged and the voltage of the cell, which in turn depends on the chemical reactions involved in the electrodes. Then, the maximum cell potential achieved, and it can be regarded as the thermodynamic reversible cell potential, is:

$$\Delta\mathrm{E}_{ideal} = E^0_{cathode} - E^0_{anode} \qquad (2)$$

However, the Gibbs free energy is related to reversible reactions taking place, and often the reactions do not take place at the equilibrium potential but rather close to it. This extra energy necessary to drive the reactions results in energy losses. In electrochemistry, the measurement of the deviation of the reactions from the equilibrium potential is given by the overpotential (η), being:

$$\eta = E^0 - E \qquad (3)$$

Where E^0 is the half-cell potential of the reaction at standard conditions. The overpotential provides a measure of the reaction irreversibility; the higher is the overpotential necessary to start the reaction, the more irreversible is the reaction. Therefore, a fuel cell's performance is generally discussed by comparing the reversible voltage and the voltage delivered after the subtraction of the overpotential losses[85]. In this context, the actual cell potential is:

$$\Delta\mathrm{E}_{actual} = E_{cathode} - E_{anode} \qquad (4)$$

The efficiency (ε) of the conversion performed by the fuel cell can be estimated by the ratio between the actual electrical work delivered and the maximum available work. Considering an H_2/O_2 FC, the thermodynamic efficiency is given by the ratio of the Gibbs energy of formation of H_2O (in liquid state), 237.34 kJ/mol, and the enthalpy of the fuel (H_2), 286.08 kJ/mol[80, 86]:

$$\varepsilon = \frac{\Delta G}{\Delta H} = \frac{237.1}{285.8} = 0.83 \approx 83\% \qquad (5)$$

Therefore, operating in reversible conditions at room temperature (25 °C, 1 atm), the maximum efficiency achievable by an H_2/O_2 FC is 83%, considering liquid water as a product[85]. However, as mentioned above, the FCs operate at conditions close to the equilibrium, and for this reason, the energy losses must be accounted for in the actual efficiency, which can be estimated by:

$$\varepsilon_{actual} = \frac{0.83 \times E_{actual}}{E_{ideal}} \qquad (6)$$

When H_2 is the fuel supplied to the FC, the only products are electricity, heat, and water. In this case, in acid media, the reaction at the anode is[2, 80]:

$$H_2 \rightarrow 2\,H^+ + 2\,e^- \quad E^0 = 0\,V \qquad (7)$$

The most common oxidizer used in the fuel cells is O_2, supplied by either an O_2 or air stream. In both cases, the cathodic reaction is the same: the oxygen reduction reaction (ORR). The main difference is that in the air stream, the O_2 is diluted, and its fraction is around 21%. Then, the cathodic reaction in acidic media is:

$$\frac{1}{2}O_2 + 2\,H^+ + 2\,e^- \rightarrow H_2O \qquad E^0 = 1.229\,V \qquad (8)$$

Therefore, by combining the anodic and cathodic reactions, the overall reaction is:

$$H_2 + \frac{1}{2}O_2 \rightarrow H_2O \qquad E^0 = 1.229\,V\ (9)$$

The cell voltage (ΔE) is given by the difference between the half-cell potential at the cathode and the anode. Therefore, the thermodynamic potential is 1.229 V, which reveals the maximum potential possibly reached in such conditions, as explained above. However, in practice, the actual potential reached is below the thermodynamic potential. This happens because there are potential losses caused by several contributions, namely, the electrode reactions activation (kinetic effects), resistance effects coming from the electrolyte and electrodes, and mass transfer processes[1-2, 80]. Figure 1-2 illustrates how some of these energy losses affect the actual potential of the cell by showing current-voltage curves for the half-cell reactions and the cell. Data taken from reference[87] for a membrane FC operating with H_2 and O_2 and both electrodes comprises 20% wt Pt catalysts supported on carbon black.

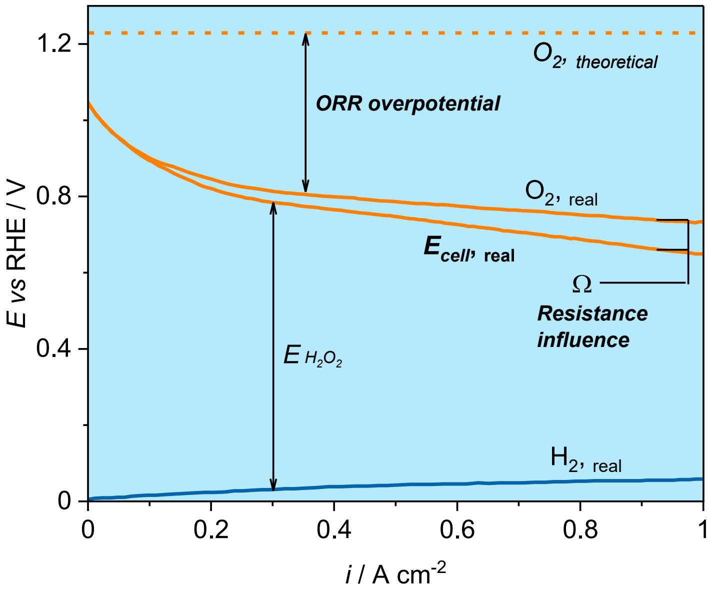

Figure 1-2: Diagram of the energetic losses on a typical PEMFC operating with H_2/O_2, adapted from reference[87].

In the illustration, the dashed orange line shows the thermodynamic potential for the ORR, that is, the ideal potential obtained in the absence of hindrances. The thermodynamic potential for the hydrogen oxidation reaction (HOR) is 0 V, and it overlaps with the *x*-axis. The solid orange lines show the real potentials for the ORR and the cell, and the solid blue line illustrates the real potential for the HOR. The polarization curves show that at low currents, the electrodes' kinetics controls the potential of the FC. However, as the current density increases and the kinetic barrier is surpassed, the resistance contributions cause another significant drop in potential, and at high current densities (not shown here), the mass transfer rate also causes a drop in potential.

The figure also shows the H_2 oxidation at the anode takes place at potentials close to the equilibrium potential, and the potentials losses are low. However, the cathodic O_2 reduction proceeds far from the thermodynamic potential and requires more energy to be driven, causing a remarkable potential drop in the cell potential. Due to the electrode's polarization, low cathodic currents start to be measured at $E \approx 0.900$ V for the ORR – resulting in losses ranging from 300 - 400 mV[88]. Therefore, as the actual potential of the cell is the difference between the two half-cells – roughly 0.700 – 0.800 V – the potential of the cell is significantly lower than the 1.229 V thermodynamically predicted.

The potential losses demonstrated are a combination of kinetic, engineering, and mass transfer limitations, and each of these potential losses imposes a specific challenge to researchers. For instance, the overpotential for the electrode reactions and mass transfer issues can be minimized by designing electrodes with enhanced performances. Such electrodes are built using good electrocatalysts and assembled in a way that allows the gases to diffuse fast within the electrode to reach the catalyst surface and the intermediates to diffuse out of the electrode, releasing the active sites of the catalyst. The mass transfer requirements are met using the gas diffusion electrodes, usually made of carbon paper[80, 89], which also supports the catalyst layer.

The H_2 oxidation reaction (HOR) occurs at high rates on the platinum electrocatalysts, and mass transfer usually controls the electrochemical rate of the reaction[2, 80]. In this sense, the main issues associated with the HOR are i) the need for the expensive Pt as catalyst[90] and ii) the need for high purity H_2 fuel. If carbon monoxide is present in the fuel stream, it adsorbs strongly to the Pt surface blocking the catalyst and causing a drop in the performance of the cell[4].

In opposition to the HOR, the ORR kinetics is somewhat sluggish and requires high overpotentials to initiate even using Pt catalysts in the cathode. As demonstrated in Figure 1-2, this activation loss reduces the conversion efficiency significantly. For this reason, the cathode limits the operation of the fuel cells and requires higher platinum loadings to perform reasonably. Typical loadings of Pt in the cathode is 0.35 mg cm^{-2} and 0.15 mg cm^{-2} for the anode[21, 87].

Nevertheless, despite the possible losses on the voltage experienced by the fuel cells, they remain regarded as excellent and promising energy conversion devices for the following reasons: they can achieve high-energy conversion efficiencies (especially compared to the internal combustion engines), and if H_2 is the fuel, only water and heat are the by-products. Well-designed fuel cells can reach 60% in energy conversion efficiency, whereas the efficiency achieved in most internal combustion engines reaches 34% because the Carnot cycle limits their operation. Additionally, since some FCs also produce heat, using co-generation, the efficiencies can go up to 80%[1]. The fuel cells have been proposed as a viable alternative to the combustion engines on account of more environmental-friendly and efficient conversion of energy delivered[2, 80, 91-92].

1.2.2 Challenges associated with the fuel cells widespread usage

The FCs technology is promising, but unfortunately, there are constraints in the FCs limiting their practical application. In this regard, the primary reasons hindering the development of FCs are economic factors, materials problems, and some issues in their operation[2]. The main obstacles to the widespread of the FCs are the high cost and long-term stability of the platinum electrocatalysts, combined with the requirements regarding the quality, storage, and transportation of the H_2 fuel.

When comparing the performance of the anode and the cathode of an FC, it was demonstrated in the previous section that the HOR is fast on Pt catalysts, and the literature reports that if high purity H_2 feeds the anode, it performs well and remains stable[4]. However, at the cathode, the scenario is different. Due to the ORR's slow kinetics, a higher platinum load is necessary to keep the appreciable operation of the cathode, which is still far from the thermodynamic potential. This leads to a significant increase in the device's cost and reduces the performance of the FC. Additionally, the oxidative and corrosive operating conditions experienced by the cathode reduce the active surface area of the Pt by the dissolution of the metal and the corrosion of the carbon-based support to the catalyst[4-7], which directly affects the efficiency of the energy conversion. The hindrances related to the cathode operation are amongst the most challenging aspects of the FCs operation. Unfortunately, this issue affects several types of FCs, as the ORR is the cathodic reaction in many of them[8].

The fact that the FCs operate under aggressive and corrosive conditions limits the range of electrode materials available to build the FC electrodes. In acidic media, the electrocatalysts replacement scenario is very complex and challenging to solve because even Pt, the start-of-art electrocatalyst, is neither sufficiently active nor stable in the long term[93]. Hence the electrocatalysts are limited to the expensive and scarce platinum group materials[90, 94].

Different material preparation strategies are used aiming to address the problem with the platinum electrocatalysts. The strategies include alloying of platinum with more abundant transition metals[19, 75, 95-96], more efficient use of platinum by optimizing the size and shape of the platinum nanoparticles[97-99], and even the attempt to replace entirely platinum[94, 100-101]. Nevertheless, this is not an easy task because to be a suitable candidate to replace the platinum, the material must at least pair its performance with the noble metal and be at least as stable as platinum is, which is difficult considering the corrosive and harsh operating conditions of the fuel cells. In this sense, M-N_x/C (where M= Fe, Co, Ni, Mn, etc.) catalysts[94, 102-104] are proposed as alternative materials to replace platinum as they exhibited activity for the ORR with stability similar to the Pt/C cathodes. However, there are challenges to overcome regarding the ORR activity and the long-term stability of such materials.

Additionally, along with the challenges associated with the catalysts and different parts of the fuel cells – catalysts, assembling, and membranes – the use of hydrogen as a fuel also imposes some issues. Hydrogen does not exist in nature, and therefore, it must be extracted/converted from any other source, which requires energy regardless of the route used to produce H_2. A significant part of the hydrogen produced comes from the steam reforming of the methane to produce a combination of hydrogen and carbon monoxide and/or carbon dioxide[105]. The process requires high pressure and temperature, and the hydrogen produced contains carbon monoxide, which poisons the catalysts.

Alternatively, commercial water electrolyzers can produce high purity hydrogen reaching efficiencies around 70%[49], and the main drawback is the cost of the power supply for the process. Notwithstanding, in places where this is not a constraint, this is an attractive route to produce hydrogen[106]. For instance, Québec produces affordable hydroelectricity from water movement, making electrolysis an ideal route for producing H_2. In such conditions, the process is affordable and has the extra advantage of being powered by a renewable energy source, making the hydrogen produced as clean as possible.

Furthermore, the hydrogen storage and transportation system are complex and prone to be heavy and bulky, which hinders transportation applications. The efficiency in delivering the gas must also be considered, and extra energy is necessary to compress and liquefy the hydrogen. The durability of the system needs to be improved as well as the refueling time.

The challenging scenario involving the FCs and hydrogen technology leads researchers to experience cycles of big hope and expectations and disappointment and disillusion. However, all the efforts to enhance the FC’s performance and cost are worthy because the benefits to the environment and the society may be uncountable if researchers surpass these challenges. If we manage to reach a point in which the use of hydrogen in fuel cells in the propulsion of vehicles becomes viable, the greenhouse gas emissions may be significantly reduced compared to the current vehicles that use ICEs. The scenario is optimistic because even though these hindrances, companies such as Toyota, Hyundai, and Honda[82-83] are producing cars fed by H_2 fuel cells.

1.3 Electrocatalysis and model surfaces

The need to have platinum as an electrocatalyst in the FCs electrodes remains one of the main hindrances to the widespread of FCs. Thus, researchers continuously search for materials that can replace the expensive and scarce platinum as electrocatalysts. In this sense, understanding the factors affecting the reaction rate is fundamental to design better electrocatalysts. For this reason, electrocatalysis is the field in the science of utmost importance in such endeavor.

A catalyst is a substance that increases the reaction rate without undergoing any chemical modification or being consumed in the reaction. Hence, a catalyst accelerates the kinetics of a reaction by either reducing the activation energy or offering an alternative pathway for the reaction, but it has no effect on the thermodynamics[86, 107]. In electrocatalysis, the electrode surface is responsible for accelerating the electrochemical rate, and consequently, it is the electrocatalyst[21, 108].

The mechanism by which an electrocatalyst accelerates the rate of an electrochemical reaction involves the adsorption of species, either reactants or intermediates, to the electrode surface. The adsorption of species decreases the activation energy because the interaction of these adsorbed species with the surface facilitates the breaking and/or forming of new bonds, resulting in an increased overall reaction rate[21, 108]. Therefore, whenever an electrode process involves the re-arrangement of chemical bonds, this reaction occurs at different rates – often by many orders of magnitude – on different substrates, and the electrocatalytic nature of the surface is revealed[9]. In practice, the electrocatalyst's action on an electrode process increases the current density at a fixed potential value or reduces the overpotential for a fixed value of current density.

Considering the importance of adsorption on electrocatalysis, it is useful to introduce Sabatier's principle. This is a fundamental principle of heterogeneous catalysis, and its application guides the prediction of the electroactivity of the catalysts for a determined reaction. Sabatier's principle states that the best catalyst for a specific heterogeneous reaction is the one where the binding strength of the adsorbed species (reactants, intermediates, and products) at the surface should be optimal, neither too strong nor too weak. In both cases, the reaction rate will decrease, but for different reasons, in the first case, the surface is blocked by the adsorbed species, and in the second case, the reaction activation energy is increased[9, 107, 109-111].

Thus, finding the best electrocatalyst for a specific application requires continuous efforts to understand the reaction kinetic limitations and mechanism, including the in-depth knowledge impact of the adsorbed species on the reaction rate and selectivity. However, when dealing with complex surfaces such as polycrystalline materials and nanoparticles with different shapes and compositions, extracting such information is intricate. This comes from the fact that these surfaces may comprise many possible active sites with different symmetry with non-uniform surface distribution[112-113]. The lack of homogeneity on the surfaces mentioned above makes it difficult to understand the interplay between the surface structure, the local electronic properties associated with the chemical composition, and the species' adsorption energy.

In this context, the model surface approach has been successfully adopted to resolve the different catalytic contributions coming from the different active sites to the overall activity of the electrocatalysts[9-17]. This is possible because by narrowing the active sites' distribution and fixing the composition of the surface, a correlation between the reactivity and selectivity can finally be established. Therefore, a model electrocatalyst is a material with a well-defined structure and composition with a high degree of homogeneity in the atomic order at the material surface[10-11, 18-20], and the surfaces of single crystals are ideally suited to meet these needs. Since this approach was introduced in the 1960s, experiments using such materials became fundamental to elucidate the structure-reactivity on the electrochemical behavior of the electrocatalysts[12-13, 16, 18, 33, 36, 112, 114-118].

The advance in surface characterization techniques experienced in the 60s propelled the progress of surface science. The discovery of the low-energy electron diffraction (LEED), Auger spectroscopy (AES), and high-resolution electron energy-loss spectroscopy (EELS) represented a landmark in the field. Then, combined these powerful techniques were coupled to the ultrahigh vacuum conditions (UHV) system to provide a detailed characterization of the surfaces at an atomic level, allowing the surface's structure and composition to be known and well defined from the experiments[119].

Single crystals electrochemistry is a fundamental tool to elucidate the nature of the active sites and how they affect the rate and selectivity of the electrocatalytic reactions. This is especially true for the reactions involved in the energy conversion processes, such as the hydrazine oxidation[120], ammonia oxidation[121-123], nitrate reduction[124-126], and oxygen reduction[24, 127-131]. One of the most crucial outcomes of such studies is the revelation that different crystallographic orientations of the substrate may display different rates for the same electrocatalytic reaction[132-134]. Therefore, such studies are fundamental to the development of fuel cells[6, 9, 21].

The ability to produce model surfaces with a wide range of structural arrangement and chemical composition using a simple and straightforward route represents a very promising route to expand the electrocatalysis knowledge and promote significant progress in the efficiency of the energy conversion.

1.3.1 Single crystals in electrochemistry

The evolution of the application of single crystals as model surfaces in electrochemistry[12, 112] follows the advance of first, the ex-situ surface structural characterization techniques (AES, X-ray photoelectron spectroscopy (XPS), LEED) performed in ultrahigh vacuum conditions (UHV)[18, 119], and later, the in-situ surface probes, for instance, the scanning tunneling microscopy (STM)[135-136]. The in-situ probes brought the remarkable advantage that the surface could be characterized directly in the electrolyte and under experimental conditions. These powerful techniques combined provided a detailed characterization of the surfaces at an atomic level, allowing the structure and composition of the surface to be known[119] and directly related to the electrochemical behavior.

In the first electrochemical experiments using single crystals, the electrode surface was characterized in UHV conditions[12], and after the characterization, the electrode was transferred to the electrochemical setup to be electrochemically characterized. The issue with this ex-situ characterization is that it did not account for changes in surfaces during the transference of the electrodes from the UHV chamber to the electrochemical setup and/or the surface reconstruction induced by the potential cycling[18, 28, 119]. For these reasons, controversial results on structure-sensitive reactions were found, which brought some doubts regarding the accuracy of the experimental methods used in such studies[112, 137]. The origin of the differences was that although surfaces with the well-defined structure were produced and characterized in UHV, the surfaces were contaminated by impurities in the atmosphere during the transference.

Clavilier et al.,[68, 70, 74, 138] solved this issue by introducing the flame annealing of the platinum single crystals surfaces as a preliminary step to the electrochemical experiments to clean the electrode surfaces without introducing any disorder on the material. The flame annealing of the electrodes has introduced a remarkable change in the field. Additionally, the instrumental techniques' progress for the alignment, cutting, and polishing of the single crystals were also remarkable, which was essential for the progress of the field. Then, finally, the results obtained by the single crystals electrodes became reproducible and consistent[12].

The most remarkable contribution of the single crystals to the electrocatalysis is that achieving such organized and homogeneous surfaces with a very narrow distribution of active sites lead to the knowledge on how the surface properties affect the electrochemical behavior and reactivity of the catalysts[13]. In this regard, the single crystal surfaces act as models for interpreting the activity of more complex surfaces. For instance, concerning Pt, the voltammograms recorded for each basal plane can be regarded as fingerprints of the material, and the information obtained from those voltammograms led to the resolution of the voltammetric features of polycrystalline Pt[12-13, 60, 112]. Then, it was demonstrated that the response of polycrystalline surfaces is composed of the different basal planes contributions.

The experiments using single crystals have brought a remarkable contribution to the ORR electrocatalysis by demonstrating that the ORR kinetics presents pronounced dependence of the surface's crystallographic orientations in both acidic[22-24], and alkaline media[25-26]. The differences are explained based on the adsorption of the intermediates, which shows a pronounced dependence on the symmetry of the single crystal planes and the specific adsorption of spectator species at the electrode surface[22, 25, 75, 137, 139].

Unfortunately, working with single crystals imposes some challenges, as the standards regarding the surface organization degree and cleanliness are high to achieve reliable results. Additionally, the proper orientation and cutting of the crystal is a challenging task where even small degrees of miscut can cause significant changes in the surface arrangement, and consequently, in the electrochemical properties. Therefore, specific instruments are required to grow, align, cut, and clean the crystals[140-143], which also demands special training for their manipulation and test. For the same reasons, it may be difficult and time-consuming to obtain alloyed single-crystals electrodes of several compositions, which limits the range of electrocatalysts to be probed by the traditional route.

In this sense, it becomes clear that both the electrocatalysis and surface science fields benefit from the implementation of new material preparation and characterization techniques. Providing new, simple, affordable, and straightforward experimental possibilities is fundamental to exploring the materials' full potentials. Often potential good electrocatalysts have specific demands regarding the experimental conditions required for their characterization. The experimentalists must search for the right tools to meet these requirements.

Therefore, to understand the behavior of complex catalytic materials as nanoparticles with different facets and shapes and polycrystalline materials, studies with single crystals-like surfaces are fundamental.

1.4 Thin films as alternative model surfaces in electrocatalysis

In the absence of suitable facilities where the necessary apparatus for the preparation of single crystals is available, the experimentalists need to seek alternatives to produce model surfaces that allow them to perform the experiments necessary to characterize the material and find a correlation between the surface properties and the behavior the material.

In this sense, the production of thin films that are well defined structurally to the point of behaving as single crystal surfaces represents a versatile instrument for interpreting surfaces' activity. The films' properties can often be controlled to provide smooth and thin layers of the active materials. The fact that the layers are thin implies a low amount of material necessary to cover the substrate, which directly affects the films' cost and application.

Notably, working with films offer advantages in modifying the active layer to be deposited, which confers a significant versatility in the applications. Several variables can be manipulated to tune the properties of the materials: the substrate nature, substrate temperature during the deposition, post-preparation annealing treatments, the nature of the deposition atmosphere and pressure, the kinetic energy of the depositing species, the thickness of the films, to name but a few of examples.

Thus, changing the deposition parameters often modifies the films' structure, crystallographic orientation, chemical composition, and surface properties. In most thin film deposition techniques[144-149], these parameters can be easily manipulated to produce a range of films with different characteristics, which is in remarkable contrast with the stiff single crystal preparation methods. Previous work in our group pulsed laser deposition (PLD) has been demonstrated to produce thin films with well-defined structures and chemical composition suitable for model studies in electrocatalysis. These films were used to study surface-structure relationships for different reactions: ammonia oxidation[121, 150], hydrazine oxidation[151], nitrate reduction, and dimethyl ether oxidation[121, 152]. Remarkably, profiting off the out-of-equilibrium character of the PLD, Au-Rh metastable alloys were deposited and used to study the electrooxidation of methanol[153].

Hence, PLD as a technique to produce model surfaces has a great potential to lead the progress in electrocatalysis and expand the variety of materials available for deposition and the properties of these materials by manipulating the deposition parameters.

1.5 Motivations to the research project and research objectives

The fuel cells are promising energy conversion devices to support the demand for more efficient, clean, and less environmentally disruptive energy sources, but their application requires improvements in several aspects comprising the technology. The key points to decrease the cost and increase the efficiency of FCs depends on the converging knowledge of theoretical simulations, the choice of materials, suitable experimental protocols in the characterization of the material and the devices themselves, and finally, the engineering component which comprises the optimization of their building process. From this perspective, the motivation of this research project is to bring new tools to the electrocatalytic studies of materials for energy conversion applications.

Hence, this project aims to present thin films with epitaxial orientation deposited by PLD as a straightforward alternative route to producing model surfaces for ORR electrocatalytic studies. The thin films with epitaxial orientation will be used as model systems in which the crystallographic orientation and surface structural properties can be correlated with the ORR electrocatalytic activity measured. Indeed, the scientific community benefits from implementing simple, easily adaptable, and less expensive materials preparation routes and uncomplicated, versatile, and easy to implement experimental procedures.

Pulsed laser deposition (PLD) will be used to deposit the films, which brings the exciting possibility of exploring alloyed epitaxial layers to extract information on the intrinsic electrocatalytic activity of materials according to their composition and structure revealing ligand and strain effects. Therefore, this proposal can potentially influence the energy conversion field by providing the films as a viable replacement for the complex and fiddly to work with single crystals surfaces.

Moreover, an alternative method in the electrocatalytic studies of mass-transfer controlled reactions is proposed: the sampled current voltammetry (SCV). The SCV methodology will be used to study the electrocatalytic properties of these films towards the ORR. This method represents an alternative to the extensively used and consolidated rotating electrode methods for the ORR studies. This experimental approach is beneficial for situations where the electrodes cannot be transformed into a disk or slurry, or an RDE assembly is not available.

This project presents a full methodology to model studies in electrocatalysis: it demonstrates how thin films with epitaxial orientation deposited by PLD can be used as model surfaces electrocatalysts for the ORR. It introduces an alternative experimental method to study the ORR on such surfaces that can be later extended to other diffusion-controlled electrochemical reactions.

The main stages of this project comprise:

1. The elucidation of the conditions in which the SCV can be comparable to the rotating disk electrode (RDE) experiments.

2. The optimization of the experimental protocol and its validation in the ORR study using SCV on polycrystalline platinum surfaces in acidic media.
3. The deposition and structural characterization of epitaxially oriented Pt and Au thin films.
4. The application of the SCV on the Pt and Au thin films with epitaxial orientation as electrocatalysts to study the ORR in acidic and alkaline media, respectively.

The main scientific contribution is brought by this research project:

- By presenting suitable model surfaces for electrocatalytic studies.
- By suggesting and validating an alternative method to study the ORR that can be extended to other electrochemical systems.

1.6 Structure of the thesis

The work developed in this thesis is divided into two main sections: in the first one, the sampled current voltammetry (SCV) is proposed as an alternative method to study mass-transfer controlled reactions. In this part of the work, SCV is tested and validated regarding the hydrodynamic voltammetry methods using the ORR on platinum electrodes. In the second part of the thesis, the ORR is assessed on gold films with preferential orientation in the [100] direction deposited by PLD using the SCV.

Therefore, this thesis will be presented in ten chapters. In the first chapter, the research project is described and put in context. A brief literature review is presented in the following chapter, and the most relevant aspects of ORR electrocatalysis will be introduced. Chapter 3 first reviews the hydrodynamic voltammetry methods comprising the rotating disk electrode (RDE) and rotating ring-disk electrode (RRDE) and summarizes the fundamental associated aspects with the application of these methods. Then, the sampled current voltammetry elementary features are introduced. Subsequently, the experimental approach is developed, and the conditions in which SCV compares to RDE voltammetry are derived. The experimental approach is validated using reactions and electrode materials with well-characterized behavior: first, using a fast electron transfer redox probe, the ferricyanide/ferrocyanide, and then, ORR on platinum electrodes. At the end of this chapter, the technical and experimental challenges are discussed. Finally, this chapter also demonstrates that the SCV experimental protocol can be modified to conform to different experiments' specific needs and shows how to make the experimental adaptations accordingly.

Chapter 4 lists the materials and methods common to most of the experiments performed in this project, and also reports the fundamental equations used in calculations. However, a brief description of specific aspects applied to that part of the work may also come within each chapter.

Chapter 5 describes the study results of the influence of the rest potential duration and value on the platinum polycrystalline electrode. These experiments aimed to optimize the experimental parameters to use in the next set of experiments. Additionally, this chapter elucidates how the conditions in which the oxygen replenishment on the electrode surface – to keep the reaction rate – were attained.

Following, chapter 6 presents the study of the ORR on a Pt/MgO(110) film electrode, which represents two of the main contributions of this thesis: the use of pulsed laser deposition (PLD) to prepare model surfaces for electrocatalytic reactions and the demonstration of the sensitivity of the SCV to detect even small changes in electrocatalytic activity. Finally, chapter 7 presents the deposition and the characterization of Au(100) thin films, demonstrating how the deposition conditions were optimized to achieve epitaxial films suitable for the ORR electrocatalysis, and in chapter 8, the Au(100) ORR electrocatalytic activity study in films with different thickness is presented and discussed.

Chapter 9 describes how the SCV can be applied in the study of adsorption reactions at the electrode surface on Pt/MgO(hkl) thin films. Finally, chapter 10 describes the main achievements and scientific contributions attained in this work and suggests future work.

2 BIBLIOGRAPHIC REVIEW: STATE OF ART RESEARCH

2.1 Introduction

This chapter presents a summarized review of relevant topics associated with the research developed in this project. A good comprehension of this research project embraces some fundamental aspects of the oxygen reduction reaction, including preliminary mechanistic aspects and the challenges associated with enhancing the ORR electrocatalysis. This chapter introduces the ORR, discusses its importance on energy conversion processes, and examines the ORR fundamentals and underlying mechanistic aspects. Additionally, it provides an overview of the electrocatalysts used to accelerate the ORR rate.

Later, it introduces thin films with preferential orientation deposited by pulsed laser deposition as versatile surfaces to perform model studies for the ORR electrocatalysis. Besides, a brief description of the PLD's fundamental aspects is presented. Finally, because the production of model surfaces aims to generate surfaces with a well-defined structure, a few considerations on thin films' growth are given at the end of the chapter.

2.2 The electrochemical oxygen reduction reaction (ORR)

The oxygen reduction reaction remains one of the most widely studied reactions by electrochemists all over the world[26, 31, 35, 51, 127-128, 154-155]. This interest comes from the fact that this electrochemical reaction plays a crucial role in some of the most promising energy conversion and storage devices, being often among the most challenging aspects of their development[27-28]. The ORR represents paramount importance for different types of fuel cells (FC) and metal-air batteries and in the H_2O_2 production technology[27]. However, even after several years of intensive research, the ORR's sluggish kinetics remains a problem[28-29] and persists as one of the biggest challenges of electrocatalysis.

The molecular oxygen (O_2) comprises two oxygen atoms linked by a non-polar covalent bond with bond strength energy of 494 kJ mol^{-1}. Therefore, at room temperature and pressure conditions, O_2 is a very stable molecule, and the cleavage of the strong O-O bond requires energy to take place. These intrinsic characteristics of the O_2 molecule make the adsorption of the O_2 at the electrocatalyst surface an essential step to initiate the ORR and facilitate the electron transfer. This specific requirement of the reaction imposes a limitation regarding the electrocatalysts: a promising electrocatalyst for the ORR must be able to adsorb O_2 and the reaction intermediates, especially OH, with optimal binding energy[29-30]. Even though the Pt surfaces adsorb the OH species slightly too strong[8], it is close to reaching the optimal adsorption energy, which helps explain why platinum is the state of art electrocatalyst for the ORR, but still far from ideal.

The complete reduction of the O_2 involves the exchange of four electrons to produce H_2O in acidic media or OH^- in alkaline media. In this sense, the complete reaction occurs as a sequence of steps involving the adsorption of O_2 on the electrocatalyst surface, multiple electrons and protons transfer, and the adsorption and desorption of reaction intermediates. The species OH^-, OO^- [156], OOH^- are proposed as intermediates in the ORR[31, 157]. According to theoretical work[121], the stability of the adsorbed oxygen and hydroxyl intermediates at the electrocatalyst surface in potentials where the ORR proceeds significantly affects the reaction kinetics on the electrocatalyst surface[29-30]. An additional complication is that parasitic reactions occur on Pt surfaces in aqueous electrolytes where the water molecules discharge on the surface to form both OH_{ads} and O_{ads} [29]. These discharge products decrease the number of active sites available to the ORR and hinder the reaction.

2.2.1 Mechanistic aspects of the ORR

As mentioned above, the mechanism of the electrochemical O_2 reduction reaction is complicated and involves many intermediates. The proposed intermediates' formation and stability depend primarily on the nature of the electrode material, pH, and electrolyte[35], and they affect the rate of the reaction[30]. Different groups worldwide have provided a combination of experimental and theoretical[30, 158] contributions regarding the ORR mechanism, but the lack of in-situ techniques that permit identifying the intermediates involved hinders concrete conclusions. Thus, even after decades of intensive research, the ORR mechanism is not well resolved[31-36], and scientists rather address reaction pathways instead of mechanism[37-39] as the first can be inferred from the experimental data.

In aqueous electrolytes, at least two pathways for the complete reduction of oxygen are possible[3, 40-41]:

i) **<u>The direct four-electron pathway</u>:** in this pathway, oxygen is directly reduced to either H_2O (in acidic medium, at pH = 0, $[H^+ (aq)] = 1$ mol dm^{-3}) either OH^- (in alkaline medium, pH=14, $[OH^- (aq)] = 1$ mol dm^{-3}) by the exchange of four electrons.

In acid solutions: $$O_2 + 4H^+ + 4e^- \rightarrow 2\,H_2O \qquad E^0 = 1.229\,V \qquad (10)$$

In alkaline solutions: $$O_2 + H_2O + 4e^- \rightarrow 4\,OH^- \qquad E^0 = 0.401\,V \qquad (11)$$

ii) **The peroxide pathway (or parallel four-electron pathway):** in this pathway, oxygen is reduced to either H_2O (in acidic medium) or OH^- (in alkaline medium) by the exchange of two plus two electrons, forming a peroxide as an intermediate.

In acid solutions: $O_2 + 2H^+ + 2e^- \rightarrow H_2O_2 \quad E^0 = 0.670\, V$ (12)

Followed by either the further reduction reaction:

$$H_2O_2 + 2H^+ + 2e^- \rightarrow 2\, H_2O \quad E^0 = 1.77\, V \quad (13)$$

Or the decomposition reaction by disproportionation:

$$2H_2O_2 \rightarrow 2\, H_2O + O_2 \qquad (14)$$

In alkaline solutions:

$$O_2 + H_2O + 2e^- \rightarrow HO_2^- + OH^- \quad E^0 = -0.065\, V \qquad (15)$$

Followed by either the further reduction reaction:

$$HO_2^- + H_2O + 2e^- \rightarrow 3\, OH^- \quad E^0 = 0.867\, V \quad (16)$$

Or the decomposition reaction:

$$2HO_2^- \rightarrow OH^- + O_2 \qquad (17)$$

Traditionally, the pathways' assessment is performed using rotating ring-disk electrode assemblies (RRDE)[39, 42-45]. In such assemblies, a disk made of the electroactive material (platinum, gold, glassy carbon are the most common) is tightly embedded in a Teflon holder, and a few millimeters outer the disk has placed a ring (usually made on platinum or gold).

The RRDE setup is comprised of a motor that allows the accurate control of the electrode's rotation rates and a bi-potentiostat that controls and records data for both the disk and the ring at the same time. A scheme illustrating an RRDE is provided in Figure 2-2. The ring is polarized at a constant potential where the H_2O_2 oxidation is diffusion controlled. Therefore, any peroxide arriving in the ring will be instantaneously oxidized, generating an anodic current density. Hence, the ring currents reflect the amount of hydrogen peroxide that leaves the working electrode surface and diffuses through the bulk solution[44-45]. The experimental data estimate the fraction of O_2 reduced to H_2O (or OH^-) and H_2O_2 (or OH_2^-) and allows for creating maps showing the ORR pathways as a function of potential applied to the disk[159].

Thus, it is essential to keep in mind that if peroxide is formed but immediately reduced without leaving the electrode surface – implicating in a 2 + 2 fast electron transfer – the ring is not able to detect it. This could mislead to the conclusion that the oxygen was reduced directly, without the peroxide formation. Therefore, the complete and unambiguous distinction between the possible reaction pathways is still missing.

Despite the challenges, in 1976, Wroblowa et al.[39] applied the RRDE methodology to distinguish the possible intermediates from the ORR by-products. Based on their experimental results, the authors presented a classical scheme for the possible ORR pathways, Figure 2-1.

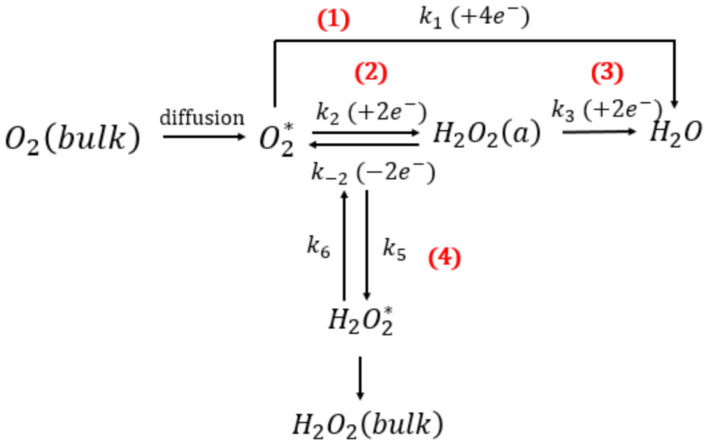

Figure 2-1: General scheme of oxygen reduction pathways, adapted from reference[39]. The * indicates species adsorbed on the electrode surface.

In the scheme, the direct four-electron reduction reaction to H_2O (or OH^-) is represented by the reaction (1); the sequential two-electron transfer reaction to produce H_2O_2 (or HO_2^-) and then, to produce H_2O (or OH^-) by an additional exchange of two-electrons is represented by (2) and (3), respectively. Finally, (4) shows the pathway when only two electrons are exchanged, and the peroxide is the final product and diffuses to the bulk electrolyte. A more detailed reaction scheme was developed later, in 1987, by Anastasijević et al., combining the available information at that time[44-45].

The direct four-electron transfer is the desired pathway when considering the application in the energy conversion devices because of the increased charge efficiency of the conversion. It does not involve the hydrogen peroxide formation, which may damage the device's parts, namely the proton exchange membrane[160]. However, this pathway is the most complex and challenging to achieve.

Based on the reaction pathways shown, adsorbed O, OH and OOH are the most probable intermediates in the ORR mechanism, and the interaction of these species with the electrode surface depends on the characteristics (structure and nature) of the electrocatalyst. Therefore, the nature of these interactions between the intermediates and the electrocatalyst surface will determine the reaction's pathway.

Some mechanistic aspects of the ORR on Pt surfaces have been proposed by combining experimental evidence and theoretical information. In this context, Nørskov et al.[30] have demonstrated employing density functional theory (DFT) calculations that on Pt(111) surfaces, there are two possible ORR mechanisms based on the adsorption mode on the electrocatalyst: the direct/dissociative mechanism and the associative mechanism. The most remarkable difference between both mechanisms is whether the molecule dissociates before or after the oxygen protonation: in the dissociative, the O_2 molecule is first dissociated and then protonated, whereas, in the associative mechanism, the dissociation follows the protonation. These results are somehow supported by experimental evidence collected through the last decades using experimental data acquired with RRDE[29, 40, 161-163]. According to these results, at least two proposals for the rate-determining step (*rds*) on the ORR co-exist: the first one proposes that the first electron transfer to the adsorbed O_2 is the *rds*[161-162], and the second one suggests that the initial adsorption of O_2 is the *rds* [40, 163]*.* A more recent review of the literature[29] has collected and discussed contributions from different authors and concluded that the *rds* vary with the potential region due to the variations in the oxygenated species' surface coverage. Therefore, both proposals regarding the *rds* may be correct.

Ford et al.[158] have extended the DFT studies to different transition metals, and they reported that on metals like Ni, Rh, Ir, and Cu, the dissociative adsorption of O_2 is dominating, while on Pd, Pt, Ag, and Au, the dominant mechanism is rather associative. Therefore, calculations support the experimental results obtained by the different metallic surfaces[19, 75, 95, 164-165] and indicate that metals' intrinsic reactivity plays an essential role in the selectivity and reaction rate of O_2 reduction.

On platinum-based electrocatalysts, the ORR pathways are similar in acid and alkaline electrolytes[35, 161]. Nonetheless, Ramaswamy et al.[35] reported mechanistic differences in alkaline media and concluded that OH's specific adsorption to the Pt surface blocks the active sites preventing the O_2 adsorption. The authors proposed that the differences of the double-layer structure in alkaline media favor the formation of the peroxide at the electrode surface. The corrosive acidic environment has mostly limited ORR catalysts to the platinum-based surfaces at low pH conditions. However, due to the ORR mechanistic differences in alkaline media[34-35], a wide range of non-noble metal surfaces as electrode materials for ORR in alkaline media[94, 100-101, 166-167].

2.2.2 Traditional methods used to study the ORR

In electrochemical reactions, several steps contribute to the reaction rate, and the overall rate is a set of the involved equilibria in which the slowest process will be the rate-determining step[46]. Since these steps include both kinetic and mass-transfer aspects, the ORR current rate experimentally measured is a combination of the sluggish kinetics of the electron transfer[30, 37] and the slow mass transfer rate of the molecular oxygen from the bulk of the electrolyte to the electrode's surface[43].

The mass transfer issues come from the fact that both the solubility and diffusion coefficient of O_2 in aqueous solutions is low and decreases with the addition of the supporting electrolytes[43]. As a result, O_2 needs time to move within the solution to the electrode surface, and according to the potential applied, the slow diffusion may limit the reaction. This causes the depletion of O_2 at the electrode surface and induces a current plateau that is not associated with the reaction's kinetics but rather with the insufficiency of O_2 to sustain the reaction rate.

Therefore, a reliable experimental protocol in the ORR electrocatalysis must ensure high and controlled mass transfer rates of the O_2 from the bulk solution to the electrode surface to keep its maximum reaction rate. Additionally, it must allow straightforward data analysis (with the separation of the kinetic and diffusional components of the current) and be comparable with work previously published in the literature. The steady-state hydrodynamic methods satisfy these requirements and comprise different experimental approaches, including the flow cells[168] (tubular or channel electrode)[169-170], wall jet, and the rotating electrodes: the rotating disk electrode (RDE) [43, 171-173], and rotating ring-disk electrode (RRDE)[42, 44-45].

The flow cells and wall jet cells may be challenging because they require a cumbersome control system, a large volume of electrolyte, familiarization with less evident experimental parameters, and specific cell configuration. They are used mostly as detector units, and their adaptation to electrocatalytic studies can be complicated, especially because of the non-uniform flow characteristics at the electrode surface[174-175], which may cause difficulties in the accurate separation of the components of the current. Therefore, the RDE and RRDE are the most widely used techniques to study the ORR[3, 46-47] due to their simplicity in operation, implementation, and versatility regarding the range of possible working electrodes. Steady-state mass transport is rapidly achieved using the hydrodynamic methods and easily reproduced over a considerable range of mass transfer coefficients[46]. Additionally, the kinetic data can be easily extracted from the Koutechý-Levich and Tafel plots[3, 37, 43, 46]. For this reason, we will focus on them.

The RDE and RRDE setups work similarly; however, the latter offers rich mechanistic information not provided by the former. The RRDE can provide mechanistic information because its configuration allows it to detect reaction intermediates at the ring. The most common working electrodes are made of glassy carbon, platinum, or gold, and the ring is generally made of platinum or gold[176-179]. A general scheme illustrating both electrodes is presented in Figure 2-2.

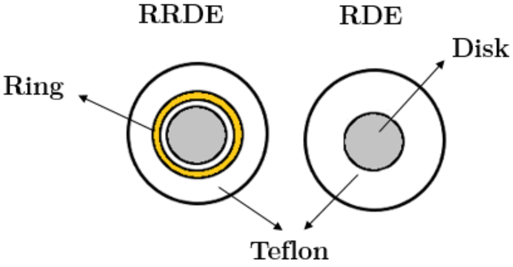

Figure 2-2: Illustration showing an RRDE and RDE.

For mass-transfer controlled reactions, the polarization curves obtained with a rotating electrode display a sigmoidal-shape characteristic of the diffusion-controlled electrode reactions. In such cases, the potential windows where the reaction is controlled by the electron transfer or diffusion of electroactive species can be easily identified, including a transition zone in which both processes contribute to the reaction rate, the mixed-control zone. A representative polarization curve obtained experimentally with an RDE for the ORR under 1600 rpm rotation rate is shown in Figure 2-3.

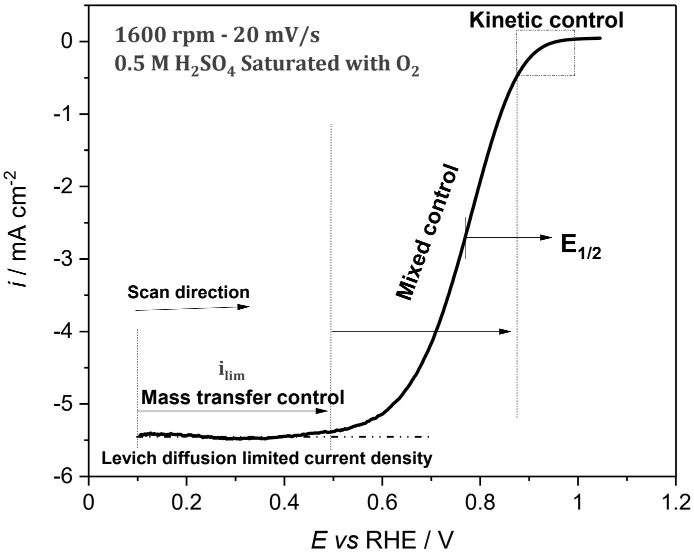

Figure 2-3: ORR polarization curve experimentally obtained using a Pt RDE setup 0.5 M H_2SO_4, 20 mV/s.

At the diffusion-controlled potential window, 0.100 – 0.450 V, the ORR kinetic is very fast and consumes all the O_2 available at the surface, then the rate at which O_2 arrives at the electrode surface controls the reaction rate. The current density value recorded is the maximum achievable for that rotation rate, and for this reason, it is known as the diffusion-controlled limiting current (i_{lim}). The limiting currents surge when overpotentials higher than the equilibrium potential of the reaction are applied, and if the electrolyte is under laminar flow, it can be estimated by the Levich equation[3, 46, 180]:

$$i_{lim} = 0.201\, nFAD^{2/3}v^{-1/6}C_{Ox}\omega^{1/2} \qquad (18)$$

Where *n* is the apparent number of electrons exchanged, *F* is the Faraday's constant (96485 C mol^{-1}), *D* is the diffusion coefficient of the active species in $cm^2\ s^{-1}$, *v* is the kinematic viscosity of the working electrolyte, $cm^2\ s^{-1}$, *C* is the concentration of the active species, in mol cm^{-3} and ω is the electrode rotation rate in rpm. Under mass-transfer control, the Levich equation reveals a linear relationship between the limiting current and the square root of the rotation rate, with the slope $m = 0.201nFAD^{2/3}v^{-1/6}C_{Ox}$. Levich plots consist of a good diagnostic strategy in the experiments, and from the slope, the *n* can be extracted, or the diffusion coefficient can be estimated.

For overpotential values typically lower than < 100 mV, the electron transfer controls the current density; this is the kinetically controlled zone. Here, the electron transfer is the slowest process, and the current density increases exponentially with the potential, accordingly to the Butler-Volmer equation[7,12]:

$$i = i_0\left[exp\left(\frac{\alpha nF}{RT}\eta\right) - exp\left(\frac{(1-\alpha)nF}{RT}\eta\right)\right] \qquad (19)$$

Where *i* stands for the current in Amperes (A), i_0 is the exchange current density in A, α is the transfer coefficient, *R* is the universal gas constant, 8.3145 J mol^{-1} K^{-1}, *T* is the absolute temperature, in K, *F* is the Faraday's constant (96485 C mol^{-1}), and η is the overpotential, in V. The Butler-Volmer relationship provides a good approximation for the electrode kinetics description when the current range is less than 10% of the limiting current and in the absence of mass-transfer limitations[3]. The exchange current density is a thermodynamic parameter that provides information about the reaction rate at the equilibrium potential[3, 46].

In the study of electrode reactions kinetics, a limit form of the Butler-Volmer equation is widely applied, the Tafel equation[3, 46]:

$$\eta = \frac{2.303RT}{\alpha nF}\log i_0 - \frac{2.303RT}{\alpha nF}\log i \qquad (20)$$

The Tafel equation holds valid for overpotentials higher enough to suppress the back reaction (or decrease its contribution to less than 1%), but not high enough to introduce mass-transfer limitations. Usually, it ranges from 50 to 200 mV far from the equilibrium potential, but it can vary with the reaction kinetics. A plot of the logarithm of the current versus the overpotential (or potential) is a Tafel plot, and the linear region is called the Tafel region. From the reciprocal of the slope of this line, $b = -\frac{2.303\,RT}{\alpha nF}$ for a cathodic reaction or $b = -\frac{2.303\,RT}{(1-\alpha)nF}$ for an anodic reaction, the Tafel slope[3, 46, 108] is obtained. The Tafel slope is one of the fundamental kinetic parameters in electrocatalysis, and it is extensively used to compare the activity of the electrode materials. It expresses how much the potential should be raised to increment the current by ten times. Therefore, the lower the slope, the higher is the activity of an electrocatalyst. Additionally, the Tafel slope may also provide mechanistic information, and in principle, points out the rate-determining step of the reaction[108].

When using the RDE or RRDE to extract kinetic information, the most significant advantage is the possibility of separation of the mass-transfer current component from the kinetics, allowing the analysis of either component to extract the desired information. This is accomplished with the help of the Koutecký-Levich equation[43, 181-182]:

$$\frac{1}{i_{disk}} = \frac{1}{i_k} + \frac{1}{i_{lim}} \qquad (21)$$

The i_{disk} is the total current measured at the disk, i_k is the kinetic current as predicted by the Butler-Volmer equation, and the i_{lim} is the limiting current according to the Levich equation. A plot of the $1/\ i_{disk}$ versus the $\omega^{-1/2}$ is called a Koutechý-Levich (K-L) plot. For a first-order and irreversible electron transfer coupled only to mass transfer, the plot must result in a straight line, whose extrapolation provides the reciprocal of the kinetic current[182-183]. If the K-L is plotted for several potentials, a Tafel plot can be build and provide a broader range of information of the electrode kinetics under study[43].

Though RRDE modification regarding the RDE may seem unimportant, it gives the RRDE the ability to detect intermediate reaction species at the ring. In the ORR case, the intermediate species formed are either H_2O_2 in acidic media or HO_2^- in alkaline media. If the peroxide species form at the electrode surface and diffuse towards the solution, the ring will oxidize them and collect the current. From the current measured at the ring, the amount of peroxide formed can be estimated, the number of electrons exchanged extracted, and therefore, the ORR pathway is determined. The RRDE setup affords the most accurate method to estimate the number of electrons exchanged in the ORR[184].

The rotating electrode methods are versatile and straightforward techniques, but as well as any other methodology, they encounter some limitations. For instance, rough surfaces can affect the velocity profile of the RDE[177] and cause uncertainty in the limiting currents experimentally measured. The presence of irregularities at the disk surface and the Teflon holder can affect the flow pattern at the disk surface, which may cause issues in the current measured and any circumstance in which the laminar flow of the electrolyte is perturbed. Another constraint concerns the rotation rates as they are usually limited to 3000 rpm and exceeding this speed may damage the disk. Furthermore, the electrode's preparation can be challenging in some cases: the electrocatalyst must be either transformed into a disk and inserted into the Teflon holder or dispersed in an ink to form a catalytic layer. The inks' preparation can also be an additional challenge because it requires optimization of its composition, fraction of the electrocatalysts/dispersant, and loading of the catalysts for each electrocatalyst tested[42]. The ink's preparation and optimization consist of the preliminary steps of electrocatalytic studies using powder electrocatalysts in an RRDE/RDE setup.

2.3 Electrocatalysis on platinum

The platinum-based electrocatalysts play a fundamental role in the main processes of energy conversion and storage, namely the fuel cells[48] and electrolyzers[49]. Platinum (Pt) has unique chemical and physical properties, and it is stable and resistant to chemical attack. Due to its physical-chemical and surface adsorption properties[160, 185-187], Pt catalyzes several different electrode reactions: the methanol oxidation[188-189] and ethanol oxidation[190-192], ammonia oxidation[118, 122-123], hydrogen oxidation[193-194] and reduction[166, 195-196], and oxygen reduction reaction[87, 196-198], to cite a few. For this reason, Pt is the state-of-art electrocatalyst for a number of electrode reactions, including the ORR.

A particular character of Pt is the fact that its surface can adsorb different species with proper adsorption strength: strong enough to break chemical bonds of the reactant species but not so strong to prevent the removal of the reactions products[160], as predicted by Sabatier's Principle[110-111]. For instance, the hydrogen adsorption and desorption on the Pt surface is a fingerprint of the Pt substrate's crystallographic orientation, and it is widely used in the characterization of Pt electrodes[60, 112, 199]. No surprise that with such affinity, Pt is the state of art catalyst also for the hydrogen reactions: evolution and oxidation[200-201].

Of course, this set of characteristics combined with its chemical stability gives Pt a special role in surface science, electrocatalysis, and energy conversion. By virtue of its described importance, Pt polycrystalline and single crystals were characterized in different electrolytes, and a wide range of information on their electrochemical behavior is available in the literature[15, 60, 112, 117, 202-204].

Concerning the ORR electrocatalysis, the pathway and reaction rate strongly depends on the nature of the electrode surface[22, 24-25, 36, 116-117, 205]. The nature of the surface encompasses structural – associated with the crystallographic arrangement of the material – and electronic effects – associated with the composition and the electronic structure of the material[133]. Thus, due to variations in the materials' properties, different materials display different activities for the ORR.

Despite the far from ideal electrocatalytic behavior and long-term stability issues, Pt is still the main material used in the FC cathodes and anodes[160]. Therefore, the development of more efficient and stable catalysts capable of lowering this overpotential is the key to the production of commercially viable FCs[2, 30, 46, 80]. Furthermore, the scarcity of Pt increases the cost of the devices[90]. Hence, it natural that researchers strive to enhance the performance of Pt and decrease the amount of Pt used in the catalytic layers on the electrodes.

In order to minimize the Pt content on the electrodes, the Pt surface properties and reactivity have been efficiently modified using different approaches:

i) Alloying Pt with other abundant and cheaper transition metals: Co, Ni or Fe[52, 75, 95, 206-207]
ii) Modifying the Pt crystalline lattice parameter by the preparation of layered electrocatalysts[8, 208-209];
iii) Introducing strain in Pt crystalline lattice[65, 210];
iv) Adding metallic layers onto Pt supports.

These strategies take advantage of electronic and strain effects to enhance the Pt performance towards the ORR. These strategies resulted in the production of materials with enhanced ORR electrocatalytic activity and stability. For instance, Stamenkovic et al.[8], reported that alloying Pt with Ni to produce $Pt_3Ni(111)$ electrocatalysts resulted in a 10-fold increase in activity compared to the Pt(111) pristine surface and 90-fold the activity of the Pt/C catalysts.

The Pt surface structure plays an essential role in the ORR electrocatalytic activity, and both the low[22-23, 25, 36, 139], and high index[116-117, 131, 211] Pt single-crystals present different activity for the ORR. Although a debate still exists about this phenomenon's origin, the ORR's structure sensitivity on Pt surfaces is mostly attributed to the sensitivity of adsorption of either intermediates or spectator anions to each one of the crystallographic orientation[22, 25, 75, 131, 139, 204, 212]. In acid electrolytes, the most active Pt surface is the Pt(110)[22, 24]. In alkaline media, the Pt activity for the ORR also depends on the structure, and the Pt(111) is the most active surface[25-26, 139].

2.4 Electrocatalysis on gold

Gold (Au) is one of the noblest metals, known to be resistant to oxidation and remaining in its metallic reduced state for a wide range of conditions. Despite its inert character, it was demonstrated that Au-based nanoparticles have interesting catalytic properties for application in catalysis[213-215] and electrocatalysis[67, 185, 216-220]. Au can catalyze both oxidation and reduction reactions, and for this reason, it has many applications[215, 218, 220-221]. The combination of Au with oxides is a trendy set of catalysts used in a series of technological applications involving exhaust emissions and sensors, CO oxidation, partial oxidation of hydrocarbons, and hydrocarbons hydrogenation. Furthermore, Au can be used as a substrate for different self-assembled materials, sensors, and anchoring nanomaterials.

On fuel cell applications, gold may play different roles[218]. Research has demonstrated that gold is a good alternative in the purification of H_2 for fuel cells by removing carbon monoxide impurities from the hydrogen feedstock stream used to feed H_2/O_2 or air-fuel cells[218]. In the absence of carbon monoxide, fuel cells may run at lower temperatures and with improved efficiency. Additionally, gold is a promising electrocatalyst for hydrazine oxidation and the H_2O_2 reduction in direct liquid N_2H_4/H_2O_2 fuel cell (DHHPFC). Yan et al. has reported a high power density for the DHHPFC that is 22 times higher than that of commercial Pt/C electrocatalyst using the same noble metal loading[222].

However, such a noble behavior also introduces some drawbacks in electrocatalysis, because as discussed in previous sections, to decrease the activation energy of the electrode reaction, at least one surface adsorption step is involved[185, 223]. If the surface is inert, small molecules either do not adsorb or adsorb weekly[223-224], which hinders the bonds cleavage and the formation of new bonds to form the products. In the ORR electrocatalysis context, the adsorption energy – or affinity – to oxygenated species is a critical criterion. In this sense, molecular oxygen does not adsorb on Au at ambient conditions[224], which hampers the O-O bond cleavage, leading to low exchange currents. Generally, Au reduces O_2 to a peroxide intermediate by exchanging two electrons and can be used as an electrocatalyst in H_2O_2 production. When the targeted application is energy conversion, the production of H_2O_2 as a final product is undesired because the current produced is reduced by half, and the peroxide produced may be hazardous for the parts of the device. Therefore, polycrystalline gold is not a good electrocatalyst for the ORR in neither acid nor alkaline media.

Considering the ORR on low index Au single-crystals in acidic media, the scenario is similar to the observed for polycrystalline electrodes. In such media, the ORR dependence on the crystallographic orientation is not pronounced, and the three surfaces, Au(100), Au(110), and Au(111), performs similarly and reduce oxygen by the exchange of only two electrons producing hydrogen peroxide as the final product[225-226].

Interestingly, in alkaline media, the situation is entirely different, and Au(100) is known as the most active surface for the (ORR) in alkaline media[127, 159, 196, 227]. This gold basal plane can reduce oxygen by the series transfer of four electrons within a specific potential window, forming a peroxide intermediate that is further reduced to OH^-. In this regard, the Au(100) surface performs quite differently from the other gold basal planes, (111) and (110), which under any conditions reduces oxygen to hydrogen peroxide and requires a higher overpotential to drive the reaction[26, 127-128].

Different research groups have proposed reasons to explain the high activity of this surface: the specific adsorption of OH at the Au(100) surface in the same potential window as the ORR take place[127, 129, 228], the four-fold geometry of the Au(100) surface[226], and the surface reconstruction with the potential cycling[228-229]. However, the absence of substantial evidence corroborating these proposals maintains the origin for the Au(100) activity unclear[230-231]. Thus, any contribution able to bring light to the factors affecting the activity of the Au(100) surface in alkaline media may guide researchers towards the design of more active electrocatalysts for technological applications.

2.5 Pulsed laser deposition: an alternative route to produce model surfaces for electrocatalysts

Pulsed laser deposition (PLD) is a physical vapor deposition (PVD) technique widely used in the deposition of films and coatings[145, 232]. PVD comprises a range of vacuum coating processes in which the film (or coating) is deposited by the condensation of atoms (neutral or ionized) from the vapor phase onto a substrate[233]. Many coating processes fit into this description, and the main difference between them is how the vapor phase is formed[233-235]. In the deposition of films by PLD, high-energy laser pulses are focused onto a target of the material to be deposited. The laser pulses then ablate a small amount of the target material to create a plasma plume, which provides the material flux for the film growth, that is condensated on the substrate[232, 236]. The PLD deposition's main stages are the laser-target interaction, the plume formation, and the deposition and growth of the film.

Thin films with a varied range of composition and properties have been successfully deposited using PLD: various types of oxides with different structures, nitrides, carbides, metals and alloys, superconductors[237]. Smith and Turner published the first PLD application report to deposit thin films in 1965, where they used a ruby laser to deposit a range of semiconductors films[238]. Nonetheless, PLD remained somehow disregarded until Djikkamp et al. used PLD to deposit a high-temperature superconductor oxide with excellent properties[237]. Afterward, the full potential of PLD started to be explored and, PLD experienced extensive experimental development and came into widespread use in the growth of films for different applications[239].

The necessary apparatus for PLD typically comprises, primarily, an ultraviolet (UV) excimer laser – such as ArF (193 nm), KrF (248 nm), and XeCl (308 nm) – employed with a pulse width of tens of nanoseconds or shorter. However, other types of lasers, such as Nd:YAG laser, may be employed for PLD[240]. To ensure that the laser beam strikes the right place on target is necessary built an optic pathway, which directs the beam onto a surface of the target[236]. The laser beam is focused inside a vacuum chamber onto the target, typically at an angle of incidence of 45˚with respect to its perpendicular surface direction. Figure 2-4 shows a typical setup for the PLD deposit of thin films.

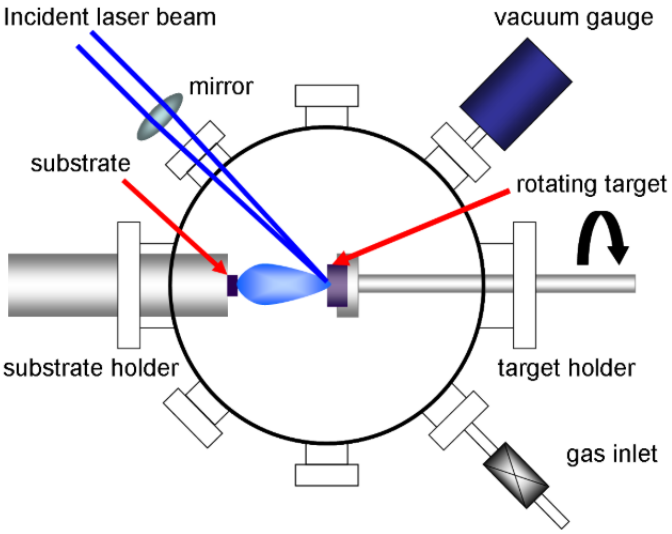

Figure 2-4: Illustration of a PLD setup[241].

The parameters involved in the deposition control the growth of the films, and, as a consequence, they have a significant impact on the properties of the film, especially considering the structure, mechanic properties, and surface morphology. The most important parameters involved in the deposition of films are the laser fluence (J/cm^2), the pulse number and duration, the background gas pressure (UHV or reactive/inert gas) inside the chamber, the distance of substrate to the target, and the substrate temperature. Therefore, by careful control of these variables, it is possible to grow films with controlled structure and stoichiometry.

Some of the advantages of the PLD:

- It is a very versatile method, which makes possible the deposition of a wide range of materials.
- The target's congruent evaporation produces films deposited with the same target stoichiometry in most situations.
- High instantaneous deposition rates achieved – which allows the deposition of the metastable alloys with possible application in catalysis.
- The high energy attained by the plasma plume formed is often intense enough to vaporize even the hardest and most heat-resistant materials.
- The deposition can be carried out under UHV or using gases with a broad range of pressures – including oxygen and nitrogen.
- PLD allows the deposition of films with a controlled crystalline structure, thickness, complex stoichiometry, and composition (e.g. starting from a metal, a succession of several layers with different composition can be grown: metallic, oxide, nitride, or mixtures of such compounds) thus multilayered or even concentration gradient structures may be obtained.
- The films' properties can be controlled by parameters of laser ablation (fluence, pulse duration, wavelength) and properties of the chamber atmosphere.

Therefore, the PLD advantages make it suitable to produce films for application in optics, electronics, and electrocatalysis. However, some drawbacks exist, and the deposition of uniform films in large areas can be very challenging, which may hinder industrial applications for the films. Nonetheless, some authors have reported achieving experimental conditions able to produce films on large wafers, up to 200 mm[242-243]. These issues may limit the usefulness of PLD in producing large-area uniform thin films, but recently, remedial measures have been proposed[244]. Additionally, the high energy of the laser pulses irradiating the target surfaces can cause the splashing of particulates, which causes droplets and clusters to appear at the surface of the films and induces surface roughening and irregular morphology. Such emission particulates will affect the growth of the subsequent layers and the electrical properties of the films. Inserting a shadow mask blocks off the large particulates and rotating both the target and substrate can help produce larger uniform films. Additionally, the complex physical models hinder theory-based improvements in the technique[245]. Finally, often important ceramic substrates used to grow epitaxial films are insulating, which creates a challenge for electrochemical applications. The combination of these issues has restrained PLD mostly to the research environment.

2.6 Considerations on the growth of thin films

The structure of the films is responsible to a great extent for their properties and applications. For this reason, researchers endeavor to control the structure of the films aiming to tune their physical-chemical properties. Thus, understanding how the crystals that made up the films arrange and grow to form the films' crystalline lattice is fundamental to achieve materials with a well-defined structure.

The objective of using PLD to deposit films in this project is to produce a range of materials suitable for ORR electrocatalytic model studies. For this purpose, the films must imitate the characteristics of the single-crystals surfaces. Accordingly, the deposition process will be adjusted to yield films with a high degree of crystallinity in the material microstructure.

The strategy adopted to achieve this goal is the deposition of epitaxial layers of the active material onto ceramic monocrystalline substrates. Hence, the epitaxy is characterized by the formation of an extended single-crystal lattice onto the substrate. According to the nature of the films deposited and the substrates, there are two possible types of epitaxy: homoepitaxy (when film and substrate are the same material) or heteroepitaxy (when the film and the substrate are different materials).[233] The type of epitaxy targeted in this work is heteroepitaxial, where metallic films will be deposited onto MgO(hkl)[246] ceramic substrates.

Considering the PLD deposition process, the film's nucleation and growth onto the substrate occur when the flux of atoms provided by the plasma plume condensates on the substrate surface. In the growth of films, many processes are involved, such as atoms deposition, re-evaporation, clusters nucleation and growth, and diffusion of species within the surface. According to the interaction of the arriving adatoms to the film's surface – which depends on the substrate surface energy – three growth modes are possible: Volmer-Weber, Stranski–Krastanow, and Frank–Van der Merwe modes[247]. The Volmer-Weber is often the growth mode involved in the growth of the metallic films with face-centered cubic structure (*fcc*) on ceramic substrates[63].

The kinetic and thermodynamic factors associated with the deposition method play a fundamental role in the crystalline lattice arrangement and growth of the *fcc* metal thin films grown on a substrate. When considering the deposition of epitaxial layers, it is imperative to find the proper balance between the ad-atoms mobility at the surface, which depends on the deposition temperature, the laser fluence, and the substrate's surface energy. By adjusting these variables, the epitaxial growth can be successfully achieved[63, 121-122, 150, 248].

Regarding the deposition of heteroepitaxial films on ceramic substrates, there are important considerations to keep in mind:

i) The growth mode may introduce stress and defects in the thin films' lattice.
ii) The stress may affect the lattice parameter, causing it to differ from the bulk material.
iii) The variation in the lattice parameters affects the structure causing the elongation or compression of the crystalline lattice, which changes the surface energy and the reactivity.

The origin of these phenomena refers to the difference between the lattice constants of the growing layer and the substrate, also known as lattice mismatch[249-251]. This happens because the arriving atoms that will form the film tend to pile up on the top of the atoms in the substrate lattice replicating the substrate periodic arrangement, which builds up tension in the film's lattice. Depending on the film thickness, its lattice may undergo relaxation to release the tension[252-253] or remain strained[251, 254]. To minimize these issues, large lattice mismatches between the film's lattice and the substrate must be avoided. MgO is a good choice for the substrate because it does not react with the metals to be deposited (Pt and Au), and it is prone to form a clean and atomically flat interface. Additionally, its lattice matches well with metals with *fcc* lattice[246].

Regarding the growth of *fcc* metallic films, the surface energy of the low index facets ((111), (110), and (100)) must be carefully considered and precautions adopted to favors the growth of the desired facet. The surface structure tends to rearrange to the lowest energy facet to minimize the surface energy. For instance, the (111) have the lowest relative surface energy regarding metallic *fcc* facets, and it is the most straightforward orientation to be attained. Nonetheless, if the target is the growth of (100)-oriented *fcc* films, one must be aware that a degree of interfacial stabilization from the substrate is fundamental[255] to grow the film in the [100] direction; otherwise, it will likely rearrange into a (111).

Remarkably, some important electrochemical reactions are structure sensitive and take place faster on the *fcc* (100) terraces[256]. This is the case for Au in alkaline media, where Au(100) is the most active electrocatalyst for the ORR, beating the performance of the polycrystalline platinum. The ammonia[114, 122, 150], dimethyl ether[257-258], and hydrazine[120, 151] oxidation reactions are also electrochemical reactions that prefer the (100) wide terraces sites. Therefore, the deposition of films preferentially oriented in this crystalline direction represents a wide window of opportunities in designing the more active electrocatalysts for a range of electrochemical reactions. Furthermore, the PLD brings additional advantages to electrocatalysis because infinite combinations of metals can form alloys, but materials with other nature than metals can be deposited.

3 SAMPLED CURRENT VOLTAMMETRY

3.1 Introduction

Rotating electrodes are the classical methods used to study the ORR kinetics and the best choice to study the kinetics of diffusion-controlled reactions. However, for situations where the working electrode is not adaptable for these methods or the rotating setups are not available, the experimentalist must find an alternative method to study the ORR.

Pt or Au epitaxially oriented thin films deposited on MgO(hkl) insulating substrates illustrate this situation well. Such films have a well-defined structure, and they may behave like a single-crystal electrode, but in this context, the use of an RDE setup is impracticable because although the films are conductive, the substrate's resistance impedes the electrical contact with the current collector. This circumstance imposes a specific and crucial challenge to their use as model surfaces in the ORR electrocatalysis. Hence, this project proposes sampled current voltammetry (SCV) as an alternative method to study the ORR on these thin films to solve this problem.

Accordingly, this chapter introduces the SCV and presents the underlying aspects associated with the technique. It also demonstrates how to design an SCV experimental protocol that yields polarization curves comparable to those obtained with an RDE setup. Experiments using the ferri-ferrocyanide redox probe provided preliminary correspondence between the SCV and the RDE polarization curves. These experiments validated the conditions where the SCVs obtained by sampling the current transients are analogous to the linear sweep voltammograms recorded with the RDE. Afterward, a similar SCV experimental protocol probed the ORR on platinum electrodes to validate the SCV approach on the ORR studies.

3.2 Overview of the sampled current voltammetry

Sampled current voltammetry is an electrochemical technique that applies potential steps to the working electrode and records the current variation with time to generate a set of current transients, Figure 3-1. The electrode potential steps from a neutral potential where negligible current flows through the cell – called rest potential – to a potential where the reaction occurs, and the electron transfer generates a faradaic current at the interface[3, 46, 50].

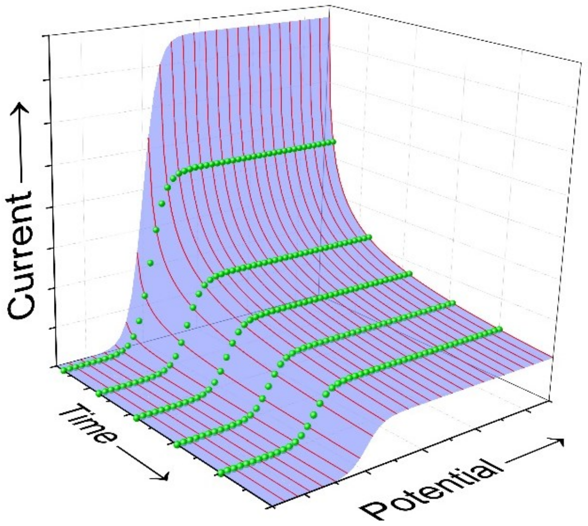

Figure 3-1: Graph showing the current variation with time according to the potential applied in the SCV[259]. The red lines show the current transients and the green solid spheres represent the reconstructed SCVs.[1]

Sampling the current measured at a fixed time in each transient and plotting versus the step potential produces a voltammogram, the reconstructed sampled current voltammogram. By sampling at a fixed time, the time dependence of the current intensity is removed, and for a soluble reactant undergoing an electron transfer affected by mass transport, the SCVs have a sigmoidal shape irrespective of the chosen sampling time[50].

The analysis of SCV waves is more straightforward and versatile than that of conventional voltammograms, and according to the sampling time, processes with different time constant can be highlighted. For instance, it is possible to focus on the faradaic currents by minimizing the capacitive contribution by sampling the current at longer sampling times. Conversely, by sampling at short times, it is possible to observe fast faradaic and adsorption processes, but the capacitance contribution cannot be neglected. Furthermore, the reconstructed sampled current voltammograms using various sampling times can reveal both kinetic and diffusional information, and high mass-transfer conditions not achievable with RDE setups can be attained by modulating the sampling time and the experimental conditions.

In particular, it is possible to compare the shape of SCVs recorded at different times to reveal subtle kinetic effects[50]. For long sampling times, the waves are under mass transport control and yield no kinetic information, but the rising part of the voltammograms is affected by the electron transfer kinetics for short sampling times.

---

[1] Figure kindly drawn by Prof. Guy Denuault.

In the absence of an irreversible surface process, one may randomly select the target potentials within the window of interest. However, when the electrode reactions involve adsorbed species, it is possible to condition the electrode surface, electrochemically or otherwise, before each potential step to ensure that every chronoamperogram arises from the same initial surface condition. In this way, all the SCV data points share the same electrode history, which contrasts with linear and cyclic voltammetry, where every data point reflects the evolving state of the electrode surface during the potential scans.

A restrained number of publications reporting the use of SCV exists in the literature, and the most relevant work published comes from work performed with microelectrodes[32, 50, 260]. Perry et al.[32, 260] have successfully explored the versatility of the SCV approach to investigate the oxygen reduction reaction (ORR) on Pt and Pt-alloyed microelectrodes. Considering planar macro electrodes, Lebedeva et al.[261] studied the ORR on PtCo/MgO(001) films using SCV, but the authors discussed only the qualitative aspects of the SCV and mentioned that the kinetic analysis would be published later. Since only preliminary studies using macro electrodes exist, a further comprehension of the applicability of the SCV in the context of the ORR is necessary.

The currents measured in the transients during the application of the potential steps control the reconstructed sampled current voltammograms' characteristic shape. If the potential applied to the working electrode is adjusted to make the reaction diffusion-controlled, the current decays with time according to the Cottrell equation[3, 46]:

$$i = \frac{nFAD^{1/2}C^B}{\sqrt{\pi t}} \qquad (22)$$

Here, n is the number of electrons exchanged, F is the Faraday's constant, 96 485.3 C mol^{-1}, A is the geometric area of the electrode in cm^2, D is the diffusion coefficient in cm^2 s^{-1}, C^B is the bulk concentration of the reactant in mol cm^{-3}, and t is the time, in seconds. Hence, under diffusion control, the current measured should scale with the reciprocal of the square root of the time.

3.3 The correspondence between the SCV and the RDE

To derive the conditions where the voltammograms obtained with the SCV are analogous to the hydrodynamic voltammograms, the definition of the limiting current and how to estimate it plays a fundamental role. For electrode potentials far from the reaction's equilibrium potential, the electron transfer's driving force is high, and the current achieves the maximum value possible. At this point, the concentration of the active species at the electrode surface, C^B, tends to zero, and therefore, the current measured under such conditions is defined as the mass transfer controlled limiting current, i_{lim} – given by the equation (23)[3, 46]:

$$i_{lim} = nFAk_mC^B \quad (23)$$

Where n is the number of electrons exchanged, F is the Faraday's constant, 96 485.3 C mol^{-1}, A is the geometric area of the electrode in cm^2, and k_m is the mass transfer coefficient in cm s^{-1}, and C^B is the bulk concentration of the reactant. The relationship revealed in equation (23) is independent of the technique used to study the electrode reaction, independent of the form of mass transport involved, and is valid for both the RDE and SCV.

Thereby, the mass transfer coefficient is sufficient to establish the correspondence between the SCV voltammograms and the RDE linear sweep voltammograms. The k_m expresses the rate at which the active species involved in the process diffuse from the bulk to the interface, and the analysis of the specific mass transfer mode involved in the electrode process provides the means to quantify it.

At the RDE, the rotation rate of the electrode establishes the steady-state mass transfer coefficient, according to[3, 46]:

$$k_m = 0.201\, D^{2/3}\nu^{-1/6}\omega^{1/2} \quad (24)$$

Where D is the diffusion coefficient of the reactant in cm s^{-2}, ν is the kinematic viscosity of the electrolyte in cm^2 s^{-1}, and ω is the rotation rate of the electrode in rpm. Values for D and ν are obtained either experimentally or from the literature.

For a potential step where planar diffusion controls the electrode process, the sampling time – τ, defined at the time where the potentiostat read the current – is the main parameter affecting the mass transfer coefficient, as defined by equation (25)[3]:

$$k_m = \sqrt{\frac{D}{\pi\tau}} \quad (25)$$

By combining equations (24) and (25), it is possible to estimate the sampling time required to match a sampled current voltammogram recorded at a stationary electrode with a linear sweep voltammogram recorded using an RDE setup at a determined rotation rate by corresponding their respective mass transfer coefficients.

The range of sampling times obtained change according to the reaction because they depend on the physical-chemical properties of the electrochemical system under analysis – concentration and diffusion coefficient of active species and viscosity of the solution. Tables 1 and 2 illustrate how the RDE rotation rate and the correspondent sampling times vary with the reaction for the ferricyanide reduction, Table 1, and for the reduction of oxygen, Table 2.

For the calculations concerning the reduction of ferricyanide, the diffusion coefficient used was 7.26×10^{-6} cm^2 s^{-1} [262], the kinematic viscosity of the electrolyte in 1 M KCl is 0.009 cm^2 s^{-1}, and the concentration of the ferrocyanide, 4 mM. For the ferricyanide reduction, the sampling times vary from 17 ms, corresponding to hypothetically to 4900 rpm, to 850 ms, which corresponds to 100 rpm.

For the ORR calculations, the diffusion coefficient used was 1.93×10^{-5} cm s^{-2}, and the kinematic viscosity of the electrolyte (0.5 M H_2SO_4) was 0.0095 cm^2 s^{-1} [263].

Table 1: Sampling times corresponding to the rotation rates in the RDE experiments for the ferricyanide reduction reaction.

Rotation rate / rpm	k_m × 10^3 / cm s^{-1}	Sampling time / ms
100	1.65	850
400	3.30	212
900	4.96	94
1600	6.61	54
2500	8.26	35
3600	9.91	24
4900	11.6	17

Table 2: Sampling times corresponding to the RDE rotation rates for the ORR.

Rotation Rate / rpm	$k_\mathrm{m} \times 10^3$ / cm s^{-1}	Sampling time / ms
100	3.1	622
400	6.3	156
900	9.4	69
1600	12.6	39
2500	15.7	25
3600	18.9	17
4900	22.0	13

Short sampling times in SCV correspond to the high rotation rates of the RDE considering the mass transfer coefficients. Mass transfer coefficients corresponding to very high rotation rates not achievable by most RDE setups are available with SCV, just by tuning the sampling time. A commercial potentiostat with no special requirements measures currents at even the shortest of the sampling times reported in Tables 1 and 2 with no issues.

However, at a short timescale, non-faradaic processes' contribution – double-layer charging – to the current measured is significant and can lead to a deceiving increase in the current measured. It becomes essential to estimate the time necessary for the capacitive current decay almost entirely so that only the faradaic currents are measured. The double-layer discharge depends on the resistive effect of the electrolyte through the ohmic drop and the capacitance of the interface[3]. The time constant of the cell, t_{dl}, estimate the time necessary for the charge/discharge of the double-layer to become negligible, defined by[3, 46]:

$$t_{dl} = R_s C_{dl} \qquad (26)$$

Where R_S corresponds to the electrolyte resistance and C_{dl} is the double-layer capacitance. In a potential step experiment, the charging of the double layer is 95% complete at 3 × t_{dl}. Thus, to eliminate the impact of double-layer charging on the amperometric response, the shortest sampling time must be at least 5 × t_{dl} [3]. Typical time constants obtained in this work are ≈ 100 µs for the RDE cell. These values mean that currents sampled above 500 µs for the RDE cell as assembled in this work should be unaffected by double-layer charging. Since SCV is a transient technique, it is worth recalling that increasing the electrode surface roughness will increase the magnitude and timescale of any current related to surface processes, such as double-layer charging, adsorption/desorption, and oxidation/reduction of adsorbates. Hence, when targeting to sample the current at shortest sampling times, it is necessary to consider these extra contributions.

The experimental validation of the methodology proposed above consisted of using an RDE setup to record polarization curves at the rotation rates varying from 100 to 2500 rpm and compare to the SCVs reconstructed at the sampling times reported listed in Tables 1 and 2 for the ferricyanide reduction and the ORR, respectively. Therefore, the validation procedure comprised two different reactions on Pt electrodes: the ferricyanide reduction, probing a fast kinetics mass-transfer controlled reaction, and the ORR, the more complex targeted reaction.

3.4 Materials and methods

Ultrapure water (Milli-Q, resistivity >18 MΩ cm) was used to prepare all solutions. All chemicals were used as received. Before each set of experiments, all glassware was soaked in acidic permanganate solution overnight, then immersed in diluted piranha solution and boiled in ultrapure water several times.

The electrochemical experiments were performed in a conventional one compartment, three-electrode electrochemical cell (Pine Research). A polycrystalline Pt RDE (geometric area 0.196 cm^2) was used as a working electrode in both cases. Before each experiment, the Pt RDE was polished with alumina slurry with grain sizes of 1.00, 0.30, and 0.05 μm on a polishing micro-cloth (both from Buhler). Afterward, the Pt disk was rinsed thoroughly with Milli-Q water and sonicated for 10 min. A flame-annealed Pt gauze was used as the counter electrode, and a mercury-mercurous sulfate electrode (filled with saturated K_2SO_4 solution, Koslow) was used as the reference electrode.

The Pt RDE electrode was cycled between 0.050 V and 1.40 V *vs.* RHE at 200 mV s^{-1} in N_2 saturated 0.5 M H_2SO_4 until a steady cyclic voltammogram was recorded. This procedure ensures the cleanliness of the surface as well as the reproducibility of the results. After the activation, the electrode was either transferred to the N_2 saturated 4 mM $Fe(CN)_6^{-3}$/ $Fe(CN)_6^{-4}$ in 1 M KCl, or fresh N_2 saturated 0.5 M H_2SO_4.

Before each measurement, N_2 purged the electrolyte solutions for at least 45 min. The electrochemical measurements were carried out at room temperature (23±1 ◦C) using an Autolab PSTAT302 potentiostat controlled by NOVA 2.1.2 (Ecochemie). All potentials are reported versus the reversible hydrogen electrode (RHE). The MMSE reference electrode was calibrated in 0.5 M H_2SO_4 against a homemade RHE ($E_{MMSE} = E_{RHE} - 0.703$ V in 0.5 M H_2SO_4). The NOVA software recorded each one of the current transients and provided the raw data for the analysis. To generate the reconstructed sampled current voltammograms, the transients were imported to the Origin 2018 software in order to i) subtract the background currents, ii) then sample the currents at the targeted sampling times, and iii) plot the currents sampled versus the step potential.

Dedicated potential waveforms were used to record the SCVs, and they were adapted to each specific case of study. The use of these waveforms allows for the preparation of the surface for the reaction, cleans the surface of possible adsorbates, and enhances the results reproducibility.

3.4.1 RDE experiments

After the activation of the Pt RDE, the linear sweep voltammograms were recorded at 20 mV/s, with rotation rates varying from 100 rpm to 2500 rpm in both cases. The potential window scanned changed according to the reaction: for the ferricyanide reduction, the lower limit was 0.40 V and the upper 1.20 V, and for the ORR, it was between 0.10 V and 1.10 V.

Aiming for the cleanliness of the surface and reproducibility of the results, the same conditioning waveform used in the SCV protocol (see below) was applied to the Pt RDE. Four potential scans at 500 mV/s within the ORR potential window were applied before recording the voltammograms for each rotation rate.

In the ORR study, the subtraction of the currents obtained in the N_2-saturated electrolyte from those recorded in O_2-saturated yielded the background currents used in the data analysis.

3.4.2 SCV experiments

To record the set of transients required to reconstruct the sampled current voltammograms, the Pt RDE was idle during the whole duration of the experiments, which ensured that the changes observed in the current density measured came exclusively from the modulation of the mass transfer coefficient through the sampling time chosen to reconstruct the SCVs.

The differences in the two electrochemical systems studied required the design and application of two different waveforms. In the ferricyanide reduction study, the waveform consisted of a conditioning step where four potential cycles scanning the potential window used in the experiments at 500 mV s^{-1} were applied. After the conditioning, the electrode was at the rest potential for 10 seconds – close to the redox mediator's open circuit potential – and then stepped to the target potential of interest for 5 seconds and stepped back to the rest potential for 10 seconds, Figure 3-2. In this waveform, the conditioning step is repeated before each potential step be applied to the electrode surface.

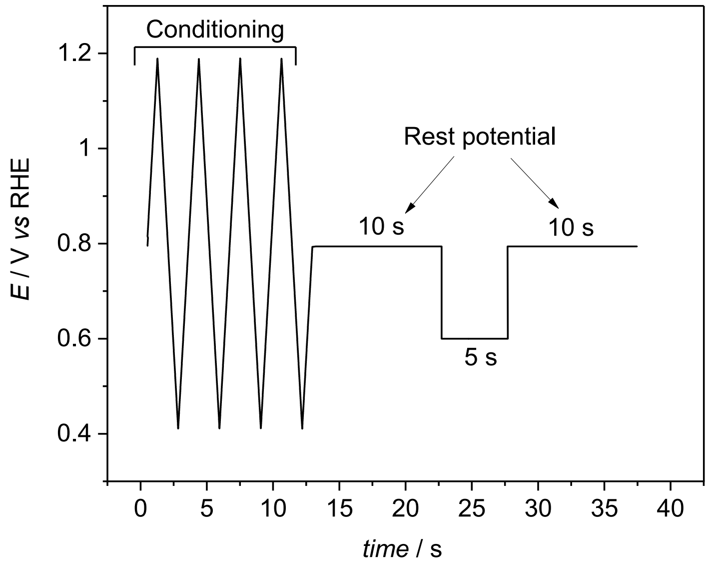

Figure 3-2: Potential waveform used to record the current transients for the ferricyanide reduction SCV study.

The waveform started with the lower potential limit and moved towards the higher potential limit with intervals of 20 mV, scanning all the potential window of interest. Increasing the number of transients recorded enhances the resolution of the reconstructed voltammograms. However, it makes the experiments longer. The balance between the number of potential steps applied and the experiments' duration requires attention when designing the experiments.

The experiments were performed with an equimolar concentration of each ion – $[Fe(CN)_6]^{3-}$ and $[Fe(CN)_6]^{4-}$ – (4 mM) in 1 M KCl. Thus, the rest potential set (≈ 0.795 V) ensured that the faradaic current was zero while the rest duration was adjusted to make sure the subsequent potential step was unaffected by the pre-conditioning cycles. Because the diffusion coefficients of the reduced ($Fe(CN)_6^{4-}$) and the oxidized ($Fe(CN)_6^{3-}$) species are similar, both species will be present at the surface to keep a Nernstian behavior in an extended potential window. Therefore, both branches of the reaction, the reduction, and the oxidation appear in the voltammograms.

The waveform used for the ORR experiments also consists of a conditioning step (same as described for the ferricyanide but in a different potential window), followed by the rest potential (near the open circuit potential) kept for 60 seconds, stepped to the target potential of interest for 1 second, and stepped back to the rest potential for 20 seconds, Figure 3-3. The waveform started at the lower potential limit and moved towards the higher potential limit scanning the entire potential window of interest but with intervals of 20 mV at diffusion-controlled potentials and 10 mV at kinetically controlled potentials to increase the resolution at that potential window. Perry et al. [32, 50, 260] developed and applied this waveform to study the ORR on Pt microelectrodes.

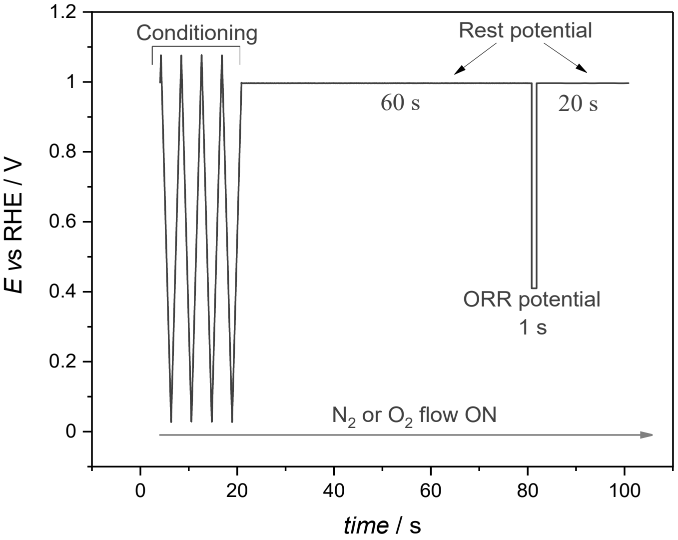

Figure 3-3: Potential waveform used to record the transients for the ORR on the polycrystalline Pt RDE.

In the ORR experiments, the same waveform was applied in N_2 and O_2-saturated solutions to produce the two sets of data: first, in N_2 to generate the background currents and then, in O_2 to generate the ORR currents. The subtraction of the background currents recorded from the ORR currents ensures that the dataset shows only faradaic ORR currents. All the plots shown for the ORR in the results sections had the background currents removed, and thus, it shows currents exclusively coming from the O_2 reduction.

3.5 Results

3.5.1 The $Fe(CN)_6^{3-}$/ $Fe(CN)_6^{4-}$ redox probe studies

The RDE polarization curves recorded for the ferri-ferrocianyde redox processes, Figure 3-4a), follow the typical sigmoidal shape characteristic of voltammograms recorded under steady-state conditions. The diffusion-controlled limiting currents for the reduction and oxidation of the active species in the solution generate a well-defined plateau between 0.580 and 0.380 V for the first and 0.900 and 1.200 V for the latter, regardless of the rotation rate. The inset shows the plot of the current density measured at 0.500 V versus the rotation rate's square root, and the straight-line seen in the graph is characteristic of a diffusion-controlled reaction.

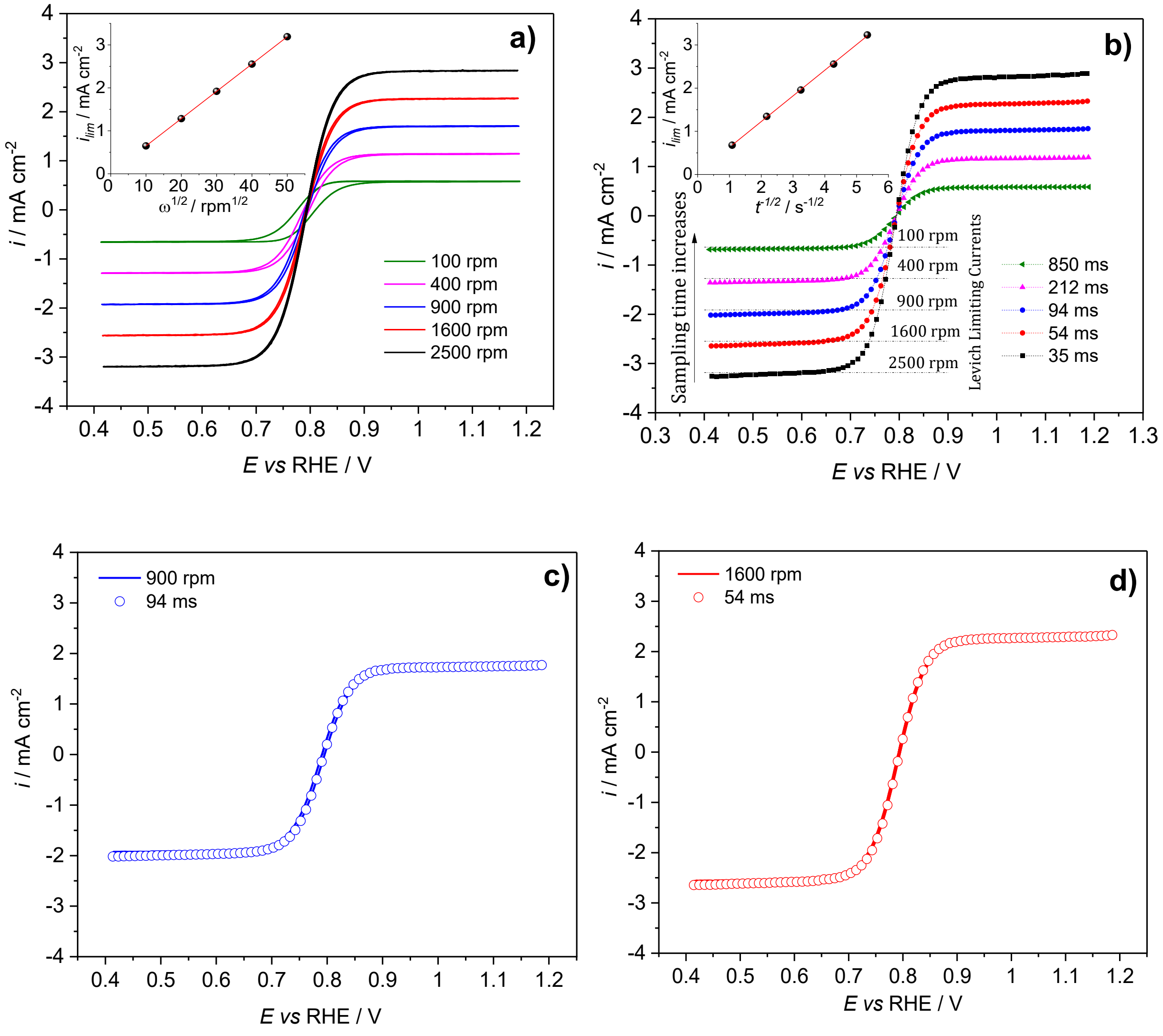

Figure 3-4: a) RDE polarization curves for the ferri-ferrocyanide redox reaction, b) reconstructed SCVs for the same reactions, c) and d) superimposition of both polarization curve for 900, and 1600 rpm, respectively.

The sampled current voltammograms recorded under quiescent conditions reconstructed using the sampling times shown in Table 1 (Figure 3-4b)) also exhibit a sigmoidal shape and appear identical to the RDE voltammograms. The limiting currents seen in the reconstructed SCVs are within experimental error, similar to the theoretical limiting currents for each RDE rotation rate, calculated using the Levich equation (dashed lines added for guidance in the plot). The Cottrell plot shown in the inset demonstrates a linear relationship, which is the expected behavior for a diffusion-controlled reaction. The lower sampling times deliver the higher mass transfer coefficients, reflected in the higher currents measured at shorter timescales, resulting from the scaling of the mass transfer coefficients with the sampling time.

The superimposition of the polarization curves obtained with both methods, Figure 3-4c) and d), shows that the curves overlap over the complete potential window. The SCV reconstructed at 94 ms overlaps the LSV recorded at 900 rpm, Figure 3-4c), and the same occurs to the SCV reconstructed at 54 ms, and the LSV recorded at 1600 rpm, Figure 3-4d).

These results demonstrate that for a model redox system, with no kinetic limitations neither adsorbates involved in the redox processes, SCV at a stationary electrode produces voltammograms similar to those at the RDE when the sampling times and rotation rates are selected to yield the same mass transfer coefficient.

3.5.2 ORR study on the Pt RDE

The RDE polarization curves (Figure 3-5a)) exhibit the characteristic features for the diffusion-controlled ORR on polycrystalline Pt in sulfuric acid solutions[51-53]: i) a sigmoidal wave, ii) a well-defined plateau for the diffusion-controlled currents at potentials below 0.40 V *vs.* RHE, iii) a linear increase of the diffusion-limited current with the square root of the rotation rate (inset in Figure 3-5a)) as predicted by the Levich equation[3], and iv) a hysteresis due to the adsorption of oxygen species on Pt at the beginning of the cathodic going scan[9, 53-55].

The initial stage of Pt surface oxidation occurs as oxygenated species adsorbs onto the Pt surface between 0.85 and 1.10 V *vs.* RHE, which coincides with part of the ORR potential window. These adsorbed species at the surface hinder the ORR and shift the wave to more negative potentials[56, 264], leading to the observed hysteresis.

The sampled current voltammograms reconstructed using the total ORR currents, Figure 3-5b), display sigmoidal waves with four main differences regarding those recorded with the RDE. First, the magnitude of the SCV limiting currents is greater than the expected limiting currents. Second, the current at the ORR wave foot (i.e., around the ORR onset potential) increases when the sampling time decreases, whereas the RDE waves remain unaffected by the rotation rate. Third, the SCVs show a broad peak around 0.6 V *vs.* RHE, which is more evident at shorter sampling times. Fourth, additional peaks appear at circa 0.13 and 0.26 V at the shortest sampling times. A plot of the reconstructed SCVs using the background-subtracted currents contributes to elucidating the nature of those differences and eliminates contributions not associated with oxygen reduction, Figure 3-5c).

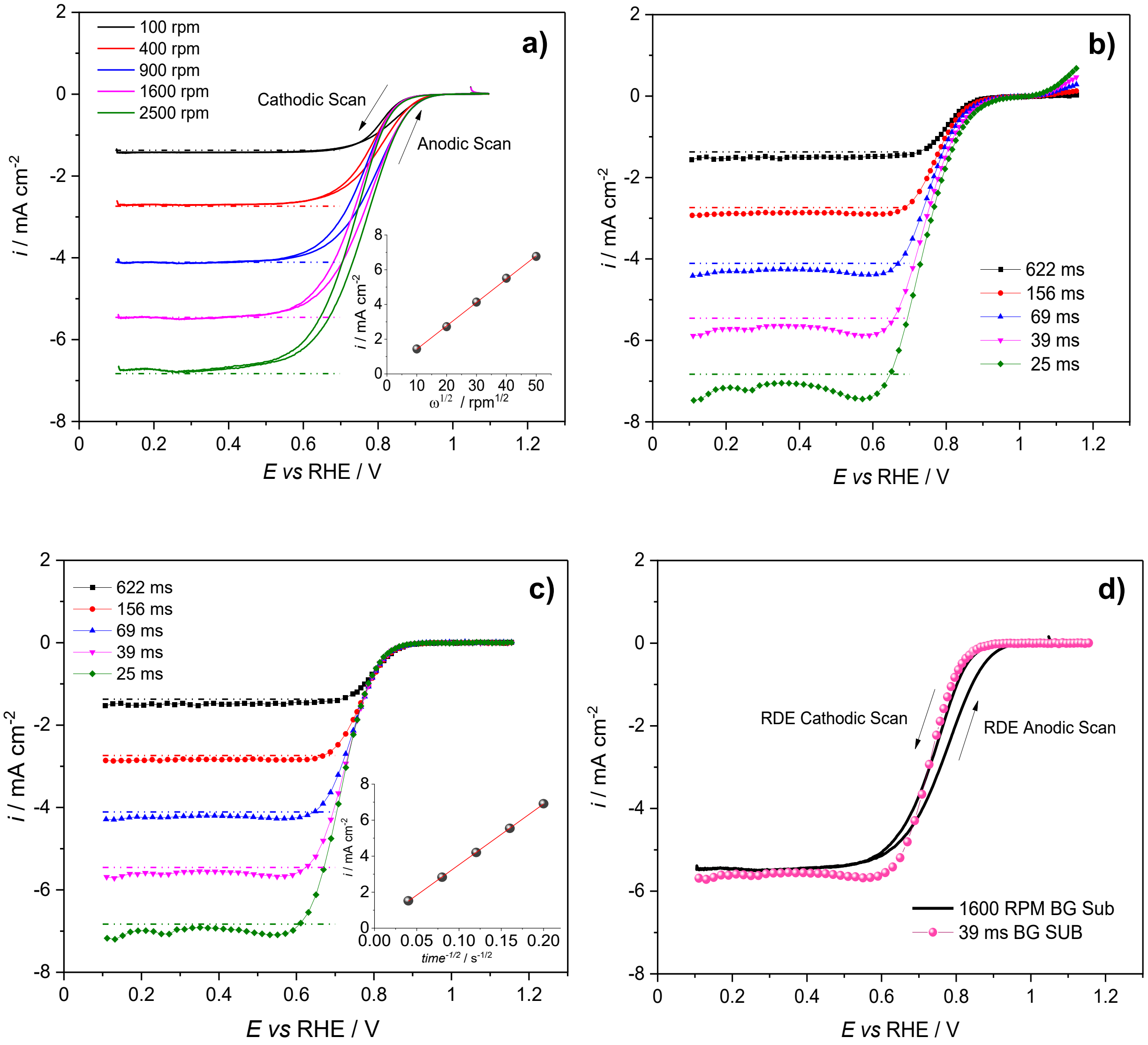

Figure 3-5: a) RDE polarization curves for the ORR on polycrystalline Pt, and reconstructed SCVs for the same reaction using total ORR currents in b), and background-subtracted currents c), d) shows the superimposed RDE and SCV polarization curves.

After subtracting the background currents, Figure 3-5c), the SCV limiting currents are closer to those obtained with the RDE. More importantly, the currents at the foot of the ORR wave overlap with one another, as observed in the RDE voltammograms. This suggests that the extra current seen at short sampling times at the foot of the SCV wave comes from the reduction of oxygen-adsorbed species at the Pt that occurred during the rest period. When compared directly, Figure 3-5d), the background-subtracted SCV superimposes almost entirely with the cathodic going scan of the RDE voltammogram but does not match the scan in the anodic direction. The match between the cathodic branch of the RDE voltammogram and the SCV arises from a simple fact:

in both cases, adsorbed oxygen species hinder the ORR and shift the reaction's onset to more negative potentials. Such interference is absent in the anodic branch of the RDE.

The analysis of the currents recorded in N_2-saturated 0.5 M H_2SO_4 elucidates how the waveform affects the electrode surface before the ORR, Figure 3-6. The N_2-saturated electrolyte reconstructed SCVs show a pronounced reduction peak at 0.797 V when sampling at 622 ms and 0.748 V *vs.* RHE when sampling at 25 ms. This peak arises from the reduction of the chemisorbed oxygen species formed when the Pt electrode was held at the rest potential, 1.00 V *vs*. RHE. The reduction of these species is a fast process, and for this reason, the peak is larger at short sampling times because the oxide coverage is significant, while at long sampling times, the peak virtually disappears as most of the oxide has been reduced. At potentials more positive than 1.00 V, the potential applied to the electrode is positive enough to drive the surface oxidation, originating anodic current densities.

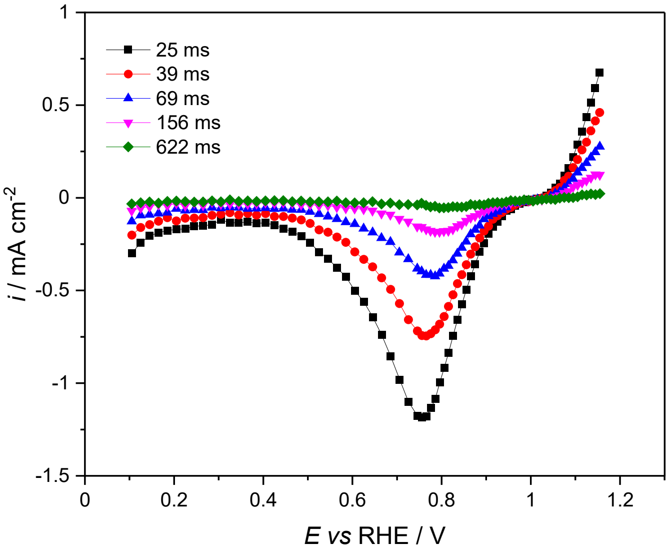

Figure 3-6: Reconstructed SCVs for the Pt RDE recorded in the N_2 saturated 0.5 M H_2SO_4 electrolyte.

As a consequence of the oxygen adsorption at the Pt surface during the rest potential in the SCV experiments, the Pt surface shares the oxidized state induced by the rest potential for the whole ORR potential window. Therefore, regardless of the initial direction of the scan, the surface's response will be the same, and there will be no difference between backward and forward scans. This contrasts with conventional voltammetry, where the state of surface changes during the potential cycling, and the previous electrode potential applied to the surface affects each point on the voltammogram.

Lowering the rest potential should decrease the initial oxide coverage and find the optimum rest potential 0.950, 0.900, 0.877, 0.800, and 0.750 V *vs*. RHE were tested as rest potentials. A study of the rest potential can be found in Chapter 5. However, in all cases, oxygen is adsorbed at the Pt surface. Furthermore, these values are at the foot of the ORR wave and led to the depletion of oxygen during the rest period. In oxygenated acidic media, it is impossible to find a suitable rest potential where the Pt surface is free from oxygen species because the onset of oxygen reduction overlaps with the onset of oxide formation. This is intrinsic to the platinum surface in acidic medium[54-56].

The analytical treatment of the RDE data encompasses the production of the Koutecký-Levich plots (K-L) using the currents measured with the RDE to extract ORR kinetic information. To generate the K-L plots, one must plot the reciprocal of the disk currents versus the square root of the rotation rate (based on the equation (21)). Likewise, using the currents measured at the transients it is possible to obtain K-L alike plots and extract kinetic information. Applying the K-L relationship to the transients, which are described by the Cottrell equation (equation (22)), gives:

$$i^{-1} = \frac{\sqrt{\pi}\sqrt{t}}{nFAD^{1/2}C^{B}} \qquad (27)$$

Considering equation 27, plotting i^{-1} *vs.* $t^{1/2}$ originates a K-L plot. For the timescale where the diffusion controls the transients, a linear relationship arises. Then, extrapolation of the linear section to very short times corresponding to infinite rates of mass transport yields the inverse of the kinetic current. If the number of the electrons exchanged in the ORR is constant over the potentials applied, the lines have the same slope, given by:

$$m = \frac{\sqrt{\pi}}{nFAD^{1/2}C^{B}} \qquad (28)$$

Accordingly, the K-L plots based on the current transients allow the estimation of the apparent number of electrons exchanged (n) for each potential applied.

According to the timescale where the reaction is diffusion controlled, the linear region on K-L alike plots built using the current transients for potentials ranging from 0.800 to 0.410 V presents different extensions, Figure 3-7. The dotted lines in the plot correspond to the linear regressions for the times where the current is purely diffusion controlled. For 0.8 V, the ORR kinetics controls most of the transient because the force driving the reduction is not high. As the potential becomes more negative, the linear region of the plot expands because the diffusion control starts earlier. Therefore, to obtain a good fitting and extract more accurate kinetic currents, the linear region of the plot should be long enough in the timescale. This constraint may limit the extraction of the kinetic currents for more positive potentials once the driving force for the electron transfer is low. To overcome this issue, it is recommended to record the transients for longer times to span the potential window.

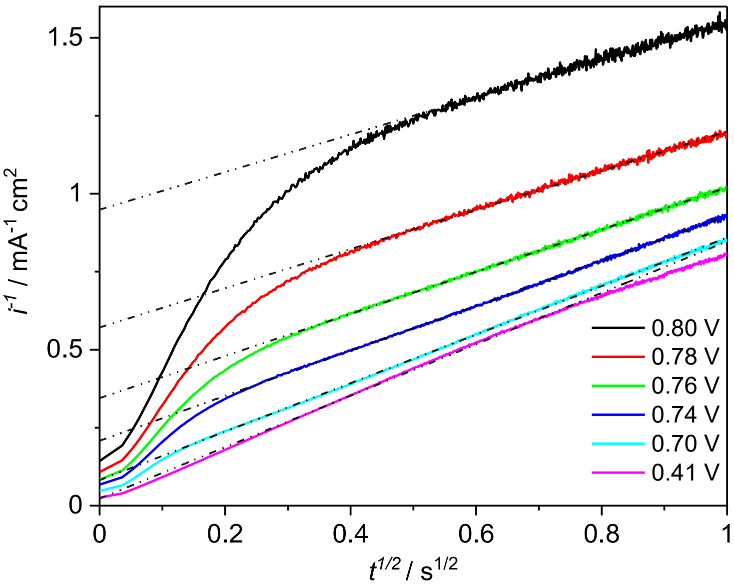

Figure 3-7: K-L plots constructed using the current transients recorded in O_2-saturated 0.5 M H_2SO_4 electrolyte for the Pt RDE.

Therefore, the plot is linear at long times because the current only comes from the diffusion-controlled reduction of oxygen, and this part is the targeted one. However, the plot is no longer linear at short times because of the extra current due to the reduction of oxygen species adsorbed on the electrode surface. The impact of the double-layer charge/discharge or adsorption of species is higher at short times for experimental conditions where the time-constant of the cell is higher since these processes will take longer to vanish. The almost parallel lines reveal that the apparent number of electrons exchanged is constant within the potential range studied.

The current measured at the transients can generate Tafel plots yielding additional kinetic information. The K-L plots' intercept affords the reciprocal of the kinetic currents (i_k) that plotted versus the potential applied during the step potential originates the Tafel plot, Figure 3-8.

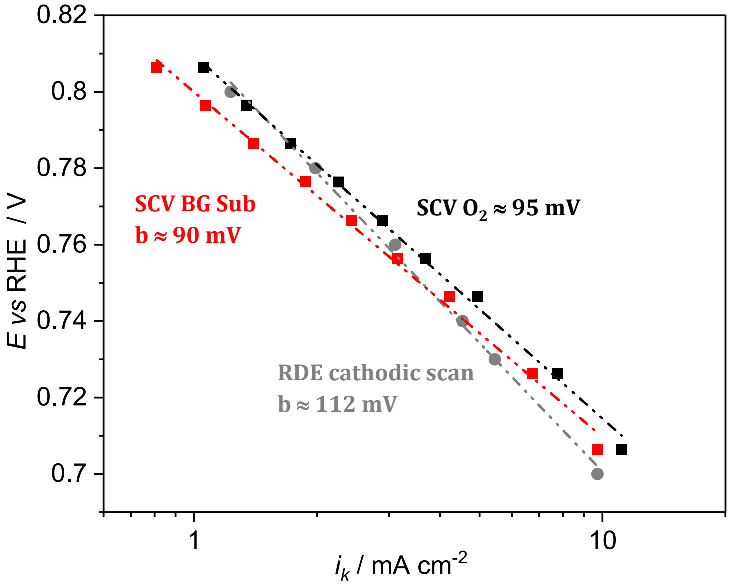

Figure 3-8: Tafel plots for the Pt RDE obtained using the ORR kinetic currents extracted from the K-L plots. For the hydrodynamic experiments, the RDE cathodic sweep was used for analysis, and for the reconstructed SCVs, the plots used both the total ORR currents and background subtracted currents.

The Tafel plots for ORR obtained from the total ORR current transients (solid black squares), the background-subtracted ORR currents (solid red squares), and the background-subtracted RDE cathodic scan (solid grey spheres) display similar current densities and slopes. The total ORR currents exhibit greater currents because it contains the ORR faradaic currents and the currents from the adsorption of oxygen to the electrode. The subtraction of the background currents eliminates the adsorption component and yields a line with lower currents and a slope 5 mV lower. Since the linear region in the K-L plot is purely diffusion-controlled, subtracting the background currents recorded in N_2-saturated electrolyte makes little difference to the kinetic currents and, therefore, to the Tafel slope.

The difference in the Tafel slopes, circa 112 mV for the RDE and 90 mV for the stationary electrode, is consistent with the electrode spending more time in the oxide region during the potential step than during the potential sweep[54, 163, 212, 265-266]. The ORR is sensitive to the presence of adsorbed oxygenated species, specifically adsorbed spectator anions, and to the competition between these species on for the Pt surface sites before the ORR. For this reason, different values of Tafel slopes have been reported for Pt electrodes in the literature. It is widely accepted in the literature that the Tafel slope changes with the extent of the oxide coverage on the electrodes prior to the reaction. In this sense, a Tafel slope of 60 mV would be reported for an oxide-covered Pt surface, whereas values ranging from 90 - 120 mV corresponds to metallic Pt surfaces[51, 54, 163, 212, [265-266]. Therefore, the higher oxide coverage on the Pt found in the SCV provokes the lower Tafel slope and explains the Tafel slopes' differences between the RDE and the SCV.

3.5.3 SCV tests on H_2SO_4 solutions: the impact of the concentration

SCV relies on the analysis of current transients resulting from a series of potential steps, where the overall current measured for each potential step is the sum of the capacitive and the faradaic components of the electrode process. For the ORR's specific case, an additional contribution to the current comes from the fast reduction of the oxygenated species adsorbed during the rest potential. The background currents' subtraction removes the oxide reduction contribution leaving the capacitive currents and the ORR faradaic currents.

In this context, the concept of the non-faradaic time-constant of the electrode (τ)[3, 46] can be applied to estimate the time necessary to discharge the capacitive currents, and it is given by equation (26). For a period $t = 3\tau$, 95% of the capacitive component in the current has been discharged. It is recommended to sample at times > than 5 τ to ensure that 100% of the double-layer charging will be complete.

The non-faradaic current measured in the potential step experiment varies according to equation[3, 46]:

$$i_{dl} = \frac{E}{R_S} e^{-t/R_S C_d} \quad (29)$$

Where i_{dl} is the double layer charging current in A, E stands for the potential applied in V, t for the time in seconds, R_S represents the electrolyte's resistance, in Ω, and C_{dl}, the double-layer capacitance, in F.

The resistance of the solution and the capacitance of the electrode significantly affect the timescale available for the reconstruction of the SCVs. Using high supporting electrolyte concentration and controlling the electrode's roughness and area minimizes this interference and broadens the sampling timescale.

Thus, to study the impact of the electrolyte concentration on the experimental time-constant associated with the electrochemical cell, the sulfuric acid concentration varied from 0.05 M to 0.5 M, and the time-constants were compared in Table 3. Electrochemical impedance spectroscopy recorded at the rest potential (closely to the OCP, and therefore, no faradaic current flow in the cell), and fitted with an RQ simple circuit composed by a resistance (R) in series with a constant phase element (Q) provided the values of the resistance of the electrolyte and the capacitance of the electrode, according to

$$C_{dl} = \frac{(Q_0 \times R_S)^{(1-n)}}{R_S} \qquad (30)$$

Where Q_0 is the admittance (the reciprocal of the impedance), and *n* is a value associated with how the behavior of Q resembles the one of a capacitor, thus, if $n = 1$, then $Q_0 = C_{dl}$.

Table 3: Electrochemical parameters experimentally measured for several sulfuric acid electrolyte concentrations.

Concentration / M	R_S / Ω	C_{dl} / μF	τ / ms	5 τ / ms
0.05	71.3	28.20	2.01	10.05
0.1	59.9	19.77	1.18	5.92
0.25	9.6	20.76	0.19	0.99
0.5	5.3	15.92	0.08	0.42

Increasing the acid concentration from 0.05 to 0.5 M causes a decrease in electrolyte resistance (R_S) as a natural consequence of the increase in the ionic conductivity of the sulfuric acid solutions[267]. The acid concentration also affects the electrodes' capacitance, and the capacitance values decrease with the increase in concentration as expected[268]. The time constant of the cell is lower for more concentrated electrolytes, and the physical meaning is that the capacitive currents decay faster in more concentrated solutions and spans the range of available sampling times at the short timescale.

Considering the results presented in Table 3, one may argue that, once we are targeting sampling times larger than 25 ms, using the lowest concentration – 0.05 M H_2SO_4 – should not impose problems, because the time-constant of the cell indicates that after 10 ms, only faradaic currents are measured, and the double layer current has decayed entirely. To examine this hypothesis, current transients recorded at the same potential were evaluated using each of these acid solutions as supporting electrolytes, Figure 3-9a).

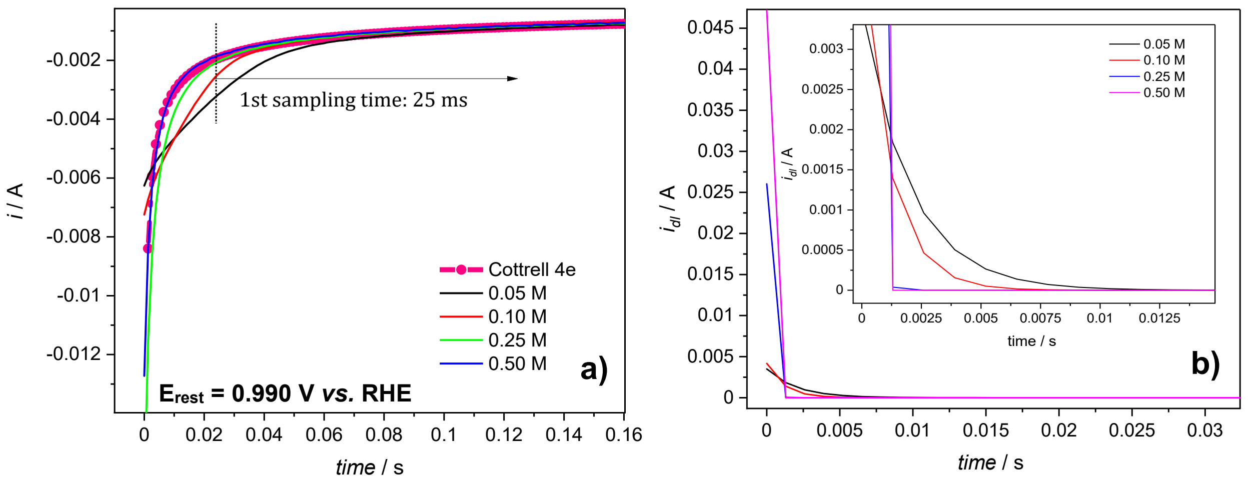

Figure 3-9: a) shows the transients recorded in O_2 saturated H_2SO_4 electrolyte with different concentrations for E= 0.250 V *vs.* RHE. In b) the plot simulates the decay of the double layer charging currents with time for the tested acid concentrations, according to equation (29).

These transients were recorded by applying 0.250 V *vs.* RHE, which lies in the ORR diffusion-controlled potential window. Therefore, the transients must behave as diffusion-controlled and obey the Cottrell relationship. For reference, a simulated Cottrell transient (obtained using the following constants: $n = 4$; $D_{O2} = 1.93 \times 10^{-5}$ cm^2 s^{-1}; $C_{O2} = 1.16 \times 10^{-6}$ mol cm^{-3} and A=0.28 cm^2) was added to be plot.

The transients shape varies significantly with the electrolyte concentration for $0 > t > 0.08$ seconds, but they superimpose at time > 0.100 seconds. At a longer timescale, the double-layer charge/discharge is complete, and the O_2 diffusion rate from the bulk of the solution to the interface controls the transients. Thus it is unaffected by the concentration of the electrolyte. In a), the plots show that at short timescale, the transients recorded in the more diluted electrolytes (0.05 and 0.10 M) deviate significantly from the Cottrell transient, and their shape is distorted, whereas those recorded in the 0.25 M and 0.50 M are more alike the Cottrell transient and they almost overlap. Using equation (29), the decay of the double layer currents, i_{dl} , was estimated for 0.250 V *vs* RHE, and employing the R_S and C_{dl} experimentally obtained and shown in Table 3, Figure 3-9b). The plots confirm that the diluted electrolytes significantly delay the decay of the capacitive currents, and it causes the distortion seen in the transients.

The quality of the data obtained by the reconstruction of the SCV depends on the quality of the current transients recorded, and for this reason, it is fundamental to understand how this distortion affects the data. The currents were sampled at 39, 69, and 156 ms and plotted versus the potential applied to yield the reconstructed SCVs, as shown in Figure 3-10 a) to c).

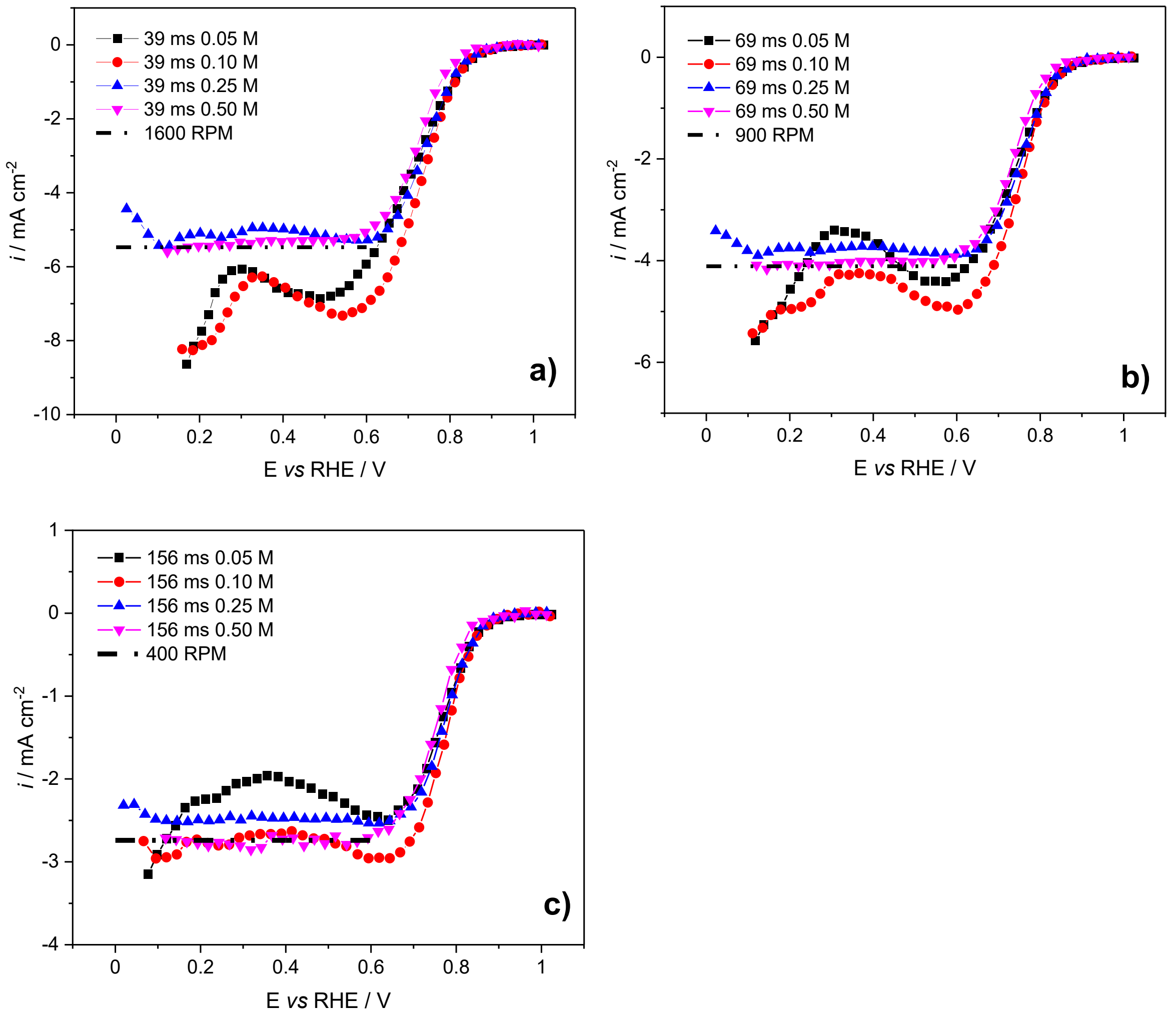

Figure 3-10: Reconstructed SCVs recorded in the different sulfuric acid concentrations for currents sampled at a) 39 ms, b) 69 ms, and c) 156 ms.

In a), the SCVs sampled at the shortest sampling time show a remarkable difference in the shape of the SCVs and the currents measured for 0.05 and 0.1 M H_2SO_4 electrolyte. The SCVs for the more diluted solutions show a round wave ranging 0.40 – 0.60 V and for E < 0.3 V, another peak (0.1 M H_2SO_4) or a steep increase of current (0.05 M H_2SO_4) is observed. In both cases, the currents are higher than the limiting current expected by the full reduction of the O_2 by exchanging four electrons, represented by the dashed black line. In this potential window, the expected scene is the plateau's observation originated from the depletion of the O_2 at the electrode surface driven by the high overpotential applied to the electrode. The polarization curves obtained in 0.25 and 0.5 M H_2SO_4 shows results very similar to the expected: the limiting current shows a plateau very close to the expected limiting current, and it shows a slight shift of the polarization curve toward positive potentials for 0.25 M due to the specific adsorption of the HSO_4^- anion to the platinum surface[51]. As seen in b) and c), the large difference in the magnitude of the current density measured vanishes as the sampling time becomes longer, however, the round wave-shaped curves remain.

The distortion of the transients primarily affects the shortest times providing a considerable deviation for the Cottrell behavior for 0.05 and 0.1 M H_2SO_4 solutions, which caused significant perturbations in the reconstructed SCVs affecting this reliability. The transients' analysis indicates that this an effect caused by the increased resistance of the electrolyte when the solution is diluted.

Furthermore, the shape of the reconstructed sampled current voltammograms seems to imply that the higher electrolyte resistance delays not only the decay of the capacitive currents but also affects other fast processes taking place before the ORR. This is evidenced by the higher current densities measured for the lower acid concentrations lying in the platinum oxide reduction, causing the appearance of the round wave where a plateau should exist and the visible part of the hydrogen adsorption, at more negative potentials. Both processes are faster than the ORR is, and since they are delayed, their contribution is accounted to the currents measured, and consequently, the ORR limiting currents and shapes of the polarization curves deviate from the typical sigmoidal-shaped curves for the ORR.

Therefore, the supporting electrolyte concentration in the time-constant of the cell must be carefully considered when considering the experimental protocol that will be applied in the study of a determined electrode process. The time constant of the cell also depends on the double-layer capacitance of the electrode, which by its turn, depends on the roughness and morphology of the working electrode. For this specific case, the time constant of the cell is not enough to estimate the lowest sampling time available. The experimentally obtained transient analysis and its direct comparison with a Cotrellian simulated transient is an excellent and simple diagnostic tool to verify the experimental conditions' suitability.

Notably, the concentration of supporting electrolytes can be easily accomplished as a range of salts can be added to the electrolyte to minimize the solution's resistance. For instance, for the ORR study on the Pt/MgO(110) film presented in chapter 6, the concentration of the acid was kept at 0.05 M H_2SO_4, but 0.1 M $KClO_4$ was added to the electrolyte to decrease the resistance of the electrolyte.

3.6 Analysis of the strengths and limitations of SCV

One of the main advantages of SCV is that when mass transport affects the measurements of the reaction rate, it produces sigmoidal current-potential curves irrespective of time scale, and thus of mass transport regime. Therefore, it is possible to exploit the analytical procedures developed to study steady-state voltammograms, which significantly facilitates the analysis and comparison of the SCVs. This is what makes SCV so interesting for electrode surfaces not amenable to RDE or microelectrode experiments. From an experimental point of view, the SCV method is straightforward to perform, even with electrode surfaces not amenable to RDE or microelectrode designs. It does not require dedicated hardware or software, and it is easily implemented with any conventional electrochemical workstations and can be operated with minimal training.

A second major advantage is that selecting the sampling time affords any number of mass transfer coefficients within a considerable range of values. As shown in Tables 1 and 2, sampling between 1 s and 20 ms affords k_m values similar to those obtained with an RDE. At the same time, sampling below 20 ms affords much larger k_m values comparable to those obtained with small microdisk electrodes. For example, sampling at 20 ms generates the same k_m as a 14 µm diameter disc, while sampling at 1 ms is equivalent to using a 3 µm diameter disc. Another advantage is that the method allows a conditioning procedure before the step to the target potential. This ensures that every transient is recorded under the same conditions. Thus, every point on the SCV shares the same electrode history. This contrasts with conventional voltammetry, where every point on the voltammogram is affected by the previous electrode potential. Although the work presented here exclusively considered an electrochemical conditioning approach, the technique allows other conditioning protocols, e.g., via chemical or photochemical conditioning.

The main drawback of SCV is that it is a transient technique, and although the SCVs have sigmoidal shapes akin to steady-state voltammograms, they still hold time-dependent information. Hence, in common with all transient techniques, the SCV currents are susceptible to distortion by surface processes (double layer charging and electrochemical activity of adsorbed species) and by instrument limitations (for instance, the response time of the current amplifier). Therefore, it is essential to select appropriate acquisition conditions and adjust the sampling time to account for any changes in the surface processes' time constant. For example, increasing the electrode surface roughness increases the time constant of all surface processes, and the SCV sampling time must be increased accordingly. While the distortion of SCV currents arising from the electrochemical activity of adsorbed species is not an issue at long sampling times, it does limit the shortest sampling times. Here, this issue was addressed by recording a background SCV and subtracting it from the main SCV.

Another limitation of the technique is that there is no information arising from the potential direction on the SCVs, in contrast with conventional voltammograms. It is impossible to distinguish a forward or backward SCV since the target potentials can be selected in any order.

3.7 Conclusions

In this chapter, the SCV was presented and validated as an alternative technique to study the ORR for situations where the hydrodynamic voltammetry is not suitable. The validation was performed using two electrochemical reactions: the ferricyanide reduction and the ORR. First, the conditions in which the reconstructed SCV polarization curves correspond to the RDE were derived, and then, the experiments were used to validate the conditions derived.

In both cases, a good correspondence between both methods was found. Therefore, it was demonstrated that the mass-transfer coefficients are the key parameter when targeting the correspondence of both methods. If we select the sampling time corresponding to the mass transfer coefficient provided by the specific rotation rate, the polarization curves tend to display comparable results. However, due to intrinsic characteristics of the Pt surface state in acidic media within the ORR potential window, the SCV corresponds to the cathodic scan of the RDE where the scan starts from an oxidized Pt surface and move towards the reduced surface. This happens because the rest potential applied before recording the ORR transients causes the oxygen adsorption on the Pt surface, and this state is shared for the whole potential window.

Hence, it should be noted that in SCV, the shortest sampling times available (corresponding to the high mass-transfer coefficients) are limited by the double-layer charging process and by any surface faradaic process such as oxide formation/reduction or hydrogen adsorption/desorption. For this reason, the evaluation of the time-constant of the cell must be performed, and the sampling times selected must be at least 5 τ to minimize distortions in the transient.

Additionally, it was demonstrated how the chronoamperograms dataset could be easily treated to produce plots analogous to the Koutecký-Levich and Tafel plots at RDEs, providing further kinetic information on the reaction. For this purpose, the user must ensure that the transients are recorded for times long enough to ensure a useful extension of the diffusion-controlled timescale to produce reliable K-L slopes and intercepts.

Therefore, SCV makes it possible to investigate reactions on electrode materials that do not lend themselves to steady-state voltammetry with rotating discs or microelectrodes, and it can be a simple and versatile tool for the search of new electrocatalysts.

4 MATERIALS AND METHODS

4.1 Materials

The materials for the ORR electrocatalytic studies are categorized into two groups: those employed in the pulsed laser deposition of the films and those used in the electrochemical characterization, Table 4.

Table 4: List of materials employed in the deposition and characterization of the films.

	Material / Grade	**Supplier**
Deposition of the films	MgO(hkl) (10 × 10 × 0.5 mm, epi polished)	MTO Corporation
	Au target (99.99%)	Kurt J. Lesker Company
	Pt target (99.9%)	Kurt J. Lesker Company
	Ni foil (99.994%)	Alfa Aesar
	Ag foil (99.99%)	Alfa Aesar
Electrochemical Characterization	$K_3[Fe(CN)_6]$ (>99%)	Acros Organics
	$K_4Fe(CN)_6 \cdot 3H_2O$ (min. 98.5%)	Alfa Aesar
	KCl (min. 99.5%)	Bioshop
	H_2SO_4 (trace metal grade)	Fisher Scientific
	KOH (semiconductor grade)	Sigma-Aldrich
	Mercury-mercury sulfate reference electrode Saturated K_2SO_4 (MMSE)	Koslow
	Mercury-mercury oxide reference electrode 20% KOH solution (MMO)	Koslow
	NaOH (99.99% metal basis)	Alfa Aesar

	$Pb(NO_3)_2$ (99.999% trace metals basis)	Sigma-Aldrich
	$KClO_4$ (99.99% trace metal grade)	Sigma-Aldrich
	Au wire (99.99%)	Alfa Aesar
	Au foil (99.99%)	Alfa Aesar
	Pt gauze (99.99%)	Alfa Aesar
	Pt foil (99.99%)	Alfa Aesar
	Pt RDE (5 mm Ø)	Pine Research
	N_2 (99.999%)	Praxair
	O_2 (99.993%)	Praxair

4.2 Deposition of films by pulsed laser deposition

Pulsed laser deposition was used to deposit the Pt/MgO(hkl) and Au/MgO(hkl) films. Both metals crystallize in face-centered cubic lattices (*fcc*), with lattice constants, *a:* for Pt, *a* = 3.9231 Å (JCPDS file 00-004-0802) and Au, *a* = 4.0786 Å (PDF card 00-004-0829). In the deposition of Pt and Au films, ceramic MgO(110) and MgO(100) were used as substrates. The MgO also crystallizes in a *fcc* crystalline structure with a lattice parameter greater than both metals, *a* = 4.2112 Å (JCPDS file 00-045-0946).

For the films' deposition, a KrF excimer laser with 248 nm laser radiation wavelength, which emits deep ultraviolet light with a pulse length of 17 ns ablated the targets. The deposition took place in a custom-made stainless-steel vacuum chamber equipped with a turbopump to provide the UHV conditions. A detailed description of the setup can be found elsewhere[122].

The parameters involved in the deposition significantly affect the growth of the films and, consequently, their structure and morphology. These are the laser fluence (J cm^{-2}), the number and duration of the laser pulses, the background gas pressure inside the chamber (UHV or reactive/inert gas), and the substrate's distance to the target, and the substrate temperature. Table 5 lists the conditions used in the deposition of the films.

Table 5: Description of the parameters used in the depositions of the films.

Parameter	Pt/MgO(110)	Au/MgO(100)
Laser Fluence (J cm^{-2})	3	3
Repetition rate (Hz)	20	20
Target to substrate distance / cm	5.5	5.5
Substrate temperature / °C	400	From room temperature to 600
Buffer layer / 2000 pulses	Ni	Ag and Ni
Number of pulses	40 000	From 25 000 to 100 000
Background pressure	UHV ≈ 10^{-5} Torr	UHV ≈ 10^{-5} Torr

During deposition, the targets continuously moved in rotational and translational directions to obtain a uniform ablation. Likewise, the substrates also rotated constantly to ensure a homogeneous distribution of the ablated flux of species on the substrate. Before the deposition of the films, the substrates were cleaned by sonication in isopropanol (for 15 min) first and then in acetone (for 15 min) and dried under an argon stream before being fixed in the sample holder. The substrate temperature varied as necessary to achieve the epitaxial growth of the desired metallic facet. Typical substrate temperature values were 400 °C for Pt and 200 °C for Au.

Before the deposition of the metallic layers, a nickel or silver buffer layer was deposited onto the MgO substrates by ablating a Ni or Ag foil, corresponding to a thickness of approximately 1 nm. Previous work in the group demonstrated that the deposition of these buffer layers enhances the film's adhesion and facilitates the epitaxial growth of the Pt layer[122]. According to the films' desired thickness, a specific number of pulses were set up to strike the target. After deposition, the samples cooled to room temperature under vacuum.

The adjustment of the laser fluence and the gas pressure within the chamber is of utmost importance because they control the kinetic energy of the ablated species[269] and the deposition rates of material onto the substrate, which affects the growth and properties of the films. The high kinetic energy achieved by the ablated species in the plasma plume gives PLD the character of an out-of-equilibrium technique. Typically, the kinetic energy ranges from 10 – 100 eV, and for this reason, it is possible to deposit materials that are permanently stuck out of thermodynamic equilibrium, i.e., metastable materials.

When depositing materials whose nature differs from the substrate's, the mismatch between the films and the substrate lattice constants must be considered. Significant lattice mismatches may cause issues in the film's crystallization and growth, introducing defects and irregularities and causing strain in the crystalline lattice. The presence of strain in the crystalline lattice imposes a problem when the films' application requires perfect crystalline structures, whereas, for some specific study cases, some strain in the film's lattice may be beneficial. Thus, the films' application and their desired structure must be thought of when choosing the substrate for the deposition.

The lattice mismatch (ε), can be estimated by the difference in the lattice constants of the film and the substrate:

$$\varepsilon = \frac{(a_{substrate} - a_{metal})}{a_{substrate}} \times 100\% \qquad (31)$$

Considering the MgO substrate, the lattice mismatch regarding Au is around 3.15 %, and regarding Pt is 6.84%. When there is a lattice mismatch, the in-plane lattice parameter of the film (direction within the plane of the film) is forced to match the substrate during the initial stage of the film growth. Thus, when the film's lattice matches forcedly to the substrate, its lattice constant deviates from the bulk's, and the film is under strain. Alternatively, the film may relax, releasing this strain. Usually, there is a critical thickness for the material where below this thickness, the film will strain, but if this thickness surpasses the critical value, the film then starts to relax.

4.3 Surface morphology characterization

The surface morphology of the Au/MgO(100) films was assessed using atomic force microscopy images (AFM Smart SPM1000-AIST-NT Inc.) acquired in intermittent mode. An AIST-NT Smart system in an acoustic enclosure deposited on an active anti-vibration support was operated with an aluminum-coated *n*-type silicon cantilever (HQ:NSC15/Al BS) from Mikro Masch with nominal values (tip radius of 8 nm, a force constant of 40 N/m, and a resonance frequency of 325 kHz). This part of the work was performed in collaboration with Professor Andreas Ruedinger's group, and they were responsible for the acquisition of the images.

4.4 Structural characterization

The X-ray-based techniques comprise an essential set of techniques for the structural characterization of crystalline materials. In this sense, the techniques used herein are X-ray diffraction (XRD) and X-ray reflectivity (XRR). The first affords a wide range of structural information, and the latter estimates the thickness of the films deposited.

The high-resolution XRD (HRXRD) comprises a collection of non-destructive techniques for the analysis of films. In such experiments, a Panalytical X-Pert Pro MRD (weighted Cu $K\alpha_1$ and Cu $K\alpha_2$ λ =1.5419 Å) – with a 4 circles cradle that allows the sample to be moved along different rotation axis: $2\theta, \omega, \varphi$ and χ. The incident angle, ω, is the one between the X-ray source and the sample. The diffracted angle, 2θ, is defined by the angle between the incident beam and the detector, φ is the sample rotation angle, χ is the sample tilt angle, Figure 4-1. Therefore, according to the sample's movement regarding the different directions, different scans can be performed, providing different information.

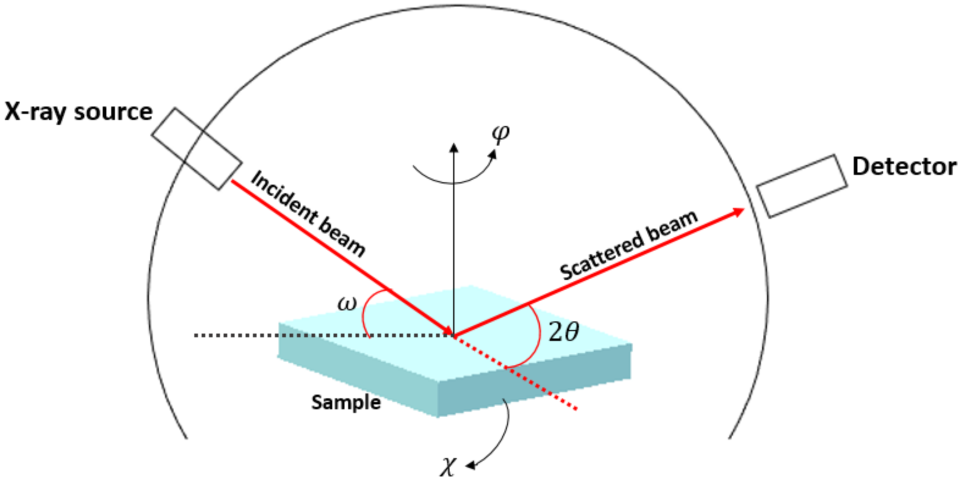

Figure 4-1: Illustration of the X-rays beam path and the different directions considering the goniometer and the sample.

Table 6 summarizes the type of scans and information obtained for the techniques used in this work.

Table 6: Summary of the X-rays based techniques used in this work.

Technique	Information obtained	Type of Scan
XRR	Estimative of the thickness of the films	$\omega - 2\theta$
XRD Bragg-Brentano	Crystallographic orientation of the films, out-of-plane lattice parameters	$\theta - 2\theta$
Pole figures	Type of epitaxy between the film and the substrate and texture of the films	φ –for various χ values
RSM	Mosaic spread (crystal quality), in-plane and out-of-plane lattice parameters, layer tilting	ω -2θ at various ω

4.4.1 X-Ray Reflectivity

To record the reflectivity curves, the X-ray beam irradiated the sample with the incidence angle varying from 0.1° to 4°, with a step size of 0.005° and a counting time of 1 second per data point.

The thickness of the films (*d*) can be estimated by measuring the distance between the maxima of two consecutive fringes (Δθ) and using the following equation:

$$d = \frac{\lambda}{2\sin\Delta\theta} \qquad (32)$$

Where *d* is the thickness of the film in Å, λ is the wavelength of the X-ray (weighted Cu $K\alpha_1$ and Cu $K\alpha_2$ λ = 1.5419 Å), and Δθ is the difference between the maxima of two consecutive fringes. Noteworthy, the quality of the reflectivity data depends on the films' roughness. If the films were rough, the fringes cannot be distinguished, and the thickness cannot be estimated.

4.4.2 θ – 2θ scans

The diffractograms in Bragg−Brentano configuration (θ−2θ mode) were recorded from 35° to 90°, with a step size of 0.016°, and counting time of 1 s per step. Aiming to account for the MgO(hkl) substrate's miscut, the substrate peak position was calibrated according to the MgO position before recording the diffractogram of the analyzed sample. Before analyzing the data, the MgO peak position was verified and corrected once more to the right position, as necessary.

4.4.3 Pole figures

The Au/MgO(100) pole figures were recorded by varying the φ angle - with respect to the axis perpendicular to the surface - from 0 to 360° at 1°/step with 0.5 s time per step, and the χ inclination angle - with respect to the normal to the surface - at 1° per step between of 0 and 85° with 0.5 s per step. The X-ray source and the detector (θ and 2θ) were fixed at the (111) position, and this direction was used as a reference.

4.4.4 Reciprocal Space Mapping

The cell parameters and the mosaicity of the Au/MgO(100) films were estimated by X-ray Reciprocal Space Mapping (RSM) using a step size of 0.05° along both the ω - 2θ axis and ω axis with 1s per step.

The RSM data allow measuring the lateral coherence length, *L*, which scales with the size of domains where long-range ordering occurs and the tilt angle, *T*, between the domains in the films and the underlying substrate. Both can be calculated from the full width at half maximum of the asymmetric reciprocal lattice plane, $\Delta Q_{//}$ and $\Delta Q_{\perp}$, as referred to by Fewster[270] and presented in Figure 4-2.

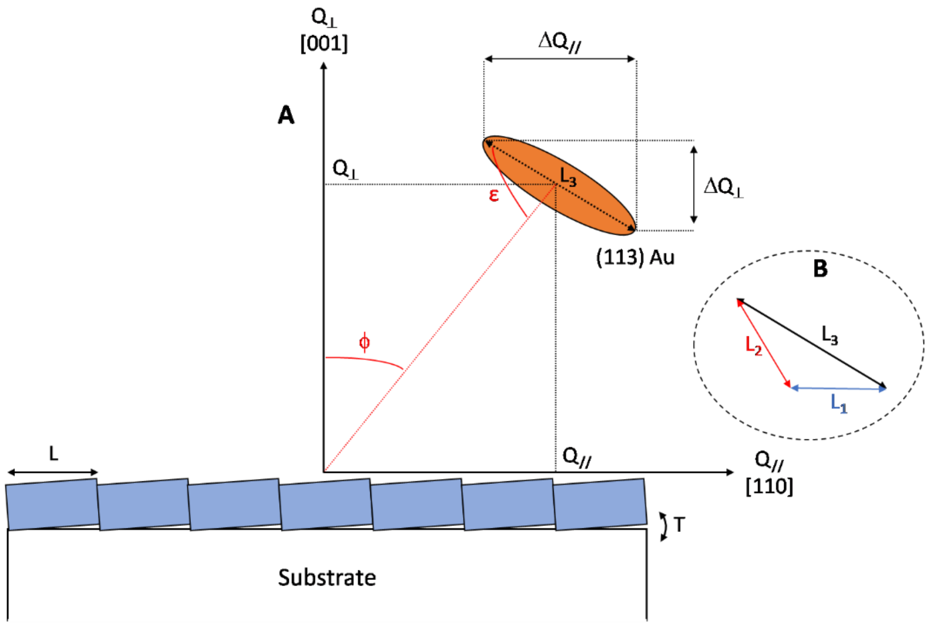

Figure 4-2: Schematic representation and definition of the scattering plane in the reciprocal space to calculate the lateral coherence length (L). (B) Decomposition of the L_3 component into 2 contributions: L_1 relative to the coherence size and L_2 the microscopic tilt.[2]

---

[2] Scheme kindly provided by Dr. Gaëtan Buvat.

Considering the figure, from trigonometry, the following is obtained:

$$\frac{L_2}{L_1} = -\frac{\cos(\epsilon)}{\cos(\varepsilon+\phi)} \text{ and } \frac{L_3}{L_2} = -\frac{\sin(\phi)}{\cos(\varepsilon)} \qquad (33)$$

In the reciprocal space unit:

$$\phi = tan^{-1}\left(\frac{Q_{//}}{Q_{\perp}}\right),\ \varepsilon = tan^{-1}\left(\frac{\Delta Q_{//}}{\Delta Q_{\perp}}\right) \text{ and } L_3 = \sqrt{\left(\Delta Q_{//}\right)^2 + (\Delta Q_{\perp})^2} \qquad (34)$$

Hence, the lateral correlation size (L) and the tilt (T) are obtained as follows:

$$|L| = \frac{1}{L_1} = -\frac{\sin(\phi)}{L_3 \times \cos(\phi+\varepsilon)},\ \text{and } T = \frac{L_2}{\sqrt{Q_{\perp}^2 + Q_{//}^2}} \qquad (35)$$

This part of the work was developed in collaboration with Dr. Gaëtan Buvat, responsible for a significant part of the film's structure characterization by RSM.

4.5 Electrochemical characterization

4.5.1 General experimental features

The first step in the electrochemical characterization of the films is their surface activation. This procedure consists of cycling the electrode potential until a stable voltammogram appears. The scan rate was either 100 or 50 mV $s^{-1,}$ and N_2 – saturated 0.5 M H_2SO_4 was the working electrolyte. Cycling in sulfuric acid electrolyte cleans electrode surface, promotes reproducibility in the results, and provides information regarding the electrochemical behavior. The activation procedure was the same for the Pt/MgO(110) and the Au/MgO(100) films, and in both cases, the voltammograms in 0.5 M H_2SO_4 provide information regarding the surface crystallographic orientation and the electrochemically active surface area (EASA).

The experiments with the thin films required a special electrochemical cell designed for their study, Figure 4-3. In this electrochemical cell, rigid support sustains the working electrode, and a gold wire placed on the top of the Pt or Au film makes electrical contact. This gold wire is never in contact with the electrolyte since it is outside of the area defined by the glass tube that contains the electrolyte. The gold wire is kept in place by a set of two O-rings that seal the glass tube (≈ 9 mm Ø). Close to the bottom of the glass tube, there is slight constriction where a metallic clamp fits tightly to hold the parts assembling the cell together.

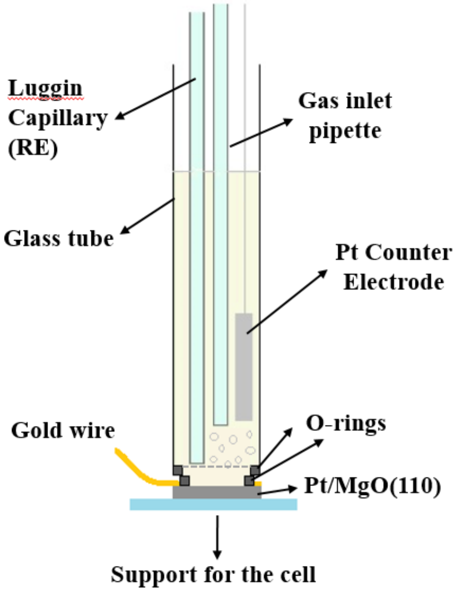

Figure 4-3: Sketch of the electrochemical cell used for the electrochemical of the thin films. Clamp and glass tube constriction omitted for clarity.

Prior to the electrochemical experiments, all the glassware was soaked in acidic permanganate solution overnight, rinsed with diluted piranha solution, rinsed thoroughly with bi-distilled water, then boiled in bi-distilled water several times. Ultrapure water (Milli-Q, resistivity >18 MΩ cm) was the solvent for the electrolytes, regardless of its nature.

The electrochemical measurements were carried out at room temperature (23±1 ◦C) using an Autolab PSTAT302 potentiostat controlled by NOVA 2.1.2 (Ecochemie). For the Pt/MgO(110) experiments, a flamed annealed platinum gauze was used as a counter electrode. For the Au/MgO(100) films, the Au wires (used for electrical contact and as a counter electrode) were chemically cleaned along with the glassware. The reference electrode changed with the electrolyte, and it was either a saturated mercury mercurous sulfate electrode (MMSE) electrode in acidic or neutral media or a mercury mercurous oxide electrode (MMO) in alkaline media. A capillary held the reference electrodes, and its tip was as close as possible to the electrode surface to minimize the ohmic drop. After the experiments, the reference electrode's potential in the working electrolyte was measured versus a homemade reversible hydrogen electrode (RHE). The average conversion factor for the MMSE was $E_{RHE} = E_{MMSE} + 0.705$ V, whereas, for the MMO, it was $E_{RHE} = E_{MMO} + 0.890$ V. Hence, all potentials are reported versus the reversible hydrogen electrode (RHE) scale.

4.5.2 Electrochemical characterization of the Pt/MgO(110) films

The activation of the surface was achieved by a potential scan from a 0.04 V to 1.05 V *vs.* RHE at 100 mV s^{-1} in N_2 saturated 0.5 M H_2SO_4 that was repeated until a steady cyclic voltammogram was recorded.

CO stripping – In order to obtain additional information regarding the surface structure, CO stripping was performed. After the electrode activation, CO purged the electrolyte for approximately 10 minutes while holding the potential at 0.080 V *vs.* RHE to allow the CO to adsorb to the platinum surface. Then, while still holding the potential at 0.080 V *vs.* RHE, Ar purged the electrolyte for 45 minutes to remove the excess of CO in the solution. The stripping voltammogram was recorded at 20 mV/s, from 0.080 to 0.900 V *vs.* RHE. These experiments were also performed on polycrystalline Pt for comparison. A Biologic potentiostat controlled by the ECLab software polarized the electrodes and recorded the CO stripping currents.

Sampled current voltammetry – To assess the ORR on the films, the electrolyte used was 0.05 M H_2SO_4 + 0.1 M $KClO_4$. The addition of the salt aimed to address a technical challenge of the SCV, as it requires high conductivity solutions. The ORR activity reports available in the literature for Pt single crystals in sulfuric acid solutions use 0.05 M H_2SO_4 as electrolyte. Such dilute solutions are used to minimize the strong specific adsorption of the sulfate anions on the Pt surface, which hampers the ORR[51]. However, as described in chapter 3, a consequence of the use of dilute solutions is an increase in R_sC_{dl} feature at the interface of the electrode. Since the aim was to get a response as close as possible from the literature, the sulfuric acid concentration was kept at 0.05 M, and 0.1 M $KClO_4$ was added as a supporting electrolyte to increase the electrolyte ionic conductivity. This choice is justified because the specific adsorption of the perchlorate anions on the Pt surface is very low, in opposition to the sulfate adsorption. $KClO_4$ (99.99% trace metal grade, Sigma-Aldrich) was re-crystallized in ultrapure water before use.

To record the transients used to reconstruct the sampled current voltammograms, the potential was stepped from the rest potential (for example, 1.00 V *vs.* RHE) to the potential window of interest for the ORR, Figure 4-4. The potential steps started from 0.150 V and went up to 1.03 V *vs.* RHE. The transients were first recorded in N_2-saturated electrolyte to generate the background currents, and then in O_2-saturated electrolyte. Then, the transients recorded in N_2 were subtracted from the transients recorded in O_2 to eliminate the background currents. Thus, unless otherwise stated, in the reconstructed voltammograms, only the background-subtracted currents were used. The O_2 flow rate was kept constant at 40 mL min^{-1} using a gas flow controller (GFC17S, Aalborg).

The optimized O_2 flow rate was 40 mL min^{-1} according to previous tests performed at diffusion-controlled potentials.

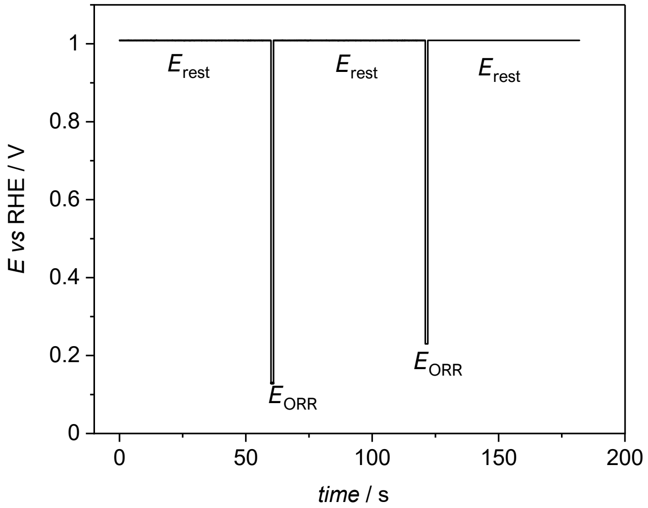

Figure 4-4: Potential waveform used to record the transients for the ORR study on the films.

Aiming to preserve the integrity of the surface, the electrodes were cycled as little as possible. For this reason, the condition cycling voltammograms in between the potential steps were eliminated, and the number of potential steps decreased. Thus, a lower number of potential steps in the diffusion-controlled potential window were applied, and more potential steps were applied in the kinetically controlled potential window to provide a better resolution for the kinetic analysis.

4.5.3 Electrochemical characterization of the Au/MgO(100) films

For the gold films' activation, the electrode potential was scanned at 50 mV/s between 0.5 and 1.7 V *vs.* RHE in N_2 saturated 0.5 M H_2SO_4 until stable voltammograms were obtained. Then, the cell was rinsed several times, first with ultrapure water and then with 1 M KOH solution, and cycled in the alkaline electrolyte until steady CVs were obtained.

Pb UPD - After activation, the electrolyte was replaced for N_2 saturated 0.1 M NaOH and cycled until a steady CV was observed. Afterward, the lead solution was added to have 2 mM Pb^{2+} in the solution, and CVs were recorded. The Pb^{2+} source was $Pb(NO_3)_2$.

Sampled current voltammetry – sample current voltammetry (SCV) measurements were performed to assess the films' electrocatalytic activity for the ORR. To record the current transients, potential pulses were applied to the working electrode, stepping from 1.09 V *vs.* RHE to the potential window of interest for the ORR. The potential window ranged from 0.30 V *vs.* RHE to 1.11 V *vs.* RHE, by steps of 20 mV from 0.30 to 0.80 V, and then by steps of 10 mV up to 1.11 V. The waveform applied was very similar to the one shown in Figure 4-4.

This procedure was first applied in N_2 - saturated 1 M KOH electrolyte to record background currents, and then in O_2 - saturated 1 M KOH electrolyte. Aiming to provide a steady and controlled O_2 flow, a gas flow controller was used.

5 STUDY OF THE OXYGEN ADSORPTION ON THE PLATINUM SURFACE DURING THE REST POTENTIAL

5.1 Introduction

The Pt surfaces' affinity with oxygenated species is a determining factor in their electrocatalytic activity for the oxygen reduction[54-55]. However, the strong bond between the Pt atoms and oxygen impairs the oxygen reduction rate because the adsorbed oxygen and hydroxyl are very stable intermediates at potentials close to the equilibrium potential of the ORR[30]. Hence, the coverage of these oxygenated species at the electrode surface affects the ORR. In this sense, hydrodynamic ORR studies on polycrystalline Pt electrodes revealed that the sweep rate used to record the polarization curves affects the ORR activity. It was found that the polarization curves shift towards more negative potentials responding to variations in the oxygen coverage at the surface[54] induced by the sweep rate.

Likewise, in the SCV experiments, the oxygen coverage on the Pt surface at potentials where the oxygen reduces is expected to affect the reconstructed SCVs. For this reason, learning how the adsorbed oxygen coverage relates to both the rest potential and the electrocatalytic behavior of the surface is fundamental to understand the applicability and the limitations of the SCV. On this matter, the ideal experimental conditions to study the ORR by SCV would be those where the rest potential yields a Pt surface free of adsorbed oxygen to favor the maximum activity of the surface. With this purpose in mind, a set of experiments using a Pt polycrystalline RDE as a working electrode was performed to find the optimal rest potential to study the ORR on the Pt electrodes by SCV. In these experiments, the rest potential value and duration were varied and the effect of these variations on the reconstructed SCVs for the ORR was assessed.

5.2 The role of the rest potential

Considering the SCV method, the rest potential by definition is a neutral potential, where the current measured is ideally zero, as, for instance, in open circuit conditions. In SCV, the rest potential adjustment is essential because it determines the electrode surface state before the potential is stepped to the interest potential at the ORR potential window. Accordingly, the surface state conditioned by the rest potential is the same over the entire scanned potential window. The duration of the rest potential is equally crucial because during this period, the active species diffuse from the bulk electrolyte to the electrode surface, replenishing the electrode-electrolyte interface with these species before the next potential pulse. In this sense, the rest potential can be regarded as a pre-concentration step. Thus, preferably, the rest potential should afford a Pt clean surface and be sufficiently long to allow the O_2 diffusion towards the electrode surface.

A good starting point to decide which potentials to test is to analyze the cyclic voltammograms recorded for the Pt RDE in the working electrolyte in the presence and absence of O_2, Figure 5-1. The evaluation reveals the potential window of interest and what could be the possible rest potentials probed.

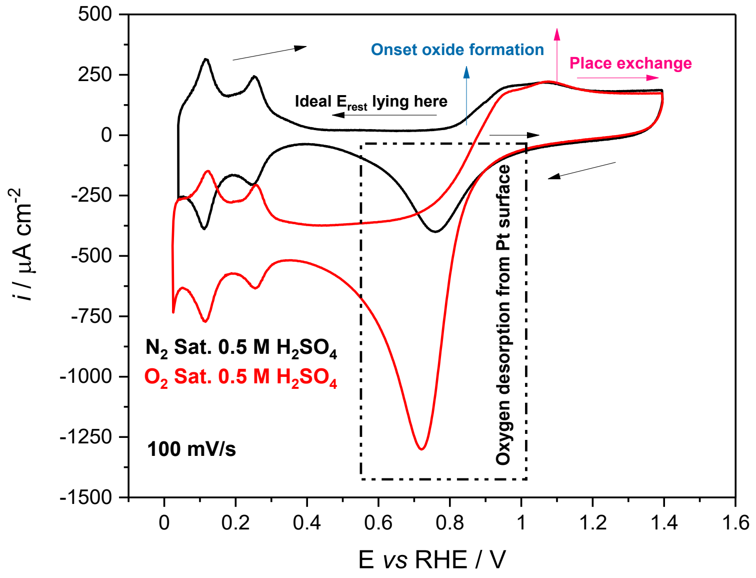

Figure 5-1: Cyclic voltammograms recorded for the Pt RDE in N_2 and O_2 saturated 0.5 M H_2SO_4 at 100 mV/s.

The voltammogram recorded in N_2 saturated electrolyte shows the typical features of platinum in acidic media. First, the hydrogen desorption and adsorption peaks appear between ≈ 0.05 and 0.380 V *vs.* RHE, followed by a short capacitive potential window and the surface oxygen adsorption, which is the initial stage of the oxidation of the Pt surface – starting at ≈ 0.800 V *vs.* RHE. As the potential becomes more positive, the repulsive forces between the oxygen atoms adsorbed in the surface become more significant as the oxygen coverage increases, driving the place exchange process. At this stage, the oxygen adsorbed at the platinum surface replaces the platinum atoms into the crystalline lattice causing dissolution of platinum and roughening of the electrode surface[9]. When the scan is reversed, the layer of oxide formed is stripped as the potential moves towards the cathodic direction, originating the cathodic peak seen at ≈ 0.750 V.

The voltammogram recorded in the O_2 saturated electrolyte shows the same features but shifted to the bottom part of the plot due to the cathodic currents associated with the ORR. The ORR kinetically controlled potential window coincides with the potential window where the oxygen adsorbs on the platinum surface, and both processes occur simultaneously.

5.3 Experimental details

The material used in these experiments and preparation of the Pt electrodes is the same as reported in Chapter 3. Please refer to that chapter for detailed experimental information. The SCV waveform applied in these experiments is the one presented in figurefigiuregureigure 3-3. It consists of the application of a conditioning potential cycling at 500 mV/s, then the rest potential is applied for 60 seconds (or 15 seconds), and the potential will step to the ORR potential for 1 second. Subsequently, the potential will return to the rest potential for 20 seconds.

Considering the features described in the CV, to study the rest potential value and duration, four different potential values were tested: 1.00, 0.952, 0.902, and 0.877 V, for 15 and 60 seconds. The experimental waveform was applied both in N_2 and O_2 saturated 0.5 H_2SO_4 electrolytes.

5.4 Results and discussion

Aiming to understand how the rest potential applied affect the reconstructed sampled current voltammograms, the polarization curves (*i vs. E*) were reconstructed by sampling the transients at different times (see Table 2) and plotting them versus the step potential applied. Such an approach affords information on the electrode's response in different timescales, revealing processes with different kinetics taking place at the surface. First, the results of the experiments performed in N_2 saturated 0.5 M H_2SO_4 are presented and discussed and following, the results in O_2 saturated electrolyte are examined.

5.4.1 Study of SCV applying different rest potentials in N_2 saturated electrolyte

Because the rest potential must be a neutral potential, the open circuit potential (OCP) is the best choice to start with because no current crosses the cell, and the system is free to move towards the equilibrium. Therefore, the measured OCP for the Pt in N_2-saturated 0.5 H_2SO_4 was around 1.002 V *vs* RHE, and this value was the rest potential set in the first set of experiments. The reconstructed voltammograms obtained when the potential rests at 1.002 V for 60 and 15 seconds are exhibited in Figure 5-2a) and b).

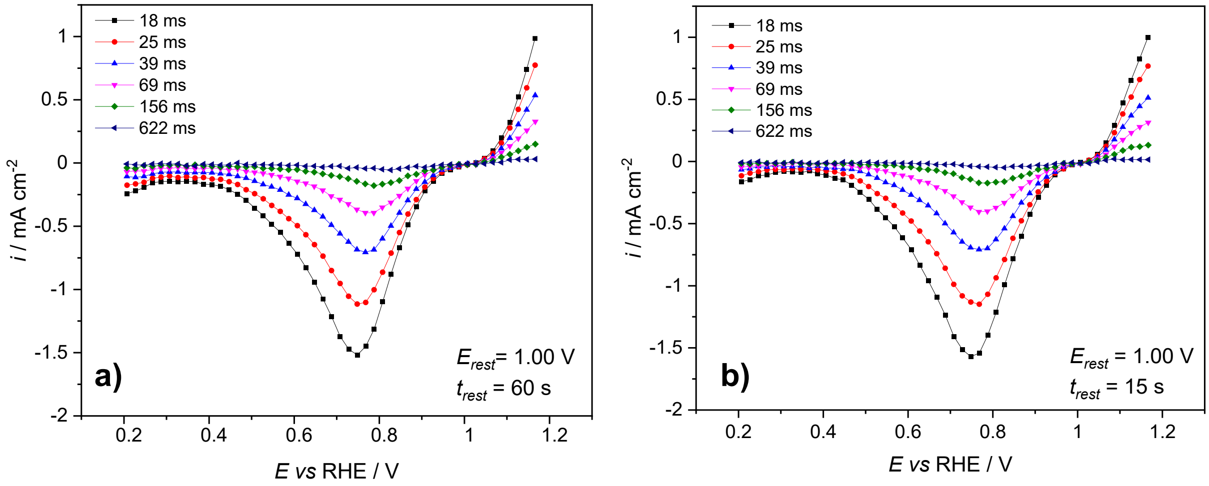

Figure 5-2: Reconstructed SCVs for E_{rest} = 1.002 V, kept for a) 60 s and b) 15 seconds in N_2 saturated 0.5 H_2SO_4. The sampling times used to reconstruct the SCVs appear in the legends.

Similar features can be seen for both rest potential duration set in the experiments. Between 0.200 – 0.400 V, the voltammograms exhibit a zone where the currents are low and coming from the capacitive processes. Then, for potentials between 0.450 and 1.00 V, a broad wave appears with a maximum at 0.750 V, and the current densities associated to this wave decrease with the sampling time. The reconstructed SCVs resemble the backward scan of the Pt RDE voltammogram in N_2-saturated electrolyte shown in Figure 5-1. The backward scan shows the surface's evolution from an oxidized to a reduced state, arising from the oxygen desorption from the surface originating the peak seen at ≈ 0.750 V.

The plots obtained for both rest potential duration show a similar trend, and they indicate that oxygen adsorbs to the surface regardless of the duration of the rest potential when 1.002 V is applied. Therefore, the peak observed in the reconstructed SCVs come from the desorption of oxygen that adsorbed onto the electrode surface during the rest potential. The oxygen coverage (θ_O, expressed by the measured cathodic currents), decreases with the sampling time highlighting the fast kinetics of the desorption process on the platinum surface. Figure 5-3 shows the superimposed SCVs for the rest potential duration by sampling at 18 and 69 ms. The plots confirm the identical response, regardless of the sampling time, demonstrating that the duration of this rest potential does not affect the oxygen surface coverage in the absence of O_2.

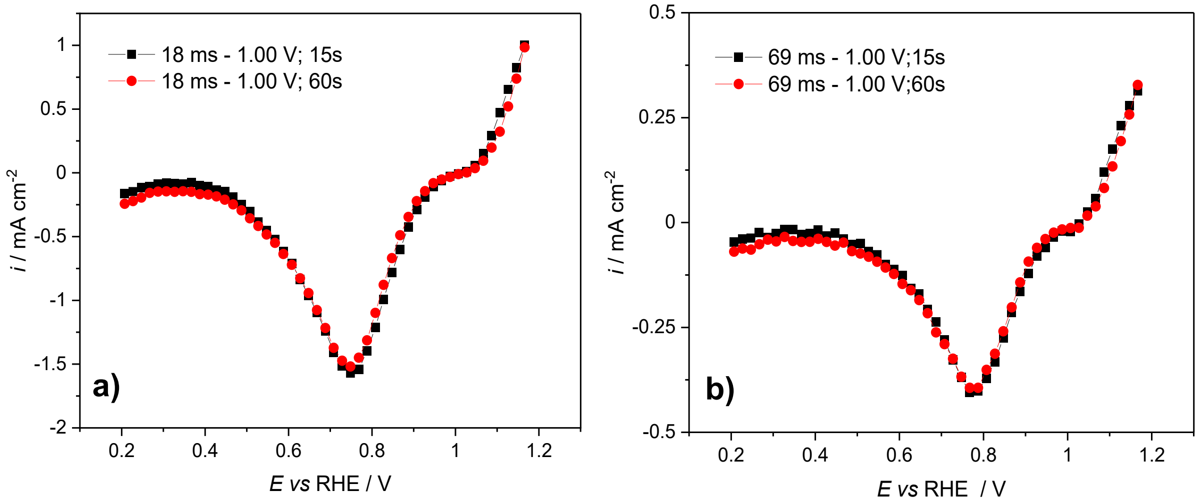

Figure 5-3: Superimposed reconstructed SCVs for E_{rest} = 1.002 for 15 s and 60 seconds in N_2 saturated 0.5 H_2SO_4 for a) 18 ms and b) 69 ms.

Similar plots obtained for the remaining rest potentials tested can be found in Appendix I. Plots of the reconstructed SCVs for all the rest potentials tested sampled at a fixed sampling time (69 ms) are shown in Figure 5-4 a) and b), as a summary of the results. In Appendix I, the plots for currents sampled at 18 ms are also shown. For all rest potentials tested, oxygen adsorbed to the electrode surface, and its desorption was seen in the reconstructed SCVs. However, the currents associated with the oxygen desorption decreased as the potential was made negative. In all cases, the duration of the rest potential did not affect the oxygen coverage at the electrode surface.

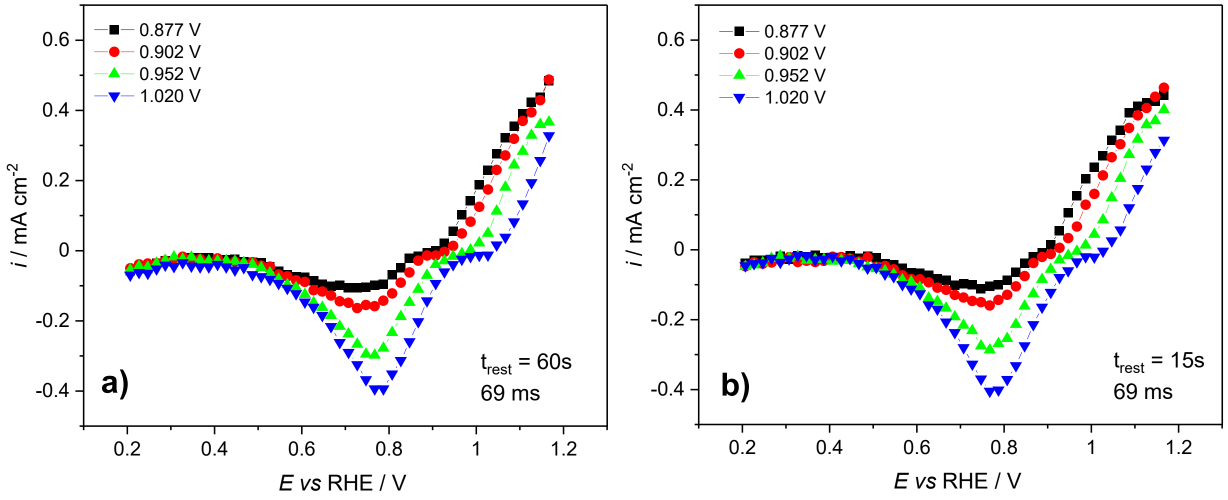

Figure 5-4: Reconstructed SCVs for the rest potentials studied at 69 ms for rest potential applied for 60 seconds in a) and in b) for 15 seconds.

The integration of the transients recorded for each potential step applied yields the charge associated with the surface processes taking place at that potential and plot it as a function of the potential to produce a chronocoulogram, Figure 5-5 a). The plot shows the results obtained for 60 seconds set as the rest potential duration when 15 seconds were set as rest potential duration, the plot is equivalent, and it can be found in Appendix I.

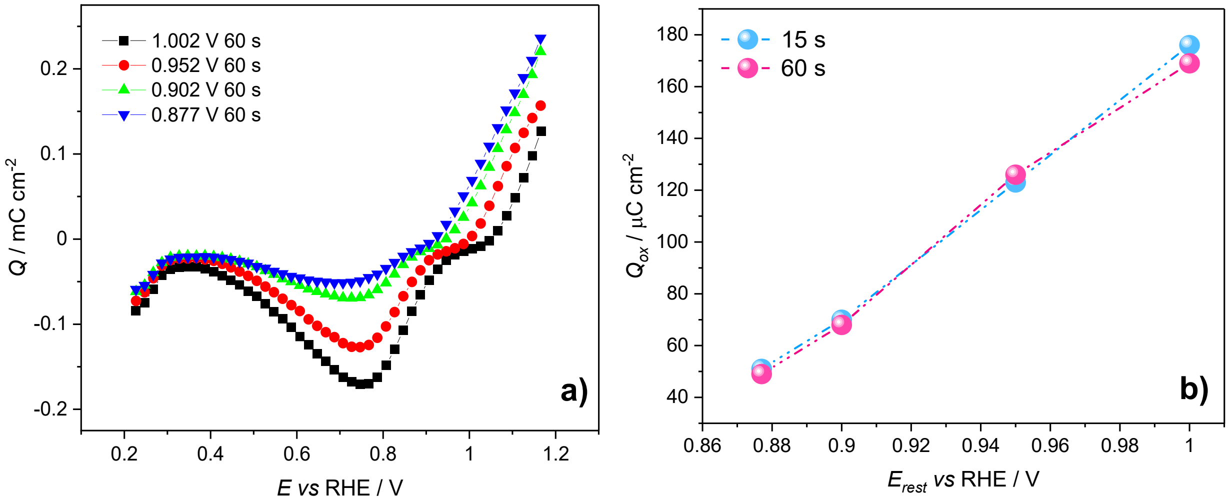

Figure 5-5: a) plots of the charges obtained as a function of the potential for the rest potentials studied applied for 60 seconds, and b) plots of the charge measured at ≈ 0.750 V *vs* the rest potential.

The charge plots replicate those shown for the current densities displaying cathodic peak charges that decrease as the rest potential applied decreases, emphasizing that the charges recorded are unaffected by the rest potential duration. A plot of the charge measured at ≈ 0.750 V plotted versus the rest potential, Figure 5-5b), demonstrates that the oxygen coverage at the surface decreases linearly with the rest potential. Assuming that oxygen is chemisorbed onto the Pt surface to form one atomic monolayer before the O_2 evolution, the charge associated with the formation or reduction of this oxide layer[271] is accepted to be 420 μC cm^{-2}. Using this value as a reference, the electrode oxygen coverage can be estimated, Figure 5-6. The plot shows that the fraction of the surface covered by oxygen varies from ≈ 0.1 to 0.4 for the range of rest potentials studied.

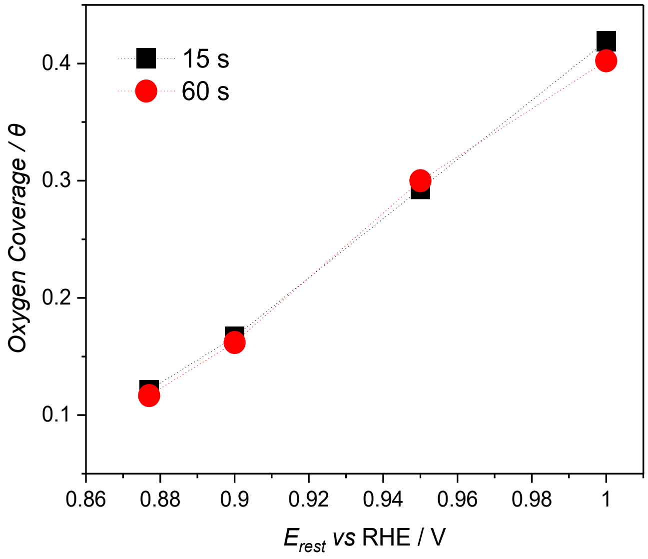

Figure 5-6: a) plot of the oxygen coverage as a function of the rest potential for rest potentials applied for 15 and 60 seconds.

Within the range of rest potentials probed, it was impossible to find a potential value where the surface was not at least partially covered by oxygen. Even so, if the aim is to minimize the oxygen coverage at the electrode surface, the rest potential should be more negative than the OCP. In this regard, the lowest oxygen coverage was found when the rest potential was set to ≈ 0.87 V. Considering the rest potential duration, both 60 and 15 seconds yielded the same coverage.

Since these experiments were performed in absence of O_2, the origin of the oxygenated species must come from the electrolyte. In this respect, Wroblowa et al.[272] studied the oxygen adsorption on platinum surfaces in aqueous sulfuric solutions and demonstrated that the oxygen adsorbed comes from the discharge of the water at the surface, which is controlled by the potential, according to the following reaction:

$$H_2O \rightleftarrows O_{ads} + 2H^+ + 2e^- \quad (36)$$

Jerkiewicz et al. [55] studied the adsorption of atomic oxygen to the Pt surface using a combination of electrochemical, analytical, and spectroscopy techniques. They reported the chemical adsorption of the atomic oxygen at potentials ranging from 0.850 V and 1.10 V *vs.* RHE and that the actual PtO oxide formation takes place between 1.20 and 1.40 V *vs.* RHE. Therefore, according to the findings reported in the literature, atomic oxygen is the species adsorbing on the Pt surface during the rest potential, and it is stripped as the potential steps to a potential negative enough to drive the reduction.

5.4.2 Study of SCV applying different rest potentials in O_2 saturated electrolyte

Once the rest potential was first studied in the absence of O_2, it is necessary to understand the effect of the rest potential on the reconstructed SCVs for the ORR. For this reason, the same experiments presented in the previous section were performed in the presence of O_2. Figure 5-7 shows the reconstructed SCVs obtained after setting 1.002 V as rest potential for a) 60 seconds and b)15 seconds.

The background-subtracted polarization curves shown for 60 seconds show the expected sigmoidal curve, with overlapping currents at the kinetically controlled potential window, and a defined plateau for the limiting current appears for all the sampling times. However, the polarization curves obtained after 15 seconds of rest potential show distortion in the kinetic currents – 0.800 – 0.980 V – that decreases as the sampling time increases. Since the amount of oxygen adsorbed in both cases in the absence of O_2 is the same, this distortion does not come from the background currents. Additionally, the presence of O_2 does not increase the oxygen adsorption on the Pt surface[272-273].

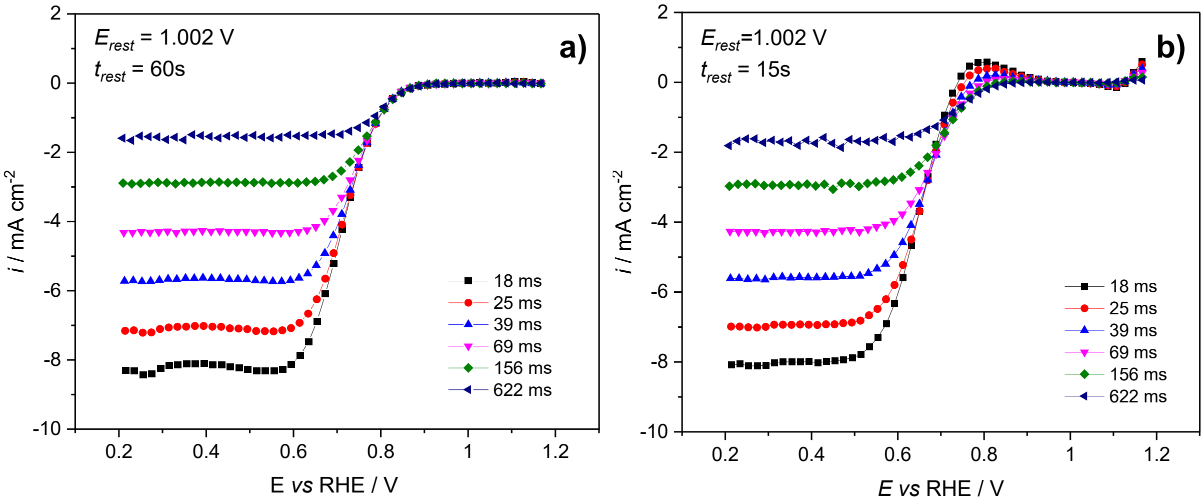

Figure 5-7: Background subtracted reconstructed SCVs for E_{rest} = 1.002 V held for a) 60 s and b) 15 seconds in O_2 sat. 0.5 H_2SO_4.

This effect demonstrates the pre-concentration function played by the rest potential, where it gives sufficient time for O_2 to diffuse from the bulk to the electrode surface, reestablishing the diffusion layer. In cases where the rest potential duration is enough to replenish the O_2 at the electrode surroundings, after the rest potential the O_2 concentration at the electrode surface should equalize the O_2 bulk concentration. Nevertheless, if the rest time is short, the concentration of O_2 at the electrode will be lower, originating a lower current for the ORR. This is the case for the 15 seconds rest potential, where the currents measured for the ORR in the transients were significantly lower than those obtained for 60 seconds. These transients can be found in Appendix II. This scenario was observed for all the rest potentials tested whenever the rest potential was 15 seconds.

Plotting the reconstructed SCVs for the same sampling time yields an overview of the effect of the rest potential on the ORR polarization curves, Figure 5-8. The plots show the total (curves in a) and c)) and background subtracted (curves b) and d)) curves for a fixed sampled time (69 ms) reconstructed after all rest potentials tested for 60 and 15 seconds. The plots show that the ORR reconstructed SCV polarization curves change with the rest potential set and its duration. This is somehow expected since the rest potential will control the surface state before the ORR, and it may also affect the initial O_2 surface concentration in the presence of O_2, disturbing the ORR currents measured.

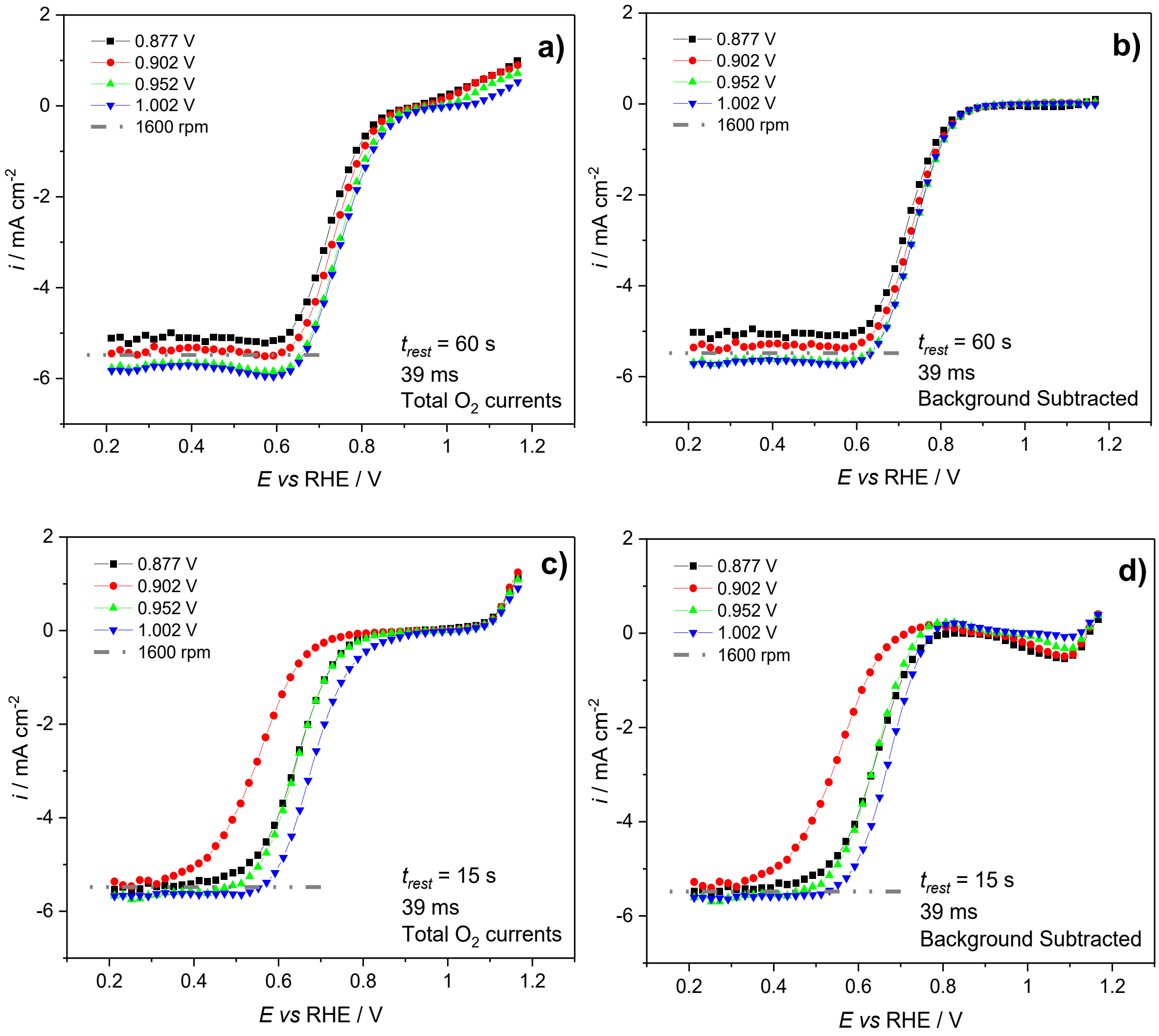

Figure 5-8: Reconstructed SCVs sampled at 39 ms for all the rest potentials tested. In a) total ORR currents for 60 s duration, b) background-subtracted currents for 60 s duration, c) shows the total currents for 15 s and, d) the background-subtracted currents for 15 s.

When the rest potential was applied for 60 seconds – Figures 5-8 a) and b) – the curves shift towards more negative potentials, and the limiting currents decrease as the rest potential decreases. The background subtraction attenuates the difference, but a small shift in the curves and the difference in the limiting currents remain. When the rest potentials are more negative than 1.002 V, O_2 is reduced during the rest potential, causing perturbation in the O_2 concentration, responsible for the observed deviation in the polarization curves. In opposition, when 1.002 V is set as rest potential, the O_2 consumption during the rest potential is negligible.

The results obtained in the previous section indicated that to keep the surface oxygen coverage as low as possible, the rest potential should be lower than the OCP, and the more negative rest potential tested (0.877 V) provided the lowest oxygen coverage. However, the results obtained in the presence of O_2 revealed that rest potentials more negative than the OCP affect the reconstructed SCVs negatively, shifting the curves to more negative potentials. Therefore, the rest potential cannot be lower than the OCP under the penalty of disturbing the initial O_2 concentration. Consequently, a compromise between both conditions must be reached, and based on the experimental results, the OCP must be used as rest potential. This recommendation comes from the fact that perturbations in the O_2 concentration are more detrimental to the ORR activity than the oxygen adsorption on the surface. In this case, the surface activity for the ORR will be the one of a slightly oxidized Pt surface.

5.5 Conclusions

The SCV experiments performed both in N_2 and O_2 electrolytes clarified aspects associated with the processes taking place at the platinum surface in the absence and presence of O_2. The comprehension of these processes is essential to set suitable experimental conditions to record the transients preventing perturbation in the reconstructed polarization curves.

Despite being recorded in the absence of O_2, the reconstructed SCVs recorded in N_2 showed cathodic currents that varied according to the rest potential and the sampling time. Such currents' emergence relates to the stripping of a layer of oxygen adsorbed to the platinum surface during the rest potential, and the extension in which oxygen adsorbs at the surface depends on the potential set as rest potential. These studies also indicate that the range of rest potential duration tested, its duration does not affect the oxygen coverage at the surface. This happens because the oxygen adsorption at the platinum surface is a fast process, and therefore the surface achieves the saturation driven by the potential applied rapidly. Considering the rest potentials tested, the highest oxygen coverage was found for 1.002 V, and it decreased linearly with the rest potential applied. The fraction of the surface covered with oxygen varied from 0.1 to 0.4.

The reconstructed SCV resulting from the transients recorded in O_2 saturated electrolyte showed that the ORR activity – reflected in the polarization curves – changes with the rest potential set and its duration. The principal reason is the change in the surface O_2 concentration observed for cases where the rest potential was negative enough to reduce $O_{2,}$ or the rest potential was too short to allow the O_2 replenishment at the electrode surface. In this sense, rest potentials that would afford a Pt surface with lower oxygen coverage cannot be set as rest potentials because the perturbation in the O_2 concentration is more detrimental to the reconstructed SCV polarization curves than the oxidation of the surface.

Hence, the results demonstrated that the choice of the rest potential and its duration is of utmost importance in the reliability and the quality of the data recorded. The rest potential must not consume the active species and be long enough to permit the concentration of O_2 at the surface to re-establish before the potential step is applied. The ideal duration can be adjusted by setting the potential step as diffusion-controlled potential and varying the rest potential duration. Comparing the magnitude of the current transients measured experimentally with a Cottrellian simulated transient informs the appropriate duration for the rest potential. A compromise must but be achieved since it is necessary to ensure a long enough duration for the rest but without extending it beyond necessary to cause a large increase in the duration of the experiments.

Thus, due to intrinsic electrochemical characteristics of the Pt in sulfuric acid (which is also extended to alkaline conditions[57]), it is not possible to find an ideal rest potential to study the ORR. This comes from the fact that at potentials negative enough to keep the Pt surface free from oxygen adsorbed, the consumption of O_2 during the rest potential harms the electrocatalytic study by depleting O_2 at the electrode surface. In this sense, the open circuit potential (1.002 V) is the most suitable potential, but under such conditions, the ORR activity observed in the SCV corresponds to the oxidized Pt surface, as demonstrated in chapter 3.

If the adsorption of species in the same potential window of the ORR is not a problem, it is easier to set the rest potential. This is shown later in the study of the ORR on Au(100) electrodes.

6 SCV APPLIED TO THE ORR ON Pt/MgO(110) FILM

6.1 Introduction

This chapter reports the deposition and characterization of the Pt/MgO(110) epitaxially oriented thin films. These films were grown to serve as a model surface to study the ORR by SCV. The (110) facet of platinum was chosen as a model because it is the most active facet for the ORR in acid electrolyte[22, 24].

Due to the ORR's sensitivity to the electrolyte concentration, the spectator species in the electrolyte, and the crystallographic orientation of the catalyst surface, the technique used to assess the ORR on a determined electrocatalyst must be able to reflect the difference in the activity. For this reason, a set of experiments probing the sensitivity of the SCV to show changes in activity were designed and performed.

6.2 Deposition of the Pt/MgO(110) films

The films were deposited by PLD, and the general characteristics of the laser setup and the deposition parameters were reported in section 4.2. Briefly, clean MgO(110) single-crystals were used as substrates, the substrate cleaning procedure is reported in the experimental section. A very thin layer (≈ 1 monolayer) of nickel was deposited between the MgO substrate and the Pt layer. For this purpose, 2000 laser pulses hit a nickel foil attached to the Pt target, and the substrate temperature was 400 °C. The Pt layer was deposited by applying 40 000 pulses to the Pt target.

6.3 Results

6.3.1 XRD characterization of the Pt/MgO(110) thin film

The diffractogram of the Pt/MgO(110) film resembles the diffraction pattern of the MgO(110) substrate, Figure 6-1. The high crystallinity of the substrate originates very intense diffraction peaks, which dominate the diffractogram, and, therefore, to distinguish all peaks, the *y*-axis is plotted on a *log* scale. Additional diffraction peaks seen in the diffractogram are attributed to the Kβ diffraction of the main diffraction peak of the MgO substrate ($2\theta \approx 55.7°$) and, to tungsten contamination ($2\theta \approx 59.49°$) coming from the X-rays source.

Regarding the Pt crystalline phase, only the (220) diffraction peak appears in the diffractogram, which means that in the out-of-plane direction – perpendicular to the substrate surface – the film grew only in the [110] direction replicating the crystallographic orientation of the MgO(110) substrate. Therefore, the epitaxial growth was successfully achieved.

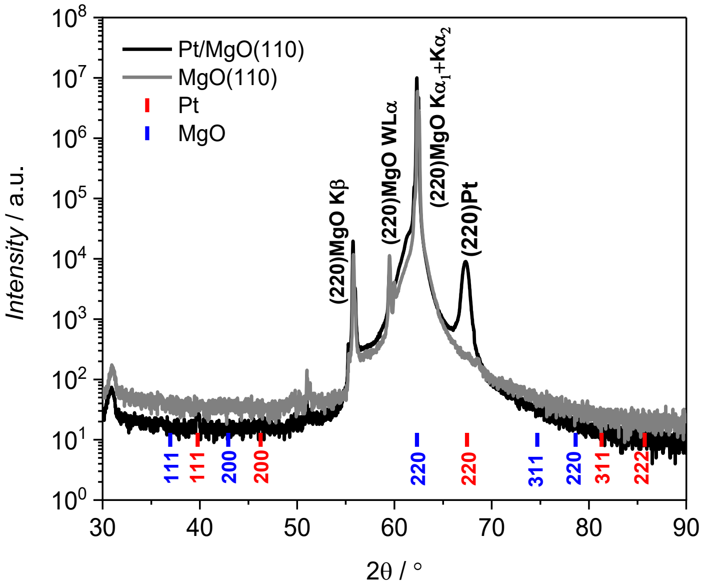

Figure 6-1: XRD pattern of the Pt/MgO(110) thin film deposited at 400 °C recorded in θ - 2θ configuration mode. The bars added to the figure mark the angular position of the Pt peaks (JCPDS card 00-004-0802) and the MgO (JCPDS card 00-045-0946) for guidance.

Platinum crystallizes with a face-centered cubic (*fcc)* structure, and the expected lattice parameter is 3.9231 Å (JCPDS card 00-004-0802). The expected 2θ position of the (220) diffraction peak is 2θ = 67.456 °, and the interplanar distance is 1.3873 Å. The experimental position of the Pt(220) diffraction peak is ≈ 67.316 °, which is shifted to lower 2θ values relative to the reference value. Consequently, the lattice parameter of the thin film (a = 3.934 Å) is higher than the value reported for bulk Pt. Considering the difference between the (220) interplanar distance of bulk platinum, 1.3873 Å, and the experimentally determined for the film, 1.3910 Å, the thin film is under tensile strain (0.266%) in the out-of-plane direction. In this regard, the fact that the lattice parameter of the MgO substrate (4.2112 Å) is larger than that of Pt's may play a role in the film's structural arrangement. However, there is a Ni buffer layer between the MgO substrate and the Pt layer, which may also contribute to the organization of the film while growing, since the interface is modified. Sacré et al.[150], reported a smaller out-of-plane lattice parameter for Pt/MgO(100) thin films by PLD, and the authors attributed this effect to the elastic deformation originated from in-plane compressive epitaxial stress induced by the Ni buffer layer. The lattice parameter of Ni is smaller than that of Pt (3.5238 Å, PDF card 01-087-0712).

6.3.2 Electrochemical characterization of Pt/MgO(110) thin films

The voltammetric response of Pt is very sensitive to the crystallographic orientation of its surface, and for this reason, each crystallographic orientation displays different features in the voltammograms[59-60]. The electrochemical behavior of each platinum facet is available in a range of electrolytes, and they serve as a fingerprint of that facet in similar conditions. Hence, the film's electrochemical characterization was performed by probing the surface with cyclic voltammetry using two different adsorption reactions: the hydrogen underpotential deposition (H_{UPD}) and the CO desorption.

The hydrogen adsorption energy on the Pt surface differs for each crystallographic facet and extension of domains, and it shows a distinct voltammetric profile for each of the basal planes. For this reason, the H_{UPD} is known as the fingerprint of clean platinum electrodes[12, 60, 112]. The fact that the adsorption and desorption of the hydrogen at the surface takes place by the exchange of one electron per Pt atom allows the determination of the electrochemically active surface (EASA) area by estimating the charge transferred in the process. The EASA is the surface area available for the reaction and due to the roughness of the surfaces, the EASA differs from the geometric surface[271]. For Pt electrodes, the H_{UPD} is the most used method to determine the EASA of the electrodes, and the charge exchanged in the process per surface unit (cm^2) varies with the crystallographic orientation of the substrate[13, 58-60]. The calculated values are 240, 208 and 147 $\mu C\ cm^{-2}$, for the Pt(111), Pt(100) and Pt(110), respectively[13, 60, 112].

As described in chapter 4, section 4.5.1, the first step in the electrodes' electrochemical characterization is the potential cycling applied to activate and prepare the surface for the characterization. This procedure yielded surfaces with reproducible behavior provided the upper potential limit is lower than the oxygen adsorption at the surface. When the voltammogram was steady the film surface was assumed to be activated. The cyclic voltammogram recorded for the Pt/MgO(110) electrode after its activation is shown in Figure 6-2. For comparison, the voltammogram recorded for the polycrystalline Pt foil in similar conditions is also shown. The potential region of interest is between 0.0 and 0.5 V, and it corresponds to the H_{UPD} region. The voltammetric profile of the Pt/MgO(110) film shows a sharp and reversible pair of peaks at around 0.140 V corresponding to the hydrogen adsorption and desorption reaction at the (110)-symmetry sites[58-60]. Instead, the polycrystalline electrode shows several peaks in this potential window due to the presence of the (100), (110), and (111) facets exposed at the surface of the electrode.

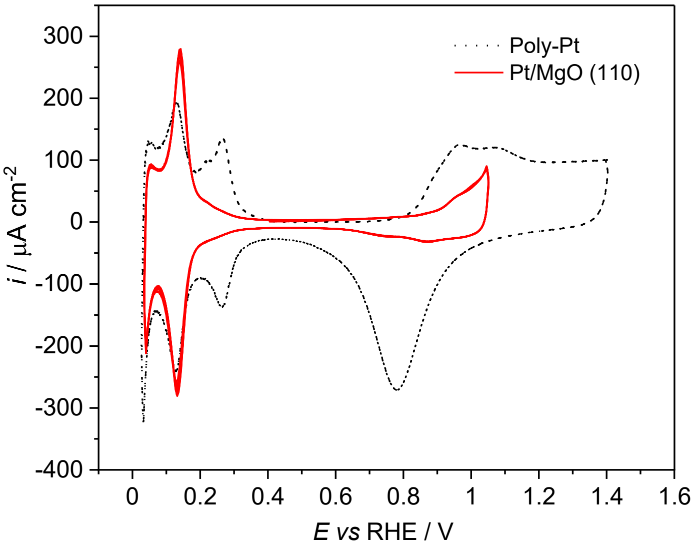

Figure 6-2: Cyclic voltammogram recorded in N_2 saturated 0.5 M H_2SO_4 at 100 mV s^{-1} for the Pt/MgO(110) thin film and a poly-Pt recorded in similar conditions.

The presence of only one pair of peaks coming from the hydrogen adsorption and desorption at approximately 0.140 V *vs.* RHE observed for the Pt/MgO(110) film is similar to the features reported for the Pt(110) – (1 × 2) reconstructed single-crystal surfaces[61, 274-275], also known as "missing row" structure[62]. When working with single-crystals, the cooling atmosphere used after the flame annealing treatment may yield either a Pt(110) – (1 × 1) unreconstructed surface or a Pt(110) – (1 × 2) surface. The first is obtained when after the annealing, the single-crystal electrode is cooled under a mixture of N_2 + CO atmosphere, and the latter, under only N_2 atmosphere[61].

The integration of the adsorption peak – between 0.075 V and 0.400 V – yielded a charge of ≈ 185.75 μC cm^{-2}, similar to the ≈ 180 μC cm^{-2} previously reported for a Pt(110) single crystal electrode[23]. The other features observed in the voltammogram come from the double-layer charge/discharge potential window, followed by the onset of the oxygen adsorption on the surface for $E > 0.80$ V preceding the oxide formation. Therefore, the Pt/MgO(110) film voltammetric response is similar to the described in the literature for Pt(110) single-crystal electrodes consisting of substantial evidence that at the surface of the films, only the Pt(110) facets are exposed.

Similar to the H_{UPD}, the CO stripping voltammograms also show different profiles according to the presence of Pt sites with different symmetry. The CO stripping curves for both polycrystalline Pt and Pt/MgO(110) thin film are presented in Figure 6-3.

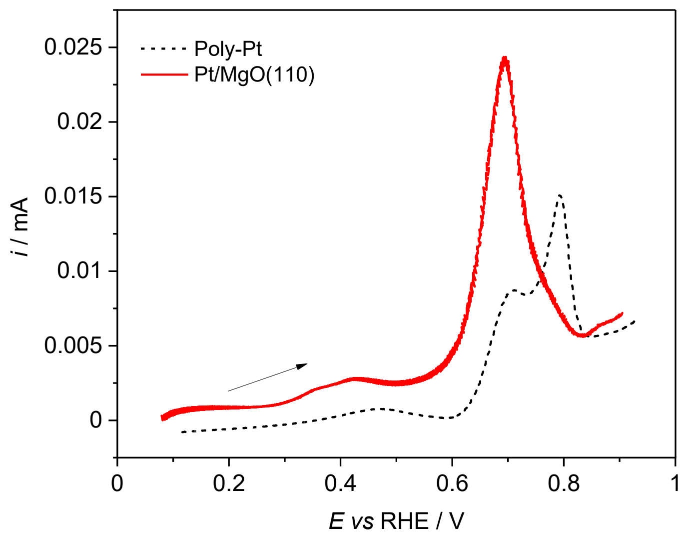

Figure 6-3: CO stripping voltammograms recorded at 20 mV s^{-1} for both the Pt/MgO(110) thin film and polycrystalline Pt in 0.5 M H_2SO_4.

The polycrystalline Pt's stripping profile shows a small pre-oxidation wave at 0.470 V and two major oxidation peaks with maxima at 0.708 and 0.792 V. This behavior is expected for polycrystalline Pt since there are multiple active sites with different symmetry that displays different CO adsorption strength[62, 112, 276]. For the Pt/MgO(110) electrode, the small pre-oxidation wave is still observed, but followed by only one prominent oxidation peak observed at 0.694 V. The CO oxidation profile obtained for the film is similar to those reported previously for Pt(110) single crystal electrodes[61-62]. The pre-oxidation wave comes from the oxidation of CO adsorbed on defects at the surface, and the prominent peak is associated with the CO adsorption at the (110) surface sites

6.3.3 Validation of the electrochemical cell and the waveform used for the films

Due to the insulating nature of the MgO substrate, working with the thin films required modification in the experimental procedure. The modifications comprise a specific electrochemical cell, specially designed for the films – described in chapter 4, the elimination of the conditioning voltammetry cycles before each potential step, and the electrolyte concentration. In the validation procedure reported in chapter 3, the waveform used in the experiments was proposed by Perry et al.[32, 50], the electrochemical cell used for the RDE, and the electrolyte was 0.5 M H_2SO_4.

Therefore, it was necessary to verify that identical SCV results could be obtained using the classical RDE electrochemical cell and the cell designed for the films. For this purpose, first, a polycrystalline Pt foil was used as a working electrode. Two different waveforms were applied to study the ORR on the Pt foil electrode: the one proposed by Perry et al.[32, 260] illustrated in Figure 3-3 and used in the SCV *vs.* RDE validation, and a simplified waveform similar to the one used by Lebedeva et al.[261], showed in Figure 4-4.

In this modified waveform, there are no potential cycles to condition the surface, and it comprises only the potential steps used to record the transients. Although the former waveform works very well for bulk Pt electrodes, it was observed that the consecutive cycling between steps introduced defects and caused roughening on the surface of the Pt(110) thin film during the experiments, Figure 6-4. In the figure, the curve in red shows the voltammetric features after cycling, with an overall increase of the current density and the appearance of a shoulder in the 0.200 – 0.300 V potential window, where hydrogen adsorbs. The increase in current indicates an increase in the area of the electrode caused by roughening of the surface, the rise of the shoulder suggests that hydrogen is adsorbing in sites with other symmetry than the (110).The shoulder currents likely comes from hydrogen adsorption on (100) domains[13, 60, 112] that emerged as defects due to the potential cycling.

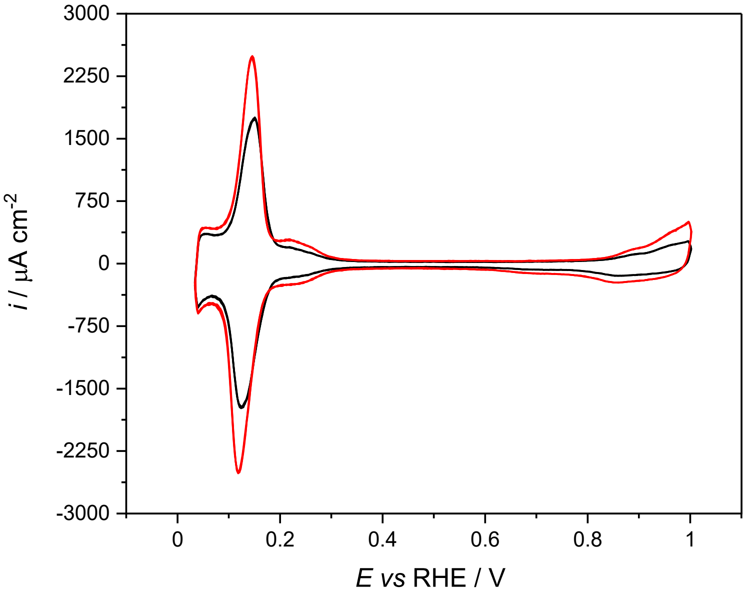

Figure 6-4: Cyclic voltammograms for the Pt/MgO(110) film at 500 mV/s in N_2-sat. 0.5 M H_2SO_4 before (solid black lines) and after (solid red lines) the application of the waveform shown in figure 3-3 recorded before the ORR. The number of cycles applied between both CVs was circa 288.

Aiming to learn how the new waveform and the cell setup affect the reconstructed SCVs, the current was sampled at 39 ms, and the voltammograms plotted together, Figure 6-5a).

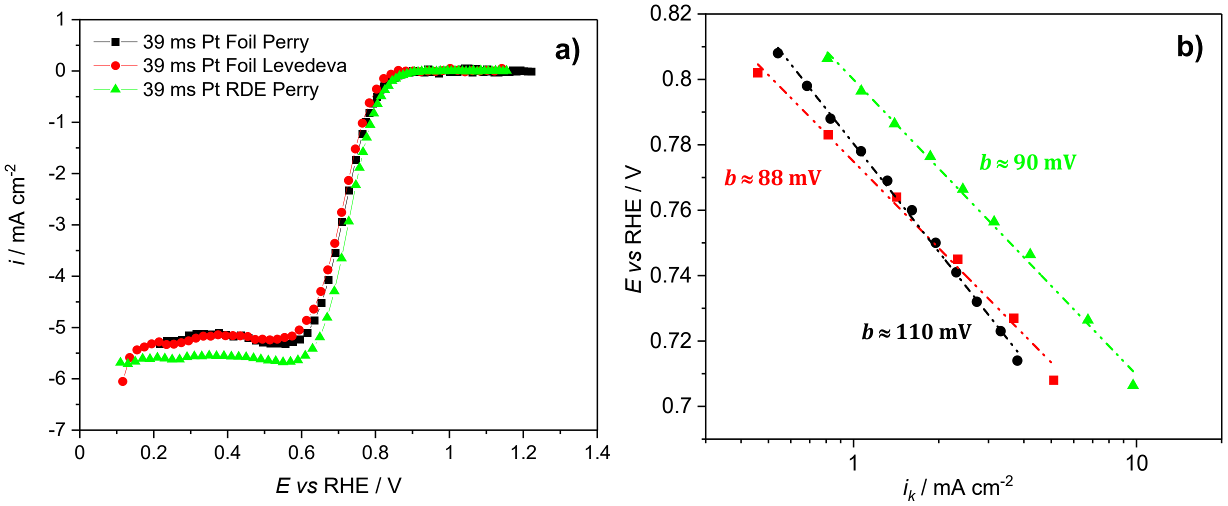

Figure 6-5: a) reconstructed SCVs for Pt polycrystalline electrodes in O_2-sat. 0.5 H_2SO_4 and b) Tafel plots obtained from K-L plots for curves in a).

The figure shows the background-subtracted polarization curves obtained using the waveform proposed by Perry et al. [32, 260] (solid black spheres), Lebedeva's simpler waveform (solid red squares), and the RDE in the classical cell (green triangles). The three reconstructed SCVs show polarization curves that superimpose to each other for most of the potential window. In the special electrochemical cell, the two waveforms give equivalent results. Furthermore, the reconstructed SCVs obtained for the Pt foil in the films' cell are similar to those obtained for the SCV in the Pt RDE used to validate the SCV protocol.

Figure 6-5b) shows the Tafel plots obtained using the kinetic currents extracted from transient Koutecky-Levich plots (1/*i* *vs.* $t^{1/2}$), as described in chapter 3. Tafel plots ranging from 88 – 110 mV were obtained for the ORR on the Pt foil. These differences in the Tafel slope values are associated with the differences in the degree of oxidation of the Pt surface experienced in each case yielded by the waveform applied to record the transients. When applying the rest potential at the OCP (Perry's protocol), the Pt surface is oxidized by the oxygen adsorbed during the rest potentials, which causes the slope to deviate from the 120 mV expected for a clean Pt surface. Tafel slopes lower than 120 mV are attributed to oxidized Pt surfaces[54, 163, 265-266].

Once the results demonstrated that neither the electrochemical cell nor the waveform causes significant changes in the response of the SCV towards the ORR, the effect of the electrolyte concentration was probed. Sulfate ions hinder the ORR due to the specific adsorption of the anions on the platinum surface[51, 212], and decreasing the concentration of the sulfuric acid shifts the polarization curves towards more positive potentials. These experiments aimed to assess if the

SCV could probe differences in the ORR activity of the platinum electrodes with the sulfate concentration.

For this purpose, another set of experiments using the cell designed for the films and the waveform shown in Figure 4-4 was conducted using 0.5 M and 0.05 M H_2SO_4, Figure 6-6a). To maintain the electrolyte's conductivity and prevent ohmic distortions on the SCVs, $KClO_4$ 0.1 M was added to the 0.05 M H_2SO_4 solution.

The background-subtracted SCVs obtained with the polycrystalline Pt foil in O_2 saturated 0.5 M H_2SO_4 and 0.05 M H_2SO_4 + 0.1 M $KClO_4$ clearly show that the higher sulfate concentration inhibits the ORR. In the diluted sulfuric acid solution, the wave shifts by circa 40 mV towards more positive potentials, and the ORR starts at more positive potentials, as expected.

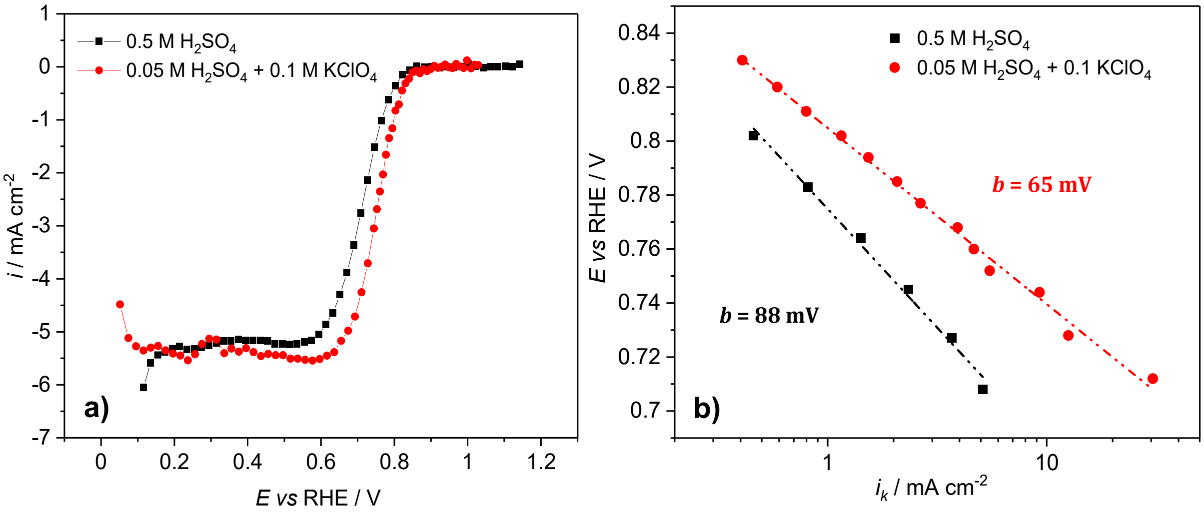

Figure 6-6: a) Reconstructed SCVs sampled at 39 ms in O_2 saturated 0.5 M H_2SO_4 (black squares) and O_2 saturated 0.05 M H_2SO_4 + 0.1 M $KClO_4$ (red circles) for the Pt foil. b) shows the Tafel plots for kinetic currents are taken from Koutecký-Levich plots of the data shown in a).

The Tafel plots, Figure 6-6b), show higher ORR currents and a smaller slope in the diluted electrolyte, reflecting the better performance of the platinum in the 0.05 M H_2SO_4. This is consistent with the specific adsorption of sulfate anions on Pt, which hinders the ORR[51, 212], and it demonstrates that SCV is sufficiently sensitive to reveal the poisoning of the electrode surface.

6.3.4 SCV applied to the study of the ORR on the Pt/MgO(110) thin film

Once the modified experimental procedure was validated, the Pt/MgO(110) thin film was then used as a working electrode, and its SCV response regarding the ORR was assessed, Figure 6-7a). The working electrolyte used in these experiments was O_2 saturated 0.05 M H_2SO_4 + 0.1 M $KClO_4$. Regardless of the sampling time, the reconstructed voltammograms show curves that overlap at the kinetic potential window and part of the mixed-controlled potential window. However, the curves show distinct shapes as the sampling time increases, and at shorter sampling times, a broad peak emerges rather than the expected limiting current plateau. The dashed lines in the figure represent the expected limiting currents for a four-electron exchange, and around 0.600 – 0.700 V, the maximum currents seen in the voltammograms are very close to that value. A Cottrell plot (a plot of the current measured versus the reciprocal of the square root of the sampling time) of currents measured at 0.670 V shows a straight line, indicating that at that potential, the reaction is indeed diffusion-controlled, Figure 6-7b).

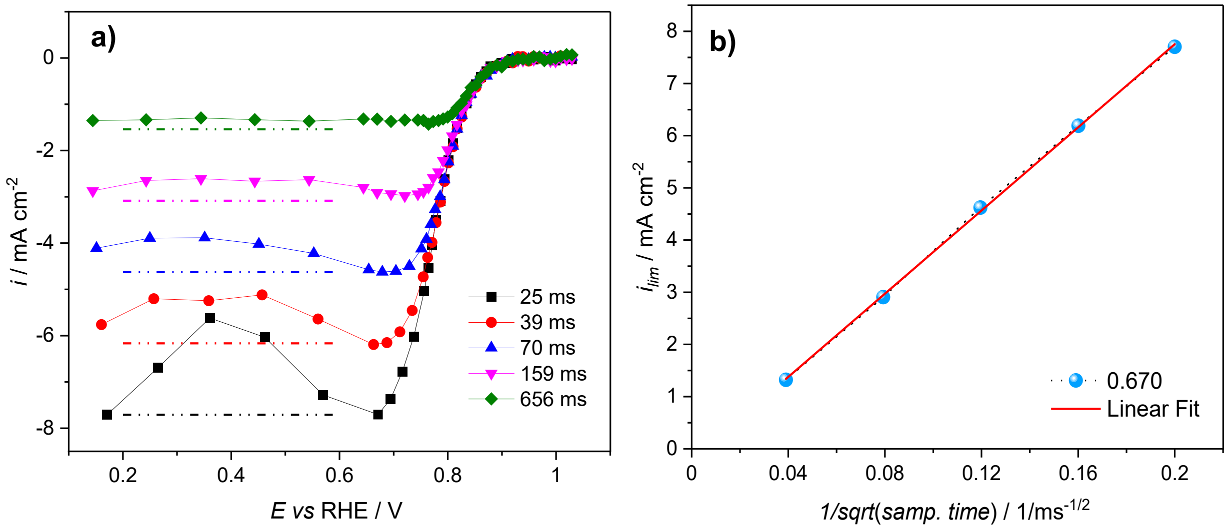

Figure 6-7: a) reconstructed SCVs obtained for the ORR on the Pt/MgO(110) film for various sampling times, b) Cottrell plots for currents measured at 0.670 V.

The anomalous behavior observed for the curves sampled at shorter times likely originates from the delayed decay of the chemisorbed oxygen reduction currents, which are highlighted by the electrolyte's higher resistance. The time constant of the cell is higher for less concentrated electrolytes, and for Pt foil electrode, the time constant of the cell goes from ≈ 0.08 ms in 0.5 M H_2SO_4 to ≈ 2.01 ms in 0.05 M H_2SO_4. The addition of the $KClO_4$ attenuated the issue, and by adding 0.1 M $KClO_4$, the time constant of the cell goes to ≈ 0.45 ms. Due to the low solubility of the salt in the electrolyte, this was the maximum concentration possible. Considering the time constant of the cell (≈ 0.45 ms), at 25 ms the double-layer currents have been discharged entirely. However, the time constant of the cell only accounts for the decay of the double-layer charging currents. Surface processes, as the reduction of the chemisorbed oxygen and the hydrogen adsorption reactions, have their own time-constant and they impact the shortest sampling times because they are not accomplished yet at that timescale. Nonetheless, the distortion affects mostly the shorter sampling times, and the SCVs obtained at longer sampling times are available for the analysis.

Finally, the ORR activity of the Pt/MgO(110) thin film is compared to that of the polycrystalline Pt, Figure 6-8. The figure shows in a) the background-subtracted sampled current voltammograms recorded in O_2 saturated 0.05 M H_2SO_4 + 0.1 M $KClO_4$ for the Pt foil and the Pt/MgO(110) thin film sampled at 39 ms, and in b) the Tafel plots for kinetic currents taken from Koutecký-Levich plots of the data shown in a).

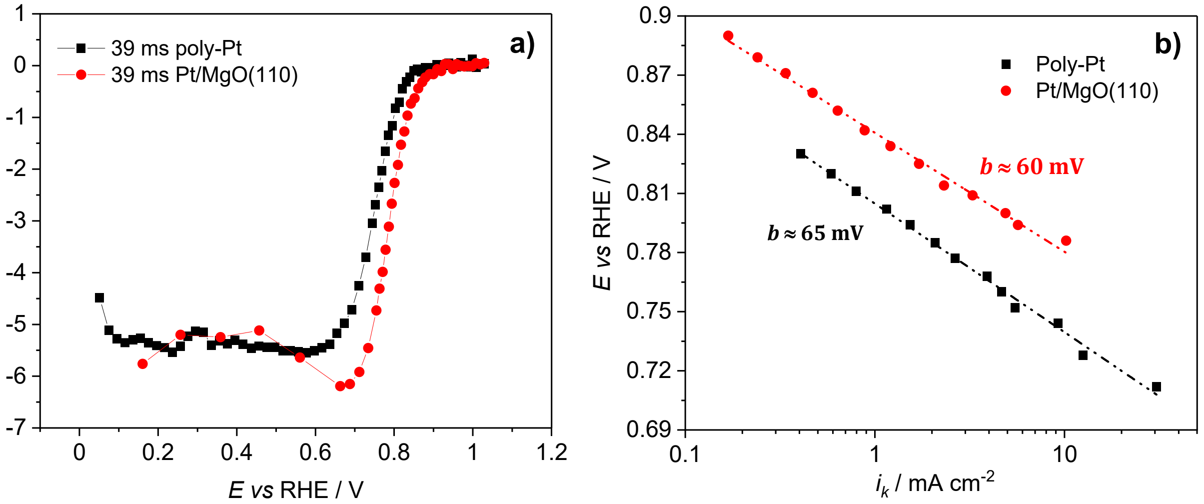

Figure 6-8: a) reconstructed SCVs recorded in O_2 saturated 0.05 M H_2SO_4 + 0.1 M $KClO_4$ for the Pt foil and the Pt/MgO(110) thin film, b) Tafel plots of the data shown in a).

The SCV curve obtained for the oriented thin film has the expected sigmoidal shape, and its half-wave potential is circa 42 mV more positive than that for the polycrystalline Pt foil. The thin film's higher activity is highlighted by the Tafel plots that show a lower slope and greater current densities for the Pt/MgO(110) thin film, Figure 6-8b). The results obtained agree with the literature as the Pt(110) surface is known to be the most active platinum low index crystallographic plane in sulfuric acid solutions[22-23].

When comparing the SCV curves obtained for poly-Pt and Pt/MgO(110) thin film, a wave with the maximum at circa 0.70 V *vs.* RHE is seen in the thin film polarization curve. This excess of charge lies in the potential window where the reduction of the platinum oxide occurs, and both Pt surfaces exhibit different behavior in this potential window. For the polycrystalline Pt, the subtraction of the background currents removes almost all of the contribution of the platinum oxide reduction to the ORR currents, and the plateau for the diffusion-controlled current appears, whereas for the Pt/MgO(110), an excess of charge remains.

6.4 Conclusions

The characterization techniques provided results that support the quality of the epitaxy of the thin film deposited by PLD. XRD structural characterization demonstrated that the film deposited grew exclusively in the [110] direction. The cyclic voltammetry in 0.5 M H_2SO_4 and the CO striping corroborates the XRD results, reinforcing the epitaxy of the Pt thin film on the MgO (110) substrate. Importantly, because the voltammetric techniques probe the surface behavior of the electrodes, this agreement between the XRD and the voltammetry demonstrates that the surface does not re-arrange and reflect the bulk crystallographic orientation.

The results presented demonstrated that the cell setup and the waveform used to record the transients do not significantly affect the SCV response for the ORR. The modified experimental protocol was able to preserve the Pt/MgO(110) surface structure during the experiment and yielded results that correspond to the expected response of the Pt(110) single crystalline surface, as the film is more active towards the ORR than the polycrystalline Pt foil.

Therefore, the study demonstrated that PLD produces well-oriented Pt films grown onto the MgO(110) substrates and the electrochemical characterization proved that such films serve as model surfaces for the ORR study. Additionally, the set of experiments ensured that sampled current voltammetry is sensitive enough to show small changes in catalytic activity arising from different concentrations of supporting electrolytes, specific adsorption of ions, and crystallographic orientation of the substrate.

7 DEPOSITION OF Au/MgO(100) THIN FILMS

7.1 Introduction

It has been proposed in the literature that the ORR mechanism in alkaline media differs from the mechanism in acidic media[35, 167], and researchers suggest that in alkaline media, some of the reaction steps take place as an outer-sphere electron transfer process[34-35, 277-278]. In such a case, the active species do not interact strongly with the electrode material surface, and the electron transfer occurs across the solvent layer surrounding the active species by tunneling[269]. Thus, the outer-sphere steps occur at approximately the same rate in most of the electrocatalysts[35, 279]. This mechanistic aspect, combined with the fact that there is a broader range of materials stable enough to be used as electrocatalysts in alkaline media, introduces flexibility in choosing electrode materials to catalyze the ORR[100, 167].

In this sense, a better understanding of the ORR mechanism and the factors affecting the electrocatalytic activity of the materials may guide researchers in the design of more active catalysts for the ORR. In alkaline media, Au(100) is one of the most active electrocatalysts for the ORR, being more active than platinum in a specific potential window[196], and significantly more active than the remaining low index Au facets, Au(111) and Au(110)[128, 225, 228]. Since Adžić et al. reported the structure sensitivity of ORR on Au single-crystals in the 80's[127-129], researchers try to understand the origin of this observation, but without succeeding completely[230]. The combination of experimental results[115, 127, 229, 231, 280-282] and DFT calculations[216, 277-278, 283] helped shed some light on the subject, but the origin of the activity remains unclear. Therefore, more information is necessary to elucidate what causes the Au(100) surface to be active for the ORR.

Experiments using model surfaces remain a handy tool to yield mechanistic and structure relationships associated with electrocatalytic reactions. Model surfaces play a special role in the study of ORR in alkaline media because the reaction involves charged species, which makes it challenging to model accurately using DFT calculations[277]. The possibility of introducing discrete modifications in the structure of the Au catalysts, for instance, strain, is an interesting route of investigation of the structure effect in an electrocatalyst's overall activity. Additionally, alloying gold with another metal while maintaining the electrocatalyst structure brings insights into the effect of electronic changes in the material activity caused by the alloying effect. The use of PLD to deposit films offers the possibility of studying both effects by manipulating the deposition parameters.

In this chapter, pulsed laser deposition is used to deposit Au preferentially oriented thin films in the [100] direction intending their utilization as model surfaces in electrocatalysis. Aiming to achieve thin films with high-quality epitaxy in the [100] direction, the effect of some variables on the structure of the films was studied, namely the deposition of a buffer layer between the substrate and the film and the substrate temperature during the deposition. The effect of these parameters on the structure of the films and their electrochemical behavior described.

7.2 Experimental details

7.2.1 Deposition of the Au/MgO(100) films

The films were deposited by PLD, and the general characteristics of the laser setup and the deposition parameters were reported in section 4.2. MgO(100) single-crystals were used as substrates, and they were cleaned prior to the deposition, as reported in the experimental section.

Nickel (Ni) and silver (Ag) were used as buffer layers to understand their effects on the films' structure and characteristics. A very thin layer (≈ 1 monolayer) of the metals was deposited between the MgO substrate and the gold layer. For those tests, 2000 laser pulses hit the Ni or Ag target, and the substrate temperature was 100 °C. The Au layer was deposited by applying 60 000 pulses to the Au target.

Additional depositions seeking to optimize the substrate temperature were performed. Ni was used as a buffer layer in these depositions, and the substrate temperature varied from room temperature to 600 °C.

This section aims to clarify what are the best conditions to deposit the Au/MgO(100) in order to achieve a film growth along the [100] direction with high crystalline quality and suitable for the electrochemical experiments: exhibiting low roughness and resistivity, and with good adhesion to the substrate.

7.2.2 The effect of the buffer layer on the epitaxy of the Au/MgO(100) films

The X-ray reflectivity (XRR) data recorded for the Au/Ag/MgO(100) and Au/Ni/MgO(100) are shown in Figure 7-1. The results show similar plots for both samples, and a set of fringes with similar widths appears. Each fringe measured corresponds to a reflection of the incident beam, and the thickness of the films (*d*) is associated with the oscillation period of the fringes. The thickness of the films is estimated using equation (32) listed in chapter 4.

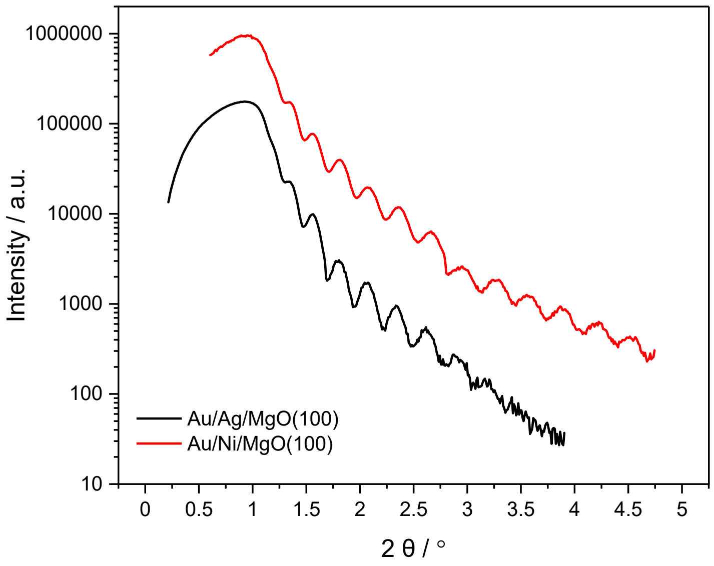

Figure 7-1: XRR curves obtained for the Au/M/MgO(100) films.

Since the only difference between the two films was the buffer layer metal, it is expected that the films have similar thickness, which was confirmed experimentally, table 7. According to equation (32), the thickness can be estimated by the distance between the maxima of two consecutive fringes. Because both films show multiple fringes, the thickness was estimated by using all distinguishable fringes appearing in the graph, and the values shown in the table express the average thickness obtained. The margin of error added represents the standard deviation of the thickness provided by each pair of fringes used in the calculation.

Table 7: The estimated thickness of the Au films deposited on MgO(100).

Sample	d / nm
Au/Ag/MgO(100)	34.97 ± 4.80
Au/Ni/MgO(100)	31.27 ± 4.69

The comparison between the XRD diffractograms obtained for both samples yields information on how the buffer layer affects the structure of the Au films, Figure 7-2. For reference, the diffractograms of the MgO(hkl) substrates and the indexed position of the main diffraction peaks for both MgO (PDF file 00-045-0946) and Au (PDF file 00-045-0784) were also added.

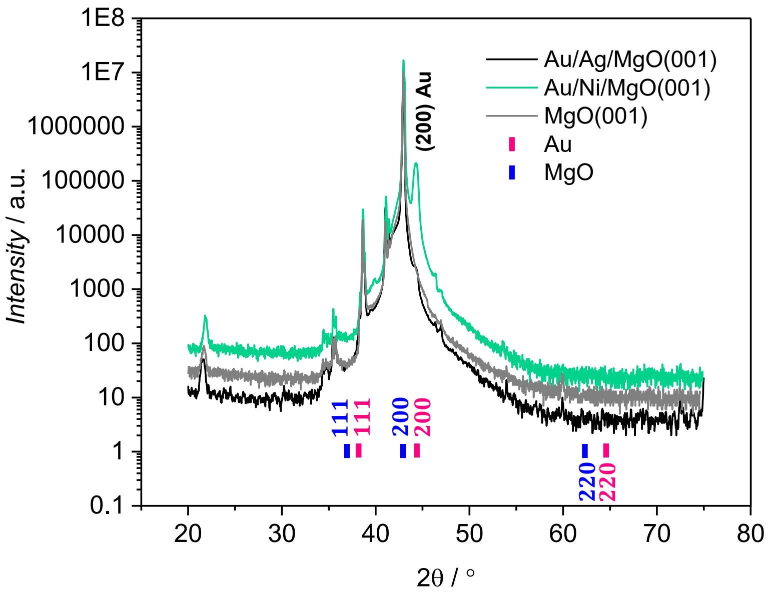

Figure 7-2: XRD diffractogram recorded in Bragg-Brentano configuration (θ to 2θ mode) for the Au/M/MgO(100) films.

Since the MgO substrate is highly crystalline and the layer of Au is thin, most of the peaks seen in the XRD patterns originate from the diffraction of the substrate. The most intense peak observed in the diffractograms (2θ ≈ 42.9°) corresponds to the diffraction of the (200) plane of the substrate. The comparison of the films diffractograms with the substrate reveals that the only peak that does not belong to the diffraction pattern of the substrate is the one located at 2θ ≈ 44 °, at the right side of the main peak of the MgO(100) substrate, more clearly seen for the film deposited on the Ni buffer layer. Therefore, this peak comes from the diffraction of the Au layer deposited onto the substrate, and regarding the Au phase, this is the only peak observed. By comparison with the Au PDF file (sticks added to the plot for guidance), the position in which this peak appears corresponds to the diffraction of the Au (200) planes. Thus, the Au layer has grown only along the [100] direction in both cases, and the films are epitaxially oriented in this direction. Some additional diffraction peaks appear in the diffractogram, and they come from the Kβ diffraction (2θ ≈ 39°) of the main diffraction peak of the MgO substrate peak and some tungsten contamination coming from the x-rays source (2θ ≈ 41°).

The main difference in the diffractograms of the two films is that the film deposited on the top of the Ni buffer layer shows an intense and sharp diffraction peak at 2θ = 44.25° that comes from the Au phase, whereas for the film deposited on the Ag buffer layer, only a fading broad shoulder appears at a similar position. Using the position of the diffraction peaks (2θ), the out-of-plane lattice parameter was estimated, Table 8. In both cases, the 2θ position of the (200) plane is shifted towards lower Bragg angles with respect to the bulk gold, and the lattice parameters are larger than that of bulk Au. As a reference, values reported for Au (PDF file 00-045-0784) were added to Table 8 along with the experimental data.

Table 8: Out-of-plane lattice parameters obtained for the Au/MgO(100) films.

Sample	(200) 2θ / °	$d_{(200)}$ / Å	$a_{(200)}$ / Å
Au Bulk	44.393	2.039	4.0786
Au/Ag/MgO(100)	44.352	2.042	4.0850
Au/Ni/MgO(100)	44.234	2.048	4.0953

This deviation in the lattice parameters when depositing films in which the nature of the material deposited, i.e., Au, differs from the substrate – the MgO in this case – also called heteroepitaxy, is expected, and several factors may contribute for this scenario[148, 252-253, 284]. First, considering the lattice parameters of the MgO substrate (4.2112 Å) and the bulk Au (4.0786 Å), there is a mismatch of -3.1 %, which may introduce some strain in the crystalline lattice of Au[148]. Epitaxial stress can arise if the films' lattice grows in perfect alignment with the substrate's lattice, forming a perfectly coherent interface between the two. Additionally, the thin film's growth mode may also introduce intrinsic stress in the lattice of the film due to the coalescence of the islands formed during the growth.

Considering the results obtained from the θ-2θ scans, the Ni buffer layer favors better epitaxial growth of the Au layer on the MgO(100) substrate. This conclusion is based on the fact that the (200) diffraction peak observed for the gold phase deposited on the Ni buffer shows higher intensity, which is regarded, in this case, as the existence of larger coherent domains diffracting in the [100] direction in the irradiated area.

To obtain more information regarding the structure of the films, pole figures were also recorded. Pole figures provide information regarding the orientation relationship between the crystallites forming the film and the substrate. In summary, they reveal if the film grows coherently aligned with the substrate or if it is tilted with respect to the substrate. Figure 7-3 shows the pole figure of the pristine MgO(100) substrate:

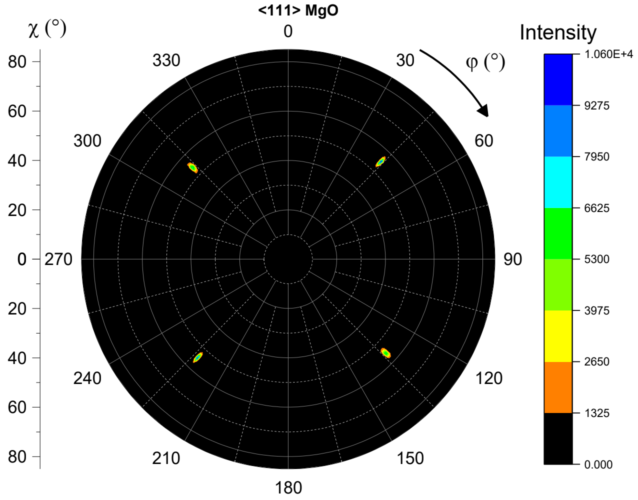

Figure 7-3: Pole figure obtained for the MgO(100) substrate in the <111> direction.

To record the pole figure, the Bragg angular position was fixed at the (111) diffraction. Therefore the pole figure provides the visualization of the (111) planes in the lattice of the MgO(100) substrate. Hence, the four spots where the intensities are concentrated corresponds to the diffraction in the [111], [1-11], [11-1], and [-111] directions according to the 4-fold symmetry of a cubic structure. The spots are located at χ = 54.5°, which approximates the angle between the (100) and the (111) planes in the cubic system, 54.75 °. In addition, these spots are separated from each other by φ = 90° in agreement with the symmetry of a cubic lattice. The high intensity and narrow spread of the intensity reflect the high crystallinity of the substrate.

The pole figures obtained for the films deposited on the different buffer layers, Figure 7-4, also show four spots in positions similar to the reported for the MgO(100) substrates.

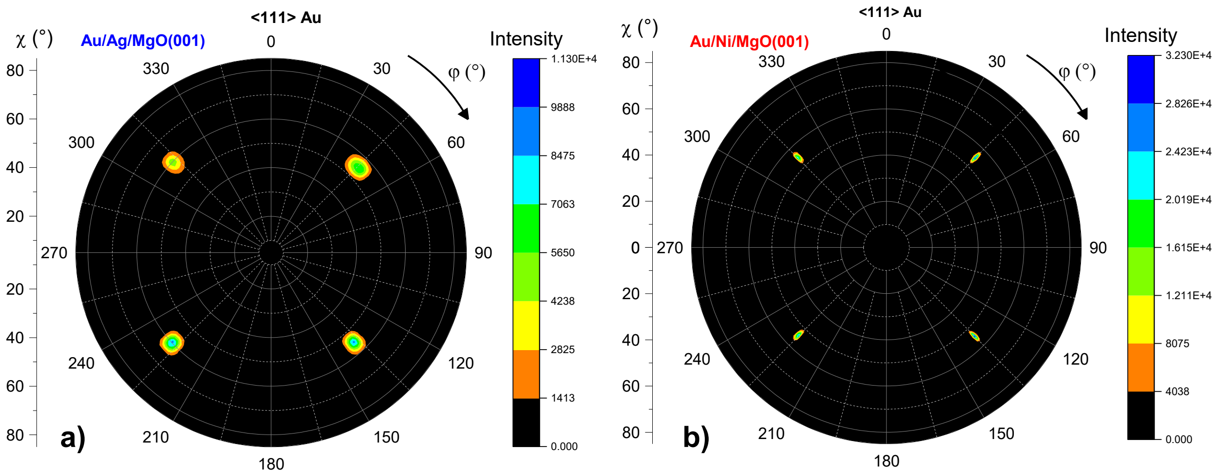

Figure 7-4: pole figures obtained for the Au/Ag/MgO(100) in a) and b) Au/Ni/MgO(100) films in the <111> direction.

However, the pole figures reveal discrete but important differences between the films. First, the position of the spots on the Au/Ni/MgO(100) films, Figure 7-4b), matches closely the position reported for the substrate, whereas the position of the spots in the Au/Ag/MgO(100), Figure 7-4a), shows two peaks at $\chi = 55°$ and $\varphi = 42.5$ and 137.5° and the remaining two at $\chi = 60$ and $\varphi = 227.5$ and 312.5°. Therefore, the χ position shifts on 5° for two of the peaks, and the spots are not evenly spaced at 90° as expected, which is indicates the lower symmetry of the crystal. These shifts mean that the crystal is slightly twisted and tilted with respect to the substrate.

Furthermore, the film deposited on the Ag buffer layer shows a broad spreading on the reflections, whereas the film deposited on the Ni buffer layer shows only a small spreading of the intensities. The spread on the intensities reveals the degree of mosaicity of the crystallites that form the films – the degree of misalignment of the crystallites regarding each other. Thus, the film deposited on the Ni buffer layer exhibit higher order of organization of the crystallites, whereas the film deposited on the Ag buffer layer provides a crystal with a higher degree of mosaicity concerning the crystallites that build the film.

Despite the differences reported, the intensity measured for the four peaks is close to the expected one for a cubic structure and indicates that in both cases, the films grew with Au(100)[010]//[010](100)MgO cube-on-cube epitaxial relationship, as observed before for fcc metallic films onto ceramic substrates[63].

7.2.3 The effect of the buffer layer on the electrochemical behavior of the Au/MgO(100) films

Cyclic voltammograms for the Au single-crystals in a range of electrolytes are known and available in the literature[26, 64, 115, 225, 285]. Regardless of the electrolyte, the three low index gold surfaces [(111), (110), and (100)] display distinct features in the voltammograms, providing the fingerprint characteristics of the Au surfaces, either in acid or alkaline media. In this sense, cyclic voltammetry is an especially useful tool in characterizing the films' surfaces and in determining whether the surface electrochemical behavior reflects the structural crystallographic orientation of the films indicated by the XRD analysis.

Cyclic voltammograms (CVs) of the films were recorded at 50 mV/s in N_2 saturated 0.5 M H_2SO_4 in a potential window between 0.5 and 1.7 V *vs.* RHE, and the currents were normalized for the geometric surface area of the electrodes (≈ 0.28 cm^2), Figure 7-5 a).

The voltammograms show similar features for both samples: a wide double layer charge-discharge potential window – observed between ≈ 0.50 to 0.95 V – followed by a region where the surface oxidation and reduction reactions occur – from approximately 1.0 to 1.7 V. Within this potential window, the voltammograms are stable. The most noticeable difference in the CVs is the current densities recorded for each sample.

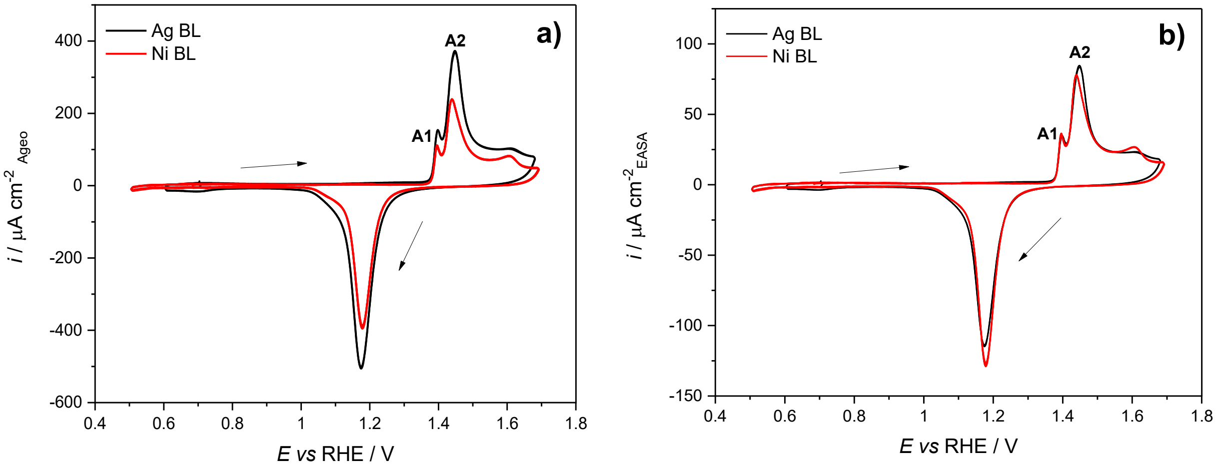

Figure 7-5: Cyclic voltammograms recorded for the Au/Ag/MgO(100) and Au/Ni/MgO(100) recorded at 50 mV/s in N_2 saturated 0.5 M H_2SO_4, currents normalized for the geometric area in a), and EASA, in b).

Since the oxidation and reduction reactions depend on the number of sites available at the electrode surface, the current measured scales with the electrodes' electrochemically active surface area (EASA). Aiming to understand if this is the origin of the observed difference in the current, the EASA of each film was estimated and the currents normalized for the EASA, Figure

7-5 b). The EASA values were estimated using the charge obtained from the integration of the oxide stripping peak observed between 1.00 - 1.30 V *vs.* RHE, and assuming a charge of 192 µC cm^{-2} for a monolayer of oxide formed on the anodic scan for Au(100) face[285]. After normalizing the current densities for the EASA, the voltammograms superimpose, indicating that the differences in the current densities come mainly from differences in the active surface area of the films. Therefore, in acidic media, the electrochemical behavior of the samples is similar.

With respect to the literature, Hamelin et al.[64] reported voltammograms for the three gold basal planes single-crystals in 0.01 M H_2SO_4 recorded at 50 mV/s, Figure 7-6a). The authors demonstrated that in this electrolyte, Au(111) has a distinct profile from Au(100) and Au(110). However, the voltammograms showed for Au(100) and Au(110) single crystals resemble each other, and both surfaces display two main anodic peaks (A_1 and A_2). For Au(100) surface, A_1 appears at ≈ 1.36 V *vs.* RHE and A_2 at ≈ 1.40 V *vs.* RHE, and the current density ratio of $\approx A_2/A_1 = 1.26$, whereas Au(110) also shows A_1 appearing at ≈ 1.40 V *vs.* RHE and A_2 at ≈ 1.47 V *vs.* RHE, and the current density ratio of $\approx A_2/A_1 = 0.84$. The experimental CVs reported do not show any similarity with the Au(111), indicating that the films' surfaces do not rearrange into the (111), the most stable facet of gold. Figure 7-6b) shows experimental voltammograms illustrating the difference in the voltammograms for Au films deposited on MgO(100) and MgO(111), and in both cases, the voltammograms are similar to the corresponding facet reported by Hamelin.

However, Au(100) and Au(110) show some similarity, and it is necessary to clarify whether the surface of the films behaves as a (100) or as a (110) facet. Considering Figure 7-5b), the average experimental values observed for A_1 and A_2 position is 1.40 V and 1.44 V *vs.* RHE, and the average ratio between both peaks is 2.29; which is closer to what was previously observed for the Au(100) than for Au(110) single-crystals. Nevertheless, additional information is necessary to characterize the electrochemical behavior of the films.

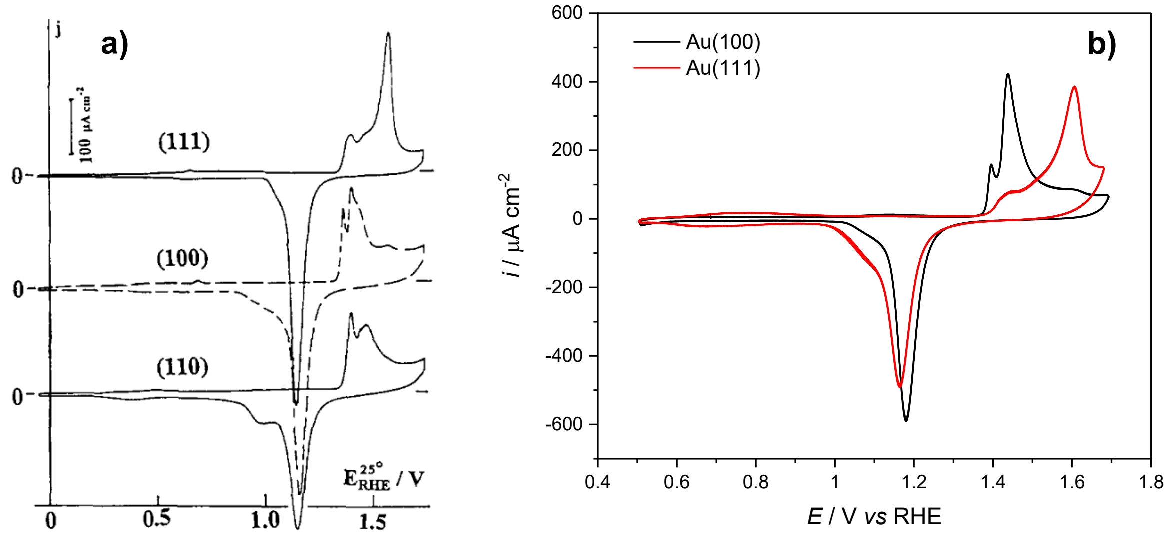

Figure 7-6: a) CVs reported in the literature[64] for Au(hkl) single-crystals recorded at 50 mV/s in 0.01 M H_2SO_4 electrolyte, and b) CVs recorded at 50 mV/s in 0.5 M H_2SO_4 for Au/Ni/MgO(100) and Au/Ni/MgO(111) films.[3]

Thus, voltammograms in N_2 saturated 1 M KOH electrolyte was also recorded, Figure 7-7. In Figure b) currents were normalized for the EASA determined previously in sulfuric acid.

The voltammograms show a wide potential window between approximately 0.1 and 0.8 V *vs.* RHE, where only double-layer charge/discharge currents emerge. Then, as the electrode potential becomes more positive, the adsorption of OH^- takes place and a series of anodic peaks appear at ≈ 1.25 V, 1.31, and 1.33 V. When the scan is reversed, one broad peak associated with the reduction of the surface is seen at 1.10 V followed by the specific OH desorption[228].

---

[3] Image reproduced with permission from the publisher.

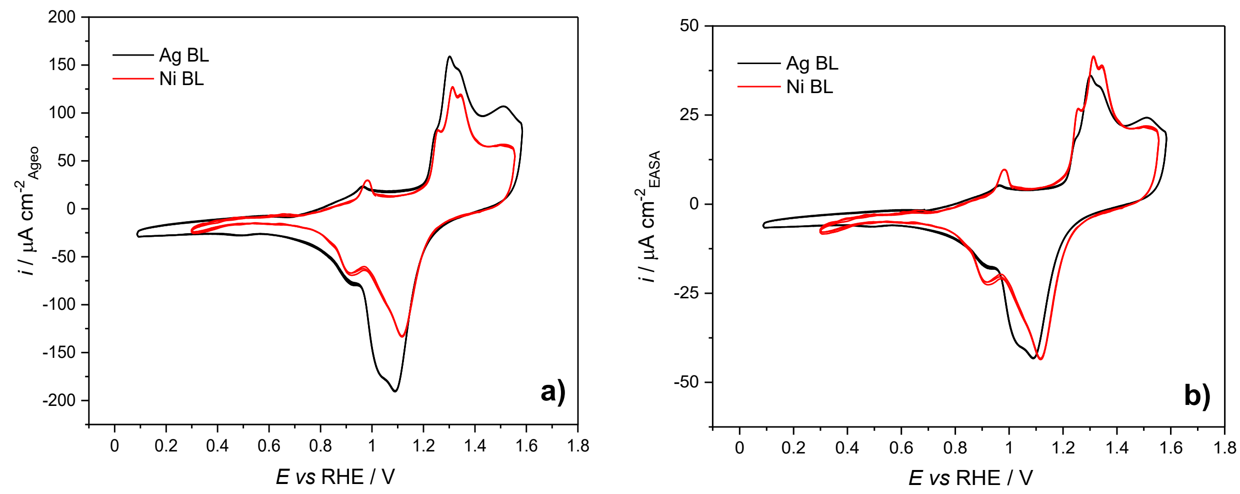

Figure 7-7: Cyclic voltammograms obtained for the Au/Ag/MgO(100) and Au/Ni/MgO(100) recorded at 50 mV/s in N_2 saturated 1 M KOH, a) and b).

The voltammogram obtained for both samples is similar, but the sample deposited onto the Ni buffer layer exhibits sharper and more defined peaks. The difference in the current densities observed comes from differences in the surface area, as the voltammograms recorded in sulfuric acid. In both voltammograms, an extra anodic of anodic and cathodic peaks appear at around 1.0 V and 0.9 V *vs.* RHE, respectively. This anodic peak has been reported in the literature for flame-annealed Au(100) single crystal electrodes[229, 286-287] and is attributed to the lifting of the reconstruction of the surface caused by the OH adsorption induced by the anodic polarization[288]. After the flame annealing, the Au(100) single crystal is an Au(100)-(5×2) reconstructed surface[135, 289]. This reconstruction is reversible, and when the electrode is polarized in the anodic direction, the surface undergoes the transition to an Au(100)-(1×1) surface. The Au(100)-(5×2) reconstructed surface is known to be stable at cathodic potentials, and once the negative charge is kept cathodic enough, the surface reconstructs in the backward scan[290]. As a result, this peak appears in all the scans and not only in the first scan recorded. An illustration of the surface atomic arrangement in both cases is shown in Figure 7-8. The voltammograms recorded for the Ni buffer layer film in alkaline media resemble those reported for flame-annealed Au(100) single crystals in 0.1 M NaOH by Prieto et al.[115] and Schmidt et al.[26] in 0.1 M KOH.

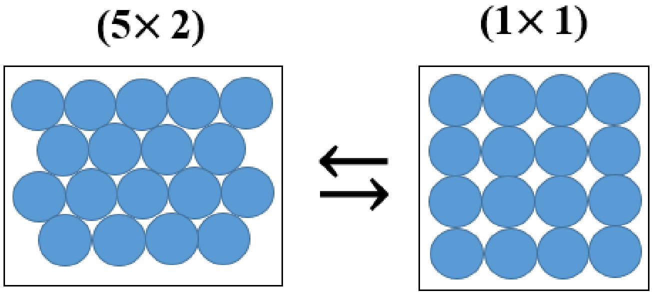

Figure 7-8: Sketch illustrating the atomic rearrangement in the potential-induced surface reconstruction of Au(100) surface.

The correspondence between the experimentally recorded voltammograms with those from the literature in both electrolytes indicates that the films exhibit electrochemical behavior similar to the Au(100) single crystal regardless of the buffer layer.

The final and crucial test in the characterization of the epitaxial films is the ORR electrocatalytic assessment. The Au(100) surface is very active for the ORR, and therefore, a film oriented in the [100] direction must reflect its structural quality by being active to the ORR.

The comparison of the reconstructed SCVs for both samples using 43 ms as sampling time allows assessing the ORR activity of both samples, Figure 7-9a). This sampling time corresponds to the same mass transport coefficient obtained by an RDE assembly rotating at 1600 rpm.

The reconstructed voltammograms show some similar features: the kinetic control potential window at potentials close to 1.0 V, followed by a zone where the ORR kinetic and diffusion control are mixed, and then two diffusion-controlled potential windows appear. The most remarkable difference between both samples is that between 0.700 and 0.850 V, the Ni buffered layer sample displays current densities that are close to the expected for a four-electron exchange process, indicating that O_2 reduces at least, partially, to OH^-. Whereas the limiting current values achieved by the Ag buffered sample indicate the exchange of two electrons, reducing O_2 to peroxide.

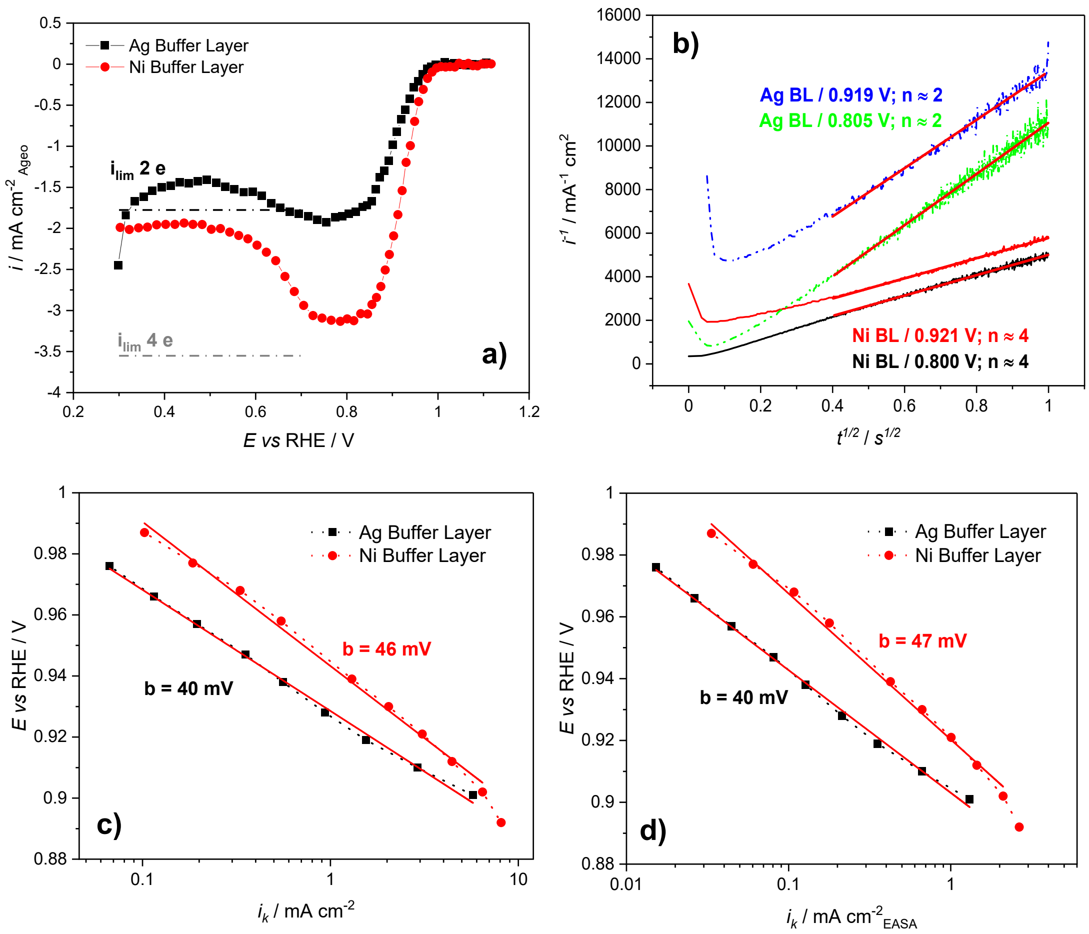

Figure 7-9: ORR characterization for the films Au/M/MgO(100): a) background-subtracted SCVs, b) K-L and c) Tafel plots normalized by the geometric area, d) Tafel plots normalized for EASA.

Aiming to obtain more kinetic information, the K-L plots were obtained by plotting 1/*i* vs. $t^{1/2}$, Figure 7-9b). From these plots, two kinetic parameters can be extracted: i) the apparent number of electrons exchanged (*n*) at the potential applied to record the transient, and ii) the kinetic currents for that potential. The first is extracted from the slope of the straight line obtained in the timescale where diffusion controls the reaction, and the latter, from the reciprocal of the *y*-axis intercept. Then, a plot of the kinetic currents as a function of the potential applied yields the Tafel plots, Figure 7-9c).

The K-L plots obtained for *E* applied ≈ 0.920 and 0.800 V, Figure 7-9b), show straight lines with different slopes for the two samples. In this scenario, this difference in the slopes likely comes from the fact that the number of electrons exchanged is different: the Ni buffered sample exchanges four electrons at both potentials, whilst the Ag buffered exchanges two electrons for the same potentials.

The Tafel plots, Figures 7-9c) and d), show a similar slope, which indicates the same rate-determining step for the ORR on both surfaces for lower overpotentials applied. Furthermore, the sample deposited on the Ni buffer layer presents currents higher than the Ag buffered layer. The kinetic current measured for E ≈ 0.920 V is 3.08 mA cm^{-2} for the first and 1.55 mA cm^{-2} for the latter. This trend remains for the EASA normalized Tafel plots, which exclude surface area effects from the activity.

The Au(100) single-crystal surface is known for reducing O_2 by the exchange of four electrons at least partially[127, 129, 225] within a wide potential window, while a two-electron transfer is characteristic of the Au(111), Au(110)[128-129, 225] and polycrystalline Au[291-293].

The polarization curve obtained for the film deposited onto the Ni buffer layer shows a broad peak at ≈ 0.800 V close to the expected limiting current for a 4-electron process. This behavior matches well the expected for an Au(100) surface.

The decrease in the number of electrons exchanged for more negative potentials is most probably associated with the presence of surface sites with symmetry different from the (100). Using stepped surfaces, it has been demonstrated that the introduction of defects – either with (111) or (110) symmetry – causes a decrease in the activity and selectivity of the Au(100) towards the ORR[159, 228, 294]. In such studies, the authors demonstrated that the presence of long (100) terraces is fundamental to achieve the highest activity and selectivity, and therefore not only the symmetry of the surface sites matter but also their long-range order. Hence, it is expected that the symmetry and the density of the surface defects in the films' surface affect the catalytic activity towards the ORR. Therefore, the films' surface activity will be as higher as the films' surface domains resemble the long-range order found in the perfect single-crystal surfaces.

The electrochemical characterization results support the XRD data and demonstrate that both films grew epitaxially in the [100] direction, but the film deposited on the Ni buffer layer shows an electrochemical behavior closer to the Au(100) single-crystal. Hence, the higher catalytic activity for the ORR displayed for the film deposited onto the Ni buffer layer is probably associated with the higher degree of organization and symmetry of the crystallites building the films, as seen in the pole figures. The XRD results suggest that the Ni buffer layer yields a film with superior crystallinity and long-range order in the crystallites, impacting the films' activity for the ORR, making them more active and selective. Additionally, the films deposited on the Ag buffer layer were more fragile and detached from the substrate during experiments. Therefore, all the subsequent depositions use Ni as the buffer layer.

7.2.4 The effect of the substrate temperature on the structure of the Au/MgO(100) films

To obtain films with the highest crystallinity possible, the effect of the substrate temperature during the deposition was also probed. For this purpose, a new set of samples where the substrate temperature during the deposition varied from room temperature to 600 °C was prepared. All other parameters were kept constant.

The reflectivity curves obtained for the films differ significantly with the substrate temperature, Figure 7-10. However, except for the samples deposited at room temperature and 100 °C, no fringes can be distinguished in the graphs. Since only films with flatter surfaces show fringes in the spectra, the XRR results indicate that the surface of the film becomes rougher as the substrate's temperature increases. Francis and Salvador[63] also reported the roughening of film surfaces with the temperature when studying the PLD deposition of Cu, Pt, Ag, and Au metallic films onto several ceramic substrates, including MgO. According to Liu et al.[295], when the lattice mismatch between the film and the substrate introduces stress in the film lattice, higher deposition temperatures might lead the roughness to increase. A possible explanation is that the surface diffusion of the adatoms arriving at the substrate increases with the temperature, favoring the agglomeration of the adatoms to form larger islands[63].

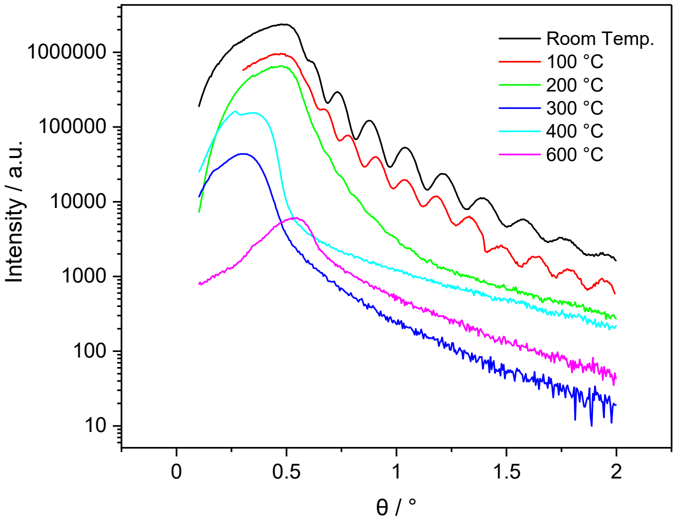

Figure 7-10: XRR curves recorded for the films deposited at various temperatures.

Using the fringes observed in the sample deposited at room temperature, the estimated thickness of the films is 25.68 ± 3.21 nm. Considering the margin of error, this value is close to the one obtained for the films deposited at 100 °C – 31.27 ± 4.69 nm. Therefore, we cannot conclude how the substrate temperature affects the thickness, and the films will be regarded as having the same thickness.

The diffractograms resulting from the θ-2θ scans show the effect of the substrate temperature on the XRD pattern of the samples, Figure 7-11a). Concerning the Au phase, one or two peaks appear in the diffractograms according to the substrate temperature: one associated to the (200) planes diffraction at 2θ = 44.39° – and/or another peak related to the diffraction of the (111) planes at 2θ = 38.18°. The diffractogram obtained for the film deposited at room temperature shows diffraction peaks only in the [111] direction, which means that the film deposited has growth preferentially along the [111] direction in the out-of-plane direction. This can be explained by the fact that *fcc* metals surfaces tend to re-arrange into the (111) facet because this is the one with lower surface energy, and therefore, the most stable thermodynamically[296]. However, when the substrate temperature is raised to 100 °C degrees, the only diffraction peak seen is the one associated with the diffraction of the (200) planes, indicating that at this temperature, the film grows along the [100] direction. The further increase of temperature up to 400 °C seems beneficial because it causes an increase in the intensity of the (200) diffraction peak. Nonetheless, at 600 °C, the (200) intensity decreases significantly, and a very intense (111) diffraction peak appears.

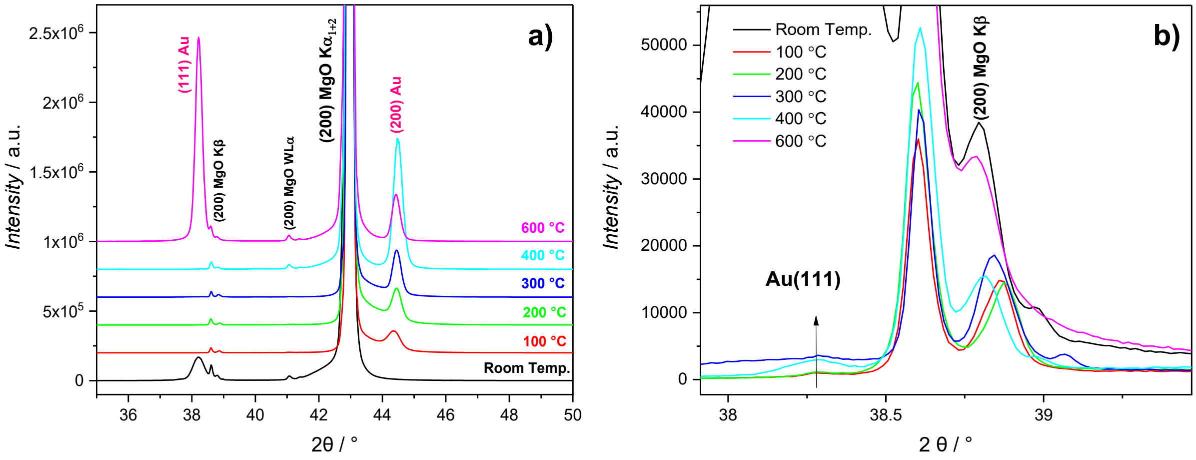

Figure 7-11: XRD diffractogram recorded in θ-2θ mode for the Au/Ni/MgO(100) films deposited at various temperatures in a), b) shows the magnified angular scale where the (111) peak may appear.

A closer analysis of the intensity of the (200) diffraction peak provides useful information on the optimal substrate temperature for the deposition, Figure 7-11b). The diffractograms show that when the temperature higher than 200 °C, the growth in the [111] direction is favored, which can compromise the epitaxy of the films. Accordingly, amidst the temperature range tested, 100 - 200 °C is the optimal choice since only the diffraction peak coming from the (200) planes are observed with high intensity, and (111) diffracting planes are absent.

The fact that even on MgO(100) substrates is somehow easy to achieve the epitaxial growth of the films along the [111] direction – especially at room temperature – can be explained by the low surface energy of this gold surface. The calculated surface energy of the Au surfaces[255, 297] has demonstrated that the surface energy of the Au low index faces increases in the following order: Au(111) < Au(100) < Au(110), Table 9 displays the calculated surface energy values for this surfaces[296]. Considering that lower surface energy results in a more stable surface, it is expected that the easiest facet to be grown will be the Au(111), followed by the (100), and the most difficult one will be Au(110). Additionally, it must be considered that higher substrate temperatures provide high mobility for the Au atoms that can reorganize in the most stable facet.

Table 9: Calculated values of surface energy for Au surfaces, data taken from literature[296].

(hkl)	Surface energy / ergs cm^{-2}
(100)	1083
(110)	1114
(111)	886

Using the angular position of the (200) peak, the lattice parameters were calculated, Table 10. The substrate temperature causes discrete changes in the lattice constant of the films resulting in different lattice parameters compared to the Au bulk.

Table 10: Out-of-plane lattice parameters obtained for the Au/Ni/MgO(100) films deposited at different temperatures.

Sample	(200) 2θ / °	d_{200} / Å	$a_{(200)}$ / Å
Au Bulk	44.393	2.039	4.0786
100 °C	44.364	2.042	4.0839
200 °C	44.455	2.038	4.0760
300 °C	44.459	2.038	4.0757
400 °C	44.497	2.036	4.0724
600 °C	44.437	2.039	4.0776

At 100 °C, the out-of-plane lattice parameter is larger than the Au bulk showing that film is under tensile stress in the perpendicular direction to the substrate. At 200 °C, the trend is the opposite:

the film's lattice parameter is smaller than the Au bulk, indicating the film is under compressive stress. The films deposited at 300, 400, and 600 °C are also under compressive stress in the out-of-plane direction.

This change in the lattice parameters is a consequence of the turnaround of intrinsic stress in the film's lattice that changes from compressive to tensile according to the stage of the film growth – nucleation, coalescence of islands, and growth of crystallites forming the film. This stress cycle is characteristic of the Volmer-Weber growth mechanism[252-253, 298] in films, and in such growth mode, the atoms arriving onto the substrate tend to form small islands during the nucleation step, later these islands coalesce and grow to cover the substrate and produce a thicker film. In this sense, the temperature plays an essential role in the turnaround stress and, therefore, in the development of the stress within the structure of the films[299].

To verify the effect of the substrate temperature in the films' crystallite size (defined as the coherently scattering domain size within the particles composing the films), the crystallite size for the Scherrer equation was used[300-302], Figure 7-12. The graphic shows that crystallites forming the films become larger as the substrate temperature increases, which is expected since higher temperature generally causes sinterization/agglomeration of the particles due to enhanced diffusion of the atoms.

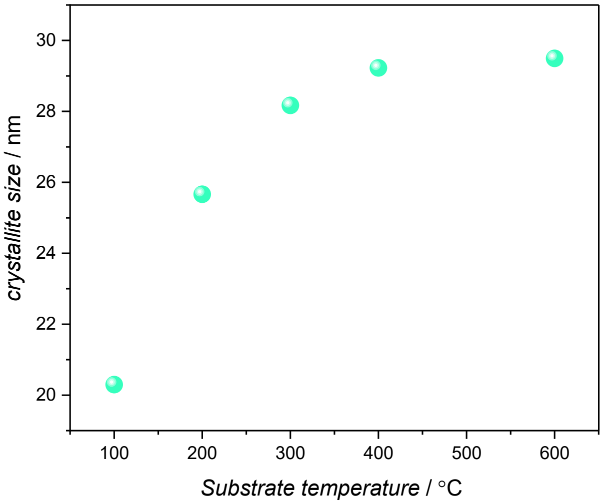

Figure 7-12: Plot of crystallite size variation with the substrate temperature.

The substrate temperature is a variable that must be considered carefully because it affects the growth of the films and, therefore, its crystallographic orientation. According to Stringfellow[303], at lower temperatures, the epitaxial layer deposited is perfect and pure. Thus, it is important to use deposition temperatures as low as possible to favor the growth of a perfect crystalline layer on the substrate. The reason is that the importance of entropy – consequently, the disorder degree of the system – increases with the temperature.

7.2.5 The effect of the substrate temperature on the electrochemical behavior of the Au/MgO(100) films

The voltammetric profile of the films does not change significantly with the temperature of the substrate, Figure 7-13. In acidic media, the voltammograms normalized for the EASA overlap almost entirely, and no remarkable differences appear. The voltammograms recorded in 1 M KOH are similar for the three samples, but the current densities at the oxidation and reduction of the surface – taking place between ≈ 1.0 and 1.6 V – vary with the temperature of the substrate. This region reveals the surface's affinity for oxygenated species, and the sample deposited at 200 °C seems to display a stronger interaction with oxygenated species than the other samples. This effect is visualized in the alkaline media, likely due to the absence of the sulfate anions in the electrolyte. The sulfate adsorbs specifically to the surface and competes with OH for the adsorption sites when the electrode is polarized positively. Therefore, in KOH electrolyte, all the surface sites are available for the adsorption of oxygenated species.

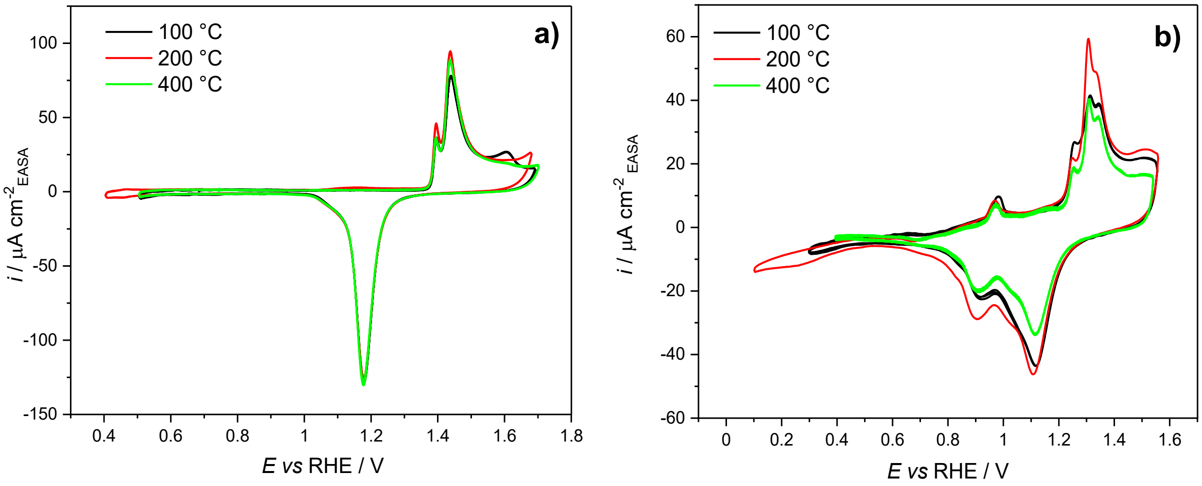

Figure 7-13: CVs recorded at 50 mV/s for films deposited at different substrate temperatures: a) and b) in 0.5 M H_2SO_4 and d) 1 M KOH.

Regardless of the deposition temperature, the samples exhibit voltammograms with profiles that resemble the one obtained for the Au(100) single crystal in analogous electrolytes[26, 64].

The reconstructed SCVs provide information regarding the ORR activity of the films, Figure 7-14. For the samples deposited at 100 and 200 °C, the SCVs show similar ORR activity: the onset potential is close to 1.0 V, and the half-wave potential is similar. Both samples show a plateau between 0.830 and 0.740 V where the limiting currents are close to the expected one for a 4-

electron transfer. For potentials more negative than 0.700 V, the limiting currents decrease to a value close to a 2-electron transfer process. This behavior is expected for the ORR catalyzed by an Au(100) surface in alkaline electrolyte[26].

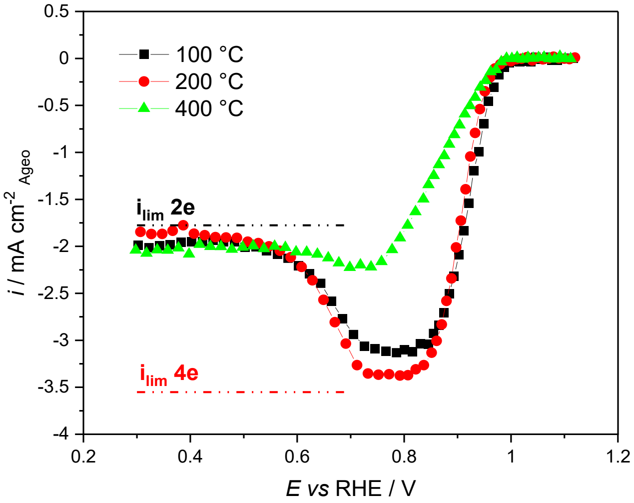

Figure 7-14: Reconstructed SCVs at 43 ms for the samples deposited at different substrate temperatures.

However, the activity obtained for the film deposited at 400 °C displays lower activity for the ORR, reflected in the potential shift for the half-wave potential. Its half-wave potential is around 50 mV more negative than the measured for the 100 °C and 200 °C deposited samples. Additionally, the 400 °C sample also displays lower selectivity, and the ORR takes place mostly by the exchange of only 2-electrons to produce a peroxide as the final product.

Despite the preferential growth in the [100] direction at 400 °C, the sample XRD pattern also shows diffraction features coming from sites with (111) arrangement. The number of sites with this symmetry at the surface is so small that they do not appear on the voltammograms; however, it appears that they are enough to hinder the ORR. Since the half-wave potential of the Au(111) facet is ≈ 200 mV more negative than the one observed for the Au(100) facet[128-129, 225], even a small fraction of (111) sites is enough to decrease the activity and selectivity of the ORR significantly[127-128]. The polarization curve obtained for the sample deposited at 400 °C resembles the one shown in the literature for the ORR on Au(111) surfaces.

7.3 Conclusions

During the deposition of Au(100)-oriented films on MgO(100) substrates, two metallic buffer layers were tested: Ni and Ag. XRD analysis showed that the two buffer layers lead to the growth of epitaxial gold films. However, the pole figures analysis showed that the Ni buffer layer provides films composed of crystallites with a higher degree of order and symmetry in the crystal. The Ag buffer layer led to the growth of films with lower crystal symmetry, twisted and tilted with respect to the substrate.

In agreement with the structural analysis, both Au/Ni/MgO(100) and Au/Ag/MgO(100) voltammograms showed characteristics that correspond to those observed on Au(100) single crystals either in acid and alkaline electrolytes. However, in 1 M KOH, the film deposited onto the Ni buffer layer showed an electrochemical behavior closer to the analogous single crystal. The Ni buffered film displayed higher ORR activity, similar to the Au(100) single crystal. The ORR activity on Au electrodes is very sensitive to the structure of the material, and the superior performance of the Ni buffered film for the ORR is a consequence of its higher degree of structural organization, as demonstrated by XRD and pole figures analysis. The Ni buffer favored greater adherence of the films to the substrates producing films that attached well to the substrate and kept the integrity during the experiments. When Ag was the buffer layer, the films were detaching more easily from the substrate, and at the end of the electrochemical experiments, they were destroyed most of the time.

The substrate temperature affects the structural and the electrochemical properties of the Au/Ni/MgO(100) films. The optimal deposition temperature to achieve the epitaxy in the [100] direction on MgO(100) substrates ranges from 100 – 200 °C. Room temperature and temperatures higher than 200 °C favors the growth of the film in the [111] direction and impairs the ORR activity.

8 ORR ON Au/MgO(100) FILMS WITH DIFFERENT THICKNESSES

8.1 Introduction

Researchers have been developing different strategies to prepare more active, stable, and less costly electrocatalysts for the ORR during the last decades[100, 167]. The approaches explored comprise the production of new materials or the modification of classic materials to enhance their ORR performance and augment their durability. The preparation of strained electrocatalysts consists of an efficient route towards producing advanced materials for the ORR[65-66, 164, 304-305]. In strained materials, the material's crystalline lattice is under stress, and its unit cell size differs from that of the bulk material. Changes in the lattice constant may affect the materials' surface properties, causing their activity to differ from that of the relaxed material.

The deliberate introduction of stress in the materials lattices became an interesting route of catalyst design after DFT calculations have proposed that the compression or the expansion of the lattice influence the adsorption properties of the materials [306-310], which is supported by a range of experimental results[65, 210, 305, 311-312]. The beneficial effect of strain in electrocatalysis has been demonstrated for various reactions: the ORR[65-66, 210, 313], the hydrogen evolution reaction[314 315], the formic acid oxidation[316], and the CO_2 reduction[317].

Studies regarding the effect of strain on the ORR on platinum electrocatalysts in acidic electrolytes are abundant in the literature since platinum is the state-of-art catalyst for the ORR in this conditions[288, 318]. DFT calculation revealed that for Pt, compressive strain affects the stability of the intermediates formed and decreases the overpotential of the reaction[66, 319], which indicates an increase in the ORR activity. This hypothesis was confirmed by experimental work where the authors report a better electrocatalytic activity for the ORR on compressive strained platinum-based electrodes[65-66, 312, 320-321].

In alkaline media, Au(100) is one of the most active surfaces for the oxygen reduction reaction [127, 159, 196, 227], and to our best knowledge, there are no studies concerning the strain effect on this electrocatalyst. Nonetheless, theoretical work has suggested that strain may enhance the adsorption of both atomic and molecular oxygen on Au(111) surfaces, facilitating the ORR[310, 322]. Extrapolating these results for Au surfaces, strained gold electrocatalysts may reveal enhanced electrocatalytic properties towards the ORR in alkaline conditions.

Traditionally, the ORR electrocatalytic studies on Au(100) surfaces were performed using single-crystal rotating disk electrode assemblies to achieve flat surfaces with a well-defined crystalline structure and ensured high mass transfer conditions[127, 225, 228-229, 282]. However, working with single-crystals requires specific instrumentation[141-143], and it provides electrodes with the same structural characteristics of the bulk material, being difficult to produce strained electrodes from single-crystals.

In this context, Temmel et al. [65, 210], have demonstrated that PLD is an excellent method to prepare platinum strained epitaxial films suitable for electrocatalytic model studies. This is possible because the crystallographic direction in which the film grows is determined by the crystallographic orientation of the substrate[63, 122, 261, 323]. Therefore, the strain is created in the film structure because its lattice constant is forced to match the substrate's lattice during the growth[252-253, 324]. Provided that the film is thin, the film structure will not undergo relaxation, and the strain is maintained in the lattice. Thus, PLD is suitable to produce films with optimal conditions to correlate strain and electrocatalytic activity.

In the previous chapter, the optimal conditions to deposit epitaxial Au/MgO(100) films were determined. In this chapter, the optimized conditions deposition were used to produce Au/MgO(100) thin films with different thicknesses, and the ORR electrocatalytic activity of these films in alkaline media was studied. The main objective in varying the films' thickness is to produce strained films and observe how this strain influences their ORR activity.

8.2 Experimental

8.2.1 Deposition of the Au/MgO(100) films

The films were deposited by PLD, and the overall characteristics of the laser setup and deposition conditions were reported in section 4.2. To produce films with different thicknesses, the number of pulses striking the Au targe was varied from 15 000 to 100 000. A Ni buffer layer was deposited on the MgO(100) prior to the Au layer deposition, and the substrate temperature was set to 200 °C.

8.3 Surface morphology and structural characterization of the films

8.3.1 AFM Images: a study of the surface of the films

The AFM images acquired for the films with various thicknesses bring information about their surface morphology and the growth mode of the films, Figure 8-1. For the thinner film, 15 000 pulses, the images reveal that the film is composed of islands with different shapes and sizes, and there are some gaps within the material. The resulting film is rough, and because the islands are not connected, the film is not conductive. When the number of laser pulses applied to the target increases to 25 000, the islands grow and then coalesce to form an almost continuous film with percolation pathways created. The film formed is still rough; however, as percolation pathways now exist, the film is conductive.

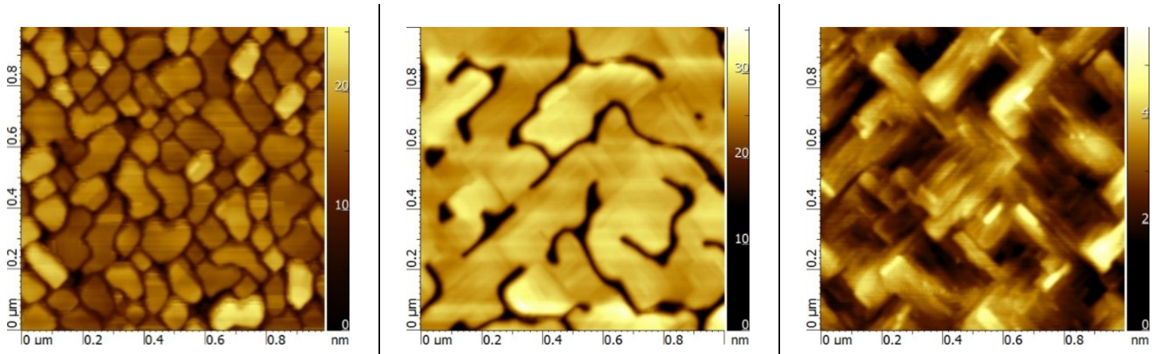

15,000 pulses – RMS: 3.39 nm | 25,000 pulses – RMS: 3.90 nm | 40,000 pulses – RMS: 0.75 nm

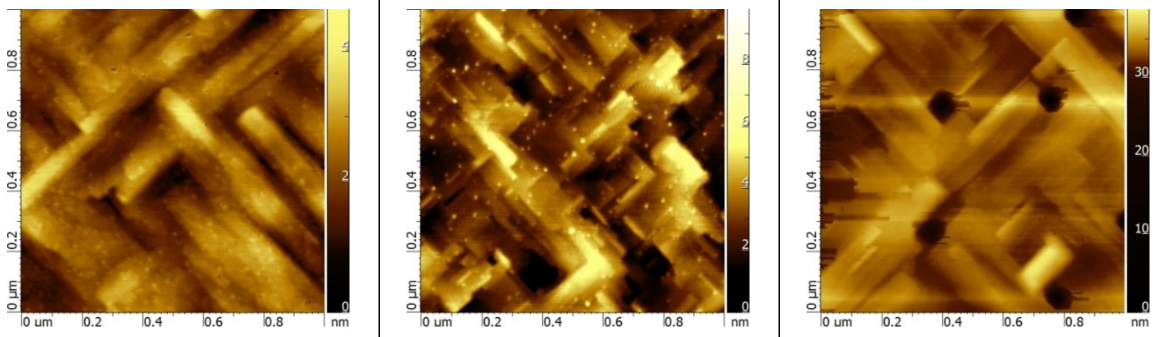

50,000 pulses – RMS: 0.56 nm | 60,000 pulses – RMS: 0.99 nm | 70,000 pulses – RMS: 2.04 nm

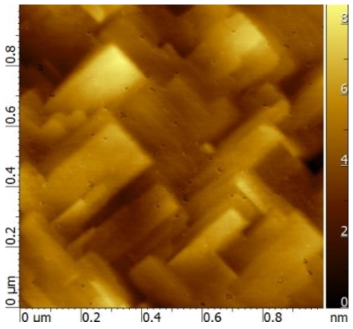

100,000 pulses – RMS: 1.13 nm

Figure 8-1: AFM images obtained for the films with various thicknesses. Images acquired by collaborators.

By increasing the number of laser pulses, the films become thicker as more Au atoms arrive on the islands, which grow and coalesce to cover the substrate entirely. Once the substrate is covered, further grain growth follows with an elongated shape in-plane direction of the substrate. The description of the Au films growth on the MgO substrate is characteristic of the Volmer-Weber growth mode in which the epitaxial phase nucleates as three-dimensional isolated islands. This growth mode is often observed when *fcc* metallic films are grown on insulating substrates by PLD[63].

8.3.2 Estimation of the films' thickness

The analysis of X-ray reflectivity curves recorded for the films allowed to estimate the thickness of the films deposited, Figure 8-2a) and b), respectively. The thickness of the films was estimated using the equation (32) listed in chapter 4.

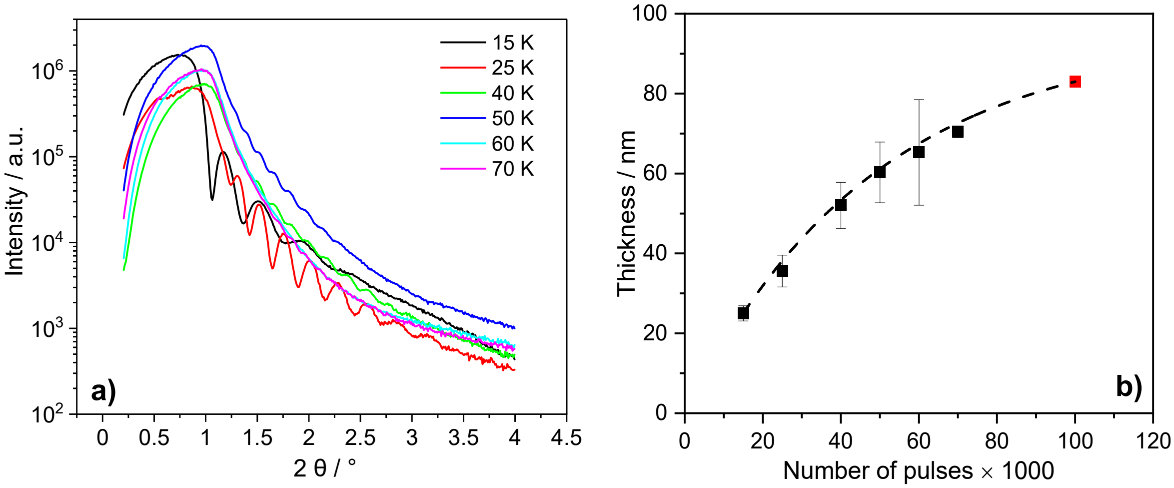

Figure 8-2: a) XRR curves of the films with different thicknesses, b) evolution of film thickness as a function of the number of pulses. The solid red square represents the extrapolated value for the 100 000 pulses film.

As expected, the fringes' oscillation period varies with the number of pulses applied to deposit the films, and the oscillation period decreases with the number of pulses, indicating that the films are becoming thicker. The estimated thickness of the films varies from ≈ 25 nm (15 000 pulses) to ≈ 71.7 nm (70 000 pulses), Figure 8-2b). For the 100 000 pulses film, the reflectivity data did not provide any distinguishable fringes. Therefore, its thickness was estimated by the extrapolation of the experimental data and estimated to be ≈ 81.7 nm. It should be kept in mind that the accuracy of the method is affected by the roughness of the films because it affects the accuracy of the position of the fringes. For instance, the thickness of the thinner samples is determined with more accuracy since the fringes in the reflectivity plot are well distinguished.

8.3.3 θ – 2θ scans

The XRD patterns of the thin films with different thicknesses yield information regarding the crystallographic orientation in the out-of-plane direction, Figure 8-3a).

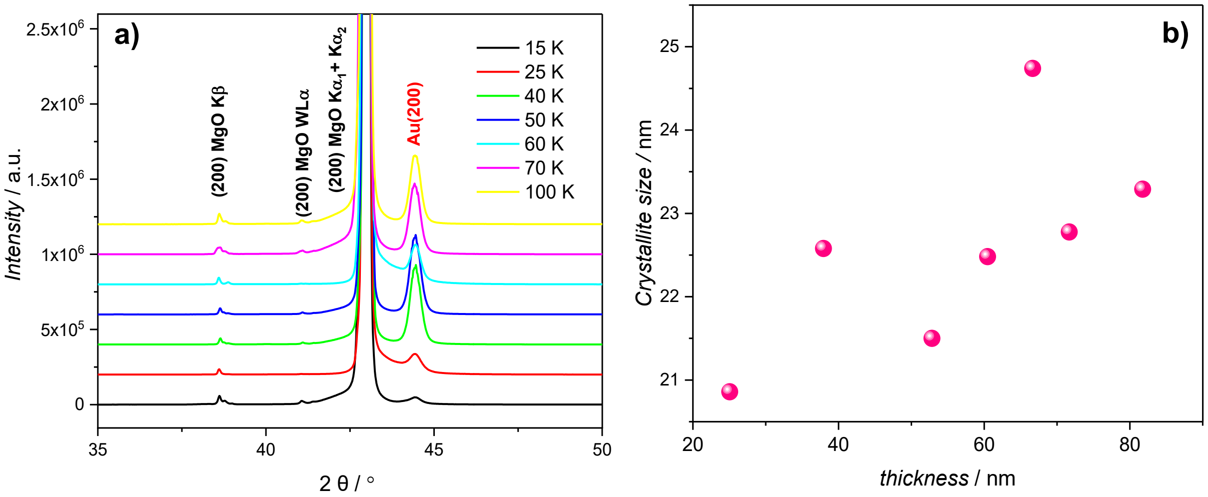

Figure 8-3: a) θ--2θ scans obtained for the thin films with various thicknesses, b) plot of crystallite size variation with the thickness of the films.

8.3.4 Pole figures analysis

The pole figures obtained, Figure 8-4, are like those shown in the previous chapter for the Au/M/MgO(100) films, and their aspects have been discussed in section 7.2.2. For this set of samples, regardless of the film's thicknesses, the film grows epitaxially in the [100] direction with a cube-on-cube epitaxy relationship between the Au film and the MgO(100) substrate. The crystal keeps the symmetry expected for the cubic lattice.

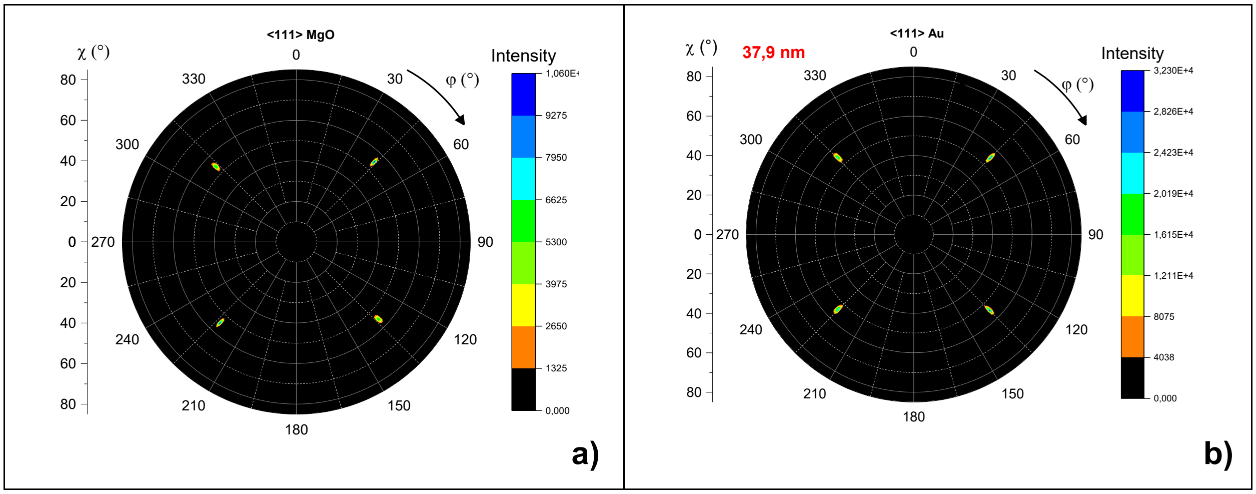

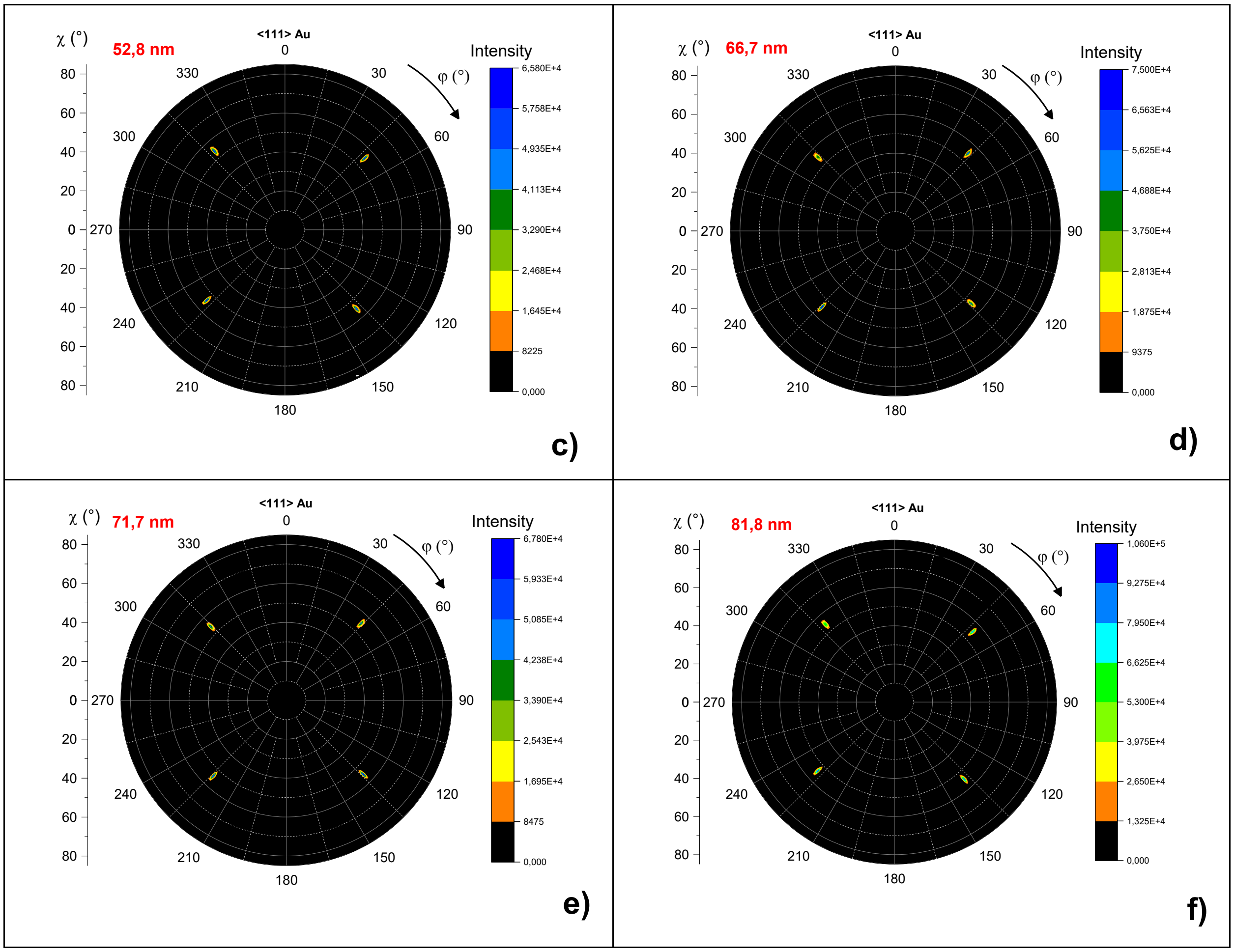

Figure 8-4: Pole figure of the MgO(100) substrate in a), and Au thin films with different thicknesses: b) 37.9 nm, c) 52.8 nm, d) 66.7 nm, e) 71.7 nm, and f) 81.8 nm thick.

8.3.5 Reciprocal space mapping analysis

The out-of-plane lattice parameter values obtained from the θ - 2θ scans are not enough to completely describe the structure of the films because they refer only to the films' structural arrangement in the direction normal to the surface. Additionally, the fact that the lattice constants of the films in the out-of-plane direction differ from the expected for the Au lattice suggests that the films' lattice constant in the in-plane direction may be different as well.

In this respect, reciprocal space mapping (RSM) is a powerful tool in the structural characterization of epitaxial films. RSM analysis provides structural information inaccessible by the symmetric θ - 2θ scans, as, for instance, the in-plane lattice parameter and the assessment of the mosaic spread of the crystals building the film. In the case of epitaxial thin films, it provides information on how perfect the crystalline lattice of the films is. To build the reciprocal space maps, the diffractometer applies small ω offsets around the angular position of the diffraction lattice point of interest and records ω-2θ scans. By the proper conversion of the diffraction data from the angular space to the reciprocal space, the Braggs law applies in a similar fashion, and the in-plane and out-of-plane lattice parameters are extracted, Figure 8-5.

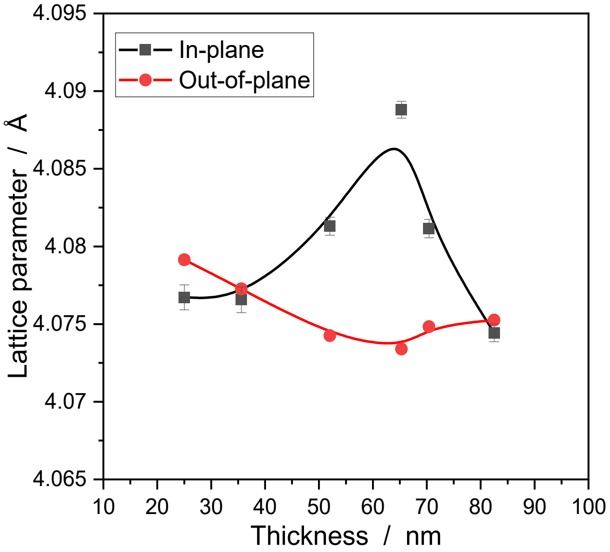

Figure 8-5: Plot of the lattice parameters in the out-of-plane and in-plane directions of the films as a function of the films' thicknesses.

Both the out-of-plane and in-plane lattice parameters vary with the thickness of the films. The out-of-plane lattice parameter is similar to the one of bulk Au (4.0786 Å) for the thinnest film and it decreases as the films become thicker up to ≈ 50 nm, where there is not much variation in the parameters, and they remain smaller than the lattice constant reported for bulk Au. The in-plane lattice parameters are close to the bulk Au for the 25 and 35 nm, and it increases for the 50 nm thick film to reach a maximum at 65 nm, and then decay for the 70 and 83 nm thick films. The in-plane lattice parameter controls the atomic distance between the atoms exposed at the surface, and for this reason, it is the most important when considering the surface properties of the films and their electrocatalytic properties. This scenario indicates that overall, the films are under compressive stress in the direction normal to the substrate surface (out-of-plane direction), whereas in the plane of the film (in-plane direction), the films are under tensile stress.

The explanation for the variation in the lattice parameters with the film's thickness lies in the fact that during the Volmer-Weber growth mode, there are cycles of compressive-tensile-compressive (CTC cycle) stress introduced in the crystalline lattice of the film according to the stage of growth[250, 325-326]. Initially, as the islands nucleate and grow, their lattice is under compressive stress, but as the islands coalesce and the grain borders forms and grow, the stress evolves to tensile stress. Finally, when the film covers the substrate and more atoms arrive at the grain borders, as the film grows thicker, compressive stress replaces the former tensile stress. These dynamic cycles of stress and relaxation during the film growth affect the structure of the films and cause changes in the lattice parameters. Thus, the CTC stress cycle observed in the deposition of films that grow through the Volmer-Weber mode comes from the complex microstructural evolution undergone during the growth of the film[249-250, 326].

In this sense, the elastic strain – deviation of the lattice parameters measured experimentally relative to the bulk lattice parameter – provide an estimative of the stress in the films:

$$\text{Elastic strain (\%)} = \left(\frac{a_{exp} - a_{Au}}{a_{Au}}\right) \times 100\% \qquad (37)$$

The variation of the estimated elastic strain of the films with respect to their thickness, Figure 8-6 demonstrates that in the in-plane direction, the films first are under compressive stress, which evolves to tensile stress to return to compressive stress as the films become thicker, exactly as in the CTC cycle described above. In the out-of-plane direction, the elastic strain is less significant and shows little variation.

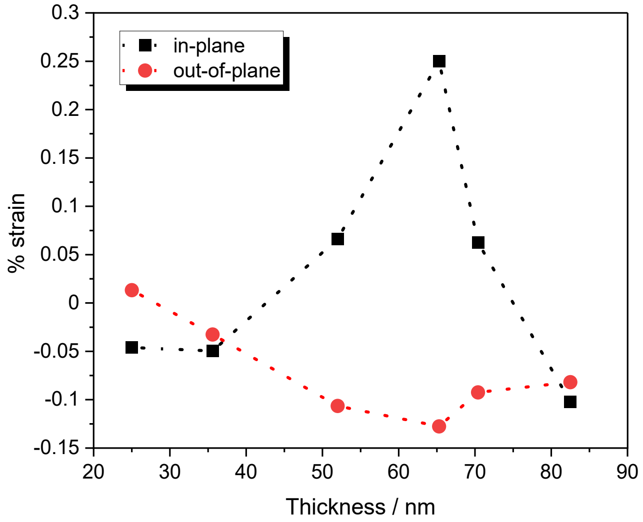

Figure 8-6: Plot of the estimated elastic strain in the structure of the film as a function of their thickness.

In the in-plane direction, the maximum value of strain in the films' lattice is around 0.25%. For Pt-based materials, enhanced electrocatalytic activity was found for strain values ranging from 0.30[65] to 1.47%[66]. Hence, the values reported for the Au films herein may be too low to cause significant changes in the films' activity.

Using data from RSM, the values of lateral coherent length, *L*, and the tilt angle, *T*, between the domains in the films and the underlying substrate, were also calculated. The experimental section

4.4.4 describes these variables in the reciprocal space and lists the trigonometric relations used in the calculations. The variation of *L* and T with the film thickness is depicted in Figure 8-7. The plots show that the domain size increases, and the tilt decrease with the thickness of the films, although the shape of the curves suggests that a plateau could be reached for thicker films.

The results mean that as the films become thicker and then more continuous, the crystals' domains are growing more coherently, i.e., better aligned with respect to each other. At the first steps of deposition, the films are composed of discontinuous and independent islands. As the deposition continues, the growth and coalescence of islands form a larger surface until reaching a continuous film for which the domains' size achieved their maximal values. Therefore, the films can be described as an ensemble of crystalline blocks with a coherence length, tilted and twisted, related to each other.

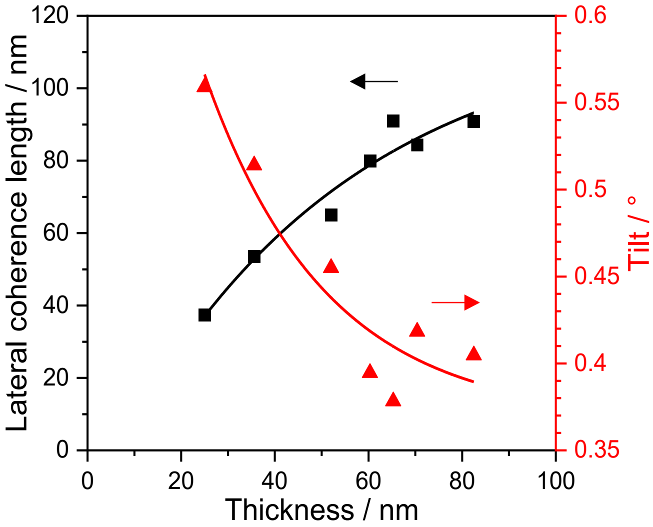

Figure 8-7: Variation of the lateral coherence length and the substrate tilt determined by X-ray reciprocal space mapping as a function of the film thickness.

8.4 Electrochemical characterization

8.4.1 Cyclic voltammetry

The electrochemical behavior of the films with various thicknesses was investigated by cyclic voltammetry in acidic and in alkaline media. Cyclic voltammograms (CVs) were recorded at 50 mV/s in N_2 saturated 0.5 M H_2SO_4 in a potential window between 0.5 and 1.7 V *vs.* RHE, and the currents were normalized for the geometric surface area of the electrodes (≈ 0.28 cm^2), Figure 8-8a). Overall, the CVs show similar features, and they were described in the previous chapter.

Restraining the analysis to the effect of the thickness of the films in the voltammetric features, the most noticeable difference in the CVs lies in the current densities recorded for each film, which are higher for thinner films.

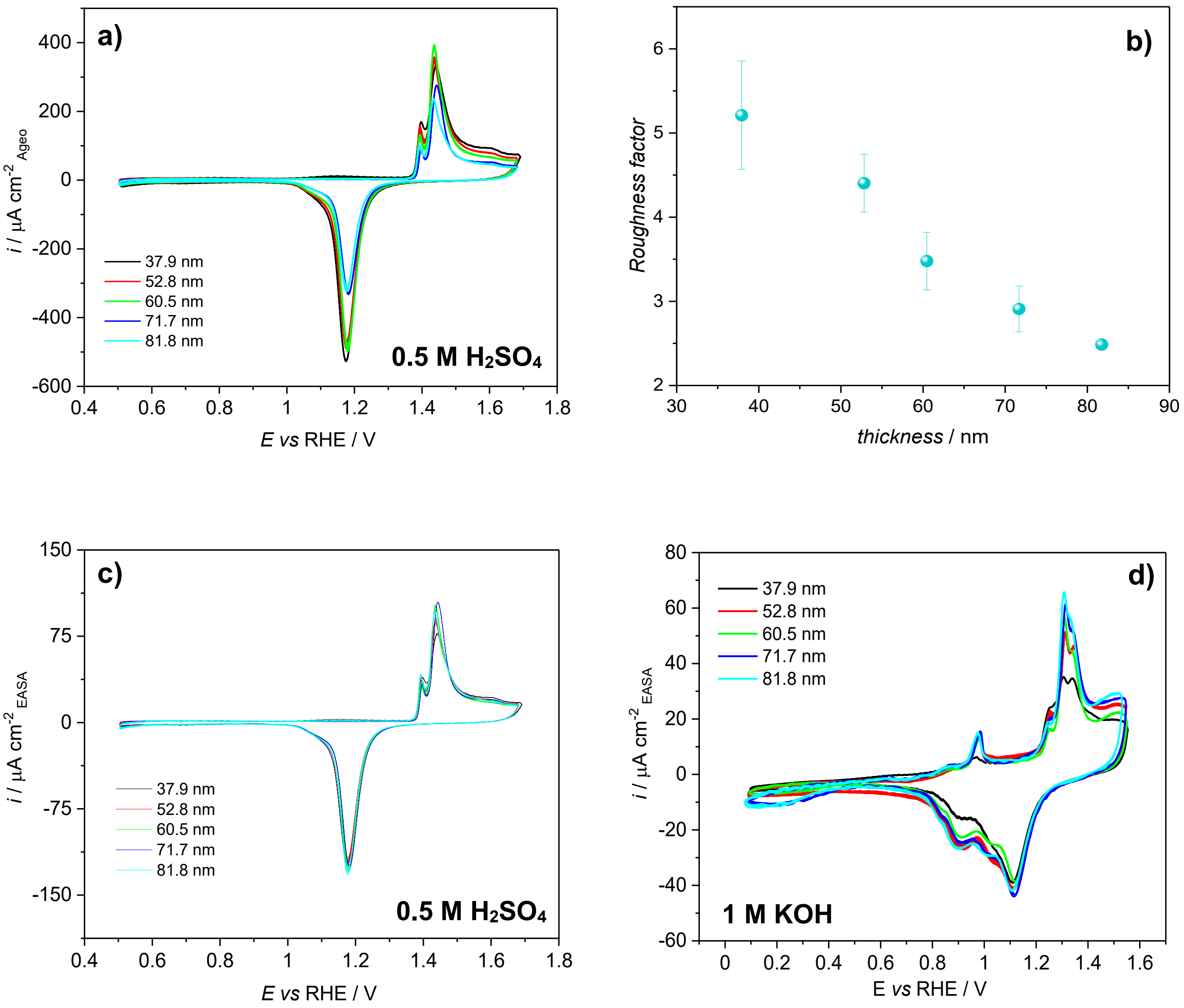

Figure 8-8: CVs of Au/MgO(100) films recorded at 50 mV/s in 0.5 M H_2SO_4, in a) and c), b) shows a plot of R_f as versus the thickness of the films, and d) CVs for the films in 1 M KOH.

The estimative of the EASA of each film according to the respective thickness was achieved using the stripping of the monolayer oxide as described in the previous chapter. From the EASA, then the roughness factor, R_f, was obtained – with R_f defined as the ratio between the EASA and the geometric surface area of the electrode. The R_f values decreased from 5 to 2 with the thickness of the films, Figure 8-8b). After the normalization for the EASA, Figure 8-8c), the CVs are superimposed, demonstrating that the differences in the current densities come mainly from the variation in the active surface area of the films.

The EASA normalized CVs recorded in 1 M KOH at 50 mV/s show similar features for all the films, Figure 8-8d). Except for the thinnest film, the CVs almost superimpose to each other. The features in the CVs were described with details in chapter 7, section 7.2.3, as well as the comparison with the electrochemical behavior reported for the Au(100) single crystal in both media. The voltammograms demonstrate that regardless of the thickness of the films, they show an electrochemical behavior similar to the analogous single crystal.

8.4.2 Lead underpotential deposition – Pb UPD

In this section, the Pb^{2+} deposition and stripping on the gold surface will be used to characterize the symmetry of active surface sites exposed in the films. Additionally, it can provide information on the evolution of the surface with the thickening of the films.

The underpotential deposition (UPD) is characterized by the deposition of a metallic monolayer onto the surface under study at potentials more positive than the reversible Nernst potential of deposition of the same metal[327-328]. The most remarkable advantage of using a foreign metal UPD as a probe is that it provides accurate and reproducible control of the adsorbate layer coverage and reflects the effect of coverage-dependent properties, as, for instance, the surface structure[327-328].

The Pb UPD is widely used to characterize gold electrode surfaces, and there are many reports in the literature describing the voltammograms obtained in the presence of lead for the low[11–13] and high index[14] gold single crystals. Once the response obtained for those very defined model surfaces is characterized, it can be used to characterize the different domains present on gold surfaces. The method has been successfully applied to characterize gold-based materials[12,15,16]. It is worthy of note that the fact that the stepped surfaces[14] are also well-characterized, which can provide information regarding the presence of defects on the surfaces.

Therefore, lead UPD is applied to obtain additional information about the surface structure and the symmetry of the surfaces obtained for the films deposited with different thicknesses.

The Pb UPD voltammograms of the thinnest conductive sample (25000 pulses, ≈ 35 nm), Figure 8-9a), shows several depositions and striping peaks. The stripping peaks are are better resolved, and for this reason, these peaks are used for the analysis. In the voltammogram, five anodic peaks are labeled from A_1 to A_5. An attempt of deconvolution of the voltammogram was performed to find the most accurate position of the peaks, Figure 8-9b). For the deconvolution, the adsorbate coverage was considered to follow a Frumkin isotherm, and the peaks were fitted with a Lorentzian function[60, 329].

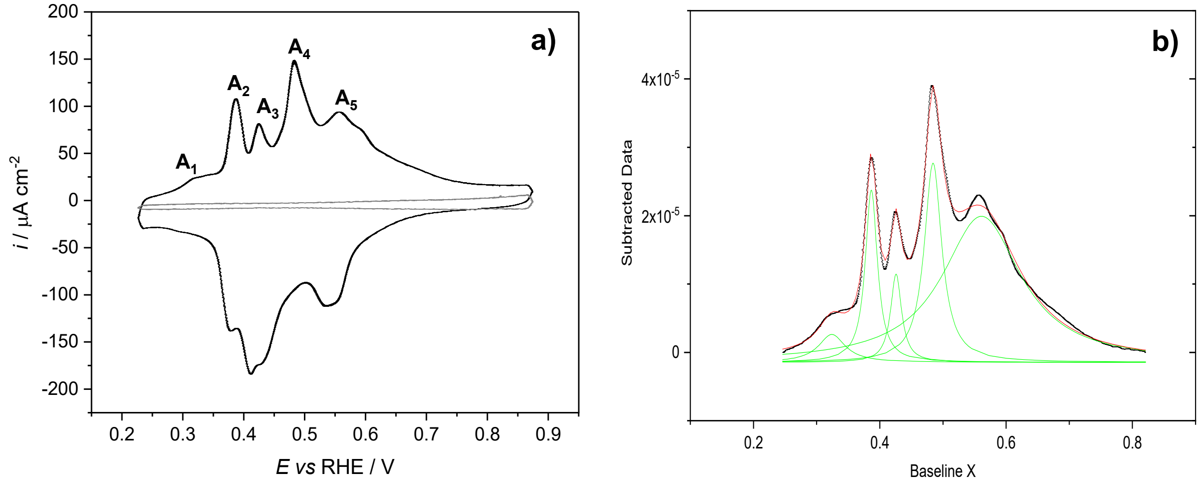

Figure 8-9: a) Pb UPD voltammetry recorded at 50 mV/s in 0.1 M NaOH + 2 mM Pb(NO$_3$)$_2$, b) deconvolution of the Pb stripping profile seen in a) data fitted with a Lorentzian function and the R-Square ≈ 0.995.

Table 11 lists the position of the peaks and their relative integrated area. For comparison, the position reported in the literature was also added. The first and smallest contribution comes from the peak A$_1$. According to the literature[330], this peak rises from the stripping of Pb^{2+} adsorbed on defective sites, kinks, or very narrow steps. A$_2$ shows a narrow peak centered at 0.386 V with the contribution to the total integrated area of nearly 12%. This potential matches closely the potential reported for the minor contribution of the (100) single crystal, seen at 0.385 V. A$_3$, centered at 0.426 V reveals a small (111) contribution is likely coming from narrow domains (either steps or narrow terraces). This conclusion is based on the fact that the potential reported, 0.435 V, is attributed to wide (111) terraces. When the domain shows a narrower size, the main peak shifts a few millivolts towards negative potentials[330-331]. Then, A$_4$ appears at 0.484 V, contributing to approximately 20 % of the integrated area. The main contribution observed for the Au(100) single crystal appears at 0.475 V, and therefore, A$_4$ also comes from the stripping of Pb^{2+} from (100) sites. The shift in the potential position comes from that the domain size existing in the surface of the film is not the same as the terrace's length found in the single crystal. Finally, A$_5$ represents the main contribution in the stripping profile, and it is attributed to the stripping of lead at the (110) sites[330-331].

Table 11: Experimental and reported data obtained for the Pb UPD on the 35 nm sample.

Label	E *vs.* RHE / V	Symmetry	Relative Integrated Area %	E *vs.* RHE / V literature[330]
A_1	0.324	kinks	3.99	E < 0.400
A_2	0.387	(100)	12.09	0.385
A_3	0.426	(111)	5.69	0.435
A_4	0.484	(100)	20.15	0.475
A_5	0.561	(110)	58.07	0.560

Therefore, the electrochemical response of this surface shows the contribution from all low index facets, which is characteristic of a polycrystalline surface. In fact, the comparison of the Pb UPD profile of the 35 nm film with one obtained for a polycrystalline gold foil reveal similarities (Figure 8-10). The peaks appear in a slightly different position because the size of the domains present on both surfaces is not the same. The polycrystalline profile shows mostly (110) and (111) sites and a small amount of (100) sites. In this sense, the film shows a higher amount of (100) sites than a polycrystalline surface.

Noteworthy is that the Pb UPD probe the symmetry of the active sites available at the electrode surface, and therefore, it is a surface analysis method. In opposition, XRD provides information on the bulk structure of the films (penetration depth may vary with the incident angle of the X-ray beam but is typically from 1 to 50 µm[332]), and for this reason, the conclusions drawn from both techniques may differ. Especially considering that under potential cycling, the surface can rearrange the surface organization to minimize the surface energy[135]. However, there is no detectable evidence in the voltammograms that the surface of the film rearranged after the potential cycling in acidic media.

Nonetheless, the AFM images may help with the explanation of such surface behavior. The images showed that although some of the islands are connected to create the percolation pathway, there were holes in the film. Likely, the electrolyte permeates into these holes exposing the other crystallographic planes on the facets of the islands. The literature shows that the Pb UPD of cubic nanoparticles that exposes a higher fraction of the (100) facets, is very similar to the profile experimentally obtained herein; therefore, the electrochemical behavior of the film resembles the one reported for cubic nanoparticles[333].

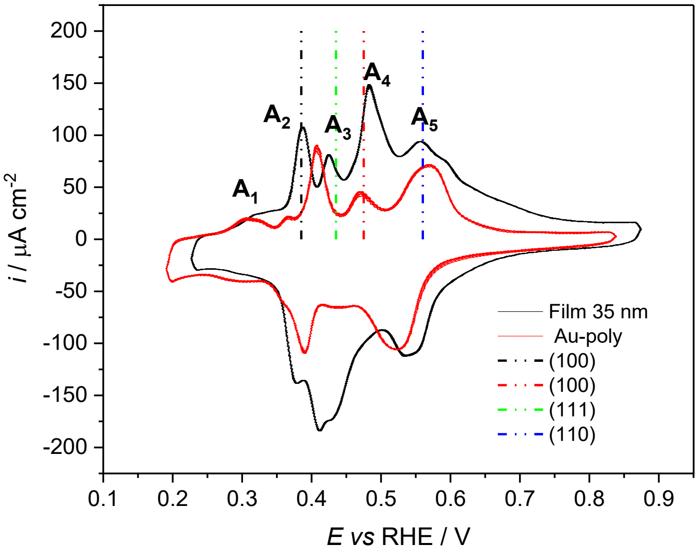

Figure 8-10: Pb UPD voltammetric profiles recorded experimentally at 50 mV/s in 0.1 M NaOH + 2 mM $Pb(NO_3)_2$, for the 35 nm film and polycrystalline gold electrodes.

For the thicker films, the symmetry of the adsorption sites changes significantly, Figure 8-11.

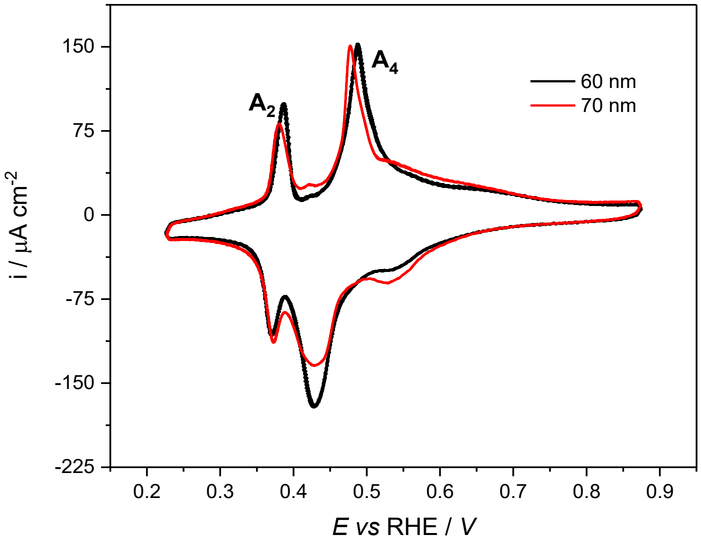

Figure 8-11: Pb UPD voltammetry recorded at 50 mV/s in 0.1 M NaOH + 2 mM $Pb(NO_3)_2$, for the 60 and 70 nm thick samples.

The samples with 60 and 70 nm thick show similar Pb UPD voltammograms compared to each other but quite different from those seen for the 35 nm sample. The thicker samples show only stripping peaks: A_2 at ≈ 0.385 – 0.387 V and A_4 at ≈ 0.477 – 0.487 V. These peaks appear in the potential expected for the (100) sites as reported in Table 11. Since they are the only peaks seen, they demonstrate that the facets of the island with other crystallographic orientations are no longer exposed, and only the (100) sites exist on the surface of the film. Therefore, the results obtained by the Pb UPD corroborate the structural data and support the voltammetric data showing an electrochemical behavior of the films are expected for Au(100) crystallographic surface.

8.4.3 Sampled current voltammetry – ORR

SCV was used to assess the ORR electrocatalytic activity of the thin films according to their thickness. After subtracting the background currents, the ORR polarization curves were reconstructed by sampling the current at 43 ms from each transient and plotted versus the potential applied to the working electrode to generate the transient, Figure 8-12a). This sampling time was chosen to correspond to the mass transfer coefficient achieved by 1600 rpm rotation rate in RDE/RRDE experiments. A polarization curve obtained for a polycrystalline gold electrode foil obtained with the same experimental protocol was added to the plots for comparison.

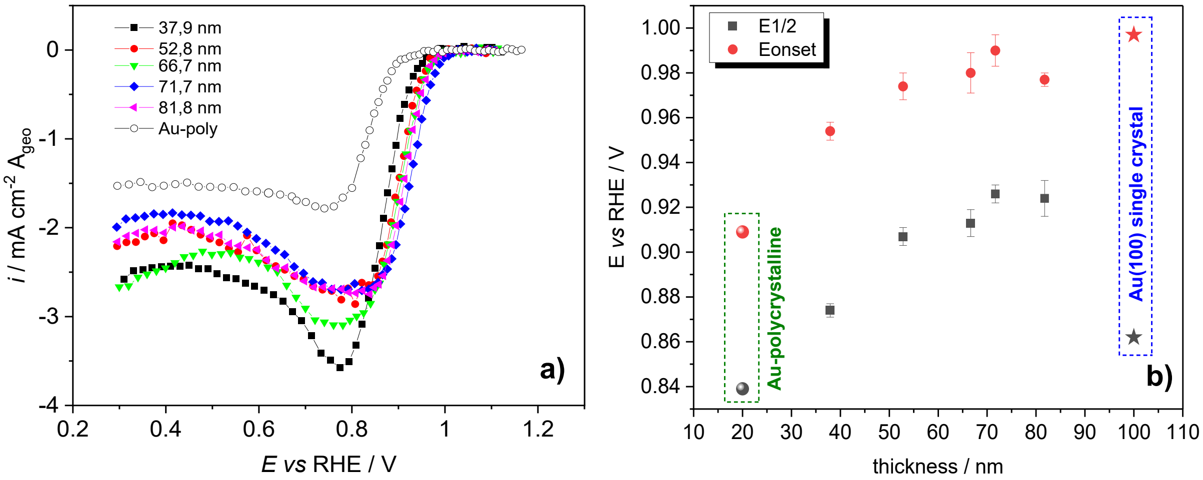

Figure 8-12: a) reconstructed SCVs for the films with different thicknesses, b) plot of $E_{1/2}$ and E_{onset} *vs.* the thickness of the films, data for the Au(100) single crystal taken from reference[9].

Overall, the reconstructed sampled current voltammograms show similar features for the films: at potentials more positive than 1.0 V, the current recorded is very close to zero; therefore, the ORR starts at appreciable rates at potentials below 1.0 V. As the potential becomes more negative the current measured increases steeply until it reaches a maximum value at nearly 0.790 V, and then it decreases to achieve a lower limiting current at approximately 0.400 V. Although the similarities between the polarization curves, they appear shifted regarding each other according to the thickness of the film. The normalization of the current densities for the respective limiting current eliminates the mass transfer effects and reveals purely kinetic effects. In this sense, the normalization of the curves corroborated these results and indicated a real kinetic effect ruled by the thickness of the film. The normalized plots are shown in Appendix III.

The SCVs obtained for the films are similar to the hydrodynamic polarization curves (using either RDE or RRDE setups) obtained by different authors for Au(100) single crystals in both 0.1 M NaOH[3,17,30] and 0.1 M KOH[9,29]. In both electrolytes, the typical polarization curve obtained for the single crystal also shows a maximum of current at around 0.650 V *vs.* RHE[9], followed by the decrease in the current due to the change in the ORR pathway, where the 4-electron transfer changes to a 2-electron transfer.

RRDE studies of the ORR on Au(100) in alkaline media[3,93,9] demonstrated that on this surface, the ORR proceeds by the series exchange of four electrons, reducing the O_2 to OH^- through the formation of OH_2^- as intermediate – for potentials between 1.00 V and approximately 0.600 V, which comprises the maximum of current measured in this work. Whereas for potentials more negative than 0.600 V, the number of electrons exchanged decreases to two to produce mainly peroxide (HO_2^-), resulting in the decrease of the current. Studies on the peroxide reduction in alkaline media on the basal plans of gold have shown that Au(100) is the most active surface for this reaction and that region with the highest current overlaps with the maximum activity for the ORR[3,30]. This potential window coincides with the potential where the specific adsorption of the OH takes place[228]. Hence, the ORR activity of the Au(100) is at least partially related to its ability to reduce the peroxide to OH^- which by its turn, is associated with the specific adsorption of OH [216, 277-278, 283].

To further characterize the electrocatalytic activity of the films, the onset potential of the ORR, E_{onset} – defined herein as the potential measured when the current density value is - 0.1 mA cm^{-2} – and the half-wave potential, $E_{1/2}$ (defined as half of the maximum current measured) were plotted as a function of the thicknesses of the films, Figure 8-13b). Data obtained for the polycrystalline electrode in 1 M KOH and an Au(100) single crystal in 0.1 M KOH (2500 rpm)[9] using an RRDE setup were added for comparison. The analysis of the E_{onset} reveals a shift of potential towards more positive potentials as the thickness of the films increases. The values shift from approximately 0.954 V to 0.990 V *vs.* RHE for the 37.9 nm and 71.7 nm film, respectively. The E_{onset} values obtained for the films are at least 40 mV more positive than the polycrystalline electrode – considering the 37.9 nm film. The films show onset for the ORR comparable to the observed for the Au(100) single crystal (0.978 V *vs.* RHE).

The values of the $E_{1/2}$ vary from 0.874 V to 0.926 V *vs.* RHE for the 37.9 nm and 71.7 nm film. These values follow the same trend as observed for the E_{onset} of the ORR and become more positive as the films become thicker. The potentials shift reveals that the thicker films are more active for the ORR, with apparent maximum activity observed for the 71.7 nm film. The values of $E_{1/2}$ obtained for the films are more positive than the obtained for gold polycrystalline and the single crystal (0.862 V *vs.* RHE).

The kinetic currents obtained from Koutecky-Levich plots, Figure 8-13a), were plotted as a function of E to yield the Tafel plots[3535], shown in Figure 8-13b).

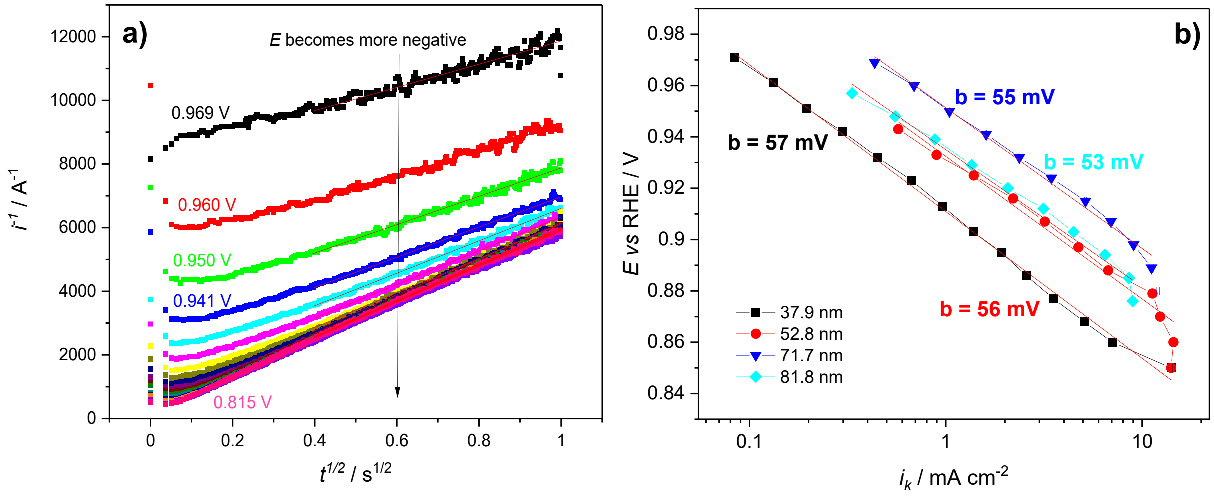

Figure 8-13: a) K-L plots for the 71.7 nm sample and b) Tafel plots for the films with several thicknesses.

The Tafel plots show straight lines closely parallel to each other. The slopes range from 53 – 57 mV, suggesting the same rate-determining step for the ORR within the film thickness studied. Nonetheless, the rate of reaction is significantly improved for the thicker films, with maximum current being achieved for the 71.7 nm thick film. The Tafel slopes found experimentally differ from the typical Tafel slopes reported in most papers for the ORR[127, 225, 231, 290, 294] on Au single crystals, 118-120 mV. Such range of slopes suggests that the rate-determining step is the first electron transfer to the oxygen molecule[231, 290, 334]. However, our values of the Tafel slope indicate that the *rds* in the thin films are different.

Schmidt et al.[26] reported two Tafel slopes for the ORR on Au(100) single crystal in 0.1 M KOH. At the low current density region, they found 47 mV, whereas, for the high current region, they reported 119 mV. The authors kept the mechanistic discussion on general terms, and they assumed the first electron transfer as the *rds* on the Au electrodes (119 mV slope found for high current density). Srejić et al.[292] also reported two slopes for Au(100)-like polycrystalline gold electrodes in 0.1 M NaOH, 63 mV, and 117 mV for the low and high current densities, respectively. Based on Paliteiro's[291] work – also on Au(100)-like polycrystalline electrodes – Srejić et al. proposed that a 60 mV slope appears when the *rds* is the diffusion of adsorbed O_2^- on the electrode surface to a more favorable site for the reaction to proceed. This proposal is similar to the one formulated by Shinagawa et al.[334], where the authors modeled possible Tafel slopes and their respective rds for several reactions, including the ORR. According to the authors, a 60 mV Tafel slope emerges when the surface coverage by the O_2^- species - which is potential-dependent – limits the ORR reaction rate.

The voltammograms obtained for the Au/MgO(100) films in acidic and alkaline media indicated an electrochemical behavior similar to the single crystal. Thus, it is hard to explain why the rds obtained for the ORR on the films differ from the Au(100) single crystal. A possible reason could be the significant differences in the surface morphology of the single crystals and the films. The single crystals have long and flat (100) terraces, whereas the films are built of an assembly of crystallites growth on the [100] direction to form a mosaic structure. The films' surface has defects and grain borders as the crystallites are not perfectly aligned. These defective sites may interact differently with the species involved in the ORR, changing the rds. This hypothesis needs to be confirmed in future work after a full description of the films' surface structure.

In this sense, the electrochemical behavior of the Au stepped surfaces (also known as vicinal to [hkl] direction or single crystals with high index) may help to understand the variation in the ORR activity observed for the films with the increasing thickness. ORR studies carried out on Au(100) vicinal surfaces demonstrated that the ORR activity observed depends on the density and the symmetry of the steps[159, 225, 294]. The introduction of steps at the Au(100) single crystal was found to decrease the overall activity for the ORR, and the number of electrons exchanged. Additionally, steps with (110) symmetry are more detrimental to the ORR performance than (111) steps[24]. Considering this scenario, the E_{onset} and $E_{1/2}$ were taken from the ORR polarization curves provided by the literature[159, 292, 294] were plotted as a function of the (100) terrace width, Figure 8-14. The plot shows that as the width of the terraces increases, both parameters shift towards more positive potentials. None of the stepped surfaces surpasses the activity observed for the Au(100) single crystal, confirming that the presence of long (100) terraces at the surface is fundamental to achieve high reaction rates and selectivity.

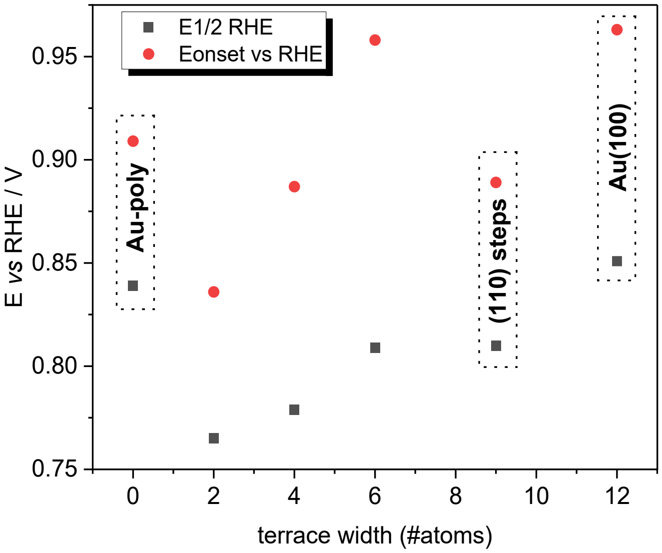

Figure 8-14: Plot showing the ORR parameters for Au stepped surfaces, data taken from references[159, 292, 294].

The most remarkable change in the structure of the Au films triggered by the variation of the thickness is the (100) domain size in the in-plane direction of the surface, increasing with the thickness of the films. The experimental values of the E_{onset} and $E_{1/2}$ were plotted as a function of the lateral coherent size, Figure 8-15. The plot shows that both parameters shift to more positive potentials as the domain size increases, and the films behave similarly to the vicinal Au(100) single crystals. As the films become thicker, they become more active, as in the case of the stepped surfaces, the longer the Au(100) terraces on the surface, the better activity.

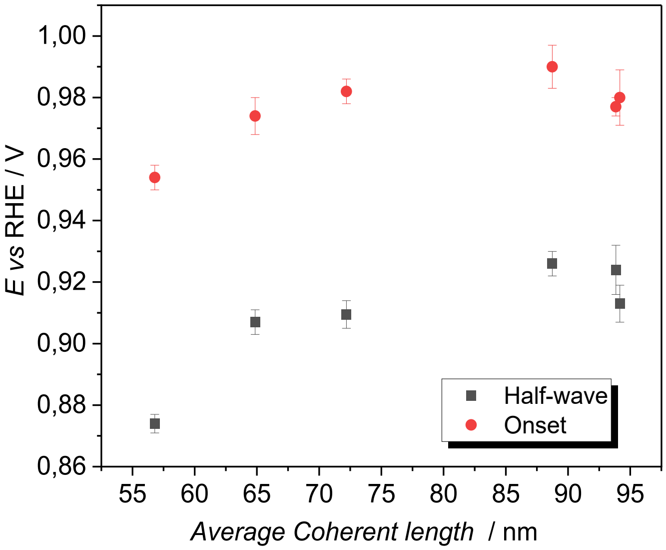

Figure 8-15: Plot of kinetic parameters experimentally obtained for the ORR for the films as a function of the average LCL obtained from the RSM analysis.

Since the presence of defects at the Au(100) surface – steps, mismatch on lattices and border grains – decreases the overall activity and the selectivity for the ORR, the broader domains found on, the thicker films offer more active surfaces for the ORR because they exhibit a long-range order, approximating to the flat and wide single-crystal domains. The presence of defects at the border of the crystallites onto the film's surface likely is in the origin of the decrease of the limiting currents.

Hence, *L* can be regarded as the length of the perfect (100) sites domains diffracting together in the crystal forming the films, analogously as the terrace's length in the single crystals. If one thinks of the film structure as a patch of crystal blocks that are misoriented and misaligned with respect to each other – which originates the mosaicity of the structure – *L* provides a measure of how long are the (100) domains before a defect appears (for example, a grain border and/or misorientation of the grains regarding the surrounding crystals).

8.5 Conclusions

Au/MgO(100) films epitaxially oriented in the [001] direction with thicknesses ranging from 25 to 83 nm were successfully grown by PLD. The electrochemical characterization supported the film's structural characterization results, and their electrochemical behavior resembles that of an Au(100) single crystal. The CVs in acidic and alkaline media showed similar features for all thicknesses, and the differences in the currents measured were mostly a consequence of differences in the electrochemically active surface area of the films.

The activity for ORR increased with the thickness of the films, as the E_{onset} for the ORR and $E_{1/2}$ became more positive as the film grows thicker, with 71.7 nm being the most active. From 71.7 to 83 nm, it seems to exist a plateau where neither the E_{onset} for the ORR nor the $E_{1/2}$ potentials shift anymore. The Tafel plots suggest that the mechanism remains unchanged with the thickness, but the 71.7 nm thick film achieved the highest reaction rate.

The RSM studies have shown that by increasing the thickness of the films, the *L* varies from 40 to 90 nm. The SCV results demonstrated that the ORR activity of the films improved as the size of the (100) domains increased. In this respect, the thin films behave similarly to Au surfaces vicinal to the Au(100), where the ORR activity increases with the width of the (100) terraces.

The magnitude of the strain introduced in the Au/MgO(100) lattice was insufficient to cause significant changes in the surface properties of the films. The higher strain found in the films' lattice was 0.25%. In Pt films, the enhance in the ORR activity was achieved for strain ranging from 0.30[65] to 1.47%[66], which suggests that to observe such effect on Au surfaces, more strain should be introduced in the lattice of the films. In order to produce more strained Au(100) surfaces, different alternatives exist. The first one consists of the introduction of another FCC metal with a higher lattice constant than Au in the films, for instance, by co-depositing lead or yttrium. Another route may use a different ceramic substrate with a higher lattice parameter than the MgO – as yttrium doped zirconia substrates (YSZ) which lattice parameters ranging 5.125 Å.

The most important finding is that the electrocatalytic activity exhibited by the Au(100) domains depends on their size and long-range order. This observation may bring light to the size effects in Au nanoparticles for the ORR[67]. These findings indicate that not only the presence of the sites with (100) symmetry but also the dimensions of these active sites play a fundamental role in the activity of the Au surfaces.

9 SCV APPLIED TO THE STUDY OF ADSORBED SPECIES

9.1 Introduction

The most important electrochemical reactions involved in the energy conversion processes, i.e., the hydrogen oxidation reaction (HOR) and the ORR, involve at least one adsorption step in the overall reaction pathway. These reactions take place at a different rate according to the electrode nature, which is at least partially associated with the adsorption strength of the involved species on the surface[95, 108]. The adsorption forces may be weaker, where the adsorbed species are still free to diffuse along the material's surface, or stronger, where a true chemical bond is formed between the adsorbate and the surface by electrons exchange or sharing. The combination of these possibilities is part of what gives metals their catalytic properties.

Platinum is the state-of-art electrocatalyst for a series of electrocatalytic reactions, and for this reason, it plays a fundamental role in electrocatalysis. Due to its surface reactivity, Pt strongly adsorbs several molecules, for instance, O_2, C_2H_2, C_2H_4, CO, and H_2 [86]. For example, the high rate at which the H_2 oxidation and evolution on Pt surfaces are related to the reversibility of the hydrogen adsorption and desorption processes on the Pt[193, 335]. On the other hand, in the ORR, the adsorption and desorption rates of the O_2, OH, and HO_2^- affect the reaction rate and the rate-determining step on metallic surfaces[29-30]. For these reasons, the study of the adsorption processes and the elucidation of their role in the reaction pathway is fundamental to disentangle reaction mechanistic aspects and develop better electrode materials for these reactions.

Using SCV in Pt microelectrodes, Perry et al. [32, 260] provided a significant contribution to the ORR study. Their studies detected the reduction of pre-adsorbed oxygen species at the electrode surface when O_2 was present in 0.1 M $KClO_4$ solutions. The formation and reduction of these species is a fast process, and their observation was possible because the current transients showed an excess of charge in a timescale shorter than 100 ms. Since the diffusion-controlled ORR can be accurately quantified, it was possible to detect the extra charge. Extending their studies to Pt alloys, they observed that the charge in excess varied according to the alloy, and it was lower for the Pt-alloyed electrodes compared to Pt electrodes. According to the authors, the excess of charge is associated with the reduction of atomic oxygen coming from the dissociation of the O_2 molecule before the ORR. Their findings support an ORR dissociative mechanism on poly-Pt surfaces in neutral pH.

Thus, Perry et al. findings demonstrated that SCV could be strategically used to study surface processes in microelectrodes by modulating the sampling times used to reconstruct the sampled current voltammograms or directly analyze the current transients. Such an approach provides an overview of the decay of surface processes with time with the advantage that the same initial surface state is shared over the entire potential window and that each transient can be analyzed independently. The detection of these adsorbed species on the Pt surface before the ORR was reported for the first time by them.

The methodology using SCV to assess the adsorption of species has been refined by a Rodrígues et al.[336], and in a recent publication, they demonstrate how to extract kinetic information on reversibly adsorbed species with detail.

Here, we explore the use of SCV to study the adsorption of species on Pt oriented thin film electrodes in acidic conditions. For this purpose, Pt/ MgO(hkl), hkl = (100), (110), and (111) thin films will be used as model surfaces.

9.2 Experimental

The Pt films were deposited by PLD, and the details of the deposition are enclosed in the experimental section. The Pt layers were deposited onto MgO(hkl) substrates – with (hkl) = (100), (110), and (111) – previously buffered with a Ni layer. The number of pulses applied on the Pt target – 40000 – yielded films with an average thickness of 13.48 ± 3.39 nm.

9.3 θ – 2θ scans

The diffraction pattern obtained for the films resembles those described in chapter 6 for the Pt/Ni/MgO(110) films, where the main features appearing in the diffractograms were discussed. Regardless of the film orientation, the pattern of high crystalline substrates dominates the diffractograms and is responsible for the most intense peaks observed, Figure 9-1a) to c), where the substrate's pattern appears for guidance.

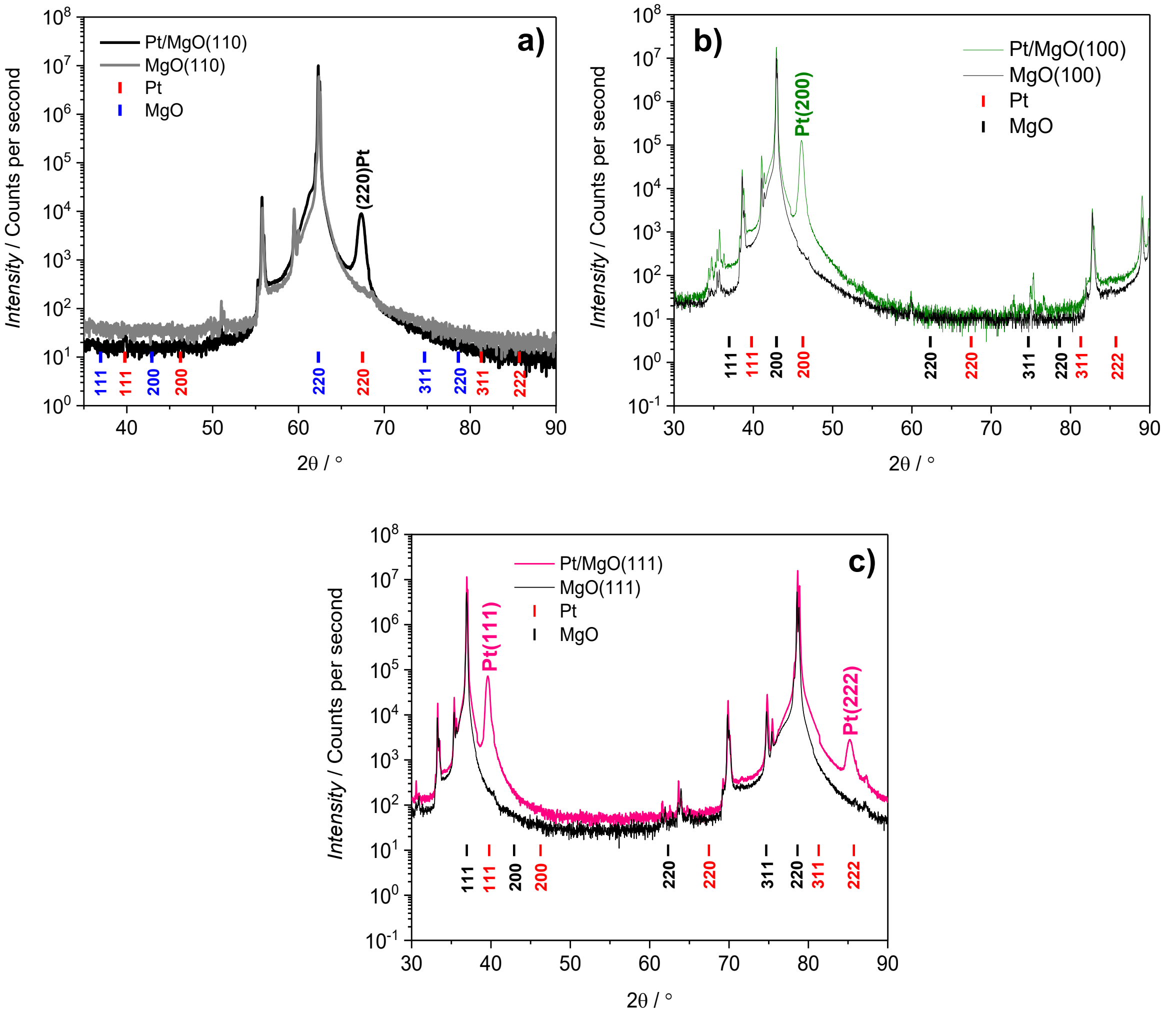

Figure 9-1: X-ray diffractograms recorded for a) Pt/Ni/MgO(110), b) Pt/MgO(100), and c) Pt/MgO(111) films.

The diffractogram obtained for the Pt/Ni/MgO(110), Figure 9-1a), was already described, and details are available in chapter 6. In Figure 9-1b), where the Pt layer was deposited onto the MgO(100) substrate, the only diffracting peak coming from the platinum phase arises at 2θ = 46.106°. This peak position is close to the expected angular position coming from the diffraction of the (200) planes of Pt (JCPDS card 00-004-0802), 2θ = 46.244°. From the experimental angular position, the estimated interplanar distance of the (200) planes are 1.9688 Å, which is greater than the 1.9616 Å reported for Pt. The Pt/Ni/MgO(111) film shows two diffraction peaks coming from the platinum layer, the first at 39.585 ° and the second at 85.237 °, Figure 9-1c). These angular positions are close to the expected for the diffraction of the (111) and (222) platinum planes. Using the (hkl) peaks' angular position, the structural parameters for the sample were obtained, Table 12.

Table 12: Out-of-plane lattice parameters obtained experimentally for the Pt/Ni/MgO(100) films.

Sample	(hkl) 2θ / °	d_{hkl} / Å	$a_{(hkl)}$ / Å	Strain / %
Pt Bulk (110)	67.456	1.3873	3.9231	*
Pt Bulk (200)	46.244	1.9616	3.9231	*
Pt Bulk (111)	39.765	2.2650	3.9231	*
Pt/Ni/MgO(110)	67.275	1.3918	3.9365	0.321
Pt/Ni/MgO(100)	46.106	1.9688	3.9376	0.367
Pt/Ni/MgO(111)	39.585	2.2768	3.9435	0.519

By comparing the interplanar distance and lattice parameters obtained for the films with those reported for bulk platinum, it can be concluded that all three oriented films are under tensile strain in the out-of-plane direction. The deviation of the films' interplanar distances with respect to the bulk platinum is likely related to the mismatch with the MgO substrates and platinum. The Pt lattice constant of the bulk material is smaller than the MgO's, with a mismatch of approximately 6.84%.

9.4 Cyclic Voltammetry

The electrodes' activation was performed by applying 15 voltammetric cycles between 0.04 V - 1.20 V at 20 V/s. Then, to follow the surface changes after applying such conditioning, voltammograms were recorded at 100 mV/s. This procedure was performed to achieve a steady voltammogram characteristic of a clean platinum facet without causing surface disorganization by introducing defects at the surface.

The features seen in the voltammograms of clean and ordered platinum electrodes are known and readily available in the literature. Single crystals experiments led to the deconvolution of the symmetry of the active sites on the surface so that the voltammogram of each of Pt low index surfaces can be regarded as a fingerprint of that surface[13, 60, 112]. This premise is useful in analyzing the voltammograms recorded for the films and allows the correlation of the surface electrochemical behavior with those of the structure of the films as provided by the XRD analysis.

The steady voltammograms obtained for the films deposited onto MgO(hkl) substrates in N_2 saturated 0.5 M H_2SO_4 are shown in Figure 9-2a) to c).

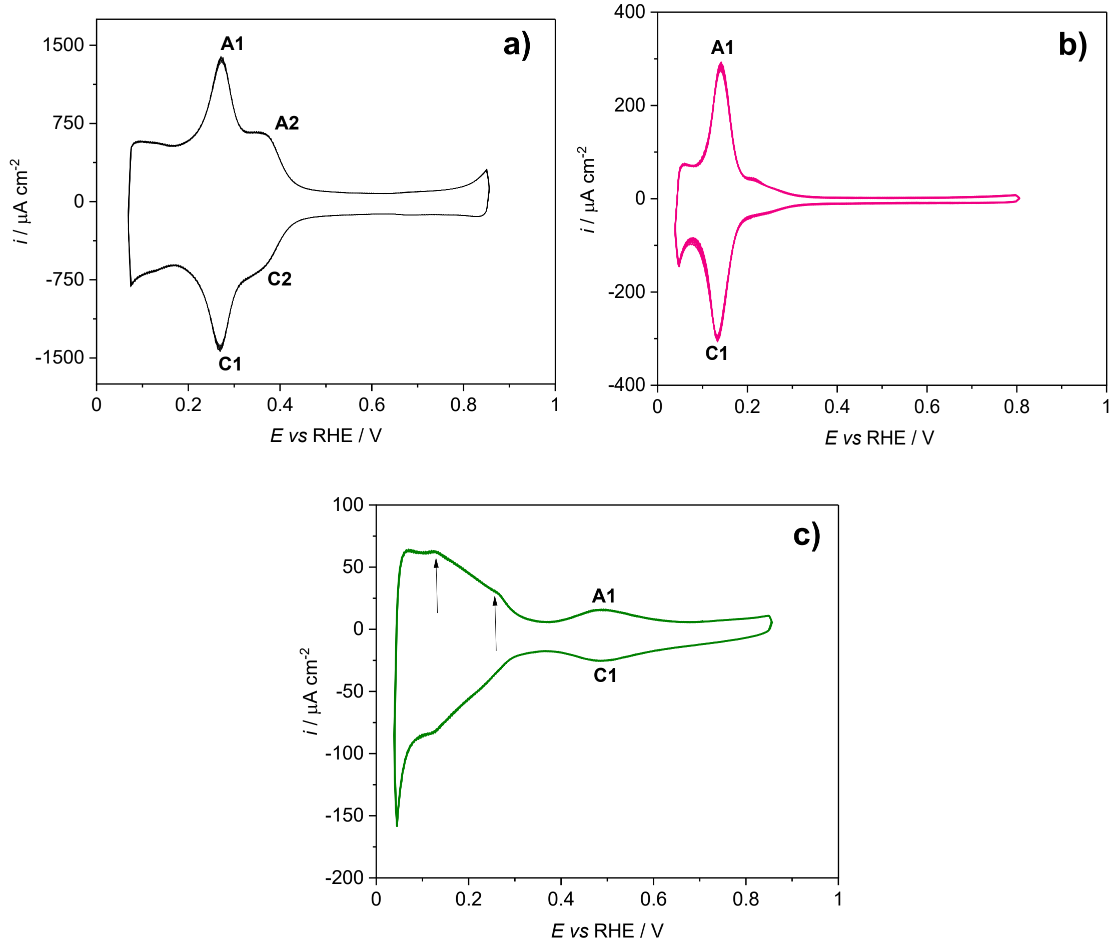

Figure 9-2: Cyclic voltammograms recorded for the Pt/MgO(100) film in a), Pt/MgO(110) in b) and Pt/MgO(111) in c) CVs recorded in N_2 sat. 0.5 M H_2SO_4 at 100 mV/s.

The voltammogram recorded for the Pt/Ni/MgO(100), Figure 9-2a), shows two pairs of anodic and cathodic reversible peaks related to the H_{UPD} at the electrode surface, followed by a double layer potential window. As the potential becomes more positive, the adsorption of oxygen starts to rise at around 0.800 V. The anodic peaks, labeled as A1 and A2, are centered at ≈ 0.272 V and 0.367 V, respectively. According to the literature, these peak positions are similar to the hydrogen desorption peaks position on the Pt(100) single crystals[60, 69, 112] on (100) step sites, at 0.270 V, and on (100) long terraces, at approximately 0.360 V *vs.* RHE. The integration of the desorption of hydrogen between 0.080 – 0.600 V *vs.* RHE – yields 219.8 $\mu C\ cm^{-2}$, a value that is slightly higher than the 208.1 $\mu C\ cm^{-2}$ calculated for a flat Pt(100) single crystal electrode when exchanging one electron per atom of Pt on the (100) surface[112]. This means that the film is not as flat as the single crystal. Hence, the voltammetric information obtained indicates that there are only sites with the (100) symmetry at the electrode surface, which agrees with the structural information extracted by XRD for this sample.

The CV recorded for the Pt/Ni/MgO(110) film is shown in Figure 9-b) for the sake of the comparison, but its features were discussed in detail in section 6.2.2, and they were shown to be consistent with the analogous platinum single crystal.

Finally, the CV recorded for the Pt/MgO(111) is shown in Figure 9-c). The features seen in the voltammogram are different from the Pt/MgO(100) and Pt/MgO(110) in the sense that the sharp and defined peaks for the H_{UPD} are not seen anymore, which is characteristic of the Pt(111) voltammogram. The Pt(111) single crystal in sulfuric acid electrolyte is known for showing a rectangular box shape in the potential window between 0.060 – 0.300 V, followed by two peaks, one at ≈ 0.350 V and a second very sharp and intense peak at ≈ 0.440 V. At more positive potentials another pair of almost reversible peaks appear at 0.700 V *vs.* RHE[13, 58, 60, 112]. The H_{UPD} obtained for the Pt/MgO(111) film shows a wide triangular-shaped box for potentials between 0.050 and 0.300 V. Within this potential window, tiny waves appear – highlighted by the arrows shown in the CV – where hydrogen desorbs for the (110) and (100) sites, and a broad wave with a maximum at ≈ 0.480 V. At potentials positive to 0.300 V, the hydrogen starts to desorb from the Pt(111) surface and then, the specific adsorption of sulfate anions on the surface takes place[112]. Thus, this broad wave is attributed to the sulfate adsorption onto (111) wide terraces domains. Because both species compete for surface sites as the potential becomes more positive, the charge obtained is a mixed charge comprising hydrogen desorption and the sulfate adsorption[112].

Thus, the voltammogram obtained for the Pt/MgO(111) film is different from the one expected for the single-crystal, but there is a dominance of the sites with (111) symmetry exposed the surface of the film. In the film's cyclic voltammograms, the most characteristic peaks reported for the Pt(111) single-crystal in the sulfuric acid electrolyte is absent. The reason is that the sharp peaks seen in the Pt(111) are associated with the long-range order of the (111) surface domains[58], thus if the surface is not highly organized with respect to the (111) sites or the (111) domains are not wide, these peaks are absent of the voltammogram. The integration of the voltammogram to extract the charge amounts to only 170 $\mu C\ cm^{-2,}$ which is lower than the expected for a (111) single crystal surface, 240 $\mu C\ cm^{-2}$ [112]. For the Pt(111) single crystal, the sulfate adsorption features provide a considerable amount of charge as both processes take place simultaneously, but they are observed only (111) well-defined surfaces with wide terraces. Because these features are absent in the film voltammograms, this may be why the charge obtained for the films is lower than the one reported for the Pt(111) single crystal.

9.5 Sampled current voltammetry

The experiments were carried out in N_2 saturated 0.5 M H_2SO_4 electrolyte using the waveform represented in Figure 3-3 (Chapter 3). This waveform comprises the conditioning voltammetry cycles between each potential step. The applied rest potential was 0.975 V for the three cases, close to the open circuit potential.

The sampled current voltammograms for the films were reconstructed for different sampling times, Figure 9-3a) to c). In all cases, the current densities measured are higher for shorter sampling times, and they decrease as the sampling time increases, which is characteristic of fast processes. In the studied potential window, three main processes are observed in all the reconstructed SCVs, hydrogen desorption (H_{UPD}), oxygen desorption (O_{des}), and oxygen adsorption (O_{ads}). For each of these processes, the potentials where they appear and the current densities associated with them depend on the crystallographic orientation of the films, Figure 9-3d).

As expected, the hydrogen desorption appears at potentials lower than 0.40 V for the three films and appears at the potentials characteristic of each Pt crystallographic orientation. The oxygen desorption waves appear between 0.550 – 0.850 V, and they show a different profile for each film, suggesting different interactions between oxygen and the surface of each film.

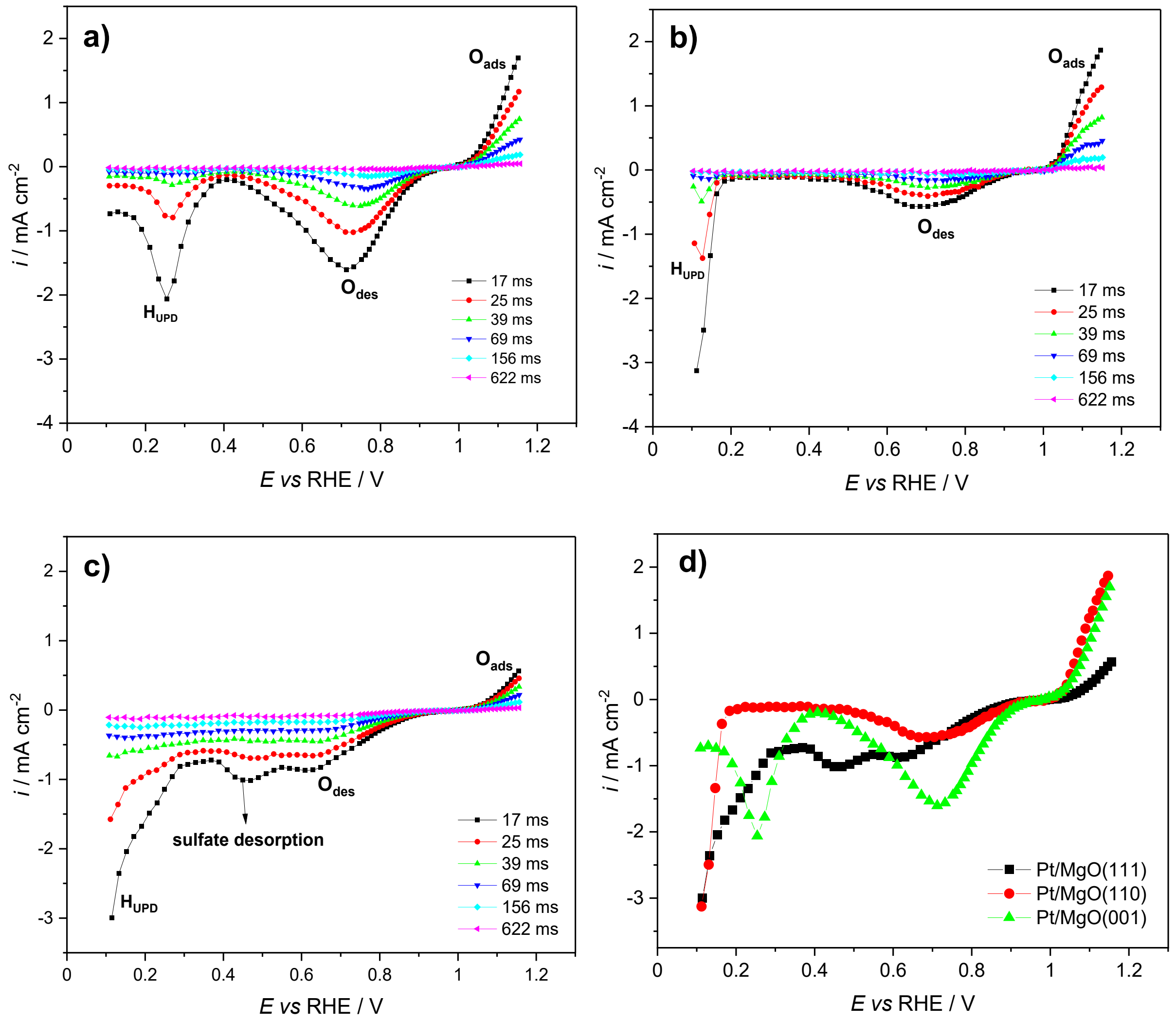

Figure 9-3: Reconstructed SCVs using various sampling times for a) Pt/MgO(100), b) Pt/MgO(110), and c) Pt/MgO(111) in N_2 sat. 0.5 M H_2SO_4, d) shows the SCVs for the three films at 17 ms.

Because the H_{UPD} has been extensively studied, the discussion will focus instead on the oxygen desorption features and their possible correlation with the ORR. The Pt/MgO(100) sample shows the most intense and well-defined peak for the oxygen desorption, suggesting stronger interaction between oxygen and the film. The less intense peak for the stripping of the oxygen adsorbed appears in the Pt/MgO(110) film, and the Pt/MgO(111) shows an intermediate behavior. Interestingly, for the Pt/MgO(111), the desorption of the sulfate on the (111) terraces appears just after the oxygen stripping (at ≈ 0.450 V) in a broad wave.

Figure 9-4a) shows a plot of the peak currents versus the reciprocal of time. The linear relationship found suggests that the peaks come from a real surface adsorption process. This plot is an analogous approach to the classical experiments using linear sweep voltammetry to study adsorption on electrode surfaces. In such experiments, the peak currents also show a linear relationship with the sweep rate[3, 337-338]. In cases where the process being studied is controlled by species diffusion in solution, the peak currents seen in a linear sweep voltammetry increase linearly with the square root of the sweep rate, whereas in SCV, the currents scale with the reciprocal of the square root of the time, following the Cottrell equation.

Figure 9-4b) shows the charge obtained from the integration of the transients applied in the whole potential window studied and plotted versus the potential. If we consider the Pt/MgO(110) and Pt/MgO(100), the samples whose electrochemical behavior is very similar to the corresponding single crystals, oxygen seems to have more affinity to the (100)-oriented film, suggested by the higher stripping charges (for E ≈ 0.700 V). In the Pt/MgO(111) case, the charge associated with the sulfate adsorption (E ≈ 0.400 V) overlaps with the oxygen stripping charge, but considering that the voltammetric features differ from the single crystal, it is difficult to draw accurate conclusions.

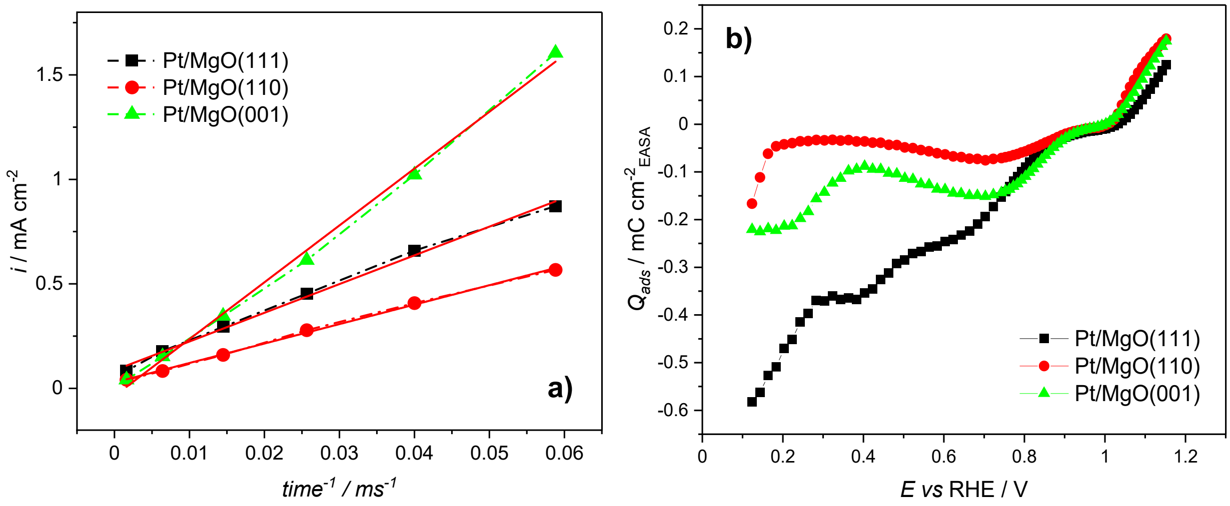

Figure 9-4: Plots of the currents at peak potentials versus 1/time for the films, and b) plots of the charges versus the potential for the films.

The ORR activity on Pt single crystals in sulfuric acid solutions follows the sequence (110) > (100) > (111), and the specific adsorption of species on Pt surfaces in the ORR potential window plays an essential role in this structure sensitivity[22, 75]. In this respect, the adsorption energy of oxygenated species on Pt surfaces is high[339], and the surface removal rate of these species affects the ORR rate[25]. The analysis of the charges experimentally obtained for the oxygen desorption on the Pt/MgO(hkl) films surfaces reveals an increase in the order (111) > (100) > (110), which agrees with the ORR activity trend reported in the literature.

9.6 Conclusions

As proposed by Perry et al.[32, 50, 260], SCV represents a powerful and versatile technique in the electrochemical characterization of surfaces. The results obtained indicate that SCV is not restrained to microelectrodes, and it can be easily applied to planar macroscopic electrodes. It provides a rich body of information not only on diffusion-controlled reactions but also on surface adsorption processes. The technique's sensitivity is demonstrated by the distinct results obtained for each surface, and SCV is sensitive enough to show the adsorption of species at the surface even for fast processes as the H_{UPD}.

The preliminary results showed that even in the absence of O_2 if the electrode is kept at potentials close to open circuit potential, the adsorption of oxygenated species occurs, and the reduction of these species is seen in the SCVs. These oxygenated species likely come from the water discharge at the electrode surface. Importantly, the experimental results indicate that this process is also structure-sensitive on Pt/MgO(hkl) films, and qualitative analysis of the charge associated with the oxygen desorption showed that it increases in the opposite order as the order of the ORR activity on the Pt(hkl) single crystals. This correlation suggests a poisoning effect of these adsorbed species, resulting in the decrease of the ORR rate. To draw more conclusive information regarding the implications of these adsorbed species to the ORR pathway on the Pt low index surfaces, more experiments are necessary. Especially because the electrochemical behavior of Pt/MgO(111) differs from that of the Pt(111) single crystal, even though sites with (111) symmetry are still dominant at the electrode's surface.

Finally, because this set of experiments were carried out in N_2 saturated electrolyte, it is not possible to verify the existence of the excess of charge observed by Perry et al. Their experiments were conducted under an O_2 atmosphere. Thus it is difficult to establish a correlation with their results. In this regard, some modifications of the experimental protocol may be necessary to preserve the films' surface order. Additional studies varying the specific adsorption strength of the spectator anions in the electrolyte and a pH study may also be an interesting route to withdraw complementary information on the adsorption of the oxygenated species on the Pt surfaces and their possible impact on the ORR.

Overall, SCV is a powerful tool in electrocatalysis, particularly when characterizing the surface behavior of new electrode materials.

10 CONCLUSION AND FUTURE PERSPECTIVES

This thesis aims to contribute to the solution of a great problem of modern society, which is how to address the increasing demand for energy in an affordable, efficient, and environmentally friendly manner. The FCs may provide a helpful contribution to this challenging issue, and they are candidates to supply power for mobile and stationary applications with high efficiency, and depending on the fuel used, by producing low pollutant emissions. Hence, the viability of the fuel cells and their commercialization may represent at least partial relief in the problems associated with the intensive use of fossil fuels.

However, there are limitations associated with the FCs operation, and several aspects must be improved to make their extensive application possible. A significant limitation lies in the cost of the Pt electrocatalysts used in the electrodes, especially at the cathode where higher loads of Pt are required to operate well. Furthermore, the cathode imposes a greater challenge because even on Pt, the oxygen reaction rate is low, and the high overpotential necessary to drive the reaction decreases the fuel cell efficiency. Thus, if Pt remains the main electrocatalyst in FCs, their utilization and operation may be limited.

Henceforth, the main motivation of this project is to bring new tools for the study of electrocatalytic reactions involved in energy conversion applications, namely in FCs. In this respect, the first objective of this thesis is to propose thin films with epitaxial orientation deposited by PLD as an alternative route to produce model surfaces for the investigation of the ORR. The film's epitaxial orientation grown by PLD results in materials with a high degree of structural organization that exhibits characteristics remarkably similar to the analogous single crystals. These thin films can then be used as model platforms to study the electrochemical behavior and the electrocatalytic activity for the ORR on a varied range of electrocatalysts. The results reported herein consist of building the foundation for the deposition of films with different characteristics, such as alloyed films, strained thin films, intercalated metallic layers, and near-surface alloys. It is fundamental to understand the effect of the deposition parameters in the structure of the film because by controlling them, it is possible to tailor materials towards specific characteristics and applications. This uncovers a vast range of materials that are not accessible with the classical single crystals' electrochemistry.

This thesis's second objective is to implement the SCV method to investigate the ORR on these thin films. SCV emerged as an alternative method to study the ORR because the MgO substrates are insulating, which makes it impossible to use the hydrodynamic methods (RDE and RRDE).

The fundamental aspects of the SCV were presented, and the experimental conditions that allow the comparison of the SCV polarization curves with the hydrodynamics' were discussed and validated.

The experimental results reported in this thesis provide evidence in favor of the suitability of the thin films with epitaxial orientation as model surfaces for ORR electrocatalytic studies. Pt thin films oriented along the [100], [110], and [111] crystallographic directions were successfully deposited onto MgO(hkl) substrates. The electrochemical characterization in acidic media showed that in the Pt/MgO(100) and Pt/MgO(110) cases, the films' surfaces reflect their bulk crystallographic orientation and provided electrochemical response very similar to the respective single crystal. In acidic media, the Pt(110) is the most active Pt facet for the ORR[22, 24]. For this reason, only the Pt/MgO(110) film was further characterized. Its ORR electrocatalytic activity was assessed in 0.05 M H_2SO_4 + 0.1 M $KClO_4$ using sampled current voltammetry, and the results showed that the film is more active than polycrystalline Pt, which agrees with the reported results for Pt(110) in similar conditions.

Concerning the Pt/MgO(111) thin films, despite the structural characterization points out for an epitaxial growth in the bulk of the film, the long-range surface order seems not enough to exhibit all the voltammetric features of the single crystal. Nonetheless, the (111) is still the dominant symmetry site on the surface. A possible explanation for this could be the film surface reorganization under potential cycling or the need for enhancement on the cleanliness conditions of the whole electrochemical system.

Additionally, Au films grown in the [100] direction were successfully deposited onto MgO(100) substrates. The structural characterization showed that Au the films deposited grew with well-defined structure along the [100] direction, and whose electrochemical behavior is remarkably similar to the reported for Au(100) single crystal. The Au(100) single crystal shows an outstanding high ORR electrocatalytic activity in alkaline media[115, 127, 225, 231, 277, 283]. However, despite the decades of research and efforts of both theoreticians and experimentalists, the origin of this activity remains unclear[227, 230-231, 277, 280, 283, 290]. Thus, studying the ORR on this surface may help elucidate catalytic aspects affecting the reaction rate and provide information on the subject.

Aiming to deposit Au(100) thin films that could behave as a single crystal, i.e., grown with good epitaxy and well-defined structure, exhibiting surfaces as flat as possible, and with low mosaicity in their structure construction, the effect of the deposition parameters used in the Au films on the quality of the films was investigated. This study provided insightful information on how the deposition parameters can be used to tailor the desired material. The study of the effect of the buffer layer, the substrate temperature during deposition, and the film's thickness has shown how the structure can change as a response to changes in these variables. For instance, the films deposited using Ni instead of Ag as buffer layer resulted in films with good adherence to the substrate and mechanical resistance, well-defined structure, and lower mosaicity spread. The main differences observed were seen in the higher ORR activity and selectivity obtained for the film deposited in the Ni buffer layer. The substrate temperature study demonstrated how the temperature can affect the structural organization of the film and its roughness. Higher deposition temperatures led the films' structure to re-arrange in the most stable facet and surface roughening. Thus, the temperature increase is especially important when the targeted growth direction is not the most stable thermodynamically.

Finally, the thickness of the films was varied, aiming to intentionally introduce strain in the Au films' lattice and explore the strain effect on the ORR electrocatalytic activity. Thus, the films were fully characterized, and the epitaxy along the [100] direction was achieved through the full range of thicknesses studied. Their electrochemical behavior revealed that regardless of their thickness, they showed voltammetric features corresponding to an Au(100) single crystal. Afterward, the ORR activity of these films was studied by sampled current voltammetry, and their ORR activity increased with the thickness of the films. The structural characterization demonstrated that the films have some strain in their lattices, but the magnitude of the strain generated seems to be too small to affect the ORR activity. Thus, the variation in the activity observed was not a strain effect.

In this respect, an interesting outcome is that the ORR activity dependence observed in the films is associated with the [100] domain size found in the crystallites building the films by means of the lateral coherent size measured by RSM. Thus, it was observed that the larger the domain size, the higher the ORR activity. If we regard the domain size as the (100) terraces width in the films' surface, a similar trend was reported in the literature for Au stepped single crystals. The ORR activity of the stepped Au surfaces increases with the width of the Au(100) terraces. This suggests that regarding the ORR on Au materials, not only the local symmetry of sites available on the surface matters but also their extension. The consequence of these finds for the design of electrocatalysts for practical applications is that ORR activities as high as the observed for the single crystals may be achieved in where cases the right active domains are wide enough.

The validation of the sampled current as an alternative method to study the ORR is an important parallel contribution of this work to the electrocatalysis field. The conditions where the SCV results can be comparable to the RDE results were derived and validated successfully. First, the reconstructed SCV for ferry-ferro redox pair using a poly-Pt disk provided results that fitted very well to the RDE results, successfully validating the mass transfer coefficient as a key parameter to match results obtained by the two methodologies. Afterward, SCV was used to study the ORR on a poly-Pt disk, and this revealed a challenging system due to the intrinsic reactivity of Pt's surface in aqueous acid solutions and limitations of the SCV itself. In SCV is extremely important to set a neutral rest potential to replenish the electrode-electrolyte interface to the initial concentrations of active species, and thus, no current should pass through the cell during the rest potential. Ideally, the rest potential should provide a surface clean of any adsorbates that could poison the surface and decrease its reactivity. However, after an extensive study of rest potential, it was demonstrated that such a condition on Pt surfaces is unattainable. This happens because maintaining the Pt surface free from oxygen adsorbed would require a rest potential more negative than its OCP. However, under such conditions, oxygen is reduced during the rest potential causing perturbation on the initial concentration in the potential steps.

Then, the OCP was set as rest potential, and the reconstructed SCV for the ORR on the poly-Pt disk corresponded to the cathodic scan in the RDE voltammetry, which refers to a slightly oxidized Pt surface. Despite these challenges, a satisfactory response to the application of the SCV on Pt electrodes to study the ORR was obtained for the poly-Pt disk and the Pt/MgO(110) film, whose results were worthy of a research paper.

Because the nature of Au differs from Pt, the application of the SCV methodology to study the ORR was easier in the sense that there no issues with the rest potential, and the expected response of the Au films for the ORR was achieved. SCV was sensitive enough to provide polarization curves that responded very well not only to the films' crystallographic orientation but also to the (100) surface domain sizes. The kinetic parameters obtained with the Koutecký-Levich and Tafel plots for the Au films also revealed the differences in the activity and allowed to assess how the ORR kinetics on the films responded to the structural changes observed.

The SCV results demonstrate the versatility of the technique and emphasize the potential for its application on systems that cannot be studied in an RDE setup. These are also a significant achievement for the ORR study as it provides a solution for situations where the RDE/RRDE setups are not available or suitable. In the work presented, SCV allowed the study of the oxygen reduction on Pt and Au surfaces under high mass transfer conditions, providing kinetic information on the ORR.

The SCV has the advantage that it can be extended to other diffusion-controlled electrochemical reactions, and in fact, other reactions are under study in our research group, for instance, the hydrazine and the hydrogen oxidation reactions. Additionally, the potential of the SCV in the study of adsorbed species at the electrode surface was also demonstrated. Hence, the SCV is a technique that can be adapted to study different reactions, as necessary, and the only instrumentation necessary is a potentiostat. Using SCV requires a set of experiments to optimize the best experimental conditions, and, at this point, the SCV procedure is like any other technique. The rest potential needs to be regarded carefully because it controls the state of the surface before the reaction takes place, and it can be adjusted by cyclic voltammetry studies in the potential window where the reaction takes place.

The research work reported in this thesis presents and validate a full methodology to perform model studies in ORR electrocatalysis. Therefore, new tools for the electrocatalytic studies of materials for energy conversion applications are now available for experimentalists in the pursue of the new electrode materials for the fuel cells.

10.1 Future perspectives

Following the outcomes reported in this thesis, a promising strategy in the search for new electrocatalysts consists of taking advantage of the versatility of the PLD to prepare a wide range of films with various composition and structure arrangements and test them for the ORR using the SCV. The preparation of alloyed films with epitaxial orientation provides an excellent model platform to establish a structure-reactivity relationship for the ORR that would not be possible or difficult, and time-consuming by other routes.

Regarding the ORR study on Au/MgO(100) films in alkaline media, the aim is to adopt different strategies to introduce more strain in the film's lattice. The first one consists of alloying Au with another FCC metal with a lattice constant larger than that of Au in the films, such as co-depositing lead or yttrium. Currently, Au/MgO(100) thin films co-deposited with Pb have been prepared but not characterized yet. Additionally, and in a second approach, few Pb layers were deposited in between the Au layers as an attempt to produce near-surface alloy. This work is in progress, and structural and electrochemical characterization will be performed. Another route to produce strained films may use a different ceramic substrate with a larger lattice parameter than the MgO – as yttrium doped zirconia substrates (YSZ) which lattice parameter is 5.125 Å. This route is a backup plan, as changing the substrate requires optimization of the deposition parameters, which is time-consuming.

Still aiming at the ORR studies, some depositions using Au and Ti were performed to produce alloys for electrocatalysis. These films must be characterized, and once the composition and structure are known, they may be used to probe the ORR. Furthermore, alloyed Au-Cu films preferentially oriented in the (100) and (111) direction have been achieved. The first was deposited aiming the ORR electrocatalysis and the later, the carbon dioxide reduction.

The SCV methodology has already been adapted and applied in the study of different electrocatalytic reactions: the hydrazine and the hydrogen oxidation reactions. The aim of such experiments is to probe the effect of the film structure arrangement and the electronic properties of the surfaces in the alloyed materials catalytic activity for the referred reactions. The application of the SCV to study both hydrazine and hydrogen oxidation is in progress, and preliminary results point out that an experimental protocol will be applied soon to those reactions on Pt-Ir alloys. Additionally, the study of the hydrogen oxidation reaction in gas diffusion electrons is also part of future work.

Following the work by Perry et al.[32, 260], where the authors reported for the first time an excess of charge in the ORR associated with the adsorption of oxygenated species on Pt surfaces before the ORR, SCV will be used to investigate the adsorption of such species on the Pt/MgO(hkl) films in acidic media. Perry's research was performed in neutral pH using polycrystalline Pt and Pt alloys microelectrodes. Their findings support the dissociative ORR mechanism, and because of the implications for the ORR mechanistic study, it is worthy of extending the approach to different conditions and observe the outcome. The aim is to investigate if the adsorption species on the Pt(hkl) films can be observed if is a structure-dependent process and how it is related to the ORR on single crystals surfaces.

11 BIBLIOGRAPHY

1. Zhang, J., *PEM Fuel Cell Electrocatalysts and Catalyst Layers*. 2008.

2. Carrette, L.; Friedrich, K. A.; Stimming, U., Fuel cells: principles, types, fuels, and applications. *Chemphyschem* **2000,** *1* (4), 162-93.

3. Bard, A. J.; Faulkner, L. R., *Electrochemical Methods Fundamentals and Applications*. 2nd ed.; John Wiley & Sons: New York, 2001; p 833.

4. Tada, T., High dispersion catalysts including novel carbon supports. In *Handbook of Fuel Cells* Wiley: 2010.

5. Gasteiger, H. A.; Gu, W.; Litteer, B.; Makharia, R.; Brady, B.; Budinski, M.; Thompson, E.; Wagner, F. T.; Yan, S. G.; Yu, P. T. In *Catalyst Degradation Mechanisms in PEM and Direct Methanol Fuel Cells*, Dordrecht, Springer Netherlands: Dordrecht, 2008; pp 225-233.

6. Borup, R. L.; Davey, J. R.; Garzon, F. H.; Wood, D. L.; Inbody, M. A., PEM fuel cell electrocatalyst durability measurements. *Journal of Power Sources* **2006,** *163* (1), 76-81.

7. Ferreira, P. J.; la O', G. J.; Shao-Horn, Y.; Morgan, D.; Makharia, R.; Kocha, S.; Gasteiger, H. A., Instability of Pt⁄C Electrocatalysts in Proton Exchange Membrane Fuel Cells. *Journal of The Electrochemical Society* **2005,** *152* (11), A2256.

8. Stamenkovic, V. R.; Fowler, B.; Mun, B. S.; Wang, G.; Ross, P. N.; Lucas, C. A.; Marković, N. M., Improved Oxygen Reduction Activity on Pt3Ni(111) via Increased Surface Site Availability. *Science* **2007,** *315* (5811), 493.

9. Marković, N. M.; Ross Jr, P. N., Surface science studies of model fuel cell electrocatalysts. *Surface Science Reports* **2002,** *45* (4-6), 117-229.

10. Čolić, V.; Bandarenka, A. S., Pt Alloy Electrocatalysts for the Oxygen Reduction Reaction: From Model Surfaces to Nanostructured Systems. *ACS Catalysis* **2016,** *6* (8), 5378-5385.

11. Tian, N.; Zhou, Z.-Y.; Sun, S.-G., Platinum Metal Catalysts of High-Index Surfaces: From Single-Crystal Planes to Electrochemically Shape-Controlled Nanoparticles. *The Journal of Physical Chemistry C* **2008,** *112* (50), 19801-19817.

12. Climent, V.; Feliu, J. M., Thirty years of platinum single crystal electrochemistry. *Journal of Solid State Electrochemistry* **2011,** *15* (7-8), 1297-1315.

13. Climent, V.; Feliu, J., Single Crystal Electrochemistry as an In Situ Analytical Characterization Tool. *Annual Review of Analytical Chemistry* **2020,** *13* (1), 201-222.

14. Kibler, L. A., Preparation and Characterization of Noble Metal Single Crystal Electrode Surfaces. International Society of Electrochemistry: Ulm, German, 2003; pp 1-56.

15. Inkaew, P. Electrochemistry of carbon monoxide on platinum single-crystal surfaces Texas Tech University, 2008.

16. Gómez-Marín, A. M.; Boronat, A.; Feliu, J. M., Electrocatalytic oxidation and reduction of H2O2 on Au single crystals. *Russian Journal of Electrochemistry* **2017,** *53* (9), 1029-1041.

17. Strbac, S.; Anastasijević, N.; Adžić, R. R. In *Electrocatalysis of oxygen on single crystal stepped surfaces of gold*, Bologna, 1988; International Society of Electrochemistry: Bologna, pp 57-59.

18. Campbell, C. T., Studies of Model Catalysts with Well-Defined Surfaces Combining Ultrahigh Vacuum Surface Characterization with Medium- and High-Pressure Kinetics. In *Advances in Catalysis*, Eley, D. D.; Pines, H.; Weisz, P. B., Eds. Academic Press: 1989; Vol. 36, pp 1-54.

19. Yu, W.; Porosoff, M. D.; Chen, J. G., Review of Pt-Based Bimetallic Catalysis: From Model Surfaces to Supported Catalysts. *Chemical Reviews* **2012,** *112* (11), 5780-5817.

20. Markovic, N. M. P. N. R.; Ross, P. N., New Electrocatalysts for Fuel Cells from Model Surfaces to Commercial Catalysts. *CATTECH* **2000,** *4* (2), 110-126.

21. Appleby, A. J., Electrocatalysis and Fuel Cells *Catalysis Reviews* **1971,** *4* (1), 221-244.

22. Markovic, N. M.; Gasteiger, H. A.; Ross, P. N., Oxygen Reduction on Platinum Low-Index Single-Crystal Surfaces in Sulfuric Acid Solution: Rotating Ring-Pt(hkl) Disk Studies. *The Journal of Physical Chemistry* **1995,** *99* (11), 3411-3415.

23. Grgur, B. N.; Marković, N. M.; Ross, P. N., Temperature-dependent oxygen electrochemistry on platinum low-index single crystal surfaces in acid solutions. *Canadian Journal of Chemistry* **1997,** *75* (11), 1465-1471.

24. Markovic, N. M.; Adzic, R. R.; Cahan, B. D.; Yeager, E. B., Structural effects in electrocatalysis: oxygen reduction on platinum low index single-crystal surfaces in perchloric acid solutions. *Journal of Electroanalytical Chemistry* **1994,** *377*, 249-259.

25. Marković, N. M.; Gasteiger, H. A.; Ross, P. N., Oxygen Reduction on Platinum Low-Index Single-Crystal Surfaces in Alkaline Solution: Rotating Ring DiskPt(hkl) Studies. *The Journal of Physical Chemistry* **1996,** *100* (16), 6715-6721.

26. Schmidt, T. J.; Stamenkovic, V.; Arenz, M.; Markovic, N. M.; Ross, P. N., Oxygen electrocatalysis in alkaline electrolyte: Pt(hkl), Au(hkl) and the effect of Pd-modification. *Electrochimica Acta* **2002,** *47* (22-23), 3765-3776.

27. Kinoshita, K., *Electrochemical Oxygen Technology*. John Wiley & Sons Inc.: 1992.

28. Koper, M. T. M., *Fuel Cell Catalysis*. John Wiley & Sons Inc.: Hoboken, New Jersey, 2009.

29. Chen, W.; Huang, J.; Wei, J.; Zhou, D.; Cai, J.; He, Z.-D. D.; Chen, Y.-X. X., Origins of high onset overpotential of oxygen reduction reaction at Pt-based electrocatalysts: A mini review. *Electrochemistry Communications* **2018,** *96*, 71-76.

30. Nørskov, J. K.; Rossmeisl, J.; Logadottir, A.; Lindqvist, L.; Kitchin, J. R.; Bligaard, T.; Jónsson, H., Origin of the overpotential for oxygen reduction at a fuel-cell cathode. *Journal of Physical Chemistry B* **2004,** *108* (46), 17886-17892.

31. Briega-Martos, V.; Herrero, E.; Feliu, J. M., Effect of pH and Water Structure on the Oxygen Reduction Reaction on platinum electrodes. *Electrochimica Acta* **2017,** *241*, 497-509.

32. Perry, S. C.; Denuault, G., The oxygen reduction reaction (ORR) on reduced metals: evidence for a unique relationship between the coverage of adsorbed oxygen species and adsorption energy. *Phys. Chem. Chem. Phys.* **2016,** *18* (15), 10218-10223.

33. Gómez-Marín, A. M.; Feliu, J. M., New Insights into the Oxygen Reduction Reaction Mechanism on Pt (111): A Detailed Electrochemical Study. *ChemSusChem* **2013,** *6* (6), 1091-1100.

34. Ramaswamy, N.; Mukerjee, S., Influence of Inner- and Outer-Sphere Electron Transfer Mechanisms during Electrocatalysis of Oxygen Reduction in Alkaline Media. *The Journal of Physical Chemistry C* **2011,** *115* (36), 18015-18026.

35. Ramaswamy, N.; Mukerjee, S., Fundamental Mechanistic Understanding of Electrocatalysis of Oxygen Reduction on Pt and Non-Pt Surfaces: Acid versus Alkaline Media. *Advances in Physical Chemistry* **2012,** *2012*, 1-17.

36. Gómez-Marín, A. M.; Rizo, R.; Feliu, J. M.; Stamenkovic, V. R.; Markovic, N. M.; Koper, M. T. M.; Rossmeisl, J.; Nørskov, J. K.; Chorkendorff, I.; Rossmeisl, J., Oxygen reduction reaction at Pt single crystals: a critical overview. *Catalysis Science & Technology* **2014,** *4* (6), 1685-1685.

37. Song, C.; Zhang, J., Electrocatalytic Oxygen Reduction Reaction. In *PEM Fuel Cell Electrocatalysts and Catalyst Layers*, Zhang, J., Ed. Springer London: 2008; pp 89-134.

38. Pletcher, D.; Sotiropoulos, S., A study of cathodic oxygen reduction at platinum using microelectrodes. *Journal of Electroanalytical Chemistry* **1993,** *356* (1-2), 109-119.

39. Wroblowa, H. S.; Yen Chi, P.; Razumney, G., Electroreduction of oxygen. *Journal of Electroanalytical Chemistry and Interfacial Electrochemistry* **1976,** *69* (2), 195-201.

40. Yeager, E., Electrocatalysts for O2 reduction. *Electrochimica Acta* **1984,** *29* (11), 1527-1537.

41. Yeager, E., Dioxygen electrocatalysis: mechanisms in relation to catalyst structure. *Journal of Molecular Catalysis* **1986,** *38* (1-2), 5-25.

42. Zhang, G.; Wei, Q.; Yang, X.; Tavares, A. C.; Sun, S., RRDE experiments on noble-metal and noble-metal-free catalysts: Impact of loading on the activity and selectivity of oxygen reduction reaction in alkaline solution. *Applied Catalysis B: Environmental* **2017,** *206*, 115-126.

43. Xing, W.; Yin, G.; Zhang, J., *Rotating Electrode Methods and Oxygen Reduction Catalysts*. 1st Editio ed.; Elsevier Ltd: 2014; p 322-322.

44. Anastasijević, N. A.; Vesović, V.; Adžić, R. R., Determination of the kinetic parameters of the oxygen reduction reaction using the rotating ring-disk electrode. Part I. Theory. *Journal of Electroanalytical Chemistry* **1987,** *229* (1-2), 305-316.

45. Anastasijević, N. A.; Vesović, V.; Adžić, R. R., Determination of the kinetic parameters of the oxygen reduction reaction using the rotating ring-disk electrode. Part II. Applications. *Journal of Electroanalytical Chemistry* **1987,** *229* (1-2), 317-325.

46. *Handbook of Electrochemistry*. 1st ed.; Elsevier: Amsterdam, 2007; p 934-934.

47. Vesovic, V.; Anastasijevic, N.; Adzic, R. R., Rotating disk electrode: A re-examination of some kinetic criteria with a special reference to oxygen reduction. *Journal of Electroanalytical Chemistry* **1987,** *218* (1-2), 53-63.

48. Debe, M. K., Electrocatalyst approaches and challenges for automotive fuel cells. *Nature* **2012,** *486* (7401), 43-51.

49. Shiva Kumar, S.; Himabindu, V., Hydrogen production by PEM water electrolysis – A review. *Materials Science for Energy Technologies* **2019,** *2* (3), 442-454.

50. Perry, S. C.; Al Shandoudi, L. M.; Denuault, G., Sampled-Current Voltammetry at Microdisk Electrodes: Kinetic Information from Pseudo Steady State Voltammograms. *Analytical Chemistry* **2014,** *86* (19), 9917-9923.

51. Katsounaros, I.; Schneider, W. B.; Meier, J. C.; Benedikt, U.; Biedermann, P. U.; Cuesta, A.; Auer, A. A.; Mayrhofer, K. J. J., The impact of spectator species on the interaction of H2O2 with platinum - implications for the oxygen reduction reaction pathways. *Physical chemistry chemical physics : PCCP* **2013,** *15* (21), 8058-68.

52. Stamenković, V.; Schmidt, T. J.; Ross, P. N.; Marković, N. M., Surface composition effects in electrocatalysis: Kinetics of oxygen reduction on well-defined Pt3Ni and Pt3Co alloy surfaces. *Journal of Physical Chemistry B* **2002,** *106* (46), 11970-11979.

53. Gasteiger, H. A.; Kocha, S. S.; Sompalli, B.; Wagner, F. T., Activity benchmarks and requirements for Pt, Pt-alloy, and non-Pt oxygen reduction catalysts for PEMFCs. 2005; Vol. 56, pp 9-35.

54. Pasti, I. A.; Gavrilov, N. M.; Mentus, S. V., Potentiodynamic Investigation of Oxygen Reduction Reaction on Polycrystalline Platinum Surface in Acidic Solutions: the Effect of the Polarization Rate on the Kinetic Parameters. *Int. J. Electrochem. Sci* **2012,** *7*, 11076-11090.

55. Jerkiewicz, G.; Vatankhah, G.; Lessard, J.; Soriaga, M. P.; Park, Y.-S., Surface-oxide growth at platinum electrodes in aqueous H2SO4 Reexamination of its mechanism through combined cyclic-voltammetry, electrochemical quartz-crystal nanobalance, and Auger electron spectroscopy measurements. *Electrochimica Acta* **2004,** *49*, 1451-1459.

56. Coleman, E. J.; Co, A. C., The Complex Inhibiting Role of Surface Oxide in the Oxygen Reduction Reaction. *ACS Catalysis* **2015,** *5* (12), 7299-7311.

57. Wiberg, G. K. H.; Arenz, M., Establishing the potential dependent equilibrium oxide coverage on platinum in alkaline solution and its influence on the oxygen reduction. *Journal of Power Sources* **2012,** *217*, 262-267.

58. Clavilier, J.; Rodes, A.; El Achi, K.; Zamakhchari, M. A., Electrochemistry at platinum single crystal surfaces in acidic media: hydrogen and oxygen adsorption. *Journal Chim Phys* **1991,** *88*, 1291-1337.

59. Rodríguez, P.; Herrero, E.; Solla-Gullón, J.; Vidal-Iglesias, F. J. J.; Aldaz, A.; Feliu, J. M. M., Specific surface reactions for identification of platinum surface domains: Surface characterization and electrocatalytic tests. *Electrochimica Acta* **2005,** *50* (21), 4308-4317.

60. Solla-Gullón, J.; Rodríguez, P.; Herrero, E.; Aldaz, A.; Feliu, J. M.; Feliu, J. M.; Aldaz, A.; Wells, P. B., Surface characterization of platinum electrodes. *Phys. Chem. Chem. Phys.* **2008,** *10* (10), 1359-1373.

61. Marković, N. M.; Grgur, B. N.; Lucas, C. A.; Ross, P. N., Surface electrochemistry of CO on Pt(110)-(1 × 2) and Pt(110)-(1 × 1) surfaces. *Surface Science* **1997,** *384* (1-3).

62. Grgur, B. N.; Markovi, N. M.; Lucas, C. A.; Jr, P. N. R., Electrochemical oxidation of carbon monoxide: from platinum single crystals to low temperature fuel cells catalysts. Part I: Carbon monoxide oxidation onto low index platinum single crystals. *J.Serb.Chem.Soc* **2001,** *66* (11-12), 785-797.

63. Francis, A. J.; Salvador, P. A., Crystal orientation and surface morphology of face-centered-cubic metal thin films deposited upon single-crystal ceramic substrates using pulsed laser deposition. *Journal of Materials Research* **2007,** *22* (1), 89-102.

64. Hamelin, A., Cyclic voltammetry at gold single-crystal surfaces. Part 1. Behaviour at low-index faces. *Journal of Electroanalytical Chemistry* **1996,** *407* (1-2), 1-11.

65. Temmel, S. E.; Fabbri, E.; Pergolesi, D.; Lippert, T.; Schmidt, T. J., Investigating the Role of Strain toward the Oxygen Reduction Activity on Model Thin Film Pt Catalysts. *ACS Catalysis* **2016,** *6* (11), 7566-7576.

66. Sethuraman, V. A.; Vairavapandian, D.; Lafouresse, M. C.; Adit Maark, T.; Karan, N.; Sun, S.; Bertocci, U.; Peterson, A. A.; Stafford, G. R.; Guduru, P. R., Role of Elastic Strain on Electrocatalysis of Oxygen Reduction Reaction on Pt. *The Journal of Physical Chemistry C* **2015,** *119* (33), 19042-19052.

67. Schneider, O., *Size Dependent Electrocatalysis of Gold Nanoparticles*. Elsevier: 2018; p 581-595.

68. Clavilier, J., The role of anion on the electrochemical behaviour of a {111} platinum surface; an unusual splitting of the voltammogram in the hydrogen region. *Journal of Electroanalytical Chemistry and Interfacial Electrochemistry* **1980,** *107* (1), 211-216.

69. Armand, D.; Clavilier, J., Quantitative analysis of the distribution of the hydrogen adsorption states at platinum surfaces: Part I. Application to Pt(100) in sulphuric acid medium. *Journal of Electroanalytical Chemistry and Interfacial Electrochemistry* **1987,** *225* (1), 205-214.

70. Clavilier, J.; Faure, R.; Guinet, G.; Durand, R., Preparation of monocrystalline Pt microelectrodes and electrochemical study of the plane surfaces cut in the direction of the {111} and {110} planes. *Journal of Electroanalytical Chemistry* **1980,** *107* (1), 205-209.

71. Armand, D.; Clavilier, J., Influence of specific adsorption of anions on the electrochemical behaviour of the Pt (100) surface in acid medium: Comparison with Pt (111). *Journal of Electroanalytical Chemistry and Interfacial Electrochemistry* **1989,** *270* (1-2), 331-347.

72. Armand, D.; Clavilier, J., Electrochemical behaviour of the (110) orientation of a platinum surface in acid medium: the role of anions. *Journal of Electroanalytical Chemistry* **1989,** *263* (1), 109-126.

73. Clavilier, J.; Feliu, J. M.; Fernandez-Vega, A.; Aldaz, A., Electrochemical behaviour of irreversibly adsorbed bismuth on Pt (100) with different degrees of crystalline surface order. *Journal of Electroanalytical Chemistry* **1989,** *269* (1), 175-189.

74. Clavilier, J.; Durand, R.; Guinet, G.; Faure, R., Electrochemical adsorption behaviour of Pt(100) in sulphuric acid solution. *Journal of Electroanalytical Chemistry and Interfacial Electrochemistry* **1981,** *127* (1), 281-287.

75. Markovic, N. M.; Schmidt, T. J.; Stamenkovic, V.; Ross, P. N., Oxygen Reduction Reaction on Pt and Pt Bimetallic Surfaces: A Selective Review. *Fuel Cells* **2001,** *1* (2), 105-116.

76. Bajpai, P., Chapter 3 - Renewable energy versus fossil resources. In *Biotechnology in the Chemical Industry*, Bajpai, P., Ed. Elsevier: 2020; pp 23-30.

77. Panwar, N. L.; Kaushik, S. C.; Kothari, S., Role of renewable energy sources in environmental protection: A review. *Renewable and Sustainable Energy Reviews* **2011,** *15* (3), 1513-1524.

78. Owusu, P. A.; Asumadu-Sarkodie, S., A review of renewable energy sources, sustainability issues and climate change mitigation. *Cogent Engineering* **2016,** *3* (1), 1167990.

79. Abas, N.; Kalair, A.; Khan, N., Review of fossil fuels and future energy technologies. *Futures* **2015,** *69*, 31-49.

80. Carrette, L.; Friedrich, K. A.; Stimming, U., Fuel Cells - Fundamentals and Applications. *Fuel Cells* **2001,** *1* (1), 5-39.

81. Ralph, T. R., Clean Fuel Cell Energy for Today

Developments in Protong Exchange Membrane Fuel Cells *Platinum Metals Rev* **1999,** *43* (1), 14-17.

82. Voelcker, J. Hydrogen Fuel-Cells Cars to Come From Toyota, Hyunday, Honda. https://www.greencarreports.com/news/1088626_hydrogen-fuel-cell-cars-to-come-from-toyota-hyundai-honda (accessed 2020-07-30).

83. How Clean Are Hydrogen Fuel Cell Electric Vehicles? https://www.ucsusa.org/sites/default/files/attach/2014/10/How-Clean-Are-Hydrogen-Fuel-Cells-Fact-Sheet.pdf (accessed 2020-07-30).

84. Ji, M.; Wei, Z., A Review of Water Management in Polymer Electrolyte Membrane Fuel Cells. *Energies* **2009,** *2* (4), 1057-1106.

85. Khotseng, L., Fuel Cell Thermodynamics. In *Thermodynamics and Energy Engineering*, Vizureanu, P., Ed. IntechOpen: 2019.

86. Atkins, P.; de Paula, J., *Elements of Physical Chemistry* 4th edition ed.; Oxford University Press Oxford, 2005.

87. Markovic, N. M.; Ross, P. N., New electrocatalysts for fuel cells from model surfaces to commercial catalysts. *CATTECH* **2000,** *4* (2), 110-126.

88. Rossmeisl, J.; Karlberg, G. S.; Jaramillo, T.; Norskov, J. K., Steady state oxygen reduction and cyclic voltammetry. *Faraday Discuss* **2008,** *140* (0), 337-46; discussion 417-37.

89. Mathur, V. K.; Crawford, J., Fundamentals of Gas Diffusion Layers in PEM Fuel Cells. In *Recent Trends in Fuel Cell Science and Technology*, Suddhasatwa, B., Ed. Springer, New York, NY: New York, 2007; pp 116-128.

90. Sealy, C., The problem with platinum. *Materials Today* **2008,** *11* (12), 65-68.

91. Badwal, S. P. S.; Giddey, S. S.; Munnings, C.; Bhatt, A. I.; Hollenkamp, A. F.; Lapkin, A.; Gu, S., Emerging electrochemical energy conversion and storage technologies. **2014**.

92. Gröger, O.; Gasteiger, H. A.; Suchsland, J.-P., Review—Electromobility: Batteries or Fuel Cells? *Journal of The Electrochemical Society* **2015,** *162* (14), A2605-A2622.

93. Kumaraguru , S.; Arisetty, A.; Gittleman, C.; Konduru, V.; Lai, Y. H.; McQuarters, A.; Ramaswamy, N., Durable High-Power Membrane Electrode Assemblies with Low Platinum Loading. (DOE), D. o. E., Ed. DOE Hydrogen and Fuel Cells Program United States of America, 2019; Vol. FY 2019 Annual Progress Report.

94. Chen, Z.; Higgins, D.; Yu, A.; Zhang, L.; Zhang, J., A review on non-precious metal electrocatalysts for PEM fuel cells. *Energy & Environmental Science* **2011,** *4* (9), 3167-3192.

95. Stamenkovic, V. R.; Mun, B. S.; Arenz, M.; Mayrhofer, K. J. J.; Lucas, C. A.; Wang, G.; Ross, P. N.; Markovic, N. M., Trends in electrocatalysis on extended and nanoscale Pt-bimetallic alloy surfaces. *Nature materials* **2007,** *6* (3), 241-247.

96. Wu, J.; Yang, H., Platinum-based oxygen reduction electrocatalysts. *Accounts of Chemical Research* **2013,** *46* (8), 1848-57.

97. Guo, S.; Zhang, S.; Sun, S., Tuning nanoparticle catalysis for the oxygen reduction reaction. 2013; Vol. 52, pp 8526-8544.

98. Hayden, B. E., Particle size and support effects in electrocatalysis. *Accounts of Chemical Research* **2013,** *46* (8), 1858-1866.

99. Mukerjee, S., Particle size and structural effects in platinum electrocatalysis. *Journal of Applied Electrochemistry* **1990,** *20* (4), 537-548.

100. Shao, M.; Chang, Q.; Dodelet, J.-P.; Chenitz, R., Recent Advances in Electrocatalysts for Oxygen Reduction Reaction. *Chemical Reviews* **2016,** *116* (6), 3594-3657.

101. Nie, Y.; Li, L.; Wei, Z., Recent advancements in Pt and Pt-free catalysts for oxygen reduction reaction. *Chem. Soc. Rev. Chem. Soc. Rev* **2015,** *44* (44), 2168-2201.

102. Jaouen, F.; Dodelet, J.-P., O2 Reduction Mechanism on Non-Noble Metal Catalysts for PEM Fuel Cells. Part I: Experimental Rates of O2 Electroreduction, H2O2 Electroreduction, and H2O2 Disproportionation. *The Journal of Physical Chemistry C* **2009,** *113* (34), 15422-15432.

103. Jaouen, F.; Marcotte, S.; Dodelet, J.-P.; Lindbergh, G., Oxygen Reduction Catalysts for Polymer Electrolyte Fuel Cells from the Pyrolysis of Iron Acetate Adsorbed on Various Carbon Supports. *The Journal of Physical Chemistry B* **2003,** *107* (6), 1376-1386.

104. Alt, H.; Binder, H.; Sandstede, G., Mechanism of the electrocatalytic reduction of oxygen on metal chelates. *Journal of Catalysis* **1973,** *28* (1), 8-19.

105. Nikolaidis, P.; Poullikkas, A., A comparative overview of hydrogen production processes. *Renewable and Sustainable Energy Reviews* **2017,** *67*, 597-611.

106. Diéguez, P. M.; Ursúa, A.; Sanchis, P.; Sopena, C.; Guelbenzu, E.; Gandía, L. M., Thermal performance of a commercial alkaline water electrolyzer: Experimental study and mathematical modeling. *International Journal of Hydrogen Energy* **2008,** *33* (24), 7338-7354.

107. Dumesic, J. A.; Huber, G. W.; Boudart, M., *Handbook of Heterogeneous Catalysis*. 2008.

108. Pletcher, D., *A First Course in Electrode Processes* 2nd edition ed.; RSC Publishing - The Royal Society of Chemistry: Cambridge, 2009.

109. Kuo, D.-Y.; Paik, H.; Kloppenburg, J.; Faeth, B.; Shen, K. M.; Schlom, D. G.; Hautier, G.; Suntivich, J., Measurements of Oxygen Electroadsorption Energies and Oxygen Evolution Reaction on RuO2(110): A Discussion of the Sabatier Principle and Its Role in Electrocatalysis. *Journal of the American Chemical Society* **2018,** *140* (50), 17597-17605.

110. Medford, A. J.; Vojvodic, A.; Hummelshøj, J. S.; Voss, J.; Abild-Pedersen, F.; Studt, F.; Bligaard, T.; Nilsson, A.; Nørskov, J. K., From the Sabatier principle to a predictive theory of transition-metal heterogeneous catalysis. *Journal of Catalysis* **2015,** *328*, 36-42.

111. Laursen, A. B.; Varela, A. S.; Dionigi, F.; Fanchiu, H.; Miller, C.; Trinhammer, O. L.; Rossmeisl, J.; Dahl, S., Electrochemical Hydrogen Evolution: Sabatier's Principle and the Volcano Plot. *Journal of Chemical Education* **2012,** *89* (12), 1595-1599.

112. Climent, V.; Feliu, J. M., Surface Electrochemistry with Pt Single-Crystal Electrodes. In *Advances in Electrochemical Science and Engineering*, 2017; pp 1-57.

113. Henry, C. R., Surface studies of supported model catalysts. *Surface Science Reports* **1998,** *31* (7-8), 231-325.

114. Vidal-Iglesias, F. J.; García-Aráez, N.; Montiel, V.; Feliu, J. M.; Aldaz, A., Selective electrocatalysis of ammonia oxidation on Pt(100) sites in alkaline medium. *Electrochemistry Communications* **2003,** *5* (1), 22-26.

115. Prieto, A.; Hernández, J.; Herrero, E.; Feliu, J. M., The role of anions in oxygen reduction in neutral and basic media on gold single-crystal electrodes. *Journal of Solid State Electrochemistry* **2003,** *7* (9), 599-606.

116. Rizo, R.; Herrero, E.; Feliu, J. M., Oxygen reduction reaction on stepped platinum surfaces in alkaline media. *Physical Chemistry Chemical Physics* **2013,** *15* (37), 15416-15425.

117. Kuzume, A.; Herrero, E.; Feliu, J. M., Oxygen reduction on stepped platinum surfaces in acidic media. *Journal of Electroanalytical Chemistry* **2007,** *599* (2), 333-343.

118. Bertin, E.; Garbarino, S.; Guay, D.; Solla-Gullón, J.; Vidal-Iglesias, F. J.; Feliu, J. M., Electrodeposited platinum thin films with preferential (100) orientation: Characterization and electrocatalytic properties for ammonia and formic acid oxidation. *Journal of Power Sources* **2013,** *225*, 323-329.

119. Hubbard, A. T., Electrochemistry at well-characterized surfaces. *Chemical Reviews* **1988,** *88* (4), 633-656.

120. Álvarez-Ruiz, B.; Gómez, R.; Orts, J. M.; Feliu, J. M., Role of the Metal and Surface Structure in the Electro-oxidation of Hydrazine in Acidic Media. *Journal of The Electrochemical Society* **2002,** *149* (3), D35-D35.

121. Sacré, N.; Duca, M.; Garbarino, S.; Imbeault, R.; Wang, A.; Hadj Youssef, A.; Galipaud, J.; Hufnagel, G.; Ruediger, A.; Roué, L.; Guay, D., Tuning Pt-Ir Interactions for NH3 Electrocatalysis. *ACS Catalysis* **2018,** *8* (3), 2508-2518.

122. Galipaud, J.; Roy, C.; Martin, M. H.; Garbarino, S.; Roué, L.; Guay, D., Electrooxidation of Ammonia at Tuned (100)Pt Surfaces by using Epitaxial Thin Films. *ChemElectroChem* **2015,** *2* (8), 1187-1198.

123. Bertin, E.; Roy, C.; Garbarino, S.; Guay, D.; Solla-Gullón, J.; Vidal-Iglesias, F. J.; Feliu, J. M., Effect of the nature of (100) surface sites on the electroactivity of macroscopic Pt electrodes for the electrooxidation of ammonia. *Electrochemistry Communications* **2012,** *22* (1), 197-199.

124. Pérez-Gallent, E.; Figueiredo, M. C.; Katsounaros, I.; Koper, M. T. M., Electrocatalytic reduction of Nitrate on Copper single crystals in acidic and alkaline solutions. *Electrochimica Acta* **2017,** *227*, 77-84.

125. Duca, M.; Sacré, N.; Wang, A.; Garbarino, S.; Guay, D., Enhanced electrocatalytic nitrate reduction by preferentially-oriented (100) PtRh and PtIr alloys: the hidden treasures of the 'miscibility gap'. *Applied Catalysis B: Environmental* **2018,** *221*, 86-96.

126. Duca, M.; Cucarella, M. O.; Rodriguez, P.; Koper, M. T. M., Direct Reduction of Nitrite to N 2 on a Pt(100) Electrode in Alkaline Media. *Journal of the American Chemical Society* **2010,** *132* (51), 18042-18044.

127. Adžić, R. R.; Marković, N. M.; Vešović, V. B.; Adzic, R. R.; Markovic, N. M.; Vesovic, V. B., Structural effects in electrocatalysis. Oxygen reduction on the Au(100) single crystal electrode. *Journal of Electroanalytical Chemistry* **1984,** *165* (1-2), 105-120.

128. Marković, N. M.; Adić, R. R.; Vešović, V. B., Structural effects in electrocatalysis: Oxygen reduction on the gold single crystal electrodes with (110) and (111) orientations. *Journal of Electroanalytical Chemistry and Interfacial Electrochemistry* **1984,** *165* (1-2), 121-133.

129. Adžć, R. R.; Marković, N. M., Structural effects in electrocatalysis: oxygen and hydrogen peroxide reduction on single crystal gold electrodes and the effects of lead ad-atoms. *Journal of Electroanalytical Chemistry* **1982,** *138*, 443-441.

130. Adžić, R. R.; Tripković, A. V.; O'Grady, W. E., Structural effects in electrocatalysis. *Nature* **1982,** *296* (5853), 137-138.

131. Garlyyev, B.; Xue, S.; Pohl, M. D.; Reinisch, D.; Bandarenka, A. S., Oxygen Electroreduction at High-Index Pt Electrodes in Alkaline Electrolytes: A Decisive Role of the Alkali Metal Cations. *ACS Omega* **2018,** *3* (11), 15325-15331.

132. Koper, M. T. M., Structure sensitivity and nanoscale effects in electrocatalysis. *Nanoscale* **2011,** *3* (5), 2054-2054.

133. Bandarenka, A. S.; Koper, M. T. M., Structural and electronic effects in heterogeneous electrocatalysis: Toward a rational design of electrocatalysts. *Journal of Catalysis* **2013,** *308*, 11-24.

134. Lebedeva, N. P.; Koper, M. T. M.; Feliu, J. M.; Van Santen, R. A., Role of crystalline defects in electrocatalysis: Mechanism and kinetics of CO adlayer oxidation on stepped platinum electrodes. *Journal of Physical Chemistry B* **2002,** *106* (50), 12938-12947.

135. Kolb, D., Reconstruction phenomena at metal-electrolyte interfaces. *Progress in Surface Science* **1996,** *51* (2), 109-173.

136. Bard, A. J.; Fan, F.-R. F.; Pierce, D. T.; Unwin, P. R.; Wipf, D. O.; Zhou, F., Chemical Imaging of Surfaces with the Scanning Electrochemical Microscope. *Science* **1991,** *254* (5028), 68.

137. Tripkovic, D. V.; Strmcnik, D.; van der Vliet, D.; Stamenkovic, V.; Markovic, N. M., The role of anions in surface electrochemistry. *Faraday Discuss.* **2009,** *140* (0), 25-40.

138. Clavilier, J.; Armand, D.; Sun, S. G.; Petit, M., Electrochemical adsorption behaviour of platinum stepped surfaces in sulphuric acid solutions. *Journal of Electroanalytical Chemistry* **1986,** *205* (1-2), 267-277.

139. Schmidt, T. J.; Stamenkovic, V.; Ross, J. P. N.; Markovic, N. M., Temperature dependent surface electrochemistry on Pt single crystals in alkaline electrolyte Part 3. The oxygen reduction reaction. *Physical Chemistry Chemical Physics* **2003,** *5* (2), 400-406.

140. Robinson, K. M.; O'Grady, W. E., X-ray surface diffraction studies of the restructuring and electrodeposition of Pb monolayers on Au(100) single crystals. *Faraday Discussions* **1993,** *95*, 55-64.

141. Arulmozhi, N.; Jerkiewicz, G., Design and Development of Instrumentations for the Preparation of Platinum Single Crystals for Electrochemistry and Electrocatalysis Research. Part 2: Orientation, Cutting, and Annealing. *Electrocatalysis* **2017,** *8* (5), 399-413.

142. Arulmozhi, N.; Jerkiewicz, G., Design and Development of Instrumentations for the Preparation of Platinum Single Crystals for Electrochemistry and Electrocatalysis Research. Part 1: Semi-Automated Crystal Growth. *Electrocatalysis* **2016,** *7* (6), 507-518.

143. Arulmozhi, N.; Esau, D.; van Drunen, J.; Jerkiewicz, G., Design and Development of Instrumentations for the Preparation of Platinum Single Crystals for Electrochemistry and Electrocatalysis Research Part 3: Final Treatment, Electrochemical Measurements, and Recommended Laboratory Practices. *Electrocatalysis* **2018,** *9* (1), 113-123.

144. Morintale, E.; Constantinescu, C.; Dinescu, M., Thin films development by pulsed laser-assisted deposition. *Physics AUC* **2010,** *20* (1), 43-56.

145. Chrisey, D. B.; Hubler, G. K., *Pulsed laser deposition of thin films*. John Wiley & Sons Inc.: New York, 1994.

146. *Pulsed Laser Deposition of Thin Films*. John Wiley & Sons. Inc.: New Jersey, 2007.

147. Arthur, J. R., Molecular beam epitaxy. *Surface Science* **2002,** *500* (1), 189-217.

148. Narayan, D. R.; Jagdish, Epitaxial Growth of Thin Films. In *Crystal Growth*, Glebovsky, V., Ed. IntechOpen: 2019.

149. Jilani, A.; Abdel-wahab, M. S.; Hammad, A. H., Advance Deposition Techniques for Thin Film and Coating. In *Modern Technologies for Creating the Thin-film Systems and Coatings*, Nikitenkov, N. N., Ed. IntechOpen: 2017.

150. Sacré, N.; Hufnagel, G.; Galipaud, J.; Bertin, E.; Hassan, S. A.; Duca, M.; Roué, L.; Ruediger, A.; Garbarino, S.; Guay, D., Pt Thin Films with Nanometer-Sized Terraces of (100) Orientation. *Journal of Physical Chemistry C* **2017,** *121* (22), 12188-12198.

151. Garbarino, S.; Imbeault, R.; Sacré, N.; Guay, D., Hydrazine Electro-Oxidation at Epitaxial Ir Pt100− Alloys. In *Encyclopedia of Interfacial Chemistry*, 2018; pp 1-8.

152. Duca, M.; Wang, A.; Buvat, G.; Sacré, N.; Garbarino, S.; Guay, D., Probing the surface sensitivity of dimethyl ether oxidation on epitaxially-grown PtRh(1 0 0) alloys: Insights into the challenge of improving on Pt(1 0 0). *Journal of Catalysis* **2019,** *369*, 405-414.

153. Imbeault, R.; Reyter, D.; Garbarino, S.; Roué, L.; Guay, D., Metastable Au xRh 100-x thin films prepared by pulsed laser deposition for the electrooxidation of methanol. *Journal of Physical Chemistry C* **2012,** *116* (8), 5262-5269.

154. Bonnefont, A.; Ryabova, A. S.; Schott, T.; Kéranguéven, G.; Istomin, S. Y.; Antipov, E. V.; Savinova, E. R., Challenges in the understanding oxygen reduction electrocatalysis on transition metal oxides. *Current Opinion in Electrochemistry* **2019,** *14*, 23-31.

155. Wan, H.; Jensen, A. W.; Escudero-Escribano, M.; Rossmeisl, J., Insights in the Oxygen Reduction Reaction: From Metallic Electrocatalysts to Diporphyrins. *ACS Catalysis* **2020,** *10* (11), 5979-5989.

156. Shao, M. H.; Liu, P.; Adzic, R. R., Superoxide anion is the intermediate in the oxygen reduction reaction on platinum electrodes. *Journal of the American Chemical Society* **2006,** *128* (23), 7408-7409.

157. Li, M. F.; Liao, L. W.; Yuan, D. F.; Mei, D.; Chen, Y.-X., pH effect on oxygen reduction reaction at Pt(111) electrode. *Electrochimica Acta* **2013,** *110*, 780-789.

158. Ford, D. C.; Nilekar, A. U.; Xu, Y.; Mavrikakis, M., Partial and complete reduction of O2 by hydrogen on transition metal surfaces. *Surface Science* **2010,** *604* (19–20), 1565-1575.

159. Štrbac, S.; Anastasijević, N. A.; Adžić, R. R., Oxygen reduction on Au (100) and vicinal Au (910) and Au (11, 1, 1) faces in alkaline solution. A rotating disc-ring study. *Journal of Electroanalytical Chemistry* **1992,** *323* (1-2), 179-195.

160. Holton, O. T.; Stevenson, J. W., The Role of Platinum in Proton Exchange Membrane Fuel Cells Evaluation of platinum's unique properties for use in both the anode and cathode of a proton exchange membrane fuel cell. *Platinum Metals Review* **2013,** *57* (4), 259-271.

161. Sepa, D. B.; Vojnovic, M. V.; Damjanovic, A., Kinetics and mechanism of O2 reduction at Pt in alkaline solutions. *Electrochimica Acta* **1980,** *25* (11), 1491-1496.

162. Damjanovic, A.; Brusic, V. *Electrode kinetics of oxygen reduction on oxide-free platinum electrodes* 1967; pp 615-628.

163. Sepa, D. B.; Vojnovic, M. V.; Damjanovic, A., Reaction intermediates as a controlling factor in the kinetics and mechanism of oxygen reduction at platinum electrodes. *Electrochimica Acta* **1981,** *26* (6), 781-793.

164. Nilekar, A. U.; Xu, Y.; Zhang, J.; Vukmirovic, M. B.; Sasaki, K.; Adzic, R. R.; Mavrikakis, M., Bimetallic and Ternary Alloys for Improved Oxygen Reduction Catalysis. *Topics in Catalysis* **2007,** *46* (3), 276-284.

165. Todoroki, N.; Kawamura, R.; Asano, M.; Sasakawa, R.; Takahashi, S.; Wadayama, T., Alloy-composition-dependent oxygen reduction reaction activity and electrochemical stability of Pt-based bimetallic systems: a model electrocatalyst study of Pt/PtxNi100x(111). *Phys. Chem. Chem. Phys* **2018,** *20*, 11994-11994.

166. Stacy, J.; Regmi, Y. N.; Leonard, B.; Fan, M., The recent progress and future of oxygen reduction reaction catalysis: A review. *Renewable and Sustainable Energy Reviews* **2017,** *69*, 401-414.

167. Ge, X.; Sumboja, A.; Wuu, D.; An, T.; Li, B.; Goh, F. W. T.; Hor, T. S. A.; Zong, Y.; Liu, Z., Oxygen Reduction in Alkaline Media: From Mechanisms to Recent Advances of Catalysts. *ACS Catalysis* **2015,** *5* (8), 4643-4667.

168. Temmel, S. E.; Tschupp, S. A.; Schmidt, T. J., A highly flexible electrochemical flow cell designed for the use of model electrode materials on non-conventional substrates. *Review of Scientific Instruments* **2016,** *87* (4), 045115.

169. Snowden, M. E.; King, P. H.; Covington, J. A.; Macpherson, J. V.; Unwin, P. R., Fabrication of Versatile Channel Flow Cells for Quantitative Electroanalysis Using Prototyping. *Analytical Chemistry* **2010,** *82* (8), 3124-3131.

170. Compton, R. G.; Unwin, P. R., Channel and tubular electrodes. *Journal of Electroanalytical Chemistry and Interfacial Electrochemistry* **1986,** *205* (1), 1-20.

171. Shinozaki, K.; Zack, J. W.; Pylypenko, S.; Pivovar, B. S.; Kocha, S. S., Oxygen Reduction Reaction Measurements on Platinum Electrocatalysts Utilizing Rotating Disk Electrode Technique: II. Influence of Ink Formulation, Catalyst Layer Uniformity and Thickness. *Journal of The Electrochemical Society* **2015,** *162* (12), 1384-1396.

172. Shinozaki, K.; Zack, J. W.; Richards, R. M.; Pivovar, B. S.; Kocha, S. S., Oxygen Reduction Reaction Measurements on Platinum Electrocatalysts Utilizing Rotating Disk Electrode Technique

I. Impact of Impurities, Measurement Protocols and Applied Corrections. *Journal of The Electrochemical Society* **2015,** *162* (10), F1144-F1158.

173. Kocha, S. S.; Shinozaki, K.; Zack, J. W.; Myers, D. J.; Kariuki, N. N.; Nowicki, T.; Stamenkovic, V.; Kang, Y.; Li, D.; Papageorgopoulos, D., Best Practices and Testing Protocols for Benchmarking ORR Activities of Fuel Cell Electrocatalysts Using Rotating Disk Electrode. *Electrocatalysis* **2017,** *8* (4), 366-374.

174. Lindgren, A.; Munteanu, F.-D.; Gazaryan, I. G.; Ruzgas, T.; Gorton, L., Comparison of rotating disk and wall-jet electrode systems for studying the kinetics of direct and mediated electron transfer for horseradish peroxidase on a graphite electrode. *Journal of Electroanalytical Chemistry* **1998,** *458* (1), 113-120.

175. Compton, R. G.; Fisher, A. C.; Tyley, G. P., Non-uniform accessibility and the use of hydrodynamic electrodes for mechanistic studies: A comparison of wall-jet and rotating disc electrodes. *Journal of Applied Electrochemistry* **1991,** *21* (4), 295-300.

176. Levich, V. G.; Ltd, S. T., *Physicochemical Hydrodynamics*. Prentice-Hall: 1962.

177. Hsueh, L.; Newman, J., Mass transfer and polarization at a rotating disk electrode. *Electrochimica Acta* **1967,** *12* (4), 429-438.

178. Bruckenstein, S.; Miller, B., Unraveling reactions with rotating electrodes. *Accounts of Chemical Research* **1977,** *10* (2), 54-61.

179. Frumkin, A.; Nekrasov, L.; Levich, B.; Ivanov, J., Die anwendung der rotierenden scheibenelektrode mit einem ringe zur untersuchung von zwischenprodukten elektrochemischer reaktionen. *Journal of Electroanalytical Chemistry (1959)* **1959,** *1* (1), 84-90.

180. Group, S. E., Instrumental Methods in Electrochemistry. Universitiy of Southampton: Southampton, United Kindgom, 2015; pp 240-240.

181. Zhang, L.; Li, H.; Zhang, J., Kinetics of oxygen reduction reaction on three different Pt surfaces of Pt/C catalyst analyzed by rotating ring-disk electrode in acidic solution. *Journal of Power Sources* **2014,** *255*, 242-250.

182. Vargas, R.; Borrás, C.; Mostany, J.; Scharifker, B. R., Kinetics of surface reactions on rotating disk electrodes. *Electrochimica Acta* **2012,** *80*, 326-333.

183. Vidal-Iglesias, F. J.; Solla-Gullón, J.; Montiel, V.; Aldaz, A., Errors in the use of the Koutecky–Levich plots. *Electrochemistry Communications* **2012,** *15* (1), 42-45.

184. Zhou, R.; Zheng, Y.; Jaroniec, M.; Qiao, S.-Z., Determination of the Electron Transfer Number for the Oxygen Reduction Reaction: From Theory to Experiment. *ACS Catalysis* **2016,** *6* (7), 4720-4728.

185. Arvia, A. J.; Salvarezza, R. C.; Triaca, W. E., Noble Metal Surfaces and Electrocatalysis. Review and Perspectives. *Journal of New Materials for Electrochemical Systems* **2004,** *7*, 133-143.

186. Schmickler, W., In Search of Lost Platinum. *ChemPhysChem* **2013,** *14* (5), 881-883.

187. Pourbaix, J. N.; Van Muylder, J., Electrochemical Properties of the Platinum Metals | Johnson Matthey Technology Review. *Platinum Metals Review* **1959,** *3* (2), 47-47.

188. Sahoo, M. K.; Rao, G. R., Enhanced Methanol Electro-Oxidation Activity of Pt/rGO Electrocatalyst Promoted by NbC/Mo2C Phases. *ChemistrySelect* **2020,** *5* (13), 3805-3814.

189. Ding, L.-X.; Liang, C.-L.; Xu, H.; Wang, A.-L.; Tong, Y.-X.; Li, G.-R., Porous Hollow Nanorod Arrays Composed of Alternating Pt and Pd Nanocrystals with Superior Electrocatalytic Activity and Durability for Methanol Oxidation. *Advanced Materials Interfaces* **2014,** *1* (3), 1400005.

190. de Souza, J. P. I.; Queiroz, S. L.; Bergamaski, K.; Gonzalez, E. R.; Nart, F. C., Electro-Oxidation of Ethanol on Pt, Rh, and PtRh Electrodes. A Study Using DEMS and in-Situ FTIR Techniques. *The Journal of Physical Chemistry B* **2002,** *106* (38), 9825-9830.

191. Bach Delpeuch, A.; Asset, T.; Chatenet, M.; Cremers, C., Influence of the Temperature for the Ethanol Oxidation Reaction (EOR) on Pt/C, Pt-Rh/C and Pt-Rh-SnO2/C. *Fuel Cells* **2015,** *15* (2), 352-360.

192. Li, M.; Liu, P.; Adzic, R. R., Platinum Monolayer Electrocatalysts for Anodic Oxidation of Alcohols. *The Journal of Physical Chemistry Letters* **2012,** *3* (23), 3480-3485.

193. Stamenkovic, V.; Markovic, N. M.; Ross, P. N. N.; M. Markovic, N.; Ross, P. N. N., Structure-relationships in electrocatalysis: oxygen reduction and hydrogen oxidation reactions on Pt(111) and Pt(100) in solutions containing chloride ions. *Journal of Electroanalytical Chemistry* **2001,** *500* (1-2), 44-51.

194. Cong, Y.; Yi, B.; Song, Y., Hydrogen oxidation reaction in alkaline media: From mechanism to recent electrocatalysts. *Nano Energy* **2018,** *44*, 288-303.

195. Zhu, J.; Hu, L.; Zhao, P.; Lee, L. Y. S.; Wong, K.-Y., Recent Advances in Electrocatalytic Hydrogen Evolution Using Nanoparticles. *Chemical Reviews* **2020,** *120* (2), 851-918.

196. Stamenkovic, V. R.; Strmcnik, D.; Lopes, P. P.; Markovic, N. M., Energy and fuels from electrochemical interfaces. 2016; Vol. 16, pp 57-69.

197. Greeley, J.; Stephens, I. E. L.; Bondarenko, A. S.; Johansson, T. P.; Hansen, H. A.; Jaramillo, T. F.; Rossmeisl, J.; Chorkendorff, I.; Nørskov, J. K., Alloys of platinum and early transition metals as oxygen reduction electrocatalysts. *Nature Chemistry* **2009,** *1* (7), 552-556.

198. Wang, Y.; Chen, K. S.; Mishler, J.; Cho, S. C.; Adroher, X. C., A review of polymer electrolyte membrane fuel cells: Technology, applications, and needs on fundamental research. *Applied Energy* **2011,** *88* (4), 981-1007.

199. Daubinger, P.; Kieninger, J.; Unmussig, T.; Urban, G. A., Electrochemical characteristics of nanostructured platinum electrodes--a cyclic voltammetry study. *Phys Chem Chem Phys* **2014,** *16* (18), 8392-9.

200. Campos-Roldán, C. A.; Alonso-Vante, N., The Hydrogen Oxidation Reaction in Alkaline Medium: An Overview. *Electrochemical Energy Reviews* **2019,** *2* (2), 312-331.

201. Sheng, W.; Zhuang, Z.; Gao, M.; Zheng, J.; Chen, J. G.; Yan, Y., Correlating hydrogen oxidation and evolution activity on platinum at different pH with measured hydrogen binding energy. *Nature Communications* **2015,** *6* (1), 5848.

202. Souza-Garcia, J.; Climent, V.; Feliu, J. M., Voltammetric characterization of stepped platinum single crystal surfaces vicinal to the (1 1 0) pole. *Electrochemistry Communications* **2009,** *11* (7), 1515-1518.

203. Furuya, N.; Shibata, M., Structural changes at various Pt single crystal surfaces with potential cycles in acidic and alkaline solutions. *Journal of Electroanalytical Chemistry* **1999,** *467* (1), 85-91.

204. Gómez-Marín, A. M.; Rizo, R.; Feliu, J. M., Oxygen reduction reaction at Pt single crystals: a critical overview. *Catalysis Science & Technology* **2014,** *4* (6), 1685-1698.

205. Perez, J.; Villullas, H. M.; Gonzalez, E. R.; Gonzalez, E. R., Structure sensitivity of oxygen reduction on platinum single crystal electrodes in acid solutions. *Journal of Electroanalytical Chemistry* **1997,** *435* (1-2), 179-187.

206. Stamenkovic, V.; Mun, B. S.; Mayrhofer, K. J. J.; Ross, P. N.; Markovic, N. M.; Rossmeisl, J.; Greeley, J.; N?rskov, J. K., Changing the Activity of Electrocatalysts for Oxygen Reduction by Tuning the Surface Electronic Structure. *Angewandte Chemie* **2006,** *118* (18), 2963-2967.

207. Koh, S.; Leisch, J.; Toney, M. F.; Strasser, P., Structure-Activity-Stability Relationships of Pt−Co Alloy Electrocatalysts in Gas-Diffusion Electrode Layers. *The Journal of Physical Chemistry C* **2007,** *111* (9), 3744-3752.

208. Zhang, J.; Vukmirovic, M. B.; Xu, Y.; Mavrikakis, M.; Adzic, R. R., Controlling the Catalytic Activity of Platinum-Monolayer Electrocatalysts for Oxygen Reduction with Different Substrates. *Angewandte Chemie International Edition* **2005,** *44* (14), 2132-2135.

209. Zhang, J.; Vukmirovic, M. B.; Sasaki, K.; Nilekar, A. U.; Mavrikakis, M.; Adzic, R. R., Mixed-Metal Pt Monolayer Electrocatalysts for Enhanced Oxygen Reduction Kinetics. *Journal of the American Chemical Society* **2005,** *127* (36), 12480-12481.

210. Temmel, S. E.; Fabbri, E.; Pergolesi, D.; Lippert, T.; Schmidt, T. J., Tuning the Surface Electrochemistry by Strained Epitaxial Pt Thin Film Model Electrodes Prepared by Pulsed Laser Deposition. *Advanced Materials Interfaces* **2016,** *3* (16), 1-10.

211. Maciá, M. D.; Campiña, J. M.; Herrero, E.; Feliu, J. M., On the kinetics of oxygen reduction on platinum stepped surfaces in acidic media. *Journal of Electroanalytical Chemistry* **2004,** *564* (1-2), 141-150.

212. Wang, J. X.; Markovic, N. M.; Adzic, R. R., Kinetic Analysis of Oxygen Reduction on Pt(111) in Acid Solutions: Intrinsic Kinetic Parameters and Anion Adsorption Effects. *Journal of Physical Chemistry B* **2004,** *108*, 4127-4133.

213. Haruta, M., When Gold Is Not Noble: Catalysis by Nanoparticles. *The Chemical Record* **2003,** *3* (2), 75-87.

214. Meyer, R.; Lemire, C.; Shaikhutdinov, S. K.; Freund, H. J., Surface chemistry of catalysis by gold. *Gold Bulletin* **2004,** *37* (1-2), 72-124.

215. Price, C. A. H.; Pastor-Pérez, L.; Ivanova, S.; Reina, T. R.; Liu, J., The Success Story of Gold-Based Catalysts for Gas- and Liquid-Phase Reactions: A Brief Perspective and Beyond. *Frontiers in Chemistry* **2019,** *7* (691).

216. Quaino, P.; Luque, N. B.; Nazmutdinov, R.; Santos, E.; Schmickler, W., Why is gold such a good catalyst for oxygen reduction in alkaline media? *Angewandte Chemie - International Edition* **2012,** *51* (52), 12997-13000.

217. Yeo, K. M.; Choi, S.; Anisur, R. M.; Kim, J.; Lee, I. S., Surfactant-Free Platinum-on-Gold Nanodendrites with Enhanced Catalytic Performance for Oxygen Reduction. *Angewandte Chemie International Edition* **2011,** *50* (3), 745-748.

218. Cameron, D.; Holliday, R.; Thompson, D., Gold's future role in fuel cell systems. *Journal of Power Sources* **2003,** *118* (1-2), 298-303.

219. Kwon, Y.; Lai, S. C.; Rodriguez, P.; Koper, M. T., Electrocatalytic oxidation of alcohols on gold in alkaline media: base or gold catalysis? *Journal of the American Chemical Society* **2011,** *133* (18), 6914-7.

220. Rodriguez, P.; Koper, M. T. M., Electrocatalysis on gold. *Physical Chemistry Chemical Physics* **2014,** *16* (27), 13583-13583.

221. Liu, Z.-P.; Hu, P.; Alavi, A., Catalytic Role of Gold in Gold-Based Catalysts: A Density Functional Theory Study on the CO Oxidation on Gold. *Journal of the American Chemical Society* **2002,** *124* (49), 14770-14779.

222. Yan, X.; Meng, F.; Xie, Y.; Liu, J.; Ding, Y., Direct N(2)H(4)/H(2)O(2) fuel cells powered by nanoporous gold leaves. *Scientific Reports* **2012,** *2*, 941.

223. Mavrikakis, M.; Stoltze, P.; Nørskov, J. K., Making gold less noble. *Catalysis Letters* **2000,** *64* (2/4), 101-106.

224. Carabineiro, S. A. C.; Nieuwenhuys, B. E., Adsorption of small molecules on gold single crystal surfaces. *Gold Bulletin* **2009,** *42* (4), 288-301.

225. Adžić, R. R. R.; Strbac, S.; Anastasijević, N.; Adzić, R. R.; Štrbac, S.; Anastasijević, N., Electrocatalysis of oxygen on single crystal gold electrodes. *Materials Chemistry and Physics* **1989,** *22* (3), 349-375.

226. McIntire, J. D. E.; Peck, W. F., Jr., Electrochemistry at single-crystal metal electrodes. Electrocatalytic effects of surface atomic structure, defects and adatoms on oxygen reduction. *Proceedings of the symposium on the chemistry and physics of electrocatalysis* **1984,** *84* (12), 102-129.

227. Markovic, N. M.; Tidswell, I. M.; Ross, P. N., Oxygen and Hydrogen Peroxide Reduction on the Au(100) Surface in Alkaline Electrolyte: The Roles of Surface Structure and Hydroxide Adsorption. *Langmuir* **1994,** *10* (1), 1-4.

228. Štrbac, S.; Adžić, R. R.; Štrbac, S.; Adžić, R. R., The influence of OH− chemisorption on the catalytic properties of gold single crystal surfaces for oxygen reduction in alkaline solutions. *Journal of Electroanalytical Chemistry* **1996,** *403* (1-2), 169-181.

229. Taylor, E. J.; Vilambi, N. R. K.; Gelb, A., The Nature of the Catalytic Peak for Oxygen Reduction in Alkaline Electrolyte on the Au(100) Surface. *Journal of The Electrochemical Society* **1989,** *136* (7), 1939-1939.

230. Duan, Z.; Henkelman, G., Theoretical Resolution of the Exceptional Oxygen Reduction Activity of Au(100) in Alkaline Media. *ACS Catalysis* **2019,** *9*, 5567-5573.

231. Mei, D.; He, Z. D.; Zheng, Y. L. L.; Jiang, D. C.; Chen, Y.-X., Mechanistic and kinetic implications on the ORR on a Au(100) electrode: pH, temperature and H–D kinetic isotope effects. *Physical Chemistry Chemical Physics* **2014,** *16* (27), 13762-13762.

232. *Pulsed Laser Deposition of Thin Films Applications Led-growth of Functional Materials* John Wiley & Sons: New Jersey, 2007.

233. Ohring, M., *The materials science of thin films*. Academic Press Limited: San Diego, 1992.

234. Baptista, A.; Silva, F. J. G.; Porteiro, J.; Míguez, J. L.; Pinto, G.; Fernandes, L., On the Physical Vapour Deposition (PVD): Evolution of Magnetron Sputtering Processes for Industrial Applications. *Procedia Manufacturing* **2018,** *17*, 746-757.

235. Martín-Palma, R. J.; Lakhtakia, A., Chapter 15 - Vapor-Deposition Techniques. In *Engineered Biomimicry*, Lakhtakia, A.; Martín-Palma, R. J., Eds. Elsevier: Boston, 2013; pp 383-398.

236. Oszwaldowski, M.; Berus, T.; Sydorczuk, P.; Rzeszutek, J., Apparatus for pulsed laser deposition of semiconductor thin films. *Review of Scientific Instruments* **2003,** *74* (6), 3160-3160.

237. Dijkkamp, D.; Venkatesan, T.; Wu, X. D.; Shaheen, S. A.; Jisrawi, N.; Min-Lee, Y. H.; McLean, W. L.; Croft, M., Preparation of Y-Ba-Cu oxide superconductor thin films using pulsed laser evaporation from high Tc bulk material. *Applied Physics Letters* **1987,** *51* (8), 619-621.

238. Smith, H. M.; Turner, A. F., Vacuum Deposited Thin Films Using a Ruby Laser. *Appl. Opt.* **1965,** *4* (1), 147-148.

239. Douglas, H. L.; Geohegan, D. B.; Puretzky, A. A.; Norton, D. P.; Rouleau, C. M., Synthesis of Novel Thin-Film Materials by Pulsed Laser Deposition. *Science* **1996,** *273* (5277), 898-903.

240. Kim, H.; Sutto, T. E.; Piqué, A., Laser materials processing for micropower source applications: a review. *Journal of Photonics for Energy* **2014,** *4* (1), 040992-040992.

241. Wang, K., *Laser Based Fabrication of Graphene*. InTechOpen: 2013.

242. Blank, D. H. A.; Dekkers, M.; Rijnders, G., Pulsed laser deposition in Twente: from research tool towards industrial deposition. *Journal of Physics D: Applied Physics* **2014,** *47* (3), 034006-034006.

243. Greer, J. A., History and current status of commercial pulsed laser deposition equipment. *Journal of Physics D: Applied Physics* **2014,** *47* (3), 034005-034005.

244. Greer, J. A., Large-area pulsed laser deposition: Techniques and applications. *Journal of Vacuum Science & Technology A: Vacuum, Surfaces, and Films* **1995,** *13* (3), 1175-1175.

245. Ashfold, M. N. R.; Claeyssens, F.; Fuge, G. M.; Henley, S. J.; Mochizuki, T.; Masuda, K.; Kakihana, M.; Tachibana, T., Pulsed laser ablation and deposition of thin films. *Chemical Society Reviews* **2004,** *33* (1), 23-23.

246. Tolstova, Y.; Omelchenko, S. T.; Shing, A. M.; Atwater, H. A., Heteroepitaxial growth of Pt and Au thin films on MgO single crystals by bias-assisted sputtering. *Scientific Reports* **2016,** *6* (1), 23232.

247. Rijnders, G.; Blank, D. H. A., Chapter 8 - Growth Kinetics During Pulsed Laser Deposition. In *Pulsed Laser Deposition of Thin Films Applications Led-growth of Functional Materials* Eason, R., Ed. John Wiley & Sons: New Jersey, 2007; pp 177-190.

248. Dos Santos, M. C.; Machado, S. A. S., Electrochemical Deposition of the First Cd Monolayer on Polycrystalline Pt and Au Electrodes. An Upd Study. *Journal of the Brazilian Chemical Society* **1998,** *9* (3), 211-218.

249. Seel, S. C.; Thompson, C. V.; Hearne, S. J.; Floro, J. A., Tensile stress evolution during deposition of Volmer–Weber thin films. *Journal of Applied Physics* **2000,** *88* (12), 7079-7088.

250. Floro, J. A.; Chason, E.; Cammarata, R. C.; Srolovitz, D. J., Physical Origins of Intrinsic Stresses in Volmer–Weber Thin Films. *MRS Bulletin* **2002,** *27* (1), 19-25.

251. Hu, S. M., Misfit dislocations and critical thickness of heteroepitaxy. *Journal of Applied Physics* **1991,** *69* (11), 7901-7903.

252. Koch, R.; Winau, D.; Rieder, K. H., The intrinsic stress of polycrystalline and epitaxial thin metal films. *Physica Scripta* **1993,** *1993* (T49B), 539-543.

253. Koch, R.; Winau, D.; Rieder, K. H., Intrinsic stress of epitaxial thin films. *Physica Scripta* **1993,** *1993* (T49B), 539-543.

254. Doerner, M. F.; Nix, W. D., Stresses and deformation processes in thin films on substrates. *Critical Reviews in Solid State and Materials Sciences* **1988,** *14* (3), 225-268.

255. Zhang, J.-M.; Ma, F.; Xu, K.-W., Calculation of the surface energy of FCC metals with modified embedded-atom method. *Applied Surface Science* **2004,** *229* (1-4), 34-42.

256. Koper, M. T. M., Structure sensitivity and nanoscale effects in electrocatalysis. *Nanoscale* **2011,** *3* (5), 2054-2073.

257. Duca, M.; Kightley, J.; Garbarino, S.; Guay, D., The Art of Decoration: Rhodium-Modified Platinum Films with Preferential (100) Orientation as Electrocatalysts for Nitrate Reduction and Dimethyl Ether Oxidation. *The Journal of Physical Chemistry C* **2017,** *121* (28), 15233-15247.

258. Lu, L.; Yin, G.; Tong, Y.; Zhang, Y.; Gao, Y.; Osawa, M.; Ye, S., Electrochemical behaviors of dimethyl ether on platinum single crystal electrodes. Part II: Pt(100). *Journal of Electroanalytical Chemistry* **2010,** *642* (1), 82-91.

259. Soares, C. O.; Rodríguez, O.; Buvat, G.; Duca, M.; Garbarino, S.; Guay, D.; Denuault, G.; Tavares, A. C., Sampled current voltammetry for kinetic studies on materials unsuitable for rotating discs or microelectrodes: Application to the oxygen reduction reaction in acidic medium. *Electrochimica Acta* **2020,** *362*.

260. Perry, S. C.; Denuault, G., Transient study of the oxygen reduction reaction on reduced Pt and Pt alloys microelectrodes: evidence for the reduction of pre-adsorbed oxygen species linked to dissolved oxygen. *Phys. Chem. Chem. Phys.* **2015,** *17* (44), 30005-30012.

261. Lebedeva, M. V.; Pierron-Bohnes, V.; Goyhenex, C.; Papaefthimiou, V.; Zafeiratos, S.; Nazmutdinov, R. R.; Da Costa, V.; Acosta, M.; Zosiak, L.; Kozubski, R.; Muller, D.; Savinova, E. R., Effect of the chemical order on the electrocatalytic activity of model PtCo electrodes in the oxygen reduction reaction. *Electrochimica Acta* **2013,** *108*, 605-616.

262. Konopka, S. J.; McDuffie, B., Diffusion coefficients of ferri- and ferrocyanide ions in aqueous media, using twin-electrode thin-layer electrochemistry. *Analytical Chemistry* **1970,** *42* (14), 1741-1741.

263. El-Deab, M. S.; Ohsaka, T., Hydrodynamic voltammetric studies of the oxygen reduction at gold nanoparticles-electrodeposited gold electrodes. *Electrochimica Acta* **2002,** *47* (26), 4255-4261.

264. Deng, Y.-J.; Arenz, M.; Wiberg, G. K. H., Equilibrium coverage of OH ad in correlation with platinum catalyzed fuel cell reactions in HClO 4. *Electrochemistry Communications* **2015,** *53*, 41-44.

265. Damjanovic, A.; Brusic, V., Electrode kinetics of oxygen reduction on oxide-free platinum electrodes. *Electrochimica Acta* **1967,** *12* (6), 615-628.

266. Banham, D. W.; Soderberg, J. N.; Birss, V. I., Pt/Carbon Catalyst Layer Microstructural Effects on Measured and Predicted Tafel Slopes for the Oxygen Reduction Reaction. *The Journal of Physical Chemistry C* **2009,** *113* (23), 10103-10111.

267. Darling, H. E., Conductivity of Sulfuric Acid Solutions. *Journal of Chemical & Engineering Data* **1964,** *9* (3), 421-426.

268. Bohinc, K.; Kralj-Iglič, V.; Iglič, A., Thickness of electrical double layer. Effect of ion size. *Electrochimica Acta* **2001,** *46* (19), 3033-3040.

269. Aziz, M. J., Film growth mechanisms in pulsed laser deposition. *Applied Physics A* **2008,** *93* (3), 579-587.

270. Fewster, P. F., *X-Ray Scattering from Semiconductors*. 2nd edition ed.; Imperial College Press London, UK, 2003; p 316-316.

271. Trasatti, S.; Petri, A.; Niki, K., Real surface area measurements in electrochemistry *Pure & Applied Chemistry* **1991,** *63* (5), 711-734.

272. Wroblowa, H.; Rao, M. L. B.; Damjanovic, A.; Bockris, J. O. M., Adsorption and kinetics at platinum electrodes in the presence of oxygen at zero net current. *Journal of Electroanalytical Chemistry* **1967,** *15*, 139-150.

273. Kongkanand, A.; Ziegelbauer, J. M., Surface platinum electrooxidation in the presence of oxygen. *Journal of Physical Chemistry C* **2012,** *116* (5), 3684-3693.

274. Attard, G. A.; Brew, A., Cyclic voltammetry and oxygen reduction activity of the Pt{1 1 0}-(1 × 1) surface. *Journal of Electroanalytical Chemistry* **2015,** *747*, 123-129.

275. Attard, G. A.; Hunter, K.; Wright, E.; Sharman, J.; Martínez-Hincapié, R.; Feliu, J. M., The voltammetry of surfaces vicinal to Pt{110}: Structural complexity simplified by CO cooling. *Journal of Electroanalytical Chemistry* **2017,** *793*, 137-146.

276. Gisbert, R.; García, G.; Koper, M. T. M. M., Oxidation of carbon monoxide on poly-oriented and single-crystalline platinum electrodes over a wide range of pH. *Electrochimica Acta* **2011,** *56* (5), 2443-2449.

277. Santos, E.; Juarez, F.; Quaino, P.; Belletti, G.; Goduljan, A.; de Campos Pinto, L. M.; Ignaczak, A.; Nazmutdinov, R.; Schmickler, W., Oxygen Reduction in Alkaline Media—a Discussion. *Electrocatalysis* **2017,** *8* (6), 554-564.

278. Ignaczak, A.; Santos, E.; Schmickler, W., Oxygen reduction reaction on gold in alkaline solutions – The inner or outer sphere mechanisms in the light of recent achievements. Elsevier: 2019; Vol. 14, pp 180-185.

279. Bard, A. J., Inner-Sphere Heterogeneous Electrode Reactions. Electrocatalysis and Photocatalysis: The Challenge. *Journal of the American Chemical Society* **2010,** *132* (22), 7559-7567.

280. Zheng, Y. L.; Mei, D.; Chen, Y. X.; Ye, S., The redox reaction of hydrogen peroxide at an Au(100) electrode: Implications for oxygen reduction kinetics. *Electrochemistry Communications* **2014,** *39*, 19-21.

281. Kim, J.; Gewirth, A. A.; And, J. K.; Gewirth*, A. A., Mechanism of Oxygen Electroreduction on Gold Surfaces in Basic Media. *Journal of Physical Chemistry B* **2006,** *110* (06), 2565-2571.

282. Štrbac, S.; Adžić, R. R., The influence of pH on reaction pathways for O2 reduction on the Au(100) face. *Electrochimica Acta* **1996,** *41* (18), 2903-2908.

283. Ignaczak, A.; Nazmutdinov, R.; Goduljan, A.; de Campos Pinto, L. M.; Juarez, F.; Quaino, P.; Santos, E.; Schmickler, W., A scenario for oxygen reduction in alkaline media. *Nano Energy* **2016,** *29*, 362-368.

284. Suemitsu, M.; Filimonov, S. N., Understanding crystal growth mechanisms in silicon–germanium (SiGe) nanostructures. In *Silicon–Germanium (SiGe) Nanostructures*, Shiraki, Y.; Usami, N., Eds. Woodhead Publishing: 2011; pp 45-71.

285. Angerstein-Kozlowska, H.; Conway, B. E.; Hamelin, A.; Stoicoviciu, L., Elementary steps of electrochemical oxidation of single-crystal planes of Au-I. Chemical basis of processes involving geometry of anions and the electrode surfaces. *Electrochimica Acta* **1986,** *31* (8), 1051-1061.

286. Dakkouri, A., Reconstruction phenomena at gold/electrolyte interfaces: an in-situ STM study of Au(100). *Solid State Ionics* **1997,** *94* (1-4), 99-114.

287. Kolb, D. M.; Schneider, J., Surface reconstruction in electrochemistry: Au(100-(5 × 20), Au(111)-(1 × 23) and Au(110)-(1 × 2). *Electrochimica Acta* **1986,** *31* (8), 929-936.

288. *Handbook of Fuel Cells Fundamentals Technology and Applications Volume 2 Electrocatalysis*. John Wiley & Sons, Ltd: Chichester, 2003; Vol. 2, p 473-473.

289. Strbac, S.; Hamelin, A.; Adzić, R. R., Electrochemical indication of surface reconstruction of (100), (311) and (111) gold faces in alkaline solutions. *Journal of Electroanalytical Chemistry* **1993,** *362* (1-2), 47-53.

290. Blizanac, B. B.; Lucas, C. A.; Gallagher, M. E.; Arenz, M.; Ross, P. N.; Marković, N. M., Anion Adsorption, CO Oxidation, and Oxygen Reduction Reaction on a Au(100) Surface: The pH Effect. *Journal of Physical Chemistry B* **2004,** *108* (2), 625-634.

291. Paliteiro, C., (100)-Type behaviour of polycrystalline gold towards O2 reduction. *Electrochimica Acta* **1994,** *39* (11-12), 1633-1639.

292. Srejić, I.; Smiljanić, M.; Rakočević, Z.; Štrbac, S., Oxygen Reduction on Au(100)-like Polycrystalline Gold Electrode in Alkaline Solution. *International Journal of Electrochemical Science* **2016,** *1112* (10), 10436-10448.

293. Zurilla, R. W.; Yeager, E., The Kinetics of the Oxygen Reduction Reaction on Gold in Alkaline Solution. *Journal of Electrochemical Society: Electrochemical Science and Technology* **1978,** *125* (7), 1103-1109.

294. Anastasijević, N. A.; Štrbac, S.; Adžić, R. R., Oxygen reduction on the Au (311) electrode surface in alkaline electrolyte. *Journal of Electroanalytical Chemistry* **1988,** *240* (1-2), 239-252.

295. Liu, Z. J.; Shen, Y. G., Temperature effect on surface roughening of thin films. *Surface Science* **2005,** *595* (1-3), 20-29.

296. Zhang, J.-M.; Ma, F.; Xu, K.-W., Calculation of the surface energy of FCC metals with modified embedded-atom method. *Applied Surface Science* **2004,** *229* (1), 34-42.

297. Vitos, L.; Ruban, A. V.; Skriver, H. L.; Kollár, J., The surface energy of metals. *Surface Science* **1998,** *411* (1-2), 186-202.

298. Floro, J. A.; Hearne, S. J.; Hunter, J. A.; Kotula, P.; Chason, E.; Seel, S. C.; Thompson, C. V., The dynamic competition between stress generation and relaxation mechanisms during coalescence of Volmer-Weber thin films. *Journal of Applied Physics* **2001,** *89* (9), 4886-4897.

299. Yu, H. Z.; Thompson, C. V., Grain growth and complex stress evolution during Volmer–Weber growth of polycrystalline thin films. *Acta Materialia* **2014,** *67*, 189-198.

300. Waseda, Y.; Matsubara, E.; Shinoda, K., *X-Ray Diffraction Crystallography*. 2011.

301. Miranda, M. A. R.; Sasaki, J. M., The limit of application of the Scherrer equation. *Acta Crystallogr A Found Adv* **2018,** *74* (Pt 1), 54-65.

302. Cullity, B. D., *Elements of X-Ray Diffraction*. 2nd ed.; Addison-Wesley Publishing Company Inc.: 1978.

303. Stringfellow, G. B., Epitaxy. *Reports on Progress in Physics* **1982,** *45* (5), 469-525.

304. Cai, Y.; Adzic, R. R., Platinum Monolayer Electrocatalysts for the Oxygen Reduction Reaction: Improvements Induced by Surface and Subsurface Modifications of Cores. *Advances in Physical Chemistry* **2011,** *2011*, 1-16.

305. Temmel, S. E.; Fabbri, E.; Pergolesi, D.; Lippert, T.; Schmidt, T. J., Tuning the Surface Electrochemistry by Strained Epitaxial Pt Thin Film Model Electrodes Prepared by Pulsed Laser Deposition. *Advanced Materials Interfaces* **2016,** *3* (16), 1600222.

306. Mavrikakis, M.; Hammer, B.; Nørskov, J. K., Effect of strain on the reactivity of metal surfaces. *Physical Review Letters* **1998,** *81* (13), 2819-2822.

307. Kitchin, J. R.; Nørskov, J. K.; Barteau, M. A.; Chen, J. G., Role of Strain and Ligand Effects in the Modification of the Electronic and Chemical Properties of Bimetallic Surfaces.

308. Zheng, X.; Li, L.; Li, J.; Wei, Z., Intrinsic effects of strain on low-index surfaces of platinum: roles of the five 5d orbitals. *Physical Chemistry Chemical Physics* **2019,** *21* (6), 3242-3249.

309. Santos, E.; Quaino, P.; Schmickler, W., On the electrocatalysis of nanostructures: Monolayers of a foreign atom (Pd) on different substrates M(111). *Electrochimica Acta* **2010,** *55* (14), 4346-4352.

310. Xu, Y.; Mavrikakis, M., Adsorption and Dissociation of O2 on Gold Surfaces: Effect of Steps and Strain. *The Journal of Physical Chemistry B* **2003,** *107* (35), 9298-9307.

311. Westsson, E.; Picken, S.; Koper, G., The effect of lattice strain on catalytic activity. *Chemical Communications* **2019,** *55* (9), 1338-1341.

312. Yang, J.; Chen, X.; Yang, X.; Ying, J. Y., Stabilization and compressive strain effect of AuCu core on Pt shell for oxygen reduction reaction. *Energy and Environmental Science* **2012,** *5* (10), 8976-8981.

313. Asano, M.; Kawamura, R.; Sasakawa, R.; Todoroki, N.; Wadayama, T., Oxygen Reduction Reaction Activity for Strain-Controlled Pt-Based Model Alloy Catalysts: Surface Strains and Direct Electronic Effects Induced by Alloying Elements. *ACS Catalysis* **2016,** *6* (8), 5285-5289.

314. Wang, X.; Zhu, Y.; Vasileff, A.; Jiao, Y.; Chen, S.; Song, L.; Zheng, B.; Zheng, Y.; Qiao, S.-Z., Strain Effect in Bimetallic Electrocatalysts in the Hydrogen Evolution Reaction. *ACS Energy Letters* **2018,** *3* (5), 1198-1204.

315. Yan, K.; Maark, T. A.; Khorshidi, A.; Sethuraman, V. A.; Peterson, A. A.; Guduru, P. R., The Influence of Elastic Strain on Catalytic Activity in the Hydrogen Evolution Reaction. *Angewandte Chemie International Edition* **2016,** *55* (21), 6175-6181.

316. Kibler, L. A.; El-Aziz, A. M.; Hoyer, R.; Kolb, D. M., Tuning Reaction Rates by Lateral Strain in a Palladium Monolayer. *Angewandte Chemie International Edition* **2005,** *44* (14), 2080-2084.

317. Huang, H.; Jia, H.; Liu, Z.; Gao, P.; Zhao, J.; Luo, Z.; Yang, J.; Zeng, J., Understanding of Strain Effects in the Electrochemical Reduction of CO2: Using Pd Nanostructures as an Ideal Platform. *Angewandte Chemie International Edition* **2017,** *56* (13), 3594-3598.

318. Rabis, A.; Rodriguez, P.; J. Schmidt, T., Electrocatalysis for Polymer Electrolyte Fuel Cells: Recent Achievements and Future Challenges. *ACS Catalysis* **2012,** *2* (5), 864-890.

319. Kattel, S.; Wang, G., Beneficial compressive strain for oxygen reduction reaction on Pt (111) surface. *The Journal of Chemical Physics* **2014,** *141* (12), 124713.

320. Kim, J.-H.; Chang, S.; Kim, Y.-T., Compressive strain as the main origin of enhanced oxygen reduction reaction activity for Pt electrocatalysts on chromium-doped titania support. *Applied Catalysis B: Environmental* **2014,** *158-159*, 112-118.

321. Du, M.; Cui, L.; Cao, Y.; Bard, A. J., Mechanoelectrochemical Catalysis of the Effect of Elastic Strain on a Platinum Nanofilm for the ORR Exerted by a Shape Memory Alloy Substrate. *Journal of the American Chemical Society* **2015,** *137* (23), 7397-7403.

322. Mavrikakis, M.; Stoltze, P.; Norskov, J. K., Making gold less noble. *Catalysis Letters* **2000,** *64* (2-4), 101-106.

323. Pas, I. A.; Fako, E.; Dobrota, A. S.; Lo, r.; Skorodumova, N. V.; Mentus, S. V., Atomically Thin Metal Films on Foreign Substrates: From Lattice Mismatch to Electrocatalytic Activity. **2019,** *20*, 39-39.

324. Venables, J. A.; Spiller, T.; Hanbucken, M.; Spiller, G. D. T. T.; Hanbucken, M., Nucleation and growth of thin films. *Reports on Progress in Physics* **1984,** *47* (4), 399-459.

325. Chason, E.; Sheldon, B. W.; Freund, L. B.; Floro, J. A.; Hearne, S. J., Origin of Compressive Residual Stress in Polycrystalline Thin Films. *Physical Review Letters* **2002,** *88* (15), 156103-156103.

326. Floro, J. A.; Hearne, S. J.; Hunter, J. A.; Kotula, P.; Chason, E.; Seel, S. C.; Thompson, C. V., The dynamic competition between stress generation and relaxation mechanisms during coalescence of Volmer–Weber thin films. *Journal of Applied Physics* **2001,** *89* (9), 4886-4897.

327. Sudha, V.; Sangaranarayanan, M. V., Underpotential Deposition of Metals: Structural and Thermodynamic Considerations. *The Journal of Physical Chemistry B* **2002,** *106* (10), 2699-2707.

328. Herrero, E.; Lisa J. Buller, A.; Abruña, H. D.; Buller, L. J.; Abruña, H. D., Underpotential Deposition at Single Crystal Surfaces of Au, Pt, Ag and Other Materials. *Chemical Reviews* **2001,** *101*, 1897-1930.

329. Kirowa-Eisner, E.; Bonfil, Y.; Tzur, D.; Gileadi, E., Thermodynamics and kinetics of upd of lead on polycrystalline silver and gold. *Journal of Electroanalytical Chemistry* **2003,** *552* (SUPPL.), 171-183.

330. Hernandez, J.; Solla-Gullon, J.; Herrero, E.; Hernández, J.; Solla-Gullón, J.; Herrero, E., Gold nanoparticles synthesized in a water-in-oil microemulsion: electrochemical characterization and effect of the surface structure on the oxygen reduction reaction. *Journal of Electroanalytical Chemistry* **2004,** *574* (1), 185-196.

331. Hernandez, J.; Solla-Gullón, J.; Herrero, E.; Feliu, J. M.; Aldaz, A., In Situ Surface Characterization and Oxygen Reduction Reaction on Shape-Controlled Gold Nanoparticles. *Journal of Nanoscience and Nanotechnology* **2009,** *9*, 2256-2273.

332. Mitsunaga, T., X-ray thin-film measurement techniques II. Out-of-plane diffraction measurements. *The Rigaku Journal* **2009,** *25* (1).

333. Hernández, J.; Solla-Gullón, J.; Herrero, E.; Aldaz, A.; Feliu, J. M., Electrochemistry of Shape-Controlled Catalysts: Oxygen Reduction Reaction on Cubic Gold Nanoparticles. *The Journal of Physical Chemistry C* **2007,** *111* (38), 14078-14083.

334. Shinagawa, T.; Garcia-Esparza, A. T.; Takanabe, K., Insight on Tafel slopes from a microkinetic analysis of aqueous electrocatalysis for energy conversion. *Scientific Reports* **2015,** *5*.

335. Strmcnik, D. S.; Rebec, P.; Gaberscek, M.; Tripkovic, D.; Stamenkovic, V.; Lucas, C.; Marković, N. M., Relationship between the Surface Coverage of Spectator Species and the Rate of Electrocatalytic Reactions. *The Journal of Physical Chemistry C* **2007,** *111* (50), 18672-18678.

336. Rodríguez, O.; Denuault, G., The electron transfer kinetics of adsorbed species derived by sampled current voltammetry. *Journal of Electroanalytical Chemistry* **2021,** *882*, 115021.

337. Laviron, E., General expression of the linear potential sweep voltammogram in the case of diffusionless electrochemical systems. *Journal of Electroanalytical Chemistry and Interfacial Electrochemistry* **1979,** *101* (1), 19-28.

338. Southampton Electrochemistry, G., *Instrumental Methods in Electrochemistrly*. Woodhead Publishing Limited: Cambridge, 2001.

339. Bligaard, T.; Nørskov, J. K.; Dahl, S.; Matthiesen, J.; Christensen, C. H.; Sehested, J., The Brønsted–Evans–Polanyi relation and the volcano curve in heterogeneous catalysis. *Journal of Catalysis* **2004,** *224* (1), 206-217.

12 APPENDIX I – RECONSTRUCTED SCVS IN N_2

Reconstructed SCVs in N_2 saturated 0.5 M H_2SO_4 electrolyte as part of the experiments reported in Chapter 5.

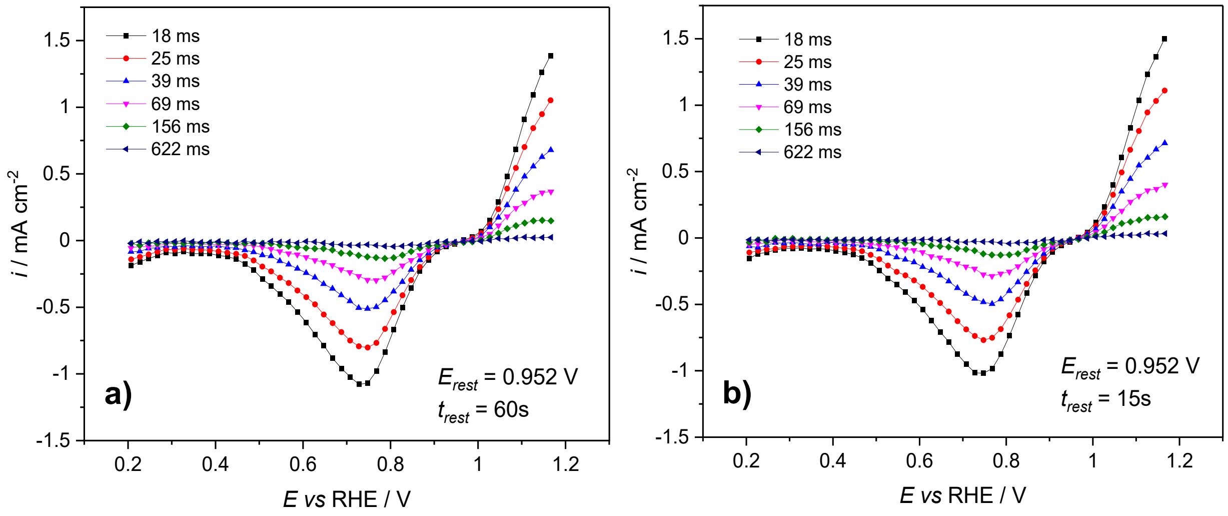

Reconstructed SCVs for E_{rest} = 0.952 V; a) kept for 60 s and b) 15 seconds in N_2 saturated 0.5 H_2SO_4.

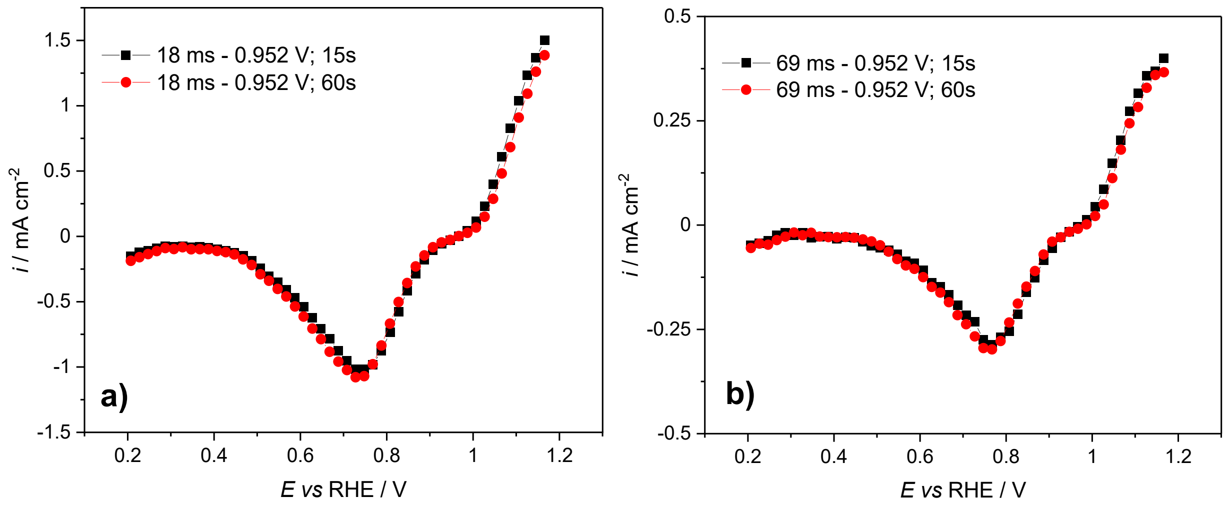

Superimposed reconstructed SCVs for E_{rest} = 0.952 V for 15 and 60 s seconds in N_2 saturated 0.5 H_2SO_4 for a) 18 ms and b) 69 ms.

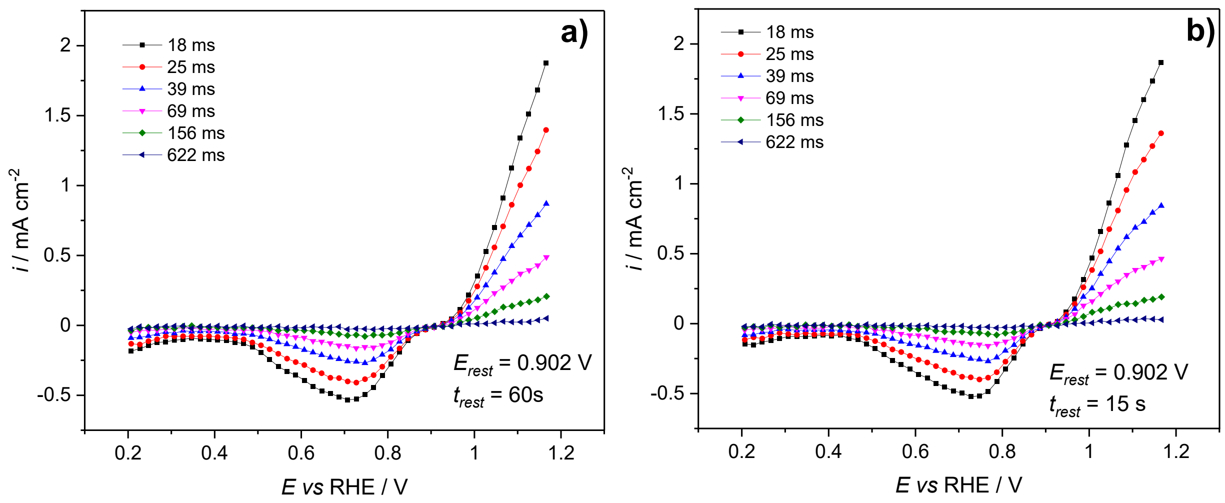

Reconstructed SCVs for E_{rest} = 0.902 V; a) kept for 60 s and b) 15 seconds in N_2 saturated 0.5 H_2SO_4.

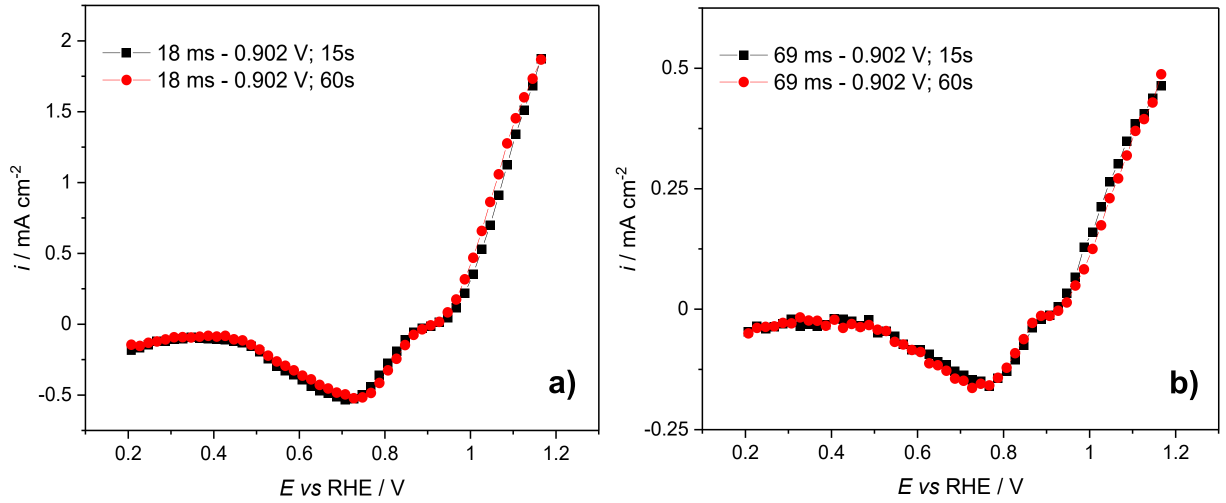

Superimposed reconstructed SCVs for E_{rest} = 0.902 V; for 60 s and 15 seconds in N_2 saturated 0.5 H_2SO_4 for a) 18 ms and b) 69 ms.

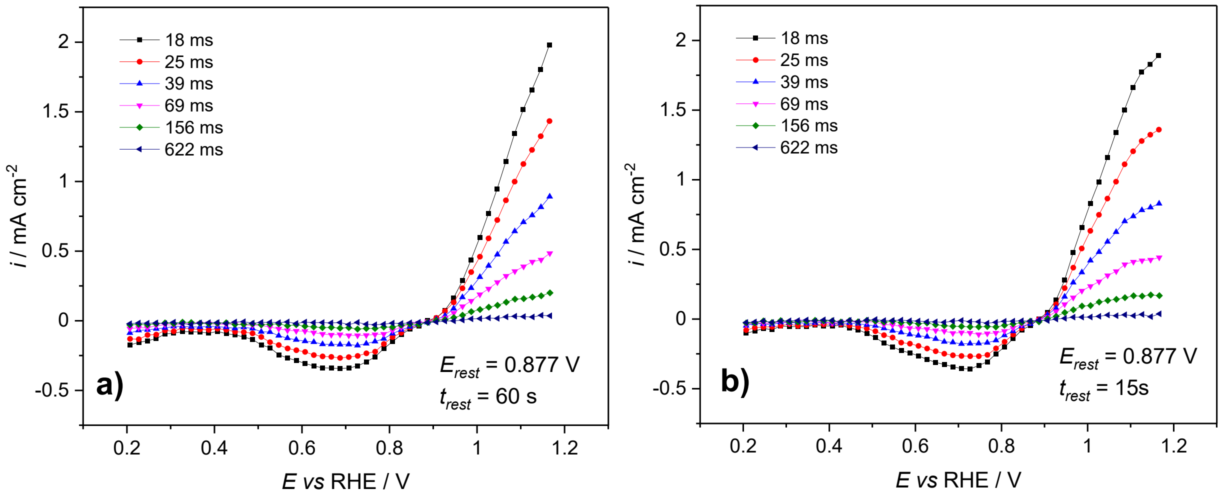

Reconstructed SCVs for E_{rest} = 0.877 V; a) kept for 60 s and b) 15 seconds in N_2 saturated 0.5 H_2SO_4.

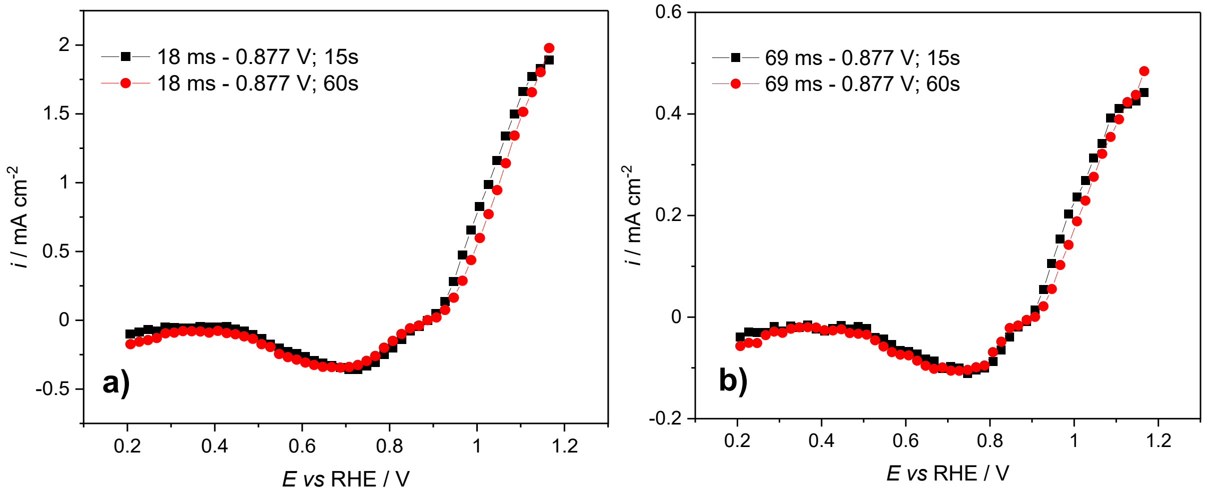

Superimposed reconstructed SCVs for E_{rest} = 0.877 V; for 60 s and 15 seconds in N_2 saturated 0.5 H_2SO_4 for a) 18 ms and b) 69 ms.

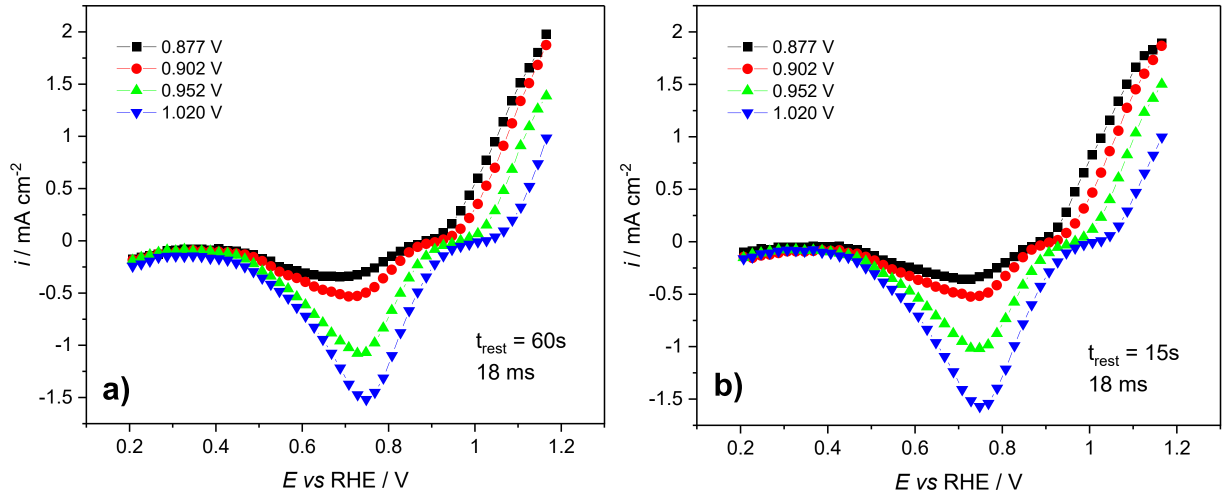

Reconstructed SCVs for the rest potentials studied at 18 ms for rest potentials applied for 60 s in a), and 15 s in b).

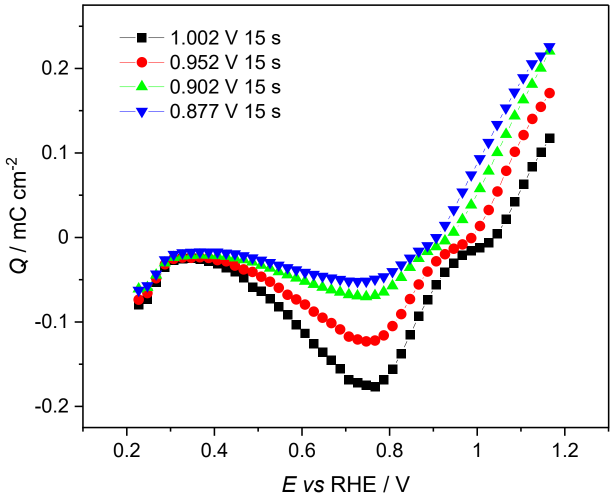

Plots of the charges obtained as a function of the potential for the rest potentials studied applied for 15s.

13 APPENDIX II – TRANSIENTS RECORDED IN N_2 AND O_2

Transients recorded in N_2 and O_2 as part of the set experiments reported in Chapter 5 section 5.4.2.

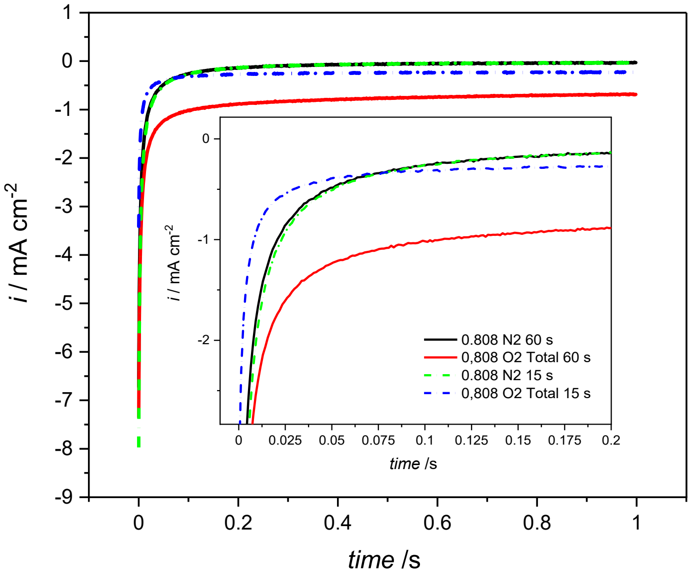

Transients recorded at 0.808 V in N_2, O_2, and background subtracted after 1.002 V rest potential applied for 60 and 15 seconds.

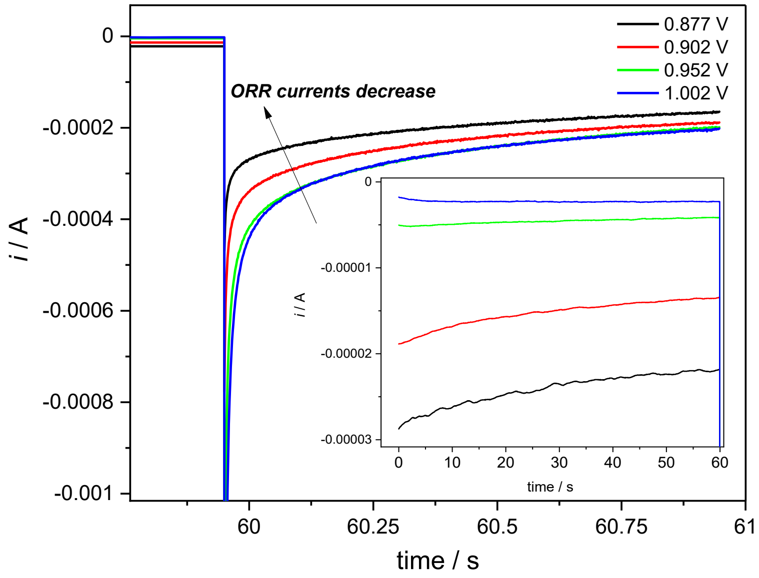

Transients recorded in the presence of O_2 for the rest potentials tested for 60 seconds and for the ORR potential 0.768 V. Inset shows a magnified view of the rest potentials transients.

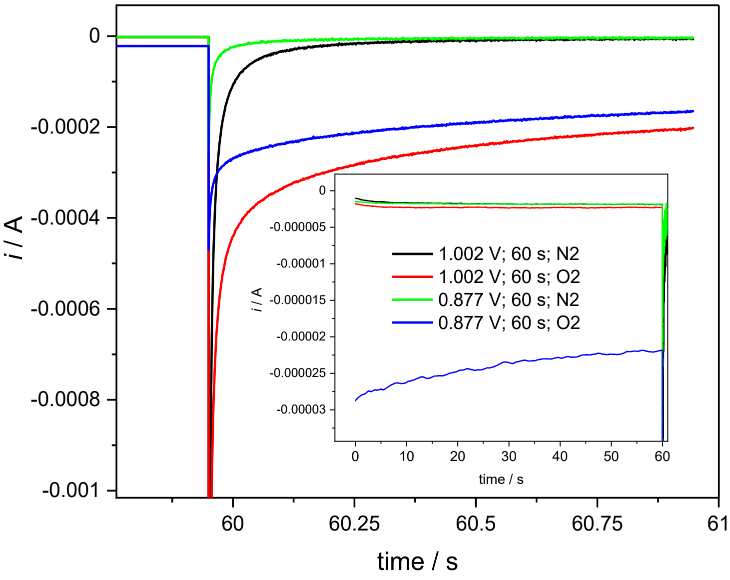

Transients recorded for rest potentials 1.002 V and 0.877 V in presence and absence of O_2 showing rest potential (inset) and the potential step for 0.768 V.

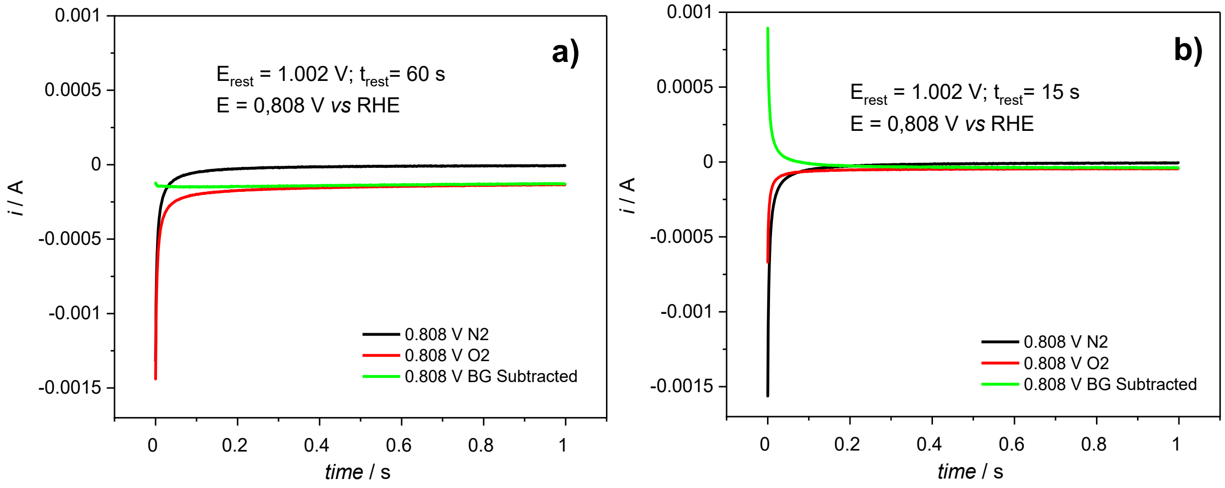

Transients recorded when the pulse potential applied was 0.808 V, after the rest potential, 1.002 V, applied for 60 s in a), and for 15 s in b), in presence and absence of O_2 showing how the rest potential duration affects the ORR currents.

14 APPENDIX III – Au/MgO(100) NORMALIZED SCVs

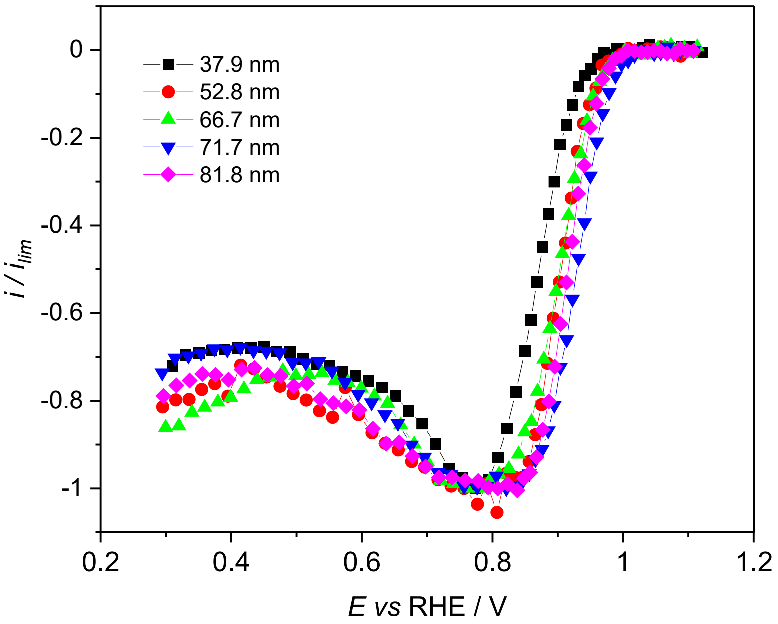

Polarization curves normalized for the limiting currents.